Forschungszentrum Karlsruhe
Technik und Umwelt

Wissenschaftliche Berichte
FZKA 6693

Contributions of the Institut für Kernphysik, Forschungszentrum Karlsruhe and of the Institut für experimentelle Kernphysik, Universität Karlsruhe to the 27th International Cosmic Ray Conference, Hamburg, 2001

A. Haungs (Editor)
Institut für Kernphysik

Februar 2002

Forschungszentrum Karlsruhe

Technik und Umwelt

Wissenschaftliche Berichte

FZKA 6693

Contributions of the Institut für Kernphysik, Forschungszentrum Karlsruhe and of the Institut für experimentelle Kernphysik, Universität Karlsruhe to the 27th International Cosmic Ray Conference, Hamburg, 2001

Andreas Haungs (Editor)

Institut für Kernphysik

Forschungszentrum Karlsruhe GmbH, Karlsruhe

2002

Als Manuskript gedruckt

Forschungszentrum Karlsruhe GmbH
Postfach 3640, 76021 Karlsruhe

Mitglied der Hermann von Helmholtz-Gemeinschaft
Deutscher Forschungszentren (HGF)

ISSN 0947-8620

Abstract

This report samples the contributions to the biannual international cosmic ray conference (ICRC 2001). The scientific activities in cosmic ray physics are focussed on the two experiments **KASCADE** and **AUGER** complemented by a number of contributions reporting about related works.

KASCADE (**KA**rlsruhe **S**hower **C**ore and **A**rray **De**tector) is a multi-detector set-up on the site of the Forschungszentrum Karlsruhe. The different detector systems allow to reconstruct a large set of observables for each single event used as redundant information for the analyses. The main aim of the experiment is the determination of the primary energy spectrum and mass composition of the cosmic rays in the knee region, i.e. at primary energies of 100 TeV - 100 PeV. The contributions of the KASCADE collaboration concentrate on results of various analyses techniques for the evaluation of energy spectra of partial mass groups. The results establish the fact that the knee is dominated by light primaries, whereas the heavy primaries show no kink in the investigated energy region. Further articles relate to aspects of understanding the shower development in the atmosphere (attenuation length, muon arrival times, muon production heights), and to tests of the high-energy hadronic interaction models underlying the reconstruction and analyses procedures of the data. Additionally the new muon detector systems at KASCADE are presented as well as the concept and possibilities of the new experiment **KASCADE Grande**, which is set-up as extension of KASCADE to measure the expected knee of the heavy part of the cosmic rays in the energy region of 100 PeV to 1 EeV.

The physics results are affected by an uncertainty of the modelling of the hadronic interactions in the atmosphere. Recent additions and improvements of the **CORSIKA** (**CO**smic **R**ay **S**imulation for **KA**scade) simulation package are reported. Of importance is here the extrapolation of the interaction mechanisms to energies far above accelerator results and the tests of its validity, which is relevant for the simulation of events for the **AUGER** experiment.

The **Pierre-Auger-Observatory** is presently set-up in Argentina's Mendoza province and consists of a large array of water Cherenkov tanks and 4 air fluorescence detectors. AUGER will measure the origin and type of the highest energy cosmic ray particles above 10 EeV which are still unknown. The Karlsruhe research group participate significantly on the construction and electronics of the fluorescence eyes.

Cosmic ray related contributions in addition to the collaboration works of the KASCADE (Grande) and AUGER experiments are also sampled. These comprise experiments concerning cosmic rays of lower energies (TRACER, PAMIR) and high-energy gamma-ray astronomy (WHIPPLE), as well as the development of new hadronic interaction models (NEXUS) and simulation studies for the atmospheric neutrino problem.

Beiträge des Instituts für Kernphysik, Forschungszentrum Karlsruhe und des Instituts für experimentelle Kernphysik, Universität Karlsruhe zur 27th Int. Cosmic Ray Conference (ICRC), Hamburg, 2001

Zusammenfassung

Der vorliegende Bericht fasst die Beiträge zur zweijährlich stattfindenden internationalen Konferenz zur kosmischen Strahlung (ICRC 2001) zusammen. Die wissenschaftlichen Aktivitäten konzentrieren sich dabei auf die Experimente **KASCADE** und **AUGER,** und werden ergänzt durch eine ganze Reihe von persönlichen Beiträgen zu relevanten Themenbereichen.

KASCADE (**KA**rlsruhe **S**hower **C**ore and **A**rray **De**tector) ist ein Multi-Detektor Aufbau auf dem Gelände des Forschungszentrums Karlsruhe. Die unterschiedlichen Detektorsysteme erlauben die Rekonstruktion einer großen Anzahl von Observablen pro Ereignis. Das Hauptziel des Experimentes ist die Bestimmung des primären Energiespektrums und der Elementzusammensetzung der kosmischen Strahlung im Energiebereich des ‚Knie' (100 TeV – 100 PeV). Die Konferenzbeiträge der KASCADE Kollaboration konzentrieren sich auf die Rekonstruktion von Energiespektren einzelner Massengruppen durch verschiedene methodische Analysetechniken. Die Ergebnisse beweisen nun, dass das Knie durch die leichte primäre Komponente dominiert wird und das Spektrum der schweren Teilchen kein Knie im untersuchten Energiebereich aufweist. Weitere Beiträge beziehen sich auf das Verständnis der Schauerentwicklung in der Atmosphäre (Abschwächungslänge, Myon-Ankunftszeiten, Myon-Produktionshöhen), und auf Tests der den Analysen zugrunde liegenden Modelle zur hochenergetischen hadronischen Wechselwirkung. Außerdem werden die erweiterten Myon-Nachweissysteme von KASCADE und das Konzept und die Möglichkeiten von **KASCADE Grande** vorgestellt. Dieses neue Experiment wird derzeit als Erweiterung von KASCADE aufgebaut, um das zu erwartende Knie der schweren primären Komponente in der kosmischen Strahlung im Energiebereich von 100 PeV bis 1 EeV zu messen.

Die erzielten Resultate sind beeinflusst durch Unsicherheiten in der Simulation hadronischer Wechselwirkungen. Über Erweiterungen und Verbesserungen des **CORSIKA** (**CO**smic **R**ay **S**imulation for **KA**scade) Programms wird berichtet. Hier ist vor allem die Extrapolation der Physik der hadronischen Wechselwirkungen zu höchsten Energien und ihr Test wichtig, da dies relevant für die Simulation von Ereignissen für das **AUGER** Experiment ist.

Das **Pierre-Auger-Observatory** wird momentan in Argentinien aufgebaut und besteht aus einem großem Array aus Wasser-Cherenkov-Tanks und 4 Fluoreszenz-Detektoren. AUGER wird Herkunft und Typ der kosmischen Teilchen höchster Energien über 10 EeV messen. Die Karlsruher Forschungsgruppe leistet einen signifikanten Anteil an der Konstruktion und der Elektronik der Fluoreszenz-Augen.

Zusätzlich zu den kollaborativen Arbeiten an den KASCADE (Grande) und Auger Experimenten werden relevante Themen zur kosmischen Strahlung diskutiert. Dies beinhaltet sowohl Experimente zur kosmischen Strahlung niedererer Energien (TRACER, PAMIR) und hochenergetische Gamma Astronomie (WHIPPLE), als auch die Entwicklung neuer hadronischer Wechselwirkungsmodelle (NEXUS) und Simulationsstudien zum atmosphärischen Neutrino Problem.

CONTENTS

Proceedings of ICRC 2001: 97 © Copernicus Gesellschaft 2001

ICRC 2001

Primary energy spectra of cosmic rays selected by mass groups in the knee region

H. Ulrich[1], T. Antoni[2], W.D. Apel[2], F. Badea[3], K. Bekk[2], A. Bercuci[2], H. Blümer[2,1], E. Bollmann[2], H. Bozdog[3], I.M. Brancus[3], C. Büttner[2], A. Chilingarian[4], K. Daumiller[1], P. Doll[2], J. Engler[2], F. Feßler[2], H.J. Gils[2], R. Glasstetter[1], R. Haeusler[2], W. Hafemann[2], A. Haungs[2], D. Heck[2], J.R. Hörandel[1], T. Holst[2], A. Iwan[1,5], K-H. Kampert[2,1], J. Kempa[5,+], H.O. Klages[2], J. Knapp[1,¶], G. Maier[2], H.J. Mathes[2], H.J. Mayer[2], J. Milke[2], M. Müller[2], R. Obenland[2], J. Oehlschläger[2], M. Petcu[3], H. Rebel[2], M. Risse[2], M. Roth[2], H. Schieler[2], J. Scholz[2], T. Thouw[2], B. Vulpescu[3], J.H. Weber[1], J. Wentz[2], J. Wochele[2], and J. Zabierowski[6]

[1]Institut für Experimentelle Kernphysik, University of Karlsruhe, 76021 Karlsruhe, Germany
[2]Institut für Kernphysik, Forschungszentrum Karlsruhe, 76021 Karlsruhe, Germany
[3]National Institute of Physics and Nuclear Engineering, 7690 Bucharest, Romania
[4]Cosmic Ray Division, Yerevan Physics Institute, Yerevan 36, Armenia
[5]Department of Experimental Physics, University of Lodz, 90236 Lodz, Poland
[6]Soltan Institute for Nuclear Studies, 90950 Lodz, Poland
[+]now at: Warsaw University of Technology, 09-400 Plock, Poland
[¶]now at: University of Leeds, Leeds LS2 9JT, U.K.

Abstract. The KASCADE experiment measures the electron and muon number of extensive air showers in the knee region with high precision. From these data shower size spectra for electrons and muons are constructed. An analysis is presented in which electron and muon size spectra in three different zenith angle bins are analysed simultaneously. With a four component assumption for the mass composition of primary cosmic rays (hydrogen, helium, carbon and iron) and using unfolding methods taking into account shower fluctuations and experimental effects energy spectra of these mass groups in the range between 10^{15} and 10^{17} eV are reconstructed. Each energy spectrum shows a steepening of the index of the resulting power law with a knee-like structure. The positions of the individual knees suggest a rigidity dependence.

1 Introduction

The KASCADE experiment (Klages et al., 1997) located at the site of the Forschungszentrum Karlsruhe, Germany at an altitude of 110 m a.s.l. measures various observables of an extensive air shower especially in the *knee*-region (10^{14} – 10^{17}eV. It consists of three major detector components: the scintillation detector array, the muon tracking detector and the central detector complex.

The field array covers an area of $200 \times 200\text{m}^2$ and consists of 252 detector stations for the detection of the electron and muon component. The stations in the inner part of the array contains four liquid scintillation counters to measure the electromagnetic part of the shower. The outer stations contain only two of these detectors but additionally below an iron-lead absorber plastic scintillators to measure muons. Using the information of these detectors it is possible to reconstruct the location of the shower core, the direction of the shower and using the NKG formula the total number of electrons N_e and the so called *truncated muon number* $N_\mu^{tr.}$. The latter one is the number of muons inside a ring around the shower core with an inner radius of 40 m and outer radius of 200 m. Simulations have shown that this quantity is more robust against systematical reconstruction errors than the total muon number. During the reconstruction the contributions of accompanying particles in each detector are taken into account. A detailed description of the setup and the reconstruction procedure can be found in (Doll et al., 1990) and (Antoni et al., 2001).

In the present analysis the electron and truncated muon number are used. The data were taken from May 1998 until December 1999 and correspond to a total number of about 35 Mio. showers. The aim of the analysis is to determine the primary energy spectra of different mass groups by analysing the shower size spectra of N_e and $N_\mu^{tr.}$ in intervals of the zenith angle simultaneously.

2 Outline of the Analysis

To reconstruct the primary energy spectrum by means of the shower size spectra (electron size or/and muon size spectra) it is useful to apply the relation between the measured flux

Correspondence to: ulrich@ik1.fzk.de

of the shower size $dJ/d\lg N$ and the primary energy flux $dJ(\lg E)/d\lg E$ for individual types of primary particles. This relation is a Fredholm integral equation of 1st kind:

$$\frac{dJ_A}{d\lg N} = \int_{-\infty}^{+\infty} \frac{dJ_A(\lg E)}{d\lg E} p_A(\lg N \mid \lg E)\, d\lg E \qquad (1)$$

$p_A(\lg N \mid \lg E)$ is the probability for a primary particle of type A with energy $\lg E$ to be reconstructed as an air shower with shower size $\lg N$. This *kernel function* p_A factorizes into three parts: the shower fluctuations $s_A(\lg N^t \mid \lg E)$, the efficiency $\epsilon_A(\lg N^t)$ for the triggering of the measurement, and the reconstruction accuracy $r_A(\lg N \mid \lg N^t)$. We assume that the probability for a trigger only depends on the particular type of particles under investigation (electrons or muons).

$$p_A(\lg N \mid \lg E) = \int_{-\infty}^{+\infty} k_A(\lg N^t)\, d\lg N^t \qquad (2)$$

with

$$k_A(\lg N^t) = r_A(\lg N \mid \lg N^t)\, \epsilon_A(\lg N^t)\, s_A(\lg N^t \mid \lg E) \qquad (3)$$

N^t is the true shower size since normally the reconstructed shower size N does not coincide with the true one.
Looking at real data integration over an interval of zenith angle must be taken into account since all the functions depend on the zenith angle via the atmospheric thickness. For the sake of simplicity this is omitted in the formulas above but is a key point in the analysis presented below.
In the present analysis four primary components were assumed: hydrogen, helium, carbon and iron. So the general equation in this case reads

$$\frac{dJ}{d\lg N} = \sum_{A=1} \int_{-\infty}^{+\infty} \frac{dJ_A(\lg E)}{d\lg E} p_A(d\lg N \mid d\lg E)\, d\lg E \qquad (4)$$

A powerful tool to solve Fredholm integral equations of 1st kind is in general known as *unfolding*. There exist several different unfolding methods each one appropriate to special problems. For the method chosen the first step is the formulation of the integral equation as a matrix equation. This will be done in the following only for one primary particle type A. Again, integration over the zenith angle is not explicitly mentioned as above.
The data are arranged in a vector with dimension n. The number of events in each bin i is y_i. Now one is searching for the corresponding histogram or vector of the energy spectrum with dimension m. These vector elements are labeled as x_j^A. Defining the matrix elements R_{ij}^A of the *response matrix* $\mathbf{R}_A$

$$R_{ij}^A = \frac{\int_{bin\ i} d\lg N \int_{bin\ j} d\lg E\, \frac{dJ_A(\lg E)}{d\lg E}\, p_A(\lg N \mid \lg E)}{\int_{bin\ j} d\lg E\, \frac{dJ_A(\lg E)}{d\lg E}} \qquad (5)$$

one obtains

$$y_i = \sum_{j=1}^{m} R_{ij}^A x_j^A \qquad (6)$$

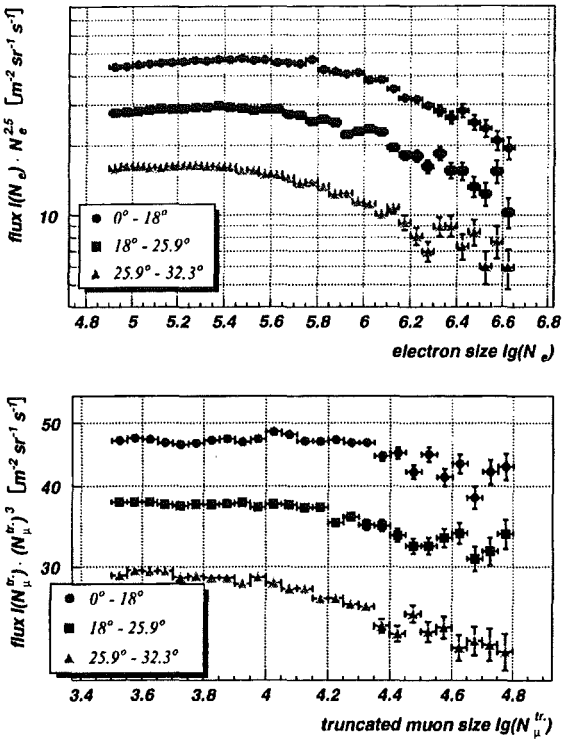

Fig. 1. Electron size spectra (upper plot) and truncated muon size spectra (lower plot) in intervals of zenith angle. The data have not been corrected for reconstruction accuracy.

The elements R_{ij}^A depend on the unknown distribution. However, for sufficiently narrow bins the result will become insensitive to the exact form of $J_A(\lg E)$. For practical purposes it is sufficient in the most cases to use a best guess of the unknown distribution. Of course, the result of the unfolding procedure must be checked for any systematical bias due to the binwidth and this simplification.

The data in the analysis consist of N_e and N_μ^{tr} spectra in three zenith angle bins: $0° < \vartheta < 18°$, $18° < \vartheta < 25.9°$ and $25.9° < \vartheta < 32.3°$. They are displayed in fig. 1. The lower histogram borders were chosen in a way that the muon and electron size spectra are not affected by the trigger threshold, so that they can be treated as independent. The data vector $\boldsymbol{y}$ consists of 6 spectra. The response matrices $\mathbf{R}_A$ of the four components are arranged in one response matrix $\mathbf{R}$ consisting of 24 submatrices, the vector $\boldsymbol{x}$ represents the four unknown energy spectra.

The unfolding method chosen is the *Gold-algorithm* (Gold, 1964). This is an iterative scheme which computes the next solution using the one obtained before. The algorithm produces only non-negative solutions and tries to minimize the χ^2 functional. Defining the error matrix $\mathbf{C}$ of the data and the modified response matrix $\mathbf{G}$ with $\mathbf{G} = \mathbf{C}\,\mathbf{R}$ the iterative scheme can be written as

$$\boldsymbol{x}^{k+1} = \boldsymbol{x}^k \frac{(\mathbf{G}^\mathbf{T}\mathbf{G}\mathbf{G}^\mathbf{T})\,\mathbf{C}\boldsymbol{y}}{(\mathbf{G}^\mathbf{T}\mathbf{G}\mathbf{G}^\mathbf{T}\mathbf{G})\,\boldsymbol{x}^k} \qquad (7)$$

where x^{k+1} is the estimate in the $k+1$-iteration, x^k the estimate in the kth iteration and y is the data vector. Products of the matrix G and its transpose $\mathrm{G^T}$ are used instead of G to fulfill the requirements of the algorithm. The number of allowed iterations can be chosen to give an acceptable small value of χ^2 or to be dependent on the convergence rate (e.g. if the value of χ^2 is not changing any more).

3 Calculating the Response Matrix

In order to obtain the response matrices $\mathbf{R}_A$ one usually simulates Monte Carlo events at least in the same order of magnitude as have been measured. When dealing with extensive air showers this is not possible. To overcome this problem of limited statistics the distributions were parametrized and the matrix elements calculated separately. The air showers were simulated using the CORSIKA package (Heck et al., 1998) version 5.623 with the QGSJet model (Kalmykov, N.N. and Ostapchenko, S.S., 1993) with activated thinning option. By using the thinning option it is possible to generate high energy air showers with high statistics. All simulations were performed using an appropriate zenith angle distribution. The distributions $s(\lg N_e \mid \lg E)$ and $s(\lg N_\mu^{tr.} \mid \lg E)$ can be very well described by the product of an error function and an inverse error function with the same mean:

$$s(\lg N_{e,\mu} \mid \lg E) \propto \mathrm{erf}(\lg N_0, \sigma_1)(1 - \mathrm{erf}(\lg(N_0, \sigma_2)) \quad (8)$$

For the determination of the efficiencies and reconstruction accuracy a second sample of full simulated EAS was generated which corresponds to a continuous E^{-2} spectrum. These showers were used as input for the KASCADE detector simulation based on the GEANT package (GEANT, 1993). The showers were analysed with the standard KASCADE analysis software. The efficiencies can be well described using an error function, the reconstruction accuracies are well described by a gaussian. All the relevant parameters are parametrized as functions of primary energy or true shower size. This procedure was performed for each of the four assumed primary particle types with the same number of simulated showers.

4 Results

After applying the unfolding algorithm to the experimental data one obtains the four energy spectra displayed in fig.2. Each of the spectra shows a knee like structure shifted to higher energy with increasing mass. The knee in the total energy spectrum at about 5 PeV (dependent on the definition of the knee) is caused mostly by the steepening of the spectra of the light components. The quoted vertical error bars display only the statistical errors. The horizontal error bars display the systematic uncertainties in the energy assignment. For reasons of a clear presentation an estimate of the systematical errors is only displayed for the iron spectrum. These systematical errors include the uncertainties in the used parametrizations and their parameters, the uncertainties in the used energy spectra for the calculation of the matrix elements, and the systematics introduced by the unfolding algorithm. The latter is mainly crosstalk between the individual components i.e. due to the limited resolution power of the algorithm. The systematical errors are largest for the iron component. The total energy spectrum is hardly affected by these systematical errors.

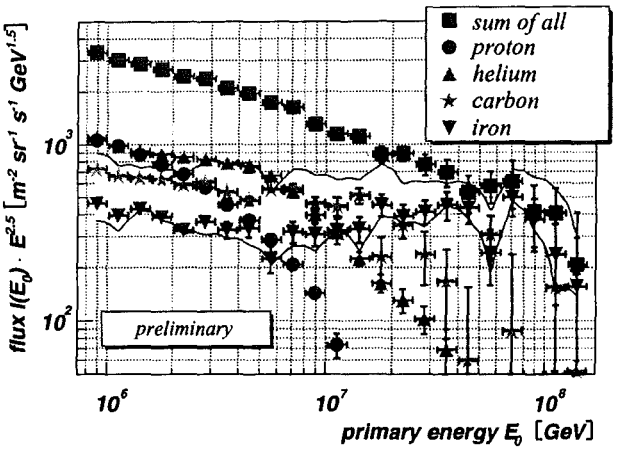

Fig. 2. Result of the unfolding procedure. The vertical error bars are statistic errors, the horizontal reflects the uncertainty in the energy assignment. The shaded yellow band displays the estimated size of systematical errors in the case of iron.

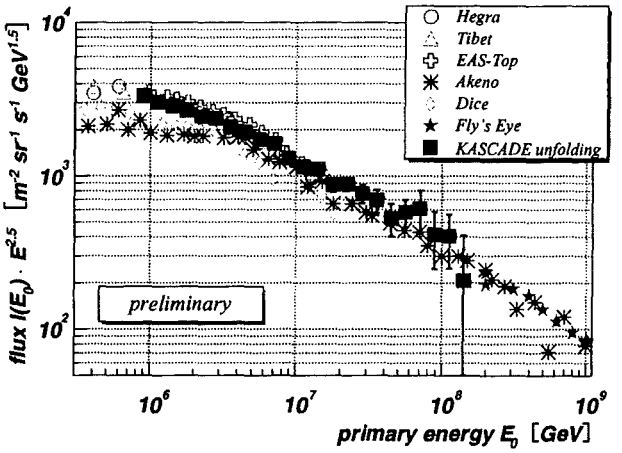

Fig. 3. Comparison of the total energy spectrum with spectra reported by other experiments. Error bars are only statistical ones.

In figure 3 the obtained total energy spectrum is compared with the results of other experiments (taken from Hörandel et al. (1999)). A very good agreement with the data of Tibet and Hegra is found. Also there's a excellent agreement when analysing the data with nonparametric methods, e.g. neural networks (Roth et al., 2001).

In fig.2 the spectra of the lighter components appear to be steeper below the knee as compared to the heavier ones. Also the starting position of the steepening of the spectrum

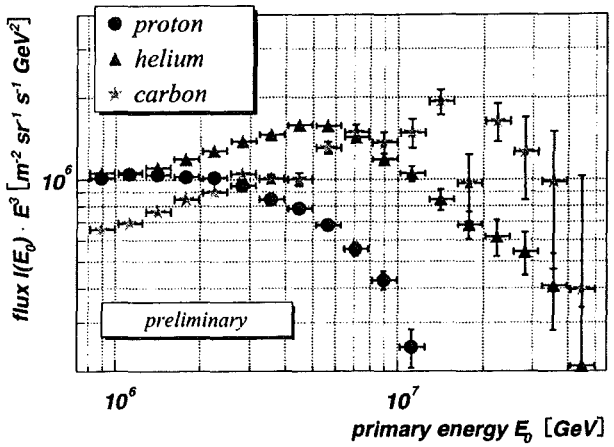

Fig. 4. The flux spectra of proton, helium and carbon primaries between 1 PeV and 10 PeV. The differential flux is scaled with E^3.

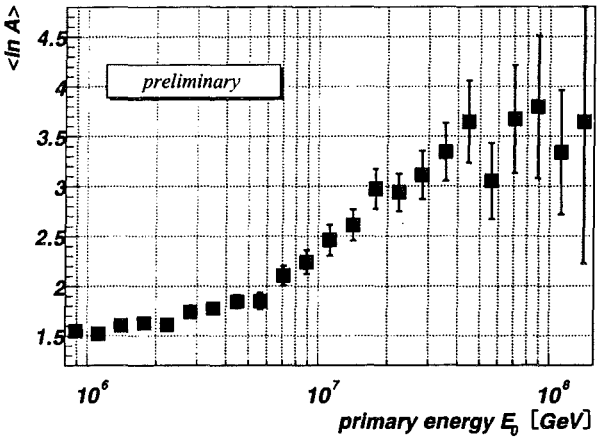

Fig. 5. The mean logarithmic mass versus primary energy. Only statistical errors are displayed.

is shifted to higher energies for the heavier components. To investigate these dependencies the spectra of hydrogen, helium and carbon are displayed in figure 4 in the energy range between 1 PeV and 10 PeV. The differential energy flux is multiplied by E^3. Again the systematical errors are omitted for reasons of a clearer representation.

The helium and carbon spectra show a relatively sharp knee whereas the proton knee appears very smooth. As can be seen the index of the power law describing the individual energy spectra below the knee is steeper for proton than for helium, and flatter for carbon than for helium. Looking at the starting positions of the index change (e.g. defined as the first point below the extrapolation from the points to the left) one finds a factor of 2-3 between proton and helium and a factor of $\approx$ 3 between helium and carbon. The factor between iron and proton is around 20, but less well defined due to the larger statistical uncertainties. The data thus suggest a rigidity dependence of the individual knees. Since systematical errors are still large this has to be treated with caution and kept in mind when drawing quantitative conclusions. Regarding these results it is on the other hand unlikely that the knee position is dependent on the atomic mass A.

As a result of the spectra in fig. 2 the chemical composition of the primary cosmic rays becomes heavier with increasing energy. This is also reflected in the mean logarithmic mass $< \ln A >$ displayed as a function of the primary energy in figure 5. It slowly starts to increase at about 2.5 PeV from a constant value up to about 45 PeV when $< \ln A >$ starts to saturate.

5 Conclusions

Using unfolding algorithms the energy spectra of four mass groups (proton, helium, carbon and iron) of the primary cosmic radiation have been reconstructed. As input the shower size spectra of electrons and muons in different angular intervals were used and analysed simultaneously. Each of the obtained spectra shows a knee-like feature. The results suggest that the position of the individual knees depends on the nuclear charge Z. Since the systematical uncertainties are still relatively large further investigations will focus on this point. All the results were obtained using CORSIKA with the QGSJet model and have to be seen in this context. Future investigation will also be carried out using other hadronic interaction models.

Acknowledgements. The KASCADE experiment is supported by Forschungszentrum Karlsruhe and by collaborative WTZ projects in the frame of the scientific -technical cooperation between Germany and Romania (RUM 97/014), Poland (POL 99/005) and Armenia (ARM 98/002). The Polish group (Soltan Institute and University of Lodz) acknowledges the support by the Polish State Committee for Scientific Research (grant No. 5 P03B 133 20).

References

Antoni, T. et al., KASCADE Collaboration, Astrop. Physics 14, 245–260, 2001.

Doll, P. et al., KASCADE Collaboration, Kernforschungszentrum Karlsruhe, Report KfK-4648, 1990.

GEANT, CERN Program Library Long Writeup W5013, CERN, Geneva, 1993.

Gold, R., Argonne National Laboratory Report ANL-6984, Argonne, 1964.

Heck, D. et al., Forschungszentrum Karlsruhe, Report FZKA 6019, 1998.

Hörandel, J. et al., KASCADE Collaboration, Proc. 26^{th} ICRC, Salt Lake City, HE 2.2.41, 1999.

Kalmykov, N.N. and Ostapchenko, S.S., Yad. Fiz. 56, 105, 1993.

Klages, H.O. et al., KASCADE Collaboration, Nucl. Phys. B (Proc. Suppl.) 52B, 92–102, 1997.

Roth, M. et al., KASCADE Collaboration, Proc. 27^{th} ICRC, Hamburg, 2001.

Proceedings of ICRC 2001: 63 © Copernicus Gesellschaft 2001

ICRC 2001

The primary energy spectrum of cosmic rays obtained by muon density measurements at KASCADE

A. Haungs[1], T. Antoni[1], W. D. Apel[1], F. Badea[2], K. Bekk[1], A. Bercuci[1,2], K. Bernlöhr[1,*], H. Blümer[1,3], E. Bollmann[1], H. Bozdog[2], I. M. Brancus[2], C. Büttner[1], A. Chilingarian[4], K. Daumiller[3], P. Doll[1], J. Engler[1], F. Feßler[1], H. J. Gils[1], R. Glasstetter[3], R. Haeusler[1], D. Heck[1], J. R. Hörandel[3], T. Holst[1], A. Iwan[5,3], K-H. Kampert[1,3], J. Kempa[5,+], H. O. Klages[1], J. Knapp[3,¶], G. Maier[1], H. J. Mathes[1], H. J. Mayer[1], J. Milke[1], M. Müller[1], R. Obenland[1], J. Oehlschläger[1], M. Petcu[2], H. Rebel[1], M. Risse[1], M. Roth[1], G. Schatz[1], H. Schieler[1], J. Scholz[1], S. H. Sokhoyan[4], T. Thouw[1], H. Ulrich[3], B. Vulpescu[2], J. H. Weber[3], J. Wentz[1], J. Wochele[1], J. Zabierowski[6], and S. Zagromski[1]

[1]Institut für Kernphysik, Forschungszentrum Karlsruhe, 76021 Karlsruhe, Germany
[2]National Institute of Physics and Nuclear Engineering, 7690 Bucharest, Romania
[3]Institut für Experimentelle Kernphysik, University of Karlsruhe, 76021 Karlsruhe, Germany
[4]Cosmic Ray Division, Yerevan Physics Institute, Yerevan 36, Armenia
[5]Department of Experimental Physics, University of Lodz, 90236 Lodz, Poland
[6]Soltan Institute for Nuclear Studies, 90950 Lodz, Poland
[*]now at: Humboldt University, Berlin, Germany
[+]now at: Warsaw University of Technology, 09-400 Plock, Poland
[¶]now at: University of Leeds, Leeds LS2 9JT, U.K.

Abstract. Spectra of local muon densities in high-energy extensive air-showers (EAS) are presented as signature of the primary cosmic ray energy spectrum in the knee region. The KASCADE central detector, with its two layers of multiwire proportional chambers and with a layer of scintillation counters, enables the measurements of muon densities at two different threshold energies. The spectra have been reconstructed for various core distances, as well as for particular subsamples, classified on the basis of the shower size ratio N_μ/N_e. The measured density spectra of the total sample exhibit clear kinks reflecting the knee of the primary energy spectrum. While relatively sharp changes of the slopes are observed in the spectrum of EAS with small values of the shower size ratio, no such feature is detected at EAS of large N_μ/N_e ratio in the energy range of 1–10 PeV. In addition to these findings the validity of EAS simulations is studied by comparing the spectra for different muon energy detection thresholds and core distances with detailed Monte Carlo simulations. No consistent energy spectrum can be derived from the data for the two muon thresholds, irrespective of assumptions on elemental composition.

1 Introduction

Though the first evidence of the existence of the knee in the primary cosmic ray energy spectrum has been presented more than 40 years ago, the knowledge of the detailed structure of the spectrum in the PeV region is still scarce, and the origin of the knee not yet understood. Frequency spectra of the observables of the necessarily indirect measurements (like number of electrons or charged particles) reflect in principle the primary energy spectrum, but a quantitative conversion to energy has to invoke a model of the shower development and on an assumption of a mass composition. Hence the determination of the energy spectrum is affected by different systematic uncertainties, especially by the dependence on the model of high-energy interactions. This also leads to a mutual dependence of the results for the energy spectrum and mass composition. It would be useful to analyze different experiments on basis of a coherent methodology as well as to compare the resulting features for various sets of different EAS parameters in the individual experiments.

In the present paper we endeavor to analyze the frequency distribution of local muon densities at fixed distances from the shower core. While the reconstruction of electron or muon size spectra necessarily implies a choice of the form of the lateral distribution function, spectra of the muon density are free from this bias. Thus independent measurements of such spectra for different fixed core distances allow a check on the lateral distribution obtained from simulations. In addition, the layout of the KASCADE experiment (Klages et al., 1997), enables the study of density spectra for two different muon energy thresholds. Hence the consistency of the simulations with respect to the muon energy spectrum can be performed.

Correspondence to: A. Haungs (haungs@ik3.fzk.de)

2 Reconstruction of local muon densities

The main detector components of KASCADE used for the present analysis are an "array" of 252 stations and a "central detector" comprising additional detector systems. The array provides the data necessary for the reconstruction of the basic EAS characteristics like electron and muon size, core location, and arrival direction of individual air showers. The special arrangement of shielded and unshielded detectors on top of each other allows an independent estimation of the electron and muon number for each individual shower (Antoni et al., 2000). The KASCADE central detector is placed at the geometrical center of the detector array. It consists of four different detector systems, covering a total area of $16\times20\,\mathrm{m}^2$. The local muon density of EAS is measured with the multiwire proportional chambers (MWPC) and the trigger plane. A setup of 32 large multiwire proportional chambers is installed (Bozdog et al., 2001) in the basement of the building. The total absorber corresponds to a threshold for vertical muons of 2.4 GeV. Only that area where muons parallel to the shower axis would penetrate the whole absorber and both chamber planes, is taken into account for the calculation of the muon density. This local muon density $\rho_\mu^\star$ is defined by the number of tracked muons $N_\mu^\star$ divided by the total sensitive area $A^\star$ of the MWPC setup. Due to the layout of the chambers, $A^\star$ depends on the angle of incidence of the shower and is calculated for each event individually ($\langle A^\star\rangle = 107\,\mathrm{m}^2$ for the selected EAS).
The second muon detection system is a layer of 456 plastic scintillation detectors in the third gap of the central detector, called trigger plane (Engler et al., 1999). The muon density ρ_μ^{tp} (with a threshold of 490 MeV for vertical incidence) is reconstructed in the following way: To remove signals from cascading hadrons in the absorber an upper limit of the energy deposit of 30 MeV in each of the 456 scintillation counters is imposed. Detectors with larger energy deposits and their immediate neighbours are not considered for further reconstruction. For the remaining detectors, the energy deposit and the sensitive area, both corrected for the shower direction, are summed up. The number of reconstructed muons N_μ^{tp} is then calculated by the sum of the energy deposits divided by the mean energy deposit of a single muon in the shower, according to Monte Carlo calculations. The density ρ_μ^{tp} is obtained as ratio of N_μ^{tp} and the sensitive area of the trigger plane for each individual event ($\langle A^{\mathrm{tp}}\rangle = 202\,\mathrm{m}^2$).
The core distances R_c of the local densities $\rho_\mu^\star$ and ρ_μ^{tp} are estimated in a plane perpendicular to the shower axis.

3 Local muon density spectra

The reconstruction of muon density spectra have been performed for two energy thresholds and for nine core distance ranges (Figs. 1 and 2). To suppress punch-through effects of the hadronic or electromagnetic component, EAS with $R_\mathrm{c} < 30\,\mathrm{m}$ are excluded. EAS with $R_\mathrm{c} > 72\,\mathrm{m}$ are excluded, too, because they can have their core outside of the fiducial area of the KASCADE array if they are very inclined. Fig. 1 and Fig. 2 show the flux spectra for the two muon thresholds in integral form. The flux values are multiplied by $(\rho_\mu^\star)^{2.3}$ and $(\rho_\mu^{\mathrm{tp}})^{2.0}$, respectively. All spectra show a slight, but significant kink with decreasing density for increasing core distance. For the fit procedure the flux $lg(\frac{dN}{d\rho_\mu})$ is assumed to follow a power law below and above a specified knee region. The fit procedure estimates the indices of these power laws, the position of the knee (if existing), and the boundaries of the different regions. The position of the knee is calculated as the weighted center of gravity of the bins inside the knee region. The "width" of the knee region for all spectra amounts to $\Delta lg(\rho_\mu/\mathrm{m}^{-2}) \approx 0.15$. The higher muon energy threshold results in steeper spectra. This indicates a comparatively larger increase of the muon density per primary energy interval with increasing muon energy threshold. The spectra for different core distances are almost parallel leading to nearly constant indices for a given muon energy threshold. This confirms previous experimental results (Antoni et al., 2001) of only slight changes of the shape of the muon lateral distributions with increasing primary energy (which is different for the electromagnetic component of EAS). For both energy thresholds there is a clear difference in the indices below and above the knee.

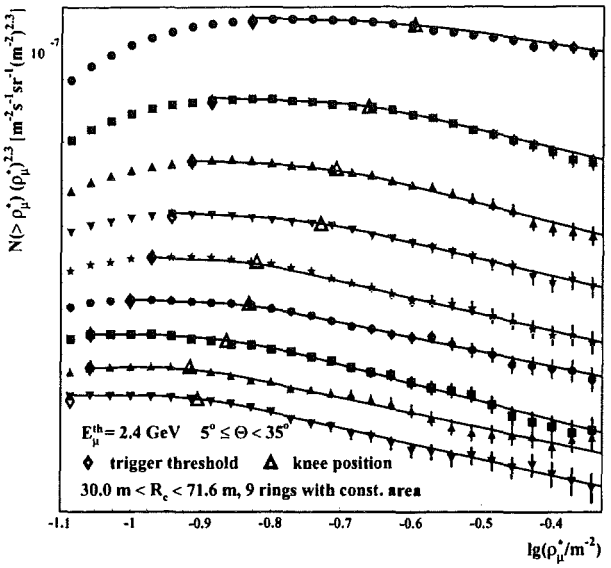

Fig. 1. Integral spectra of the local muon density $\rho_\mu^\star$ as measured by the MWPC system for different core distances R_c (from top to bottom with increasing R_c). The upper limits of the radial bins are 37.0, 42.9, 48.0, 52.7, 57.0, 60.9, 64.7, 68.2, and 71.6 m, respectively. The lines represent the results of the fit procedure.

The total sample of EAS as displayed in Figs. 2,3 is further on separated in "electron-rich" and "electron-poor" showers performed by a cut in the ratio $lg(N'_\mu)/lg(N'_e)$ (at a value of 0.75, optimized by Monte Carlo calculations). The measured shower sizes are converted to the sizes of vertical show-

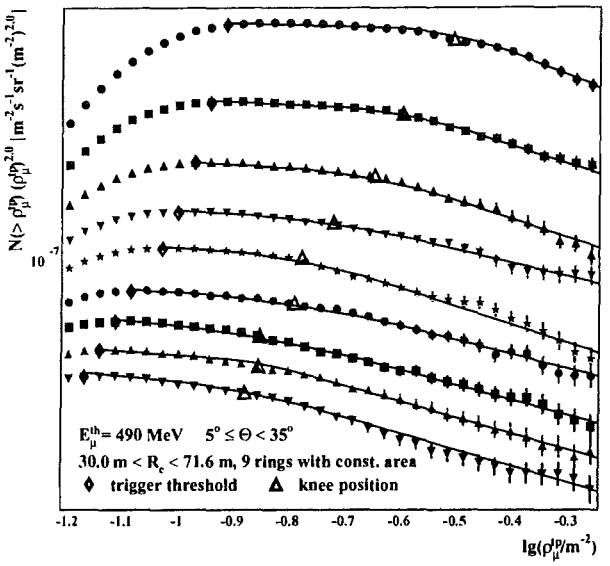

Fig. 2. Same as Fig. 1 but for the local muon density ρ_μ^{tp} measured by the trigger plane.

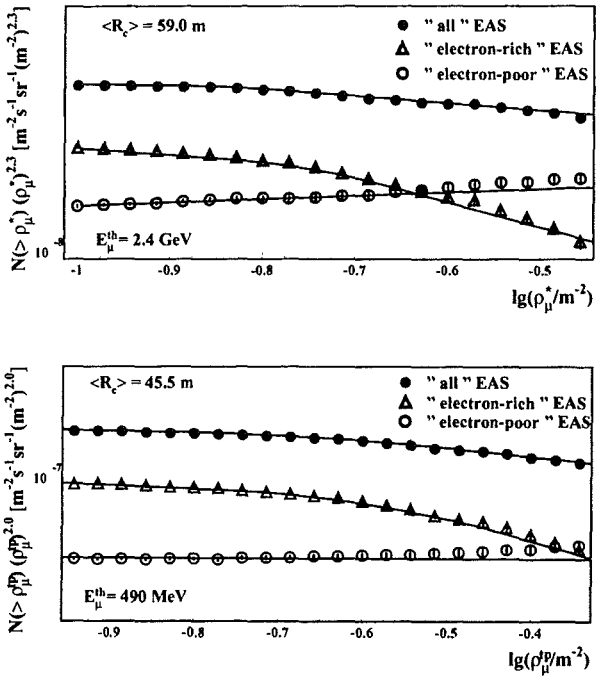

Fig. 3. Examples for measured spectra of different muon content. The "all"-particle spectra have already been shown in Figs. 1 and 2 and are here compared with the spectra of "electron-poor" and "electron-rich" EAS for the same core distance range.

ers to eliminate the influence of the different zenith angles:
$ln(N_e') = ln(N_e) - \frac{X}{\Lambda_e} \cdot (\sec\theta - 1)$
$ln(N_\mu') = ln(N_\mu^{tr}) - \frac{X}{\Lambda_\mu} \cdot (\sec\theta - 1)$
where N_e, N_μ^{tr}, and θ are the reconstructed quantities of the EAS, and $X = 1022\,\mathrm{g/cm^2}$ is the depth of the observation level. The quantities Λ_e and Λ_μ denote the absorption lengths of the electron and muon components in the atmosphere. The values were obtained from Monte Carlo simulations and parameterised as $\Lambda_e = 104.3 + 13.5 \cdot lg(N_e)\,\mathrm{g/cm^2}$ and $\Lambda_\mu = 5 \cdot \Lambda_e$. Especially the electron number depends significantly on the zenith angle due to the rapidly increasing atmospheric absorption. The cut value is optimized by Monte Carlo calculations. For both subsamples the spectra are deduced in the same way as the "all-particle" spectra.
As example Fig. 3 shows the reconstructed local muon density spectra for $\langle R_c \rangle = 45.5\,\mathrm{m}$ for the lower muon energy threshold and for $\langle R_c \rangle = 59.0\,\mathrm{m}$ for the higher threshold. Spectra for all, for the electron-rich (predominantly light ion induced), and for the electron-poor (predominantly heavy ion induced) showers are displayed. The general features of the spectra are similar for all core distance ranges; the component of electron-rich EAS dominates the flux below the knee while it strongly decreases after the kink. No knee is seen in the component of electron-poor EAS. The resulting slopes of the spectra, especially the differences of the slope-values for the two thresholds and subsamples, are very similar for the various core distances. Whereas the assumed fit functions describe the all-particle spectra well, the spectra for the EAS subsamples are not well described by power laws above the densities of the knee at the all-particle spectra.

4 Comparisons with simulations

For the interpretation of the measured muon density spectra in terms of the primary energy spectrum a-priori knowledge inferred from Monte Carlo simulations of the air-shower development is necessary. The present analysis is based on a large set of CORSIKA (v 5.62) simulations (Heck et al., 1998) including a full simulation of the detector response. The simulations have been performed using the interaction model QGSJET (Kalmykov et al., 1997) for the high-energy interactions and GHEISHA (Fesefeldt 1985) for interactions below $E_{\mathrm{lab}} = 80\,\mathrm{GeV}$ and subsequent decays. The electromagnetic part of the showers is treated by EGS4 (Nelson et al., 1985). Observation level, earth's magnetic field, and the particle thresholds are chosen in accordance with the experimental situation of KASCADE. The simulations cover the energy range of $5 \cdot 10^{14} - 3.06 \cdot 10^{16}\,\mathrm{eV}$. The calculations are performed for three zenith angular ranges ($0° - 15°$, $15° - 20°$, $20° - 40°$) and for three primary masses: protons, oxygen and iron nuclei. The output of the simulations is analyzed by the same procedures as applied to the measured data, reducing systematic uncertainties.

When relating the density spectra to the primary energy spectrum of cosmic rays a power law spectrum $dN\,/\,dE_0 \propto E_0^{-\gamma}$ is assumed. The energy spectrum can be written as $dN\,/\,d\rho_\mu \cdot d\rho_\mu\,/\,dE_0$, where $d\rho_\mu\,/\,dE_0$ has to be deduced from the EAS simulations and $dN\,/\,d\rho_\mu \propto (\rho_\mu)^{-\beta}$ is taken

from the experimental results. Thus the spectral index γ can be expressed by $\gamma = \delta \cdot (\beta - 1) + 1$ with δ from the simulations ($\rho_\mu \propto {E_0}^\delta$). It could be shown (Antoni et al., 2001a) that this assumption of a power law is valid for all primary masses, all core distance ranges and both muon energy thresholds, whereas the value of δ certainly varies. If the correct elemental composition is adopted, all measured muon density spectra (of the total sample or of a certain subsample) should result consistently in the true primary energy spectrum, irrespective which core distance and muon energy threshold are considered.

The muon density spectra for the different core distances agree within their statistical uncertainties for the resulting slopes and knee positions of the primary mass (Antoni et al., 2001a). This supports the confidence in the lateral distribution predicted by the Monte Carlo simulations. Nevertheless there remain obvious systematic differences in the results for the two muon energy thresholds, observed for all core distances. The systematic differences might arise from possibly incorrect assumptions on mass composition due to the sensitivity of the muon spectrum to primary mass. Such an effect, however, should be considerably reduced when analysing the electron-rich and electron-poor subsamples which should be enriched in light and heavy primaries, respectively. But the systematic differences for the two thresholds remain. Uncertainties by the unknown composition can not explain the systematic discrepancy displayed by the results from the two different muon energy thresholds. Therefore we conclude that an incorrect description of the muon energy spectrum by the Monte Carlo simulations is the origin of the discrepancy. The effect does not only occur for the QGSJet model used for the present analysis. A smaller sample of reference showers generated with the VENUS (Werner 1993) model has been used to study the observed difference. A general shift to a steeper primary energy spectrum ($\Delta\gamma \approx 0.2$) and a lower knee position is found. This can be explained by the differences in the muon energy spectrum (Fig. 4) caused by the high-energy interaction model (see also Antoni et al., 2001b). The larger number of produced muons will modify the density to primary energy relation in the observed way. However, the inconsistency with respect to the two different muon energy thresholds persists. The considered muon energies are comparatively low, and are treated in the CORSIKA simulation code mainly by the low-energy interaction model GHEISHA. Thus the inconsistencies are most probably due to the low-energy model. Fig. 4 shows the muon energy spectrum also for the case of simulated EAS with QGSJET as high-energy model and the UrQMD (Bass et al., 1998) program as generator of the low energy interactions and the decays. Here an primary energy and muon threshold dependent change of the muon numbers is observed, which will lead to a more consistent description of the measurements.

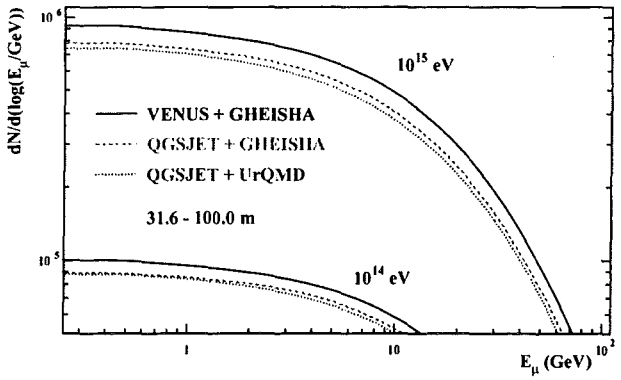

Fig. 4. Mean muon energy spectra for vertical proton induced showers of fixed energies, generated with different high-energy and low-energy interaction models. The spectra are displayed for the radial range of interest and in integral form.

5 Conclusions

In view of the systematic discrepancies related with the measure for two muon energy thresholds, it is difficult to draw definite conclusions but some general features of the primary energy spectrum can be stated: The all-particle energy spectrum exhibits a knee at $E_{\mathrm{knee}} \approx (3-5) \cdot 10^{15}$ eV with a change of the spectral index of order $\Delta\gamma \approx 0.2 - 0.3$. This knee is only seen in the light ion subsample, at the same position but with a distinctly larger steepening of $\Delta\gamma \approx 0.5$. The heavy ion component of the cosmic ray flux displays no steepening in the energy range of 1–10 PeV and a smaller slope than the light component below the knee.

Acknowledgements. The KASCADE experiment is supported by Forschungszentrum Karlsruhe and by collaborative WTZ projects in the frame of the scientific-technical cooperation between Germany and Romania (RUM 97/014), Poland (POL 99/005) and Armenia (ARM 98/002). The Polish group (Soltan Intitute and University of Lodz) acknowledges the support by the Polish State Committee for Scientific Research (grant No. 5 P03B 133 20).

References

Antoni, T., et al. - KASCADE collaboration, Astrop.Phys., 14, 245, 2001.
Antoni, T., et al. - KASCADE collaboration, Astrop.Phys., 2001a, in press; astro-ph/0103363.
Antoni, T., et al. - KASCADE collaboration, Astrop.Phys., 2001b, in press; astro-ph/0102443.
Bass, S.A., et al., Prog. Part. Nucl. Phys., 41, 225, 1998.
Bozdog, H., et al., NIM A, 2001, in press.
Engler, J., et al., NIM A, 427, 528, 1999.
Fesefeldt, H., PITHA-85/02, RWTH Aachen, 1985.
Heck, D., et al., FZKA 6019, Forschungszentrum Karlsruhe, 1998.
Kalmykov, N., et al., Nucl. Phys. B (Proc. Suppl.), 52B, 17, 1997.
Klages, H.O., et al., Nucl. Phys. B, Proc. Suppl., 52B, 92, 1997.
Nelson, W.R., et al., SLAC 265, Stanford Linear Accelerator, 1985.
Werner, K., Phys. Rep., 232, 87, 1993.

Proceedings of ICRC 2001: 88 © Copernicus Gesellschaft 2001

ICRC 2001

Nonparametric determination of energy spectra and mass composition of primary cosmic rays for slant depth

M. Roth[1], T. Antoni[1], W.D. Apel[1], F. Badea[2], K. Bekk[1], A. Bercuci[1], H. Blümer[1,3], E. Bollmann[1], H. Bozdog[2], I.M. Brancus[2], C. Büttner[1], A. Chilingarian[4], K. Daumiller[3], P. Doll[1], J. Engler[1], F. Feßler[1], H.J. Gils[1], R. Glasstetter[3], R. Haeusler[1], A. Haungs[1], D. Heck[1], J.R. Hörandel[3], T. Holst[1], A. Iwan[3,5], K-H. Kampert[1,3], J. Kempa[5,+], H.O. Klages[1], J. Knapp[3,¶], G. Maier[1], H.J. Mathes[1], H.J. Mayer[1], J. Milke[1], M. Müller[1], R. Obenland[1], J. Oehlschläger[1], M. Petcu[2], H. Rebel[1], M. Risse[1], G. Schatz[1], H. Schieler[1], J. Scholz[1], T. Thouw[1], H. Ulrich[3], B. Vulpescu[2], J.H. Weber[3], J. Wentz[1], J. Wochele[1], J. Zabierowski[6], and S. Zagromski[1]

[1]Institut für Kernphysik, Forschungszentrum Karlsruhe, 76021 Karlsruhe, Germany
[2]National Institute of Physics and Nuclear Engineering, 7690 Bucharest, Romania
[3]Institut für Experimentelle Kernphysik, University of Karlsruhe, 76021 Karlsruhe, Germany
[4]Cosmic Ray Division, Yerevan Physics Institute, Yerevan 36, Armenia
[5]Department of Experimental Physics, University of Lodz, 90236 Lodz, Poland
[6]Soltan Institute for Nuclear Studies, 90950 Lodz, Poland
[+]now at: Warsaw University of Technology, 09-400 Plock, Poland
[¶]now at: University of Leeds, Leeds LS2 9JT, U.K.

Abstract. The data measured by the KASCADE (KArlsruhe Shower Core and Array DEtector) experiment are the basis for a multi-component analysis with the aim to determine the mass composition of the primary cosmic rays in the knee region. We discuss the methods used for estimating mass and energy of primary particles by utilizing neural network and nonparametric classification methods. By applying such techniques, measured data have been analyzed in an event-by-event mode and the mass and energy of individual EAS inducing particles are reconstructed. Results of all-particle energy spectra and relative abundances for different groups of primary particles are presented on basis of the electron and muon size data measured for different slant depths. The analyses of measured data indicate a transition to a heavier composition above a knee energy of ca. 5 PeV. It turns out that the mass composition depends on the particular set of observables (e.g. electron size N_e, truncated muon size N_μ^{tr}, hadron size N_h, most energetic hadron $E_h^{\max}$,...) being considered simultaneously in the analysis. Though different sets of observables result in a qualitativly similar mass composition, quantitatively this leads to conspicuous differences. In this way the limitations of a particular interaction model are revealed and the necessity of detailed studies of correlations of EAS observables as a test of the hadronic interaction model is demonstrated.

1 Introduction

The basic astrophysical questions in high-energy cosmic rays (CR) relate to the sources, the acceleration mechanisms and the propagation of CR through space. In particular, the observation of the change of the power law slope (the *knee*; Kulikov and Khristiansen (1959)) of the all-particle spectrum at an energy of a few times 10^{15} eV has induced considerable interest and experimental activities. Nevertheless, despite of many conjectures and attempts, the origin of the knee phenomenon has not yet been convincingly explained.

Due to the rapidly falling intensity and low fluxes, cosmic rays of energies above a few 10^{14} eV can be studied only indirectly by observations of extensive air showers (EAS) which are produced by successive interactions of the cosmic particles with nuclei of the Earth's atmosphere. EAS develop in the atmosphere as avalanche processes in three different main components: the most numerous electromagnetic (electron-photon) component, the muon component and the hadronic component. The properties of EAS are usually measured with large ground-based detector arrays. In most experiments only one or two components are studied. The KASCADE experiment (Doll et al., 1990; Klages et al., 1997) studies all three main components simultaneously and a large number of shower parameters are registered for each event. The determination of the primary's mass and energy, however, are obscured by the considerable fluctuations of EAS development.

Due to the complexity of this process the analysis of the EAS variables to deduce the properties of the primary particle relies on the comparison with Monte Carlo simulations (MC) of the shower development, including the detector response. Usually only one or two EAS parameters are measured and various simplified procedures are used to describe the relation between the observed EAS properties and the nature and energy of the primary particle. The simplification often implies the use of parameterizations of the aver-

Correspondence to: M. Roth (roth@ik3.fzk.de)

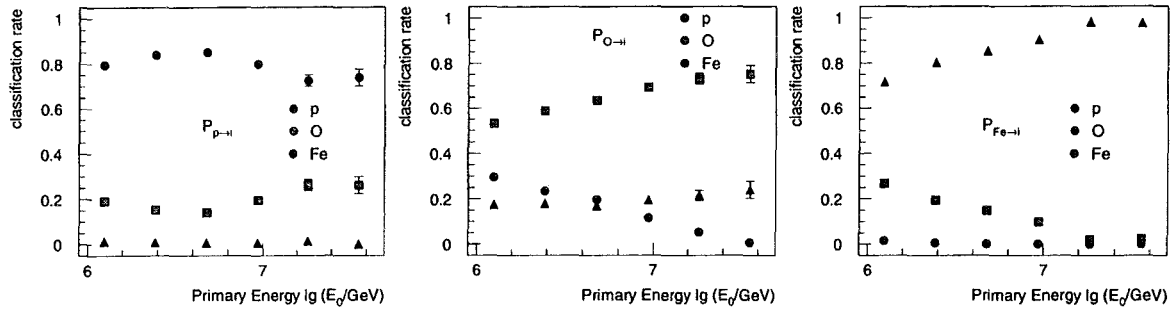

Fig. 1. Classification rate for three classes (p,O and Fe). The used observables are $N_\mu^{\rm tr}$ and $N_{\rm e}$.

age behavior, which may bias the results and limit the accuracy because fluctuations are neglected or not properly accounted for. For the analysis of multivariate parameter distributions and accounting for fluctuations more sophisticated methods are needed. The Bayesian methods and the neural network approaches, currently in vogue, meet these necessities. The methods facilitate an event-by-event analysis. Nonparametric procedures (Chilingarian, 1989) yield not only an estimate of the primary energy and mass composition, but they also allow to specify the uncertainty of the results in a quantitative way. For a detailed description of the applied methods see Antoni et al. (in press).

In the following we report on an investigation of the primary energy spectrum and mass composition in the energy range of $10^{15} - 5 \times 10^{16}\,\mathrm{eV}$, based on the analysis of c. 4,000,000 EAS events. A subset of approximately 8000 showers with cores near the center of the hadron calorimeter yields information on all three components and has been studied in more detail. The simulated showers have been calculated with the program CORSIKA (Heck et al., 1998) and have been convoluted with the apparatus response using the GEANT code (CERN Long Writeups, 1993).

2 Simulation and reconstruction

The CORSIKA code incorporates several high-energy interaction models and is continuously under improvement. In particular, we consider the latest version of QGSJet (Kalmykov and Ostapchenko, 1993). QGSJet is a model based on the Gribov-Regge theory, and extrapolates the interaction features in a well defined way into energy regions which are far beyond energies available at accelerators, and especially into the extreme forward direction. For the low-energy interactions CORSIKA includes the GHEISHA code (Fesefeldt, 1985). The influence of the Earth's magnetic field on charged particle propagation is taken into account. As density profile of the atmosphere the U.S. standard atmosphere is chosen.

Samples of c. 300,000 proton, oxygen and iron-induced showers have been simulated. The energy distribution follows a power law with a spectral index of -1.5 in the energy range of $10^{14}\,\mathrm{eV}$ to $10^{17}\,\mathrm{eV}$. The zenith angles are distributed in the range $[0°, 35°]$. The centers of the showers are spread uniformly over the area of the detector array. In addition, simulations are used where the shower core exceeds the surface of the hadron calorimeter by 2 m on each side. The signals observed in individual detectors are determined by tracking all secondary particles down to observation level and passing them through a detector response simulation program based on the GEANT package (CERN Long Writeups, 1993).

The reconstruction of the EAS observables which has been described in detail elsewhere (Haungs et al., 1996; Antoni et al., 2001; Unger et al., 1997; Hörandel, 1998; Weber et al., 1999), applies an iterative procedure for reconstructing the shower size parameters. At the end the algorithms deliver reconstructed observables like the electron and truncated muon sizes $N_{\rm e}$, $N_\mu^{\rm tr}$ (Weber et al., 1999), observables of the multiwire proportional chambers (Haungs et al., 1996) N_μ^*, D_{-6}, D_6 as well as hadronic observables like the reconstructed number of hadrons $N_{\rm h}^{E>100\,\mathrm{GeV}}$, the energy of the most energetic hadron observed in the shower $E_{\rm h}^{\rm max}$, and the energy sum of all reconstructed hadrons $\sum E_{\rm h}$ (Unger et al., 1997; Hörandel, 1998).

3 Mass composition and energy determination

Due to the finite number of simulated EAS and the correspondingly limited statistical accuracy it is hardly reasonable to use the full set of observables simultaneously to achieve a reliable result about mass composition. Hence we consider simultaneously only a few observables.

Each simulated or measured event is represented by an observation vector $x = (N_{\rm e}, N_\mu^{\rm tr}, \ldots)$ of the n observables. Applying the technique described elsewhere (Antoni et al., in press) the likelihood (probability density distribution) $\hat{p}(x|\omega_i)$ of an event x for each class $\omega_i \in \{\mathrm{p}, \mathrm{O}, \mathrm{Fe}\}$ can be calculated, i.e. the probability of an event x belonging to a given class ω_i. The classification rates $P_{ij} = \hat{P}_{\omega_i \to \omega_j}$ give the

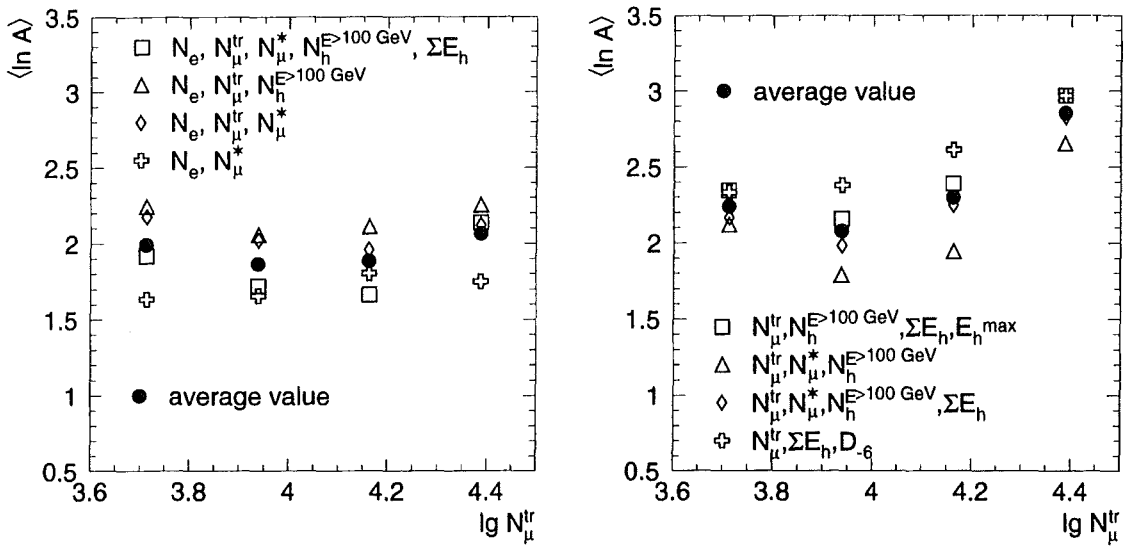

Fig. 2. Mean logarithmic mass $\langle \ln A \rangle$ resulting from the analysis of different sets of observables vs. lg $N_\mu^{\rm tr}$ (QGSJet prediction). The sets displayed on the right do not include the observable $N_{\rm e}$. The error bars are omitted to simplify the presentation of the synopsis, but are not larger than 25%. The knee energy corresponds to lg $N_\mu^{\rm tr} \approx 4.15$.

fraction of correctly, P_{ii}, and wrongly, P_{ij} $(i \neq j)$, classified events. An example for three mass classes is given in Figure 1. Of course, the sum of each row has to be 100%. Taking into account these classification rates the relative abundances of the different sets of observables included in the analysis are calculated and comprised in the determined mean logarithmic mass (see Figure 2). Of course, this procedure to calculate $\langle \ln A \rangle$ is to some extent arbitrary, but this is always implicit, when $\langle \ln A \rangle$ is used. In Figure 2 only the subset of showers is used where the shower core is within a circle of 6 m relative to the centre of the calorimeter. Remarkably, all sets omitting the electron size $N_{\rm e}$ (right graph) result in a heavier composition and a more pronounced increase above the knee. As the electron size has the strongest mass sensitivity, as well as the smallest fluctuations, the mass compositions are predominantly determined by $N_{\rm e}$ and $N_\mu^{\rm tr}$ (left). Compositions resulting from sets of less sensitive observables differ from these values (right).

The fact that different combinations of observables taken into account in the analysis, lead apparently to different mass compositions (shown in Figure 2), reveals inadequacies of the reference model, i.e. that the degree of the intrinsic correlations for different observables differs from those of the real data. Otherwise the determined mass compositions should be identical within the statistical errrors.

To estimate the primary energy E the most important parameters are $N_{\rm e}$ and $N_\mu^{\rm tr}$, where $N_\mu^{\rm tr}$ carries most of the information. Thus we use as data basis all data of the array. Due to the large computing time requirements we do not apply the Bayesian algorithms here and use instead neural networks only. In principal there are no basic arguments to prefer one particular method. Previous publications have demonstrated the consistency and equivalence of neural network and Bayesian methods in EAS analyzes (Roth, 1999; Chilingarian et al., 1997). Detailed studies show that the neural network estimator reconstructs the energy without any bias independently of the primary particle. Only the spread of the estimated energies varies from proton (largest) to iron (smallest). Figure 3 presents the reconstructed energy spectra of measured data resulting from the analysis of three different angular intervals. Within the errors no systematic discrepancy can be stated. The best-fit results are $\langle \gamma_1 \rangle = 2.76 \pm 0.003 \pm 0.03$, $\langle \gamma_2 \rangle = 3.1 \pm 0.02 \pm 0.06$ and $\langle E_{\rm knee} \rangle = 5 \times 10^6$GeV, including statistical errors as well as the methodical error derived from different training parameters of the neural network. It is obvious that the statistical errors are considerably smaller than the systematic uncertainties resulting from the small number of simulated events and from interaction models.

In the present status of our analysis procedure it is hardly possible to introduce more than three classes for the reconstruction of the mass composition. If this were to be attempted additional observables had to be included. A finer binning of the energy scale (beyond the energy resolution $(\Delta E/E)_{\rm est}$) for the spectra of single masses would require to deconvolute the resolution effects. In the actual analysis this step has not been performed and only the mean logarithmic variation of the mass composition (and no detailed energy spectra of the different mass classes) are presented in Figure 4. Remarkably, within the errors no systematic dis-

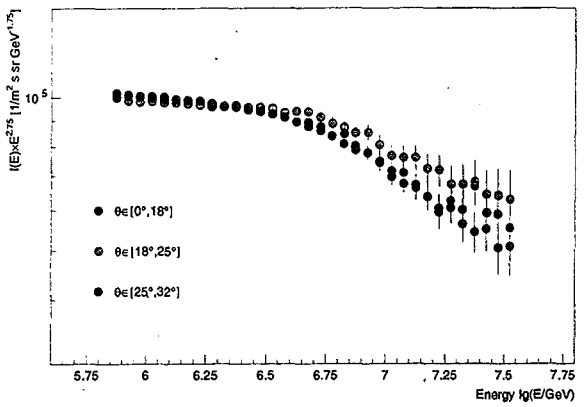

Fig. 3. Differential energy spectra resulting from the analysis of data of the KASCADE experiment using a neural network for three different zenith angle intervalls. The network was trained with CORSIKA showers using QGSJet. The used observables are $N_\mu^{\rm tr}$ and N_e.

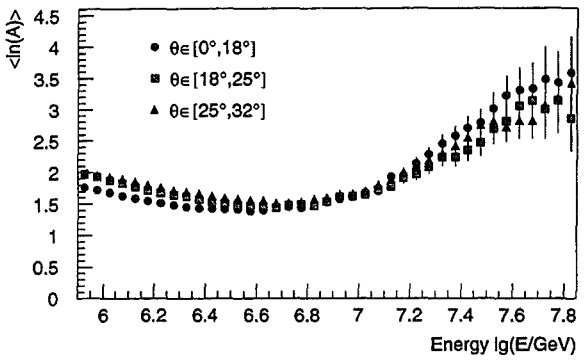

Fig. 4. Mean logarithmic mass as a function of primary energy from a neural network analysis, see legend of Figure 3.

crepancy can be stated, either. To analyze the data beyond this limit we need, in the simplest case, to construct from the misclassification matrices a matrix $A_{\rm AA';EE'}$ deconvoluting mass and energy resolution effects. Hence, we cannot infer any significant fine structure from the all-particle energy spectrum beyond the resolution of $(\Delta E/E)_{\rm est}$.

4 Conclusion

It should be stressed that the present study emphasizes the methodical aspects of how to infer energy spectrum and mass composition of CR. A final answer requires improved statistical accuracy both in experiment and simulation and, first of all, a reduction of systematic uncertainties due to the incomplete knowledge of high-energy interactions. Nevertheless, our findings on spectrum and mass composition are compatible within the methodical accuracy to the results of other experiments.

Acknowledgements. The KASCADE experiment is supported by Forschungszentrum Karlsruhe and by collaborative WTZ projects in the frame of the scientific-technical cooperation between Germany and Romania (RUM 97/014), Poland (POL 99/005) and Armenia (ARM 98/002). The Polish group (Soltan Intitute and University of Lodz) acknowledges the support by the Polish State Committee for Scientific Research (grant No. 5 P03B 133 20).

References

Antoni, T. et al., (KASCADE Collaboration), *Astropart. Phys.* **14**, 245, 2001.

Antoni, T. et al. (KASCADE Collaboration), *Astropart. Phys.*, in press, 2001.

CERN Program Library Long Writeups W5013, 1993.

Chilingarian, A.A., *Comput. Phys. Commun.* **54**, 381, 1989.

Chilingarian, A.A. et al., *Nucl. Phys. B (Proc. Suppl.)* **52B**, 237, 1997.

Doll, P. et al., KfK-Report 4686, Kernforschungszentrum Karlsruhe, 1990.

Fesefeldt, H., Report PITHA 85/02, RWTH Aachen, Germany, 1985.

Haungs, A. et al., *Nucl. Inst. Meth.* **A 372**, 515, 1996.

Heck, D. et al., FZKA-Report 6019, Forschungszentrum Karlsruhe, 1998.

Hörandel, J.R., FZKA-Report 6015, Forschungszentrum Karlsruhe, 1998, in German.

Kamata, K., Nishimura, J., *Prog. Theoret. Phys. Suppl.* **6**, 93, 1958.

Kalmykov, N.N., Ostapchenko, S.S., *Yad. Fiz.* **56**, 105, 1993.

Klages, H.O. et al., *Nucl. Phys. B (Proc. Suppl.)* **52B**, 92, 1997.

Kulikov, G.V. and Khristiansen, G.B., *Soviet Physics JETP* **35**, 441, 1959.

Roth, M., FZKA-Report 6262, Forschungszentrum Karlsruhe 1999, in German.

Unger, J. et al., *Proc.* 25^{th} *Int. Cosmic Ray Conference*, Durban **6**, 145, 1997; J. Unger, FZKA-Report 5896, Forschungszentrum Karlsruhe 1997, in German.

Weber, J.H. et al., *Proc.* 25^{th} *Int. Cosmic Ray Conference*, Durban **6**, 153, 1997; Weber, J.H., FZKA-Report 6339, Forschungszentrum Karlsruhe 1999, in German.

Proceedings of ICRC 2001: 137 © Copernicus Gesellschaft 2001

ICRC 2001

A measurement of the primary cosmic–ray energy spectrum using the hadronic air shower component

J. R. Hörandel[1], T. Antoni[2], W. D. Apel[2], F. Badea[3], K. Bekk[2], A. Bercuci[2], H. Blümer[1,2], E. Bollmann[2], H. Bozdog[3], I. M. Brancus[3], C. Büttner[2], A. Chilingarian[4], K. Daumiller[1], P. Doll[2], J. Engler[2], F. Feßler[2], H. J. Gils[2], R. Glasstetter[1], R. Haeusler[2], A. Haungs[2], D. Heck[2], T. Holst[2], A. Iwan[1,5], K-H. Kampert[1,2], J. Kempa[5,+], H.O. Klages[2], J. Knapp[1,*], G. Maier[2], H. J. Mathes[2], H. J. Mayer[2], J. Milke[2], M. Müller[2], R. Obenland[2], J. Oehlschläger[2], M. Petcu[3], H. Rebel[2], M. Risse[2], M. Roth[2], G. Schatz[2], H. Schieler[2], J. Scholz[2], T. Thouw[2], H. Ulrich[1], B. Vulpescu[3], J. H. Weber[1], J. Wentz[2], J. Wochele[2], and J. Zabierowski[6]

[1]Institut für Experimentelle Kernphysik, University of Karlsruhe, P.O. Box 3640, 76021 Karlsruhe, Germany
[2]Institut für Kernphysik, Forschungszentrum Karlsruhe, 76021 Karlsruhe, Germany
[3]National Institute of Physics and Nuclear Engineering, 7690 Bucharest, Romania
[4]Cosmic Ray Division, Yerevan Physics Institute, Yerevan 36, Armenia
[5]Department of Experimental Physics, University of Lodz, 90236 Lodz, Poland
[6]Soltan Institute for Nuclear Studies, 90950 Lodz, Poland
[+]now at: Warsaw University of Technology, 09-400 Plock, Poland
[*]now at: University of Leeds, Leeds LS2 9JT, U.K.

Abstract. The *knee* in the cosmic–ray energy spectrum is investigated by measurements of the hadronic shower size spectra with the KASCADE hadron calorimeter. Two observables are used to characterize the shower size, the number of hadrons and the hadronic energy sum. Five energy thresholds for the reconstructed hadrons are introduced, in order to check for systematic effects in the procedures applied. A *knee* in the hadronic shower component is confirmed at energies corresponding to 2 PeV (7 PeV), if a pure proton (iron) composition is assumed.

1 Introduction

The all–particle cosmic–ray energy spectrum can be well described by a power law $dN/dE \propto E^{\gamma}$ in the energy range from 10 GeV up to 10 EeV. The most prominent structure is a change of the spectral index from $\gamma_1 \approx -2.7$ to $\gamma_2 \approx -3.1$ around energies of 3 PeV.

The *knee* has been discovered in the electromagnetic component about 40 years ago (Kulikov et al. 58). Meanwhile many experiments using different techniques have seen the *knee* in the all–particle spectrum, for a recent compilation see for example (Hörandel 01). The origin of the change in spectral slope is still under discussion. Explanation attempts include particle physics reasons, like new high–energy interactions in the atmosphere, or astrophysical reasons, like a rigidity dependent escape probability from the galaxis, as predicted by some cosmic–ray propagation models, resulting in a changing cosmic–ray composition around the *knee*.

To clarify the situation the experiment KASCADE (Klages et al. 97) measures the electromagnetic, muonic, and hadronic shower components simultaneously. The data allow to check the high–energy interaction models which are necessary for their astrophysical interpretation (Antoni et al. 99) (Milke et al. 01) and, therefore, cover the possible particle physics reasons for the *knee*. KASCADE measures a *knee* around 3 to 5 PeV simultaneously in all three shower components (Glasstetter et al. 98) (Glasstetter et al. 99).

Two observables have been used to investigate the hadronic component: the number of hadrons as well as their energy sum. From the shower size spectra a primary energy spectrum with a *knee* around 5 PeV has been derived (Hörandel et al. 99). In this article we report on progress of the analysis of the hadronic component.

Correspondence to: J.R. Hörandel (joerg@ik1.fzk.de)

2 Experimental set up

To investigate the cosmic rays from several 10^{13} eV up to 10^{17} eV the air shower experiment KASCADE ("KArlsruhe Shower Core and Array DEtector") has been built on site of the Forschungszentrum Karlsruhe in southern Germany, (110 m a.s.l.). The experiment consists of three major parts, a scintillator array, an underground muon tracking detector, and a central detector.

The 200 × 200 m^2 scintillator array is formed by 252 detector stations housing liquid scintillation counters to measure the electromagnetic component and, under an absorber of 10 cm lead and 4 cm iron, plastic scintillators to register muons with an energy threshold of 230 MeV. The position of the shower core, the angle of incidence as well as the number of electrons and muons is obtained from these detectors.

Three layers of 144 m^2 streamer tubes in an underground tunnel shielded by 1 m of concrete and soil, corresponding to an energy threshold of 800 MeV, form the muon tracking

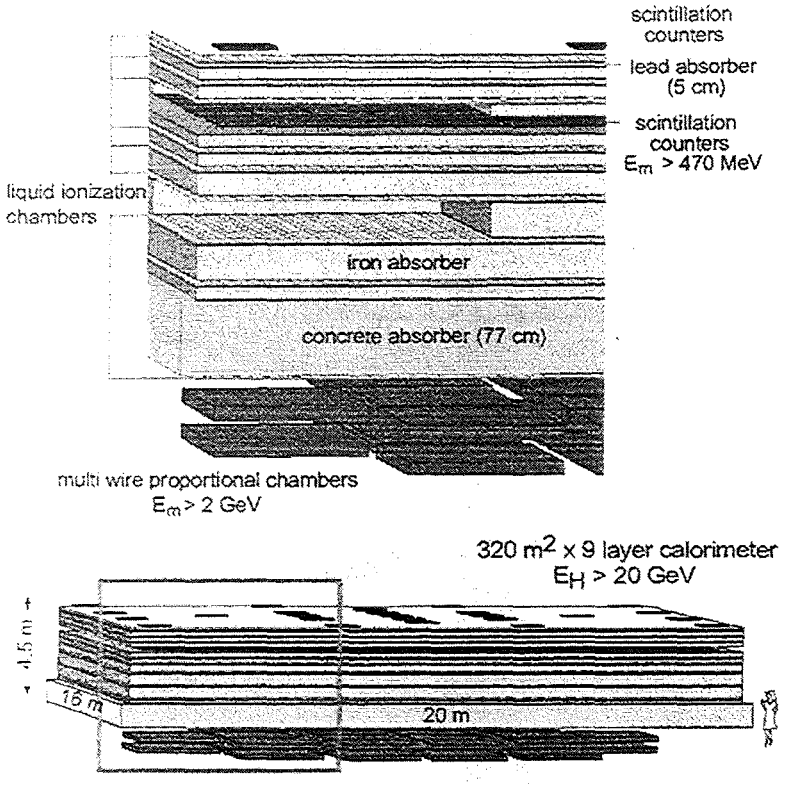

Fig. 1. Schematic view of the KASCADE central detector, detailed view (top) and total view (bottom). Main component is an iron sampling calorimeter equipped with nine layers of liquid ionization chambers and one layer of scintillation counters for triggering.

detector.

Main part of the central detector system is a 320 m^2 hadron calorimeter, sketched in Figure 1, formed by 4000 t iron, lead, and concrete absorber material, with a thickness of 11 hadronic interaction lengths. The absorber is interspaced by nine layers of ionization chambers filled with the liquids TMS or TMP (Engler et al. 99). In total 11 000 ionization chambers are installed, each containing four independent channels with a size of 25 x 25 cm^2. The fine segmentation of the read–out allows to reconstruct individual hadrons even in the core of air showers, measuring their point and angle of incidence as well as their energy. A layer of plastic scintillators below the third absorber layer — with an energy threshold for muons of 470 MeV — serves as a fast trigger. Below the calorimeter, two layers of multi–wire proportional chambers and one layer of limited–streamer tubes are detecting muons with a threshold of 2 GeV.

3 Simulations

EAS simulations were performed using the program CORSIKA (Heck et al. 98) version 5.644 with the hadronic interaction model QGSJET version from 1997 (Kalmykov et al. 97). Primary protons, helium, carbon, magnesium and iron nuclei have been chosen for the calculations as representatives for the most abundant mass groups, and a spectral index of $\gamma = -2.0$ is used. Using weights for each event, an appropriate energy spectrum is obtained for the investigations — see below. In the energy range from 10^{14} to 10^{17} eV about 130 000 showers with a zenith angle distribution from 0° to 42° have been simulated for each element. The shower cores are distributed uniformly within an area extending the calorimeter boundaries by 2 m. The detector response is obtained by using a detector simulation program based on the GEANT code.

4 Event selection and observables

For the analysis, events with zenith angle $\Theta \leq 30°$ and a shower core inside the calorimeter have been selected. From the reconstructed hadrons in the calorimeter the number of hadrons above an energy threshold of 50, 100, 200, 500 GeV, and 1 TeV, is calculated. Since the calorimeter measures the energy of individual hadrons, the sum of the hadron energies above threshold may serve as quantity for the hadronic shower size as well. Application of different thresholds and observables for the hadronic shower size allows to study systematic effects in the reconstruction.

Data measured from October 1996 to March 2001 are used for the analysis. About $4.5 \cdot 10^5$ events out of about $2 \cdot 10^8$ events recorded by KASCADE hit the central calorimeter and survive all cuts required in this analysis.

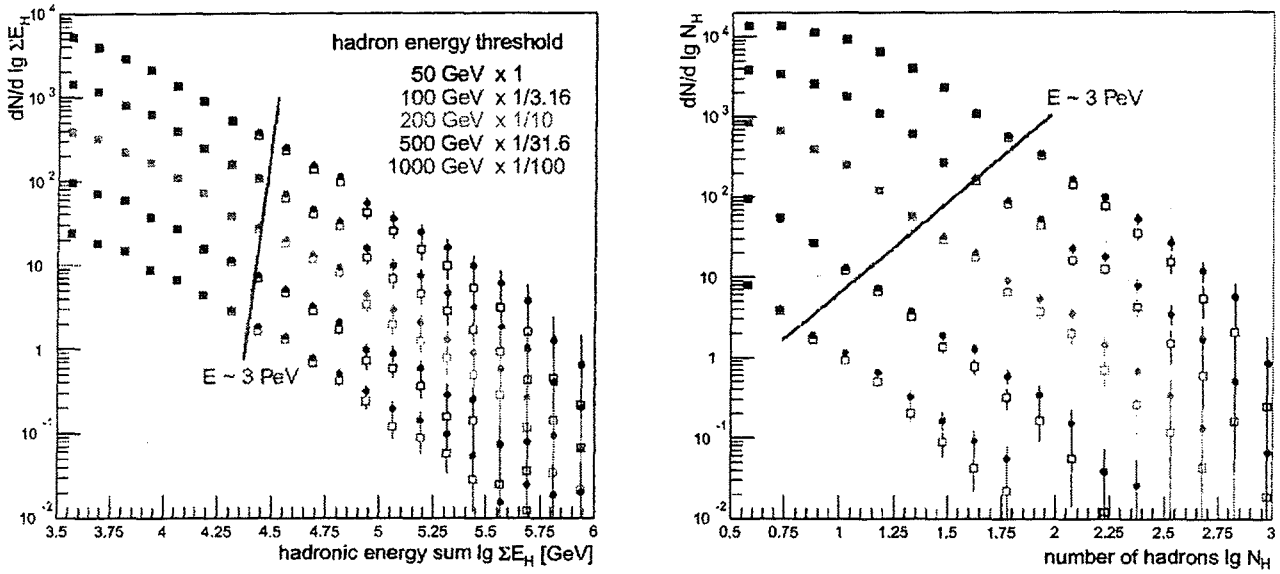

Fig. 2. Simulated hadronic shower size spectra for primary protons, using the hadronic energy sum (left) and the number of reconstructed hadrons (right) for several energy thresholds. A spectrum with $\gamma = -2.7$ is assumed for the filled symbols, a *knee* at 3 PeV with a change to $\gamma = -3.1$ is assumed for the open symbols. The spectra are multiplied by the specified factors to reduce overlapping data points.

5 Results from simulations

A major question of cosmic–ray physics in the *knee* region is the origin of its structure. In a first step we examine the question how a *knee* in the primary spectrum would influence the hadronic shower size spectra measured near sea level. Simulated differential shower size spectra for primary protons are shown in Figure 2 for energy thresholds of the reconstructed hadrons of 50, 100, 200, 500 GeV, and 1 TeV. Both observables, hadronic energy sum and number of hadrons, are presented. Two shapes for the primary spectrum are assumed in the simulations: A power law with an index of $\gamma = -2.7$ and two power laws with $\gamma_1 = -2.7, \gamma_2 = -3.1$, intersecting at an energy $E_k = 3$ PeV.

A particular primary energy corresponds to different shower sizes for different energy thresholds. This is indicated by the lines in the figure, the same primary energy corresponds to smaller shower sizes with raising hadron thresholds. For the hadronic energy sum, 3 PeV correspond to about $\lg(\sum E_H/\mathrm{GeV}) \approx 4.45$ for primary protons, almost independent of the energy threshold, only a small dependence is visible. For the number of hadrons the dependence is rather strong, the assumed *knee* position corresponds to $\lg N_H \approx 1.85$ for $E_H > 50$ GeV changing to $\lg N_H \approx 0.80$ for $E_H > 1$ TeV.

For both observables, the hypothetical *knee* in the primary spectrum clearly appears in the shower size spectra for all thresholds. The resulting spectra agree well with each other for shower sizes smaller than the assumed *knee* position and start to exhibit deviations at larger shower sizes. The shower sizes corresponding to the assumed *knee* position are indicated by the lines.

6 Results from measurements

Measured shower size spectra are plotted in Figure 3, again for several thresholds for the reconstructed hadrons.

The hadronic energy sum spectra are fitted using an ansatz of two power laws:

$$\frac{dN}{d\lg\sum E_H} = \begin{cases} C\cdot(\lg\sum E_H)^{-\beta_1} & ; \quad \lg\sum E_H/\mathrm{GeV} \leq \\ C\cdot(\lg\sum E_H)^{-\beta_2} & ; \quad \lg\sum E_H/\mathrm{GeV} > \end{cases}$$

with two spectral indices β_1 and β_2, a *knee* position ξ, and an overall normalization C as free parameters.

The fits for the 5 thresholds have been repeated using different bin widths for the spectra and different limits for the fits. The results for the *knee* positions and spectral indices are

$E_H >$	β_1	ξ	β_2
50 GeV	1.63 ± 0.03	4.40 ± 0.03	1.72 ± 0.03
100 GeV	1.63 ± 0.04	4.40 ± 0.03	1.71 ± 0.02
200 GeV	1.60 ± 0.03	4.39 ± 0.03	1.72 ± 0.02
500 GeV	1.58 ± 0.02	4.39 ± 0.03	1.73 ± 0.02
1 TeV	1.59 ± 0.05	4.34 ± 0.03	1.72 ± 0.02 .

The *knee* positions are indicated in Figure 3 as yellow squares. A trend to smaller values for increasing thresholds, as predicted by the simulations, is observed in the measurements as well. These *knee* positions correspond to primary

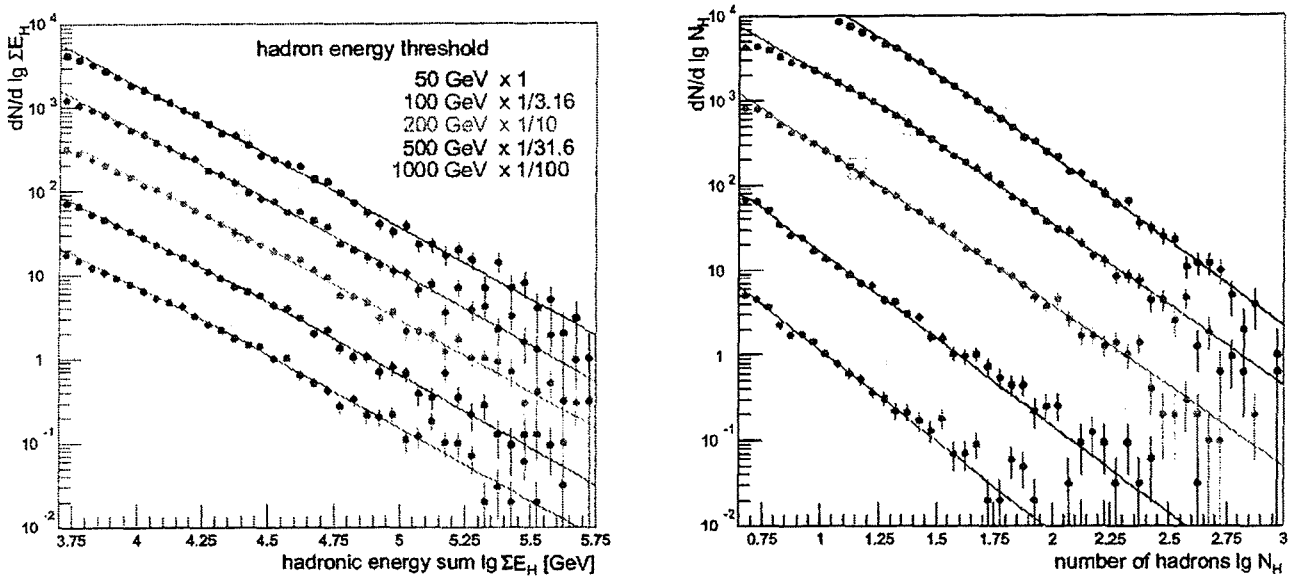

Fig. 3. Measured hadronic shower size spectra using the hadronic energy sum (left) and the number of reconstructed hadrons (right) for several energy thresholds. The spectra are multiplied by the specified factors to reduce overlapping data points.

energies of 2 PeV, if we assume as primary composition pure protons, and to about 7 PeV if we assume iron nuclei only. The slopes before and after the kink are almost independent of the threshold with an average spectral difference $\Delta\beta \approx 0.11 \pm 0.02$.

Fitting the N_H spectra is more critical, since the lever arm below the *knee* is very small for the higher energy thresholds, as can be inferred from Figure 2. Therefore, no *knee* positions are quoted for the two highest energy thresholds. Two power laws, as mentioned above for the energy sums, were fitted to the shower size spectra. The resulting *knee* positions are indicated in Figure 3 with yellow squares. The position of the kink is shifted towards lower hadron numbers with raising energy thresholds, as predicted by the simulations. The *knee* positions $\lg N_H^{50} = 1.75 \pm 0.05$, $\lg N_H^{100} = 1.35 \pm 0.05$, and $\lg N_H^{200} = 1.15 \pm 0.05$ correspond to primary energies of 2 PeV for primary protons and about 7 PeV for iron nuclei. The spectral indices are approximately $\beta_1 \approx 1.80 \pm 0.05$ below and $\beta_2 \approx 2.0 \pm 0.1$ above the *knee*.

7 Conclusion

The fine segmented hadron calorimeter of the KASCADE experiment allows to study hadronic shower size spectra. Two observables, the number of hadrons and the hadronic energy sum, have been used for the investigations, applying five thresholds for the energy of the reconstructed hadrons.

Simulations show that a hypothetical *knee* in the primary cosmic-ray energy spectrum clearly appears in the hadronic shower size spectra.

The measurements consistently exhibit a *knee* at primary energies corresponding to 2 PeV for pure protons and to about 7 PeV, if we assume iron nuclei only. Earlier results (Hörandel et al. 99) could be confirmed.

The conversion of the shower size spectra for the five thresholds into primary energy spectra is in progress. From the two observables and five thresholds, ten energy spectra can be reconstructed, allowing for checks on systematic errors in the procedures applied.

Acknowledgements. The KASCADE experiment is supported by Forschungszentrum Karlsruhe and by collaborative WTZ projects in the frame of the scientific technical cooperation between Germany and Romania (RUM 97/014), Poland (POL 99/005) and Armenia (ARM 98/002). The Polish group (Soltan Institute and University of Lodz) acknowledges the support by the Polish State Committee for Scientific Research (grant No. 5 P03B 133 20).

References

Antoni, T. et al., 1999, J. Phys. G: Nucl. Part. Phys. **25**, 2161
Engler, J. et al., 1999, Nucl. Instr. Meth. **A 427**, 528
Glasstetter, R. and Hörandel, J.R., 1998, Proceedings of the 16^{th} European Cosmic Ray Symposium, Alcala, 563
Glasstetter, R. and Hörandel, J.R., 1999, Nucl. Phys. B (Proc. Suppl.) **75A**, 238
Heck, D. et al., 1998, Report FZKA 6019, Forschungszentrum Karlsruhe
Hörandel, J.R. et al., 1999, Proc. 26^{th} ICRC, Salt Lake City **1**, 337
Hörandel, J.R., 2001, Proc. 27^{th} ICRC, Hamburg
Kalmykov, N. et al., 1997, Nucl. Phys. B (Proc. Suppl.) **52B**, 17
Klages, H.O. et al., 1997, Nucl. Phys. B (Proc. Suppl.) **52B**, 92
Kulikov, G.V., and Khristiansen, G.B., 1958, JETP **35**, 635
Milke, J. et al., 2001, Proc. 27^{th} ICRC, Hamburg

Proceedings of ICRC 2001: 2370 © Copernicus Gesellschaft 2001

ICRC 2001

Search for extremely high energy gamma rays with the KASCADE experiment

F. Feßler[1], G. Schatz[1,‡], T. Antoni[1], W. D. Apel[1], F. Badea[2], K. Bekk[1], A. Bercuci[1,2], H. Blümer[1,3], E. Bollmann[1], H. Bozdog[2], I. M. Brancus[2], C. Büttner[1], A. Chilingarian[4], K. Daumiller[3], P. Doll[1], J. Engler[1,‡], H. J. Gils[1], R. Glasstetter[3], R. Haeusler[1], A. Haungs[1], D. Heck[1], J. R. Hörandel[3], T. Holst[1], A. Iwan[3,5], K-H. Kampert[1,3], J. Kempa[5,+], H. O. Klages[1], J. Knapp[3,¶], G. Maier[1], H. J. Mathes[1], H. J. Mayer[1], J. Milke[1], M. Müller[1], R. Obenland[1], J. Oehlschläger[1], M. Petcu[2], H. Rebel[1,‡], M. Risse[1], M. Roth[1], H. Schieler[1], J. Scholz[1], T. Thouw[1], H. Ulrich[3], B. Vulpescu[2], J. H. Weber[3], J. Wentz[1], J. Wochele[1], J. Zabierowski[6], and S. Zagromski[1]

[1]Institut für Kernphysik, Forschungszentrum Karlsruhe, 76021 Karlsruhe, Germany
[2]National Institute of Physics and Nuclear Engineering, 7690 Bucharest, Romania
[3]Institut für Experimentelle Kernphysik, University of Karlsruhe, 76021 Karlsruhe, Germany
[4]Cosmic Ray Division, Yerevan Physics Institute, Yerevan 36, Armenia
[5]Department of Experimental Physics, University of Lodz, 90236 Lodz, Poland
[6]Soltan Institute for Nuclear Studies, 90950 Lodz, Poland
[*]now at: Humboldt University, Berlin, Germany
[+]now at: Warsaw University of Technology, 09-400 Plock, Poland
[¶]now at: University of Leeds, Leeds LS2 9JT, U.K.
[‡]nominally retired

Abstract.

Data observed with the KASCADE extensive air shower experiment have been analyzed with respect to a possible contribution by primary gamma rays in the energy range of 0.3 to 10 PeV. The study makes use of the good definition of electron and muon numbers by the experiment. Possible gamma induced events are mainly identified by their low muon to electron ratios but, in addition, the steepness and smoothness of the electron lateral distributions are exploited. No positive identifications can be claimed but our results confirm and, in the lower part of the energy range, improve upper limits of a possible gamma contribution made by previous experiments. The distribution on the sky of the 53 most 'gamma-like' events out of a sample of 13.6 million events is indistinguishable from that of all the events registered. The results are based on a measurement time of approximately half a year.

1 Introduction

Gamma rays represent a small but important fraction of primary cosmic rays. Their importance derives mainly from the fact that gamma rays, being electrically neutral, are not deflected by interstellar or intergalactic magnetic fields and therefore their direction of incidence points back to their point of origin. In the TeV range the imaging atmospheric Cherenkov technique has thus been able to identify a (still small) number of galactic and extragalactic point sources. The highest gamma ray energies measured by this technique are close to 50 TeV (Tanimori et al., 1998). But the gamma ray spectrum is expected to extend to even higher energies: The interstellar matter in our galaxy is permanently bombarded by the charged component of cosmic rays. Their interactions will lead to the production of neutral pions whose decay then results in gamma rays of energies up to roughly a tenth of that of the charged particles and the spectrum of the latter is known to extend beyond 10^{20} eV. It therefore appeared worthwhile to search the data registered by the KASCADE experiment for evidence which might be attributed to primary gamma rays.

Previous experiments (Aglietta et al., 1996; Chantell et al., 1997) have set upper limits of the order of 10^{-5} to 10^{-4} for the gamma ray fraction among primary cosmic rays in the energy range above a few hundred TeV. Identifying such a small fraction is not trivial, especially in view of the large fluctuations inherent in extensive air showers (EASs) which are the only means at present to register high energy cosmic rays. The main feature which can be exploited for discriminating primary gamma rays from charged cosmic ray particles is the ratio of electrons to muons on observation level. Gamma rays interact in the atmosphere predominantly by producing electron-positron pairs. The corresponding production of pairs of muons is suppressed by more than four orders of magnitude due to the larger muon mass. It is only via the photoproduction of hadrons that muons occur to an appreciable extent in EASs induced by gamma rays.

Correspondence to: F. Feßler (fessler@ik3.fzk.de)

The KASCADE experiment is well suited for such an investigation due to its large detector area for muons. In addition, the large dynamic range of the KASCADE array scintillators allows a good definition of the lateral electron distribution which can be used to further discriminate gamma induced EASs. Our basic procedure is to compare the measured data to simulated gamma induced events. This implies that assumptions about high energy strong interactions enter into our results only to the extent that they influence hadron photoproduction and the subsequent interactions of the secondary hadrons. The cross section for photoproduction has been measured at the HERA collider at DESY up to equivalent laboratory energies of 20 TeV (Derrick et al., 1992; Ahmed et al., 1993) and it is well described by theory. Hence the extrapolation to the higher energies required here appears justified. These data have been incorporated in the CORSIKA EAS simulation program (Heck et al., 1998) which was used for the simulations. Inaccuracies in the treatment of secondary hadron interactions are not supposed to be of prime importance in our situation because the error of the determined muon number is governed by statistics for the events with a small muon number which are of interest for the present investigation. The Monte Carlo program which describes the detector response to the CORSIKA output is based on the GEANT program (GEANT 1994).

2 Measurements and data analysis

The experiment has been described in detail before (Klages et al., 1997). Therefore we only give here a brief account of the main features relevant for the present analysis. The KASCADE array consists of 252 detector stations set up as a square grid of 13 m spacing on a total area of 200×200 m^2. All stations contain scintillation detectors for registering electrons with a total detector area of 490 m^2. The dynamic range of these detectors is at least 5000. 192 of the detector stations also contain scintillation counters for the measurement of muons with a total area of 620 m^2. Of the KASCADE central detector, only the 456 scintillation detectors of the trigger plane were used to register muons. Their total area is 205 m^2. Their threshold is slightly higher than that of the array muon detectors (400 MeV versus 230 MeV). This difference could have been accounted for in the analysis but was instead ignored because the corrections would have been much smaller than the statistical accuracy.

The signals from the electron detectors were analysed by the usual KASCADE procedures to yield electron number N_e, steepness of the lateral electron distribution ('age'), core position and, from timing, the direction of incidence of the shower. For more details of the analysis cf. Antoni et al. (2001). The electron counters were also used to trigger data acquisition. The muon number N_μ was determined by a maximum likelihood method assuming a fixed lateral distribution. The latter assumption is of course an approximation

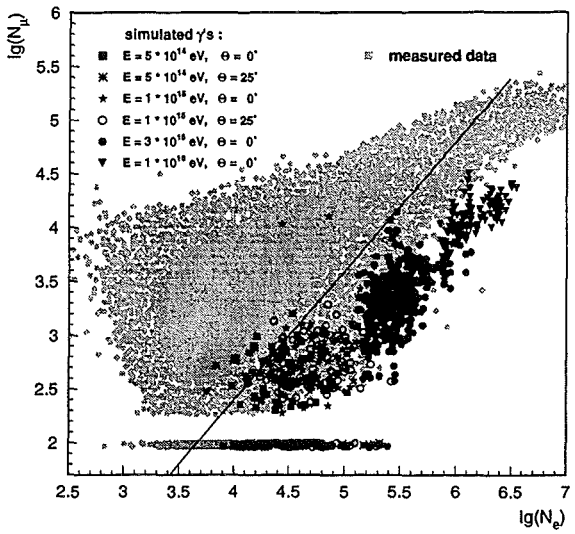

Fig. 1. Distribution of the observed events in the $lg(N_e) - lg(N_\mu)$ plane (light blue) with simulated gamma showers superimposed. The horizontal band at $lg(N_\mu) = 2$ represents EAS with no registered muon (and hence an estimated muon number 0).

but unavoidable because the number of registered muons was always small for the showers of interest. The trigger threshold was set so low that electron and muon numbers could only be determined for about a quarter of all triggered events. As the result of the analysis we obtain a two-dimensional spectrum on the $lg(N_e) - lg(N_\mu)$ plane.

3 Gamma hadron discrimination

Fig. 1 shows the distribution of the reconstructed events as the light blue data points. Superimposed are simulated gamma events of fixed energy and zenith angle. They concentrate along the lower edge of the observed showers, as expected.

For further analysis we concentrate on the events below the straight line in fig. 1. They amount to 34534 out of a total of 13.6 millions. In the region above this line the density of observed events is so large that identification of the few possible gamma induced events appears hopeless. EASs induced by heavy nuclei exhibit a large muon to electron ratio and are therefore expected to be located at the upper edge of the observational range in fig. 1. The events near to and to some extent overlapping the simulated gamma events, on the other hand, are expected to be mainly due to primary protons. A further reduction of the hadron background therefore depends on a suppression of proton induced showers which, according to simulations, exhibit much steeper lateral distributions (small 'age') than those initiated by gamma rays. We therefore compare in fig. 2 the ages of observed and simulated events and remove all data outside the band

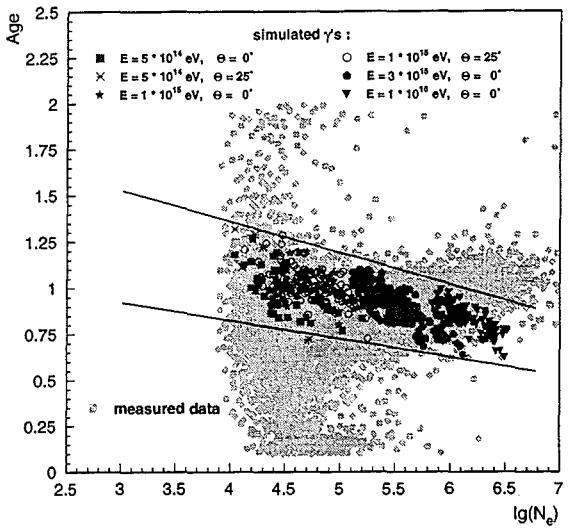

Fig. 2. Age distribution of observed events below the straight line in fig. 1 versus $lg(N_e)$ with simulated gamma showers superimposed. Only events in between the two straight lines are retained for further analysis.

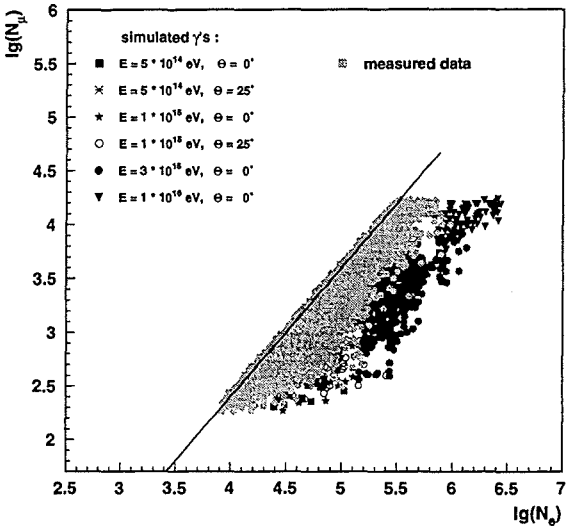

Fig. 3. Distribution of the observed events surviving the age and χ^2 cuts in the $lg(N_e) - lg(N_\mu)$ plane superimposed upon simulated gamma showers. Events above $lg(N_\mu) = 4.2$ have been omitted here because they have not yet been corrected for saturation in the muon detectors.

between the two straight lines. Proton induced EASs are furthermore characterized by their large fluctuations of all shower observables. This feature is exploited very advantageously for gamma/hadron separation by the imaging atmospheric Cherenkov technique to measure extraterrestrial gamma rays in the TeV range (for details cf. Fegan 1997). The parameters which characterize an EAS: shower size N_e, age and core position, are determined via minimizing the quantity

$$\chi^2 = \sum_1^D \frac{(n_i - m_i)^2}{m_i}$$

Here D is the number of detectors included in the analysis, n_i the number of electrons observed in detector i and m_i the corresponding theoretical value. Furthermore we have assumed that the fluctuations of the n_i are Poissonian. Since gamma induced showers are expected to show a more regular lateral distribution than proton induced ones the minimum value of χ^2 will be on average larger for the latter ones. The mean value of χ^2 is known to be equal to the number of degrees of freedom $F = D - 4$. Therefore the ratio χ^2/F is usually quoted but this does not take into account that the variance of χ^2 also depends on F which is not constant in our case. We therefore use the ratio of $\chi^2 - F$ to its standard deviation as a further discriminator. The latter is calculated accounting for the fact that the quantities n_i are not described by Gaussian but rather by Poissonian distributions. A more detailed description of this procedure is given elsewhere (Schatz 2001). Again we remove events for which this ratio is larger than that of the simulated gamma events. Fig. 3 displays the distribution of the 16712 events remaining after these cuts in the $lg(N_e) - lg(N_\mu)$ plane.

The (altogether 9300) events for which no muon was registered (displayed in the horizontal band near $lg(N_\mu) = 2$ in fig. 1) were analysed in a corresponding way and yield a statistically independent estimate of the number of gamma rays.

The usual method applied by previous experiments (Aglietta et al., 1996; Chantell et al., 1997; Karle et al., 1995) to set an upper limit to the number of gammas among the observations is to choose a separating line (in our case in the $lg(N_e) - lg(N_\mu)$ plane) and assume that all events on one side of the line represent gamma rays. In our opinion this procedure is unnecessarily conservative because the distribution of observed events in the region of simulated gamma ray showers does not bear any resemblance with the one expected for gamma rays. Their density decreases strongly from upper left to lower right. This implies that most of the events have to be attributed to the tail of hadron induced showers. The distribution of gamma induced events would form a ridge approximately parallel to the straight line in fig. 3. In our opinion, a more realistic procedure of estimating an upper limit of the number of gamma events can be obtained in the following way: The distribution of gamma induced events in the $lg(N_e) - lg(N_\mu)$ plane is known from simulations. It is then possible to determine the maximum number of events exhibiting the same distribution which may be contained in the observations without producing a marked excess anywhere. A simple statistical algorithm serving this purpose has been developed (Schatz 2001). This then gives us an upper limit to the gamma ray flux when the duration of

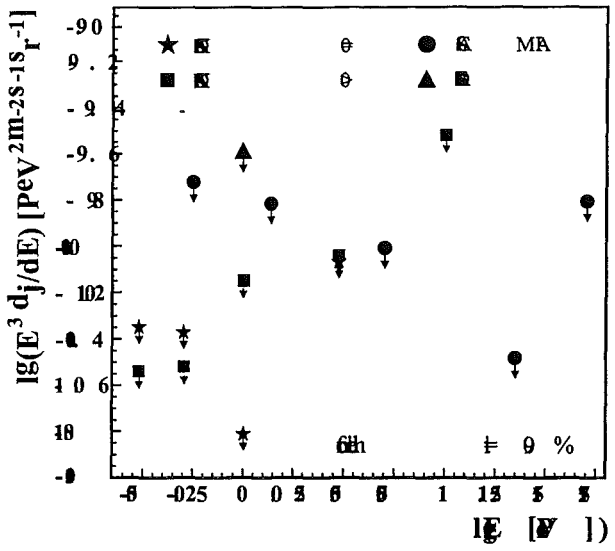

Fig. 4. Comparison of our derived upper limits with previous results by the CASA-MIA (Chantell et al., 1997) and EAS-TOP (Aglietta et al., 1996) experiments. Two limits are given for the KASCADE experiment derived from events with $N_\mu = 0$ and $N_\mu \neq 0$.

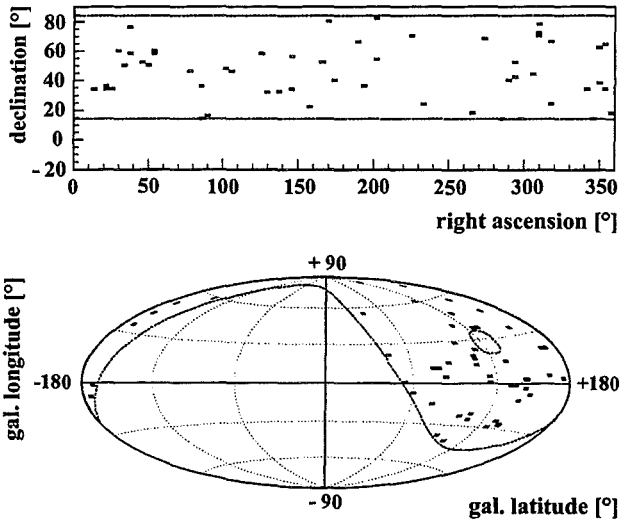

Fig. 5. Distribution of the 53 most 'gamma-like' events on the sky in equatorial and galactic coordinates. The dashed lines indicate the limits of the KASCADE acceptance.

the measurements, detector area, solid angle, and detection efficiency are taken into account. The latter is obtained from the number of simulated events surviving all cuts.

Fig. 4 compares our result with those of the CASA-MIA (Chantell et al., 1997) and EAS-TOP (Aglietta et al., 1996) experiments. Since these authors have given their results as the maximum gamma ray fraction of their observed spectrum we have calculated a corresponding gamma flux by multiplying their ratios with the energy spectra reported by the same groups (Glasmacher et al., 1999 and Aglietta et al., 1999, respectively). We prefer this presentation of the results because the determination of the energy spectrum of primary cosmic rays may be subject to systematic uncertainties which stem from hadronic interaction models and whose size is difficult to estimate.

4 Distribution on the sky

As mentioned in the introduction high energy gamma rays are expected to be produced by interactions of charged cosmic ray particles with interstellar matter in the galaxy. (Extragalactic gamma rays are not expected in the energy range of this study due to their absorption by the cosmic microwave background.) Hence their origins should be concentrated near the galactic plane. We have therefore investigated the distribution on the sky of events which appear most 'gamma-like' (i.e. whose distance to the straight line in figs. 1 and 3 is the largest). Fig. 5 displays the distribution of 53 such events in equatorial and galactic coordinates. Obviously there is no enhancement of the intensity with respect to the galactic plane. This is supported by a Kolmogorov-Smirnov test comparing their distribution to that of all data.

Acknowledgements. The KASCADE experiment is supported by collaborative WTZ projects in the frame of scientific-technical cooperation between Germany and Romania (RUM 97/014), Poland (POL 99/005) and Armenia (ARM 98/002). The Polish group (Soltan Institute and University of Lodz) acknowledges the support by the Polish State Committee for Scientific Research (grant no. 5 P03B 133 20).

References

Aglietta, M., et al., Astropart. Phys., **6**, 71, 1996.
Aglietta, M., et al., Astropart. Phys., **10**, 1, 1999.
Ahmed, T., et al. (H1 collaboration), Phys. Lett., B **299**, 374, 1993.
Antoni, T., et al. (KASCADE collaboration), Astropart. Phys. **14**, 245, 2001
Chantell, M. C., et al., Phys. Rev. Lett., **79**, 1805, 1997.
Derrick, M., et al. (ZEUS collaboration), Phys. Lett., B **293**, 465, 1992.
Fegan, D. J., J. Phys. G: Nucl. Part. Phys., **23**, 1013, 1997.
GEANT, Application Software Group, CERN Program Library, 1994.
Glasmacher, M. A. K., et al., Astropart. Phys., **10**, 291, 1999.
Heck, D. et al., Report FZKA 6019, Forschungszentrum Karlsruhe, 1998.
Karle, A., et al., Phys. Lett., B **347**, 161, 1995.
Klages, H. O., et al., Nucl. Phys., (Proc. Suppl.) **52B**, 92, 1997.
Schatz, G., *Some Statistical Methods Employed for the Gamma Ray Search with KASCADE*, unpublished report, May 2001; a ps-file of the report is available upon request to bgschatz@t-online.de.
Tanimori, T., et al., Astrophys. J., **492**, L33, 1998.

Proceedings of ICRC 2001: 161 © Copernicus Gesellschaft 2001

ICRC 2001

Attenuation and Absorption Lengths of EAS measured with the KASCADE Experiment

G. Maier[1], T. Antoni[1], W.D. Apel[1], F. Badea[2], K. Bekk[1], A. Bercuci[1,2], H. Blümer[1,3], E. Bollmann[1], H. Bozdog[2], I.M. Brancus[2], C. Büttner[1], A. Chilingarian[4], K. Daumiller[3], P. Doll[1], J. Engler[1], F. Feßler[1], H.J. Gils[1], R. Glasstetter[3], R. Haeusler[1], W. Hafemann[1], A. Haungs[1], D. Heck[1], J.R. Hörandel[3], T. Holst[1], A. Iwan[3,5], K-H. Kampert[1,3], J. Kempa[5,+], H.O. Klages[1], J. Knapp[3,¶], H.J. Mathes[1], H.J. Mayer[1], J. Milke[1], M. Müller[1], R. Obenland[1], J. Oehlschläger[1], M. Petcu[2], H. Rebel[1], M. Risse[1], M. Roth[1], G. Schatz[1], H. Schieler[1], J. Scholz[1], T. Thouw[1], H. Ulrich[3], B. Vulpescu[2], J.H. Weber[3], J. Wentz[1], J. Wochele[1], and J. Zabierowski[6]

[1]Institut für Kernphysik, Forschungszentrum Karlsruhe, 76021 Karlsruhe, Germany
[2]National Institute of Physics and Nuclear Engineering, 7690 Bucharest, Romania
[3]Institut für Experimentelle Kernphysik, University of Karlsruhe, 76021 Karlsruhe, Germany
[4]Cosmic Ray Division, Yerevan Physics Institute, Yerevan 36, Armenia
[5]Department of Experimental Physics, University of Lodz, 90236 Lodz, Poland
[6]Soltan Institute for Nuclear Studies, 90950 Lodz, Poland
[+]now at: Warsaw University of Technology, 09-400 Plock, Poland
[¶]now at: University of Leeds, Leeds LS2 9JT, U.K.

Abstract.

An analysis of attenuation and absorption lengths of the electron number using data of the KASCADE air shower experiment is presented. The following methods are used to determine these quantities: The method of constant intensity, the attenuation of the electron number at the knee with increasing atmospheric depth, the decrease of the flux at a constant electron number with increasing zenith angle and the variation of the flux with ground pressure. The differences in the results are explained with respect to methodical uncertainties. An estimation of the influence of intrinsic shower fluctuations on the results is given.

Attenuation lengths between 175 and 196 g/cm^2 and absorption lengths between 100 and 120 g/cm^2 depending on electron number are obtained.

1 Introduction

The longitudinal development of the electromagnetic part of extensive air showers (EAS) is characterized by an approximately exponential decrease in particle numbers for atmospheric depths far behind the shower maximum. This decline is described by the attenuation length Λ_{N_e}r, the variation of the rate at fixed electron number with atmospheric depth by the absorption length Λ_{rate}.

The definitions are for the attenuation length:

$$N_e(X) \propto \exp\left(-X/\Lambda_{N_e}\right) \quad (1)$$

Correspondence to: G.Maier (maier@ik1.fzk.de)

and for the absorption length:

$$j(>N_e, X) \propto \exp\left(-X/\Lambda_{rate}\right) \quad (2)$$

where $N_e(X)$ describes the electron number at atmospheric depth X in the usual unit of g/cm^2 and $j(>N_e, X)$ the rate of showers with more than N_e electrons at given depth.

The absorption length depends on the form and the steepness of the primary energy spectrum, while the definition of the attenuation length is independent of that. The commonly used conversion of Λ_{rate} into Λ_{N_e} by multiplying Λ_{rate} with the spectral index is only valid with the assumptions of a primary energy spectrum following a power law with constant spectral index, a composition of only one primary component and no intrinsic shower fluctuations.

Λ_{N_e} and Λ_{rate} depend on absorption and production rates of the electromagnetic particles and therefore on the hadronic interaction. The most important hadronic quantities in this context are the cross-sections and inelasticities, which are not well know from accelerator experiment at EAS energies. Detailed measurements of the attenuation and absorption lengths as functions of electron number make it possible to study these quantities by comparing them with simulations of EAS.

2 Experiment and reconstruction

The KASCADE experiment located at the Forschungszentrum Karlsruhe, Germany (110 m a.s.l.), is designed to measure with its multi-detector setup a variety of observables of EAS (Klages et al., 1997). KASCADE consists of three ma-

jor detector systems, a large field array, a muon tracking detector and a central detector.

In the present analysis data from the 200x200 m^2 scintillator array are used. The 252 detector stations of the array are uniformly spaced on a grid with a separation of 13 m. Each station in the inner part of the array contains liquid scintillator detectors to measure the electromagnetic component, those of the outer part contain additionally under a shielding of iron and lead a plastic scintillator to measure the number of muons. Detailed description of the detectors is given by Doll et al. (1990) and Antoni et al. (2001).

The iterative shower reconstruction procedure determines the electron number N_e mainly by maximizing a log-likelihood functional with the NKG formula. For the number of electrons N_e the signals in the detectors are corrected for contributions of other particles like γ's, μ's and hadrons. Shower directions are determined by fitting a conical shower front to the measured arrival times. A more detailed presentation of the reconstruction methods can be found in Antoni et al. (2001).

A total number of about 40 Mio. showers, covering the time between May 1998 and December 1999, enter into the analysis.

3 Methods

3.1 Method of constant intensity

The idea behind the method of constant intensity (Nagano et al., 1984) is to select showers with same primary energy and then observe their attenuation with increasing atmospheric depth. Assuming a direct connection between the primary energy spectra and the electron number spectra, application of equal intensity cuts to integral electron number spectra in different angular bins select showers with approximately equal primary energy. Measuring the attenuation of the electron number with increasing zenith angle yields Λ_{N_e}.

3.2 Attenuation of the electron number at the knee

Assuming that the knee in the electron number spectra is a consequence of a knee in the primary energy spectrum, the shift of the position of the knee with increasing atmospheric depth is a measure of the attenuation of the electron number.

This is in a sense a special case of the method of constant intensity, but the shape of the electron number spectra are influenced by intrinsic shower fluctuations. The knee positions are shifted in a nontrivial way towards larger electron numbers, the assumption of constant flux at the knee is therefore only approximately correct.

The knee positions are fitted in the present analysis with the following function (Glasstetter et al., 1997):

$$dj/dN_e \propto \begin{cases} N_e^{-\gamma_1} \\ N_e^{-\gamma(N_e)} = N_e^{a_2 \log N_e + a_1} \\ N_e^{-\gamma_2} \end{cases} \qquad (3)$$

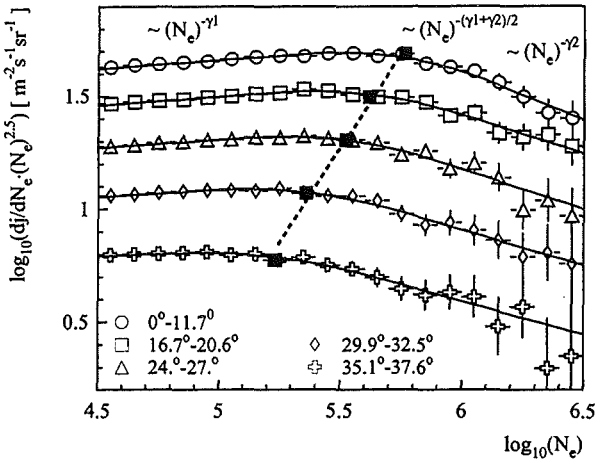

Fig. 1. Knee region of the differential electron number spectra for five intervalls in zenith angle. Knee-positions are indicated by the filled squares. Solid lines show the fits described in the text. Only spectra of every second angular bin are plotted.

The respective function is valid in a region below the knee ($\log N_e \leq \log N_{e,k} - \epsilon$), in the knee region ($\log N_{e,k} - \epsilon < \log N_e < \log N_{e,k} + \epsilon$) and above the knee ($\log N_e \geq \log N_{e,k} + \epsilon$). The half-width of the knee region is fixed at $\epsilon = 0.38$ on a logarithmic electron number scale. The coefficients a_1 and a_2 are determined by the condition that the function and its first derivative are continuous.

3.3 Absorption length - angular method

The absorption length is determined from the integral electron number spectra by analysing the decrease of the shower rate at a constant electron number with increasing atmospheric depth.

The results of this methods are obviously sensitive to the knee in the electron number spectra. This knee effect (Bourdeau et al., 1980) appear due to the different occurrence of the change in the spectral index in the electron number spectra in different angular bins. Therefore only the absorption lengths above the knee region have physical significance.

3.4 Absorption length - barometric method

The influence of atmospheric ground pressure was analysed by counting the number of showers above a certain electron number in two hour time intervals. The atmospheric ground pressure varies only little within these time intervals. The decrease of the intensity with increasing ground pressure yields the absorption length.

The major difference between the angular and the barometric method is the amount of variation in atmospheric depth. While in the angular method it is about 300 g/cm^2, it is only about 30 g/cm^2 in the barometric method. This allows a precise scanning of the longitudinal development in different atmospheric depths.

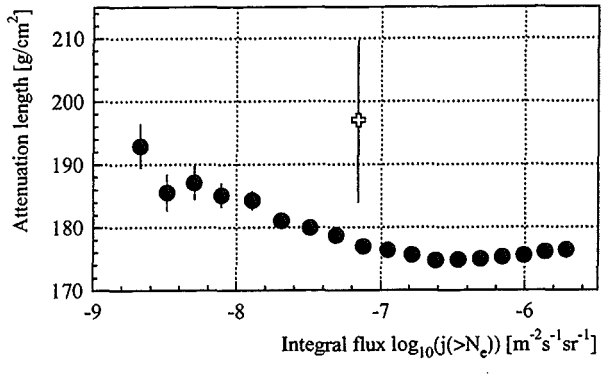

Fig. 2. Attenuation lengths Λ_{N_e} determined by the method of constant intensity (filled circles) and the attenuation of the electron number at the knee (open cross).

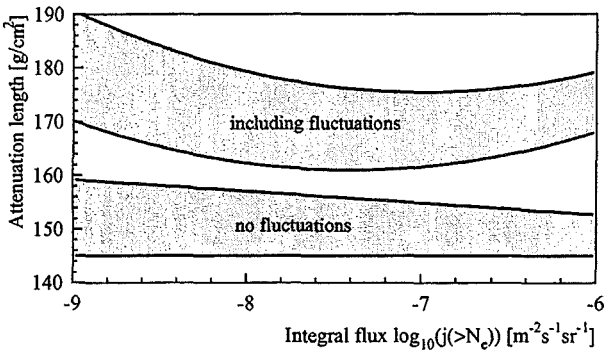

Fig. 3. Attenuation lengths from simulated electron number spectra determined with the method of constant intensity. The shaded region reflects the uncertainties due to the choice of the input parameters.

4 Results

4.1 Attenuation length

The differential electron number spectra of KASCADE are shown in Figure 1 for five intervalls of zenith angle. The attenuation of the knee position is indicated by the dashed line, resulting in $\Lambda_{N_e} = 197 \pm 13$ g/cm^2. The quoted error is of statistical kind. The systematic error is difficult to estimate, but at least of the order. For example, a simple fit of the spectra by two straight lines and taking the knee position at their intersection yields an attenuation length of about 170 g/cm^2. The attenuation length depends therefore strongly on the method used to determine the position of the knee.

Figure 2 shows the resulting attenuation lengths from the method of constant intensity as a function of integral flux. Λ_{N_e} increases with decreasing flux, i.e. with increasing primary energy. This is on the one side due to deeper penetration of showers with higher energy into the atmosphere, on the other side an effect of the modification of the electron number spectra by intrinsic shower fluctuations (see following section).

The large difference in value and error between the result from the knee position and the method of constant intensity comes in parts from the uncertainties resulting from the fit of the electron number spectra.

4.2 Influence of intrinsic shower fluctuations, reconstruction accuracy and detector response

The method of constant intensity is sensitive to the form of the electron number spectra. Intrinsic shower fluctuations, reconstruction accuracy and detector response modify this form. These effects were studied by simulations. The EAS are simulated with the CORSIKA package (Heck et al., 1998). The reconstruction accuracy and detector efficiencies are determined by a detector simulation based on GEANT (GEANT , 1993).

For this analysis, trial electron number spectra with intrinsic shower fluctuations, reconstruction accuracy and the detector response switched off and on are produced in the same angular bins as the data. The energy spectra assumed in the simulations are taken from a previous analysis of KASCADE (Glasstetter et al., 1999).

The trial electron number spectra were analysed with the method of constant intensity in the same manner as the data. Figure 3 shows the resulting attenuation length. The lower region shows attenuation lengths determined from the trial electron number spectra without any fluctuations and detector influences, the upper region with all effects included. The shaded regions reflect the uncertainties due to the choice of the input parameters for the simulation, i.e. of the spectral indices, composition and parametrisations of the fluctuations.

Several effects can be seen. First, all attenuation lengths are shifted by about 15-30 g/cm^2 towards higher values. Second, they are increasing at high fluxes. This is due to the poorer reconstruction accuracy for very small showers. The rise of the attenuation lengths for low fluxes is caused by intrinsic shower fluctuations, only. Comparison of figure 3 with figure 2 shows that the simulation is not fully in agreement with the results from the data. This is thought to be due to the simplified assumption in the parametrisation of the intrinsic shower fluctuation by Gaussian functions on logarithmic electron number scale.

Figure 3 demonstrates, that the results of the method of constant intensity are strongly influenced by fluctuations. Any interpretation of the presented attenuation lengths has to take shower fluctuations into account. We gues that the results of all other methods are influenced by fluctuations in the same order of magnitude.

4.3 Absorption length

The results of the analysis of the absorption length Λ_{rate} are shown in figure 4. The cross hatched region expresses the influence of the knee structure in the shower number spectra. As mentioned before, these values of Λ_{rate} are biased by the

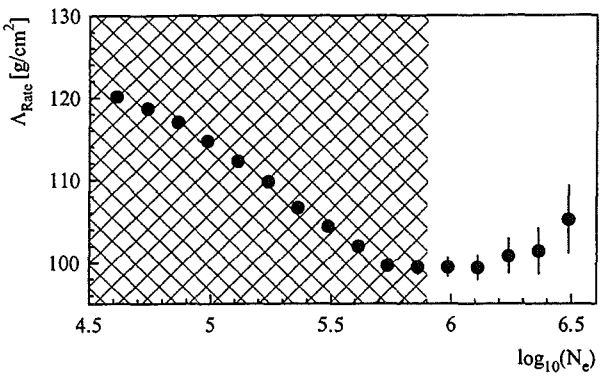

Fig. 4. Absorption length versus electron number determined by the angular method. The cross hatched background indicates the region influenced by the knee.

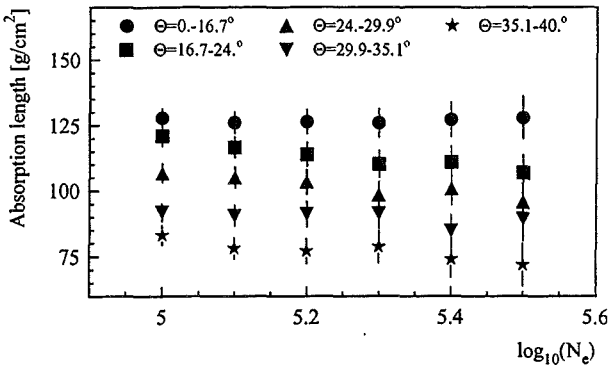

Fig. 5. Absorption length for showers with different zenith angles determined by the barometric method.

different knee positions of spectra in different zenith angles. Above the knee, the absorption length increases like the attenuation length (see also Nagano et al. (1984)). The rough estimation of Λ_{N_e} from Λ_{rate} by $\Lambda_{rate} = \Lambda_{N_e} \cdot \gamma_2^{integral} \approx \Lambda_{N_e} \cdot 1.8$ is consistent with the attenuation lengths in Figure 2.

The barometric method yields absorption lengths in different atmospheric depths. Λ_{rate} decreases with increasing zenith angle (Figure 5), i.e. the longitudinal development deviates from an exponential form and becomes steeper with increasing atmospheric depth.

Since observation time is about 19 months, no seasonal influence on the described results is expected.

5 Conclusion

We presented measurements of the atmospheric attenuation of the electromagnetic component in EAS. An increase of the attenuation length with increasing energy follows from the method of constant intensity as well as from measurements of absorption lengths. The effect of shower fluctuations on the results is significant and shifts the attenuation lengths by about 15-30 g/cm^2. Deviations from the exponential form of the attenuation are shown by the barometric method.

Acknowledgements. The KASCADE experiment is supported by Forschungszentrum Karlsruhe and by collaborative WTZ projects in the frame of the scientific-technical cooperation between Germany and Romania (RUM 97/014), Poland (POL 99/005) and Armenia (ARM 98/002). The Polish group (Soltan Intitute and University of Lodz) acknowledges the support by the Polish State Committee for Scientific Research (grant No. 5 P03B 133 20)

References

Antoni, T., et al., KASCADE Collaboration, *Astrop.Phys*, **14**, 245-260, 2001 .

Bourdeau, M.F., et al., *J.Phys.G:Nucl.Phys.* **6**, 401-410, 1980.

CERN Program Library Long Writeup **W5013**, CERN, Genf, 1993.

Doll, P., et al., KASCADE Collaboration, Kernforschungszentrum Karlsruhe, Report **KfK 4648**, 1990.

Glasstetter, R., et al., KASCADE Collaboration, *Proc. 25th Int.Cosmic Ray Conf.*, Durban, **2**, p.157, 1997.

Glasstetter, R., et al., KASCADE Collaboration, *Proc. 26th Int.Cosmic Ray Conf.* Salt Lake City, **1**, p.222, 1999.

Heck, D. et al., Forschungszentrum Karlsruhe, Report **FZKA 6019**, 1998.

Klages, H.O., et al., KASCADE Collaboration, *Nucl.Phys.B (Proc.Suppl.)* **52B**, 92-102, 1997.

Nagano, M., et al., *J.Phys.G:Nucl.Phys.* **10**, 1295-1310, 1984.

Nagano, M., et al., *J.Phys.G:Nucl.Phys.* **10**, L235-L239, 1984.

Proceedings of ICRC 2001: 201 © Copernicus Gesellschaft 2001

ICRC 2001

The influence of the detector system on the measurements of muon arrival times in Extensive Air Showers (EAS)

R. Haeusler[1], T. Antoni[1], W.D. Apel[1], F. Badea[2], K. Bekk[1], A. Bercuci[1,2], K. Bernlöhr[1,*], H. Blümer[1,3], E. Bollmann[1], H. Bozdog[2], I.M. Brancus[2], C. Büttner[1], A. Chilingarian[4], K. Daumiller[3], P. Doll[1], J. Engler[1], F. Feßler[1], H.J. Gils[1], R. Glasstetter[3], A. Haungs[1], D. Heck[1], J.R. Hörandel[3], T. Holst[1], A. Iwan[3,5], K-H. Kampert[1,3], J. Kempa[5,+], H.O. Klages[1], J. Knapp[3,¶], G. Maier[1], H.J. Mathes[1], H.J. Mayer[1], J. Milke[1], M. Müller[1], R. Obenland[1], J. Oehlschläger[1], M. Petcu[2], H. Rebel[1], M. Risse[1], M. Roth[1], G. Schatz[1], H. Schieler[1], J. Scholz[1], T. Thouw[1], H. Ulrich[3], B. Vulpescu[2], J.H. Weber[3], J. Wentz[1], J. Wochele[1], J. Zabierowski[6], and S. Zagromski[1]

[1]Institut für Kernphysik, Forschungszentrum Karlsruhe, 76021 Karlsruhe, Germany
[2]National Institute of Physics and Nuclear Engineering, 7690 Bucharest, Romania
[3]Institut für Experimentelle Kernphysik, University of Karlsruhe, 76021 Karlsruhe, Germany
[4]Cosmic Ray Division, Yerevan Physics Institute, Yerevan 36, Armenia
[5]Department of Experimental Physics, University of Lodz, 90236 Lodz, Poland
[6]Soltan Institute for Nuclear Studies, 90950 Lodz, Poland
[*]now at: Humboldt University, Berlin, Germany
[+]now at: Warsaw University of Technology, 09-400 Plock, Poland
[¶]now at: University of Leeds, Leeds LS2 9JT, U.K.

Abstract. Arrival time distributions of EAS muons carry information about the production profile of the EAS muonic component. The measured distributions are affected and distorted by various interwoven effects which arise from the time resolution of the timing detectors, from fluctuations of the reference time and the number of detected muons spanning the arrival time distribution of a single EAS event. The origin of these effects is discussed and correction procedures which involve detailed simulations are proposed.

1 Introduction

The temporal structure of the EAS muon component reflects the longitudinal EAS profile, and muon arrival time distributions map the distribution of the muon production heights, in particular, when observed at large distances from the shower axis. Thus muon arrival time distributions should carry some information on the mass of the EAS primaries, unless the intrinsic fluctuations of the muon generation processes and limitations of the detector response do obscure the discriminating features. In fact, experimental muon arrival time distributions have experienced various intriguing distortions which depend not only on the time resolution of the timing detectors, but also on the observed muon multiplicity, i.e. on the number n of registered muons spanning the arrival time distribution of the particular EAS event. Measurements of muon arrival time distributions, correlated with other EAS parameters are a current subject of the KASCADE experiment (Brancus et al., 1998; Antoni et al., 2001; Haeusler, 2000; Badea, 2001).

Correspondence to: R. Haeusler (haeusler@ik3.fzk.de)
Contact author: T. Antoni

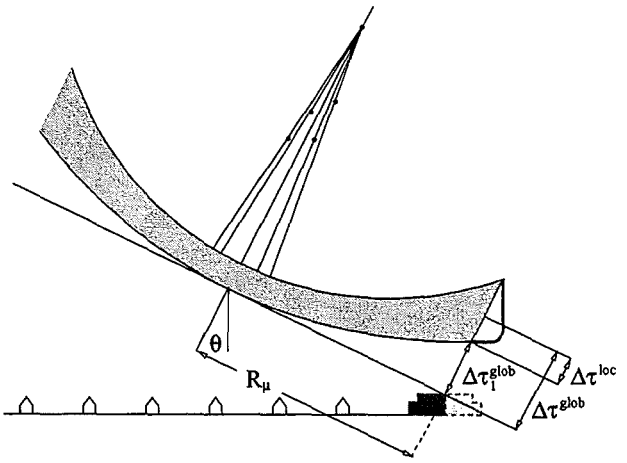

Fig. 1. Characterisation of the EAS temporal structure by global and local arrival times.

In this context we study muon multiplicity effects, entangled with the response and time resolution of the apparatus and demonstrate procedures, used to reveal from measured data the basic time structure of the observed EAS.

Arrival times of muons, registered by the timing detectors at a certain distance R_μ (in the shower plane) from the shower axis refer to a defined zero time (Fig. 1). For the reference zero the arrival time τ_c of the shower centre could be

used (global arrival times). However, there are often difficulties to reconstruct this time with sufficient accuracy. Hence alternatively local arrival times are considered which refer to the arrival time of the foremost muon, registered locally. In event-by-event observations the single EAS relative arrival time distributions can be characterised by mean values $\Delta\tau_{mean}$ and by various quartiles like the median $\Delta\tau_{0.5}$, the first and the third quartiles $\Delta\tau_{0.25}$ and $\Delta\tau_{0.75}$, which pronounce different features of the single distributions. The variation of the distributions of these quartiles, in particular of their mean values and variances, with the distance R_μ from the shower centre, is called the EAS time profile. In case of global time parameters it informs about the curvature of the shower disk and the shower thickness, while local quantities characterise only the structure of the shower thickness. The following discussion is mainly focused on the implications of observations of local time quantities.

2 Fluctuations of the arrival time of the foremost muon

Following the considerations of (Villiers et al., 1986) it can be argued that the arrival time $\Delta\tau_1$ of the foremost muon (relative to a fictitious zero time, representing the muon front, approximated by a sample with a large number n of muons), its expectation value and fluctuations depend on the particular value of the multiplicity n. Fig. 2 shows muon arrival time distributions accumulated from many showers with the expectation values $\langle\Delta\tau_1(n)\rangle$ of the arrival time of the foremost muon for subsamples of different multiplicities.

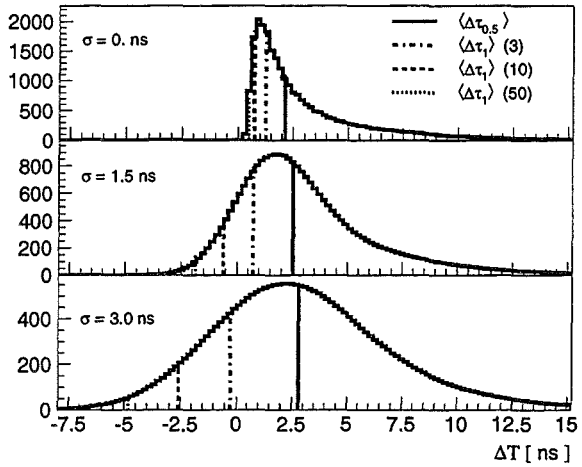

Fig. 2. Muon arrival time distributions $\tau_1(n) - \tau_c$ with the multiplicity dependence of $\langle\Delta\tau_1(n)\rangle$ and the influence of the time resolution. The shown distributions stem from the accumulation of 100 simulated Fe and 100 simulated proton induced EAS (zenith angle of incidence 0°) of $3 \cdot 10^{15}$ eV, observed in the range $70\,\mathrm{m} \leq R_\mu < 80\,\mathrm{m}$.

With increasing n and in the case of infinite time resolution ($\sigma = 0$ ns) of the timing detector $\langle\Delta\tau_1(n)\rangle$ approaches the fictitious arrival time of the shower front (which appears for small R_μ and the infinite time resolution near τ_c). In addition to the fluctuations of the arrival times of the first muon due to the registered multiplicity (which in reality involves also the influence of the detector response) there is the influence of the finite time resolution. It broadens the observed distributions and smears out the original asymmetry. As an example also the expectation for the (global) median $\langle\Delta\tau_{0.5}\rangle$ is shown. The averaged global median does not depend much on the time resolution. In contrast the local quantities underly the trends of $\langle\Delta\tau_1(n)\rangle$, i.e they increase with the multiplicity and with the time resolution. These features are illustrated in Fig. 3 and lead to local shower profiles which are distinctly influenced by the detector qualities (time resolution and response for the muon multiplicity).

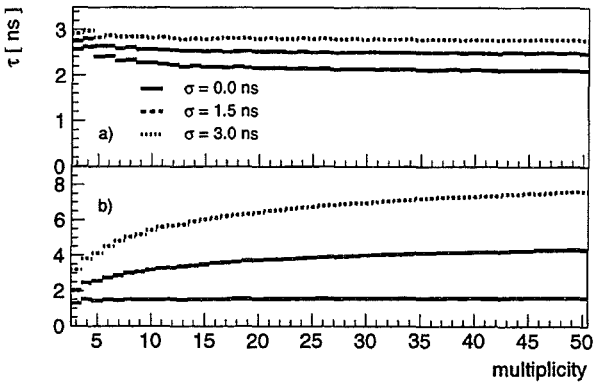

Fig. 3. Multiplicity and time resolution dependence for the mean values of global a) and local b) time parameters of single muon arrival time distributions.

The influence is very pronounced in the central region with the largest multiplicities. As displayed in Fig. 4 for different primary energies and proton and iron showers, the profiles approach the ideal case at larger distances from the core (> approx. 250 m), where the time resolution gets less important, but features discriminating different primaries in global profiles are disappearing (Brancus et al., 2001).

3 How to account for muon multiplicity effects

In actual experimental observations of muon arrival time distributions like in the KASCADE experiment the profiles are derived from EAS events, including all different multiplicities ($n > n_s$), as registered by the timing detectors. Due to the lateral distribution of the EAS muon component the average (registered) multiplicities in an EAS are depending on R_μ. They depend also on the type and energy of the primary, and even if the energy is approximately specified, the

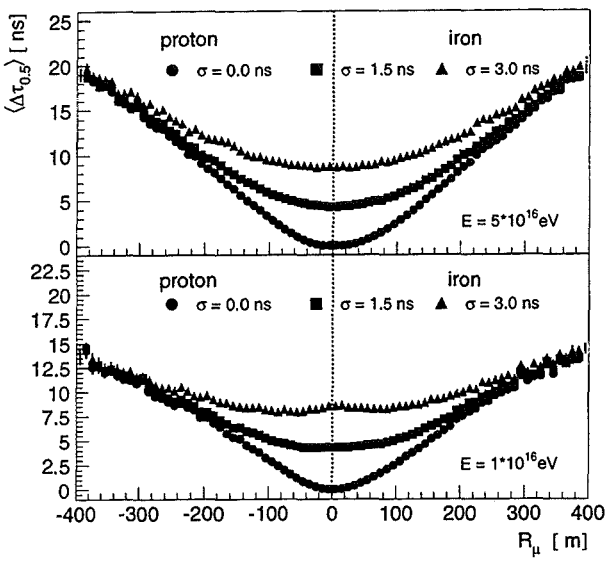

Fig. 4. Local time profiles of proton and iron induced EAS for different primary energies and different time resolution, virtually registered with a detector eye of 400 detectors of 0.5 m^2 (approximately like the timing facility of the KASCASDE central detector).

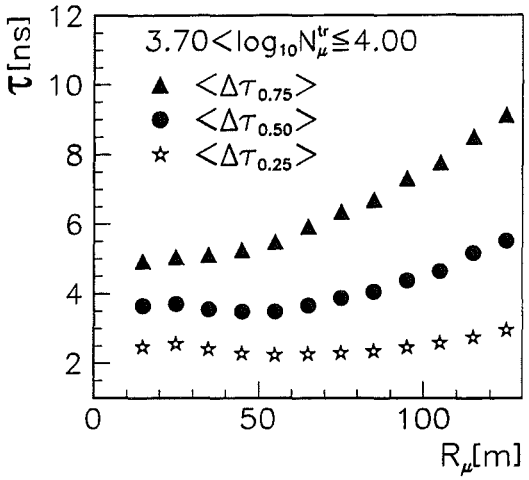

Fig. 5. The variation of the mean values of the median, first and third quartile distributions with the distance from the shower axis, extracted without multiplicity correction for an EAS sample within a particular range of $\log_{10} N_\mu^{tr}$ (indicating the primary energy range of approx. $1.6 \cdot 10^{15}$ eV to $3.2 \cdot 10^{15}$ eV) (Brancus et al., 1998).

observed time profiles originate from a superposition of various multiplicities, varying with the distance from the shower core. That feature leads to interference effects, distorting the predicted quasi-parabolic shape of the time profile. Fig. 5, which displays measured EAS time profiles (Brancus et al., 1998), exhibits this effect.

In principle, it would be desirable to extract the shower profile for each multiplicity separately. However, this attempt would meet serious problems of the statistical accuracy of the results. The main problem, however is that the appearance of the distortions depends on the response qualities of the particular detector arrangement, so that measurements by different detectors are hardly directly comparable. There are various ways to approach a representative result about the EAS time structure from measurements of local quantities.

- The standard concept to compare experimental results with theoretical predictions are procedures simulating the experimental conditions and response folded with the predictions and comparing the resulting distributions with the measured results. This will give an impression about agreement or disagreement and on the undistorted time profiles, but does not immediately enable the comparison with other experiments of different (often unknown) quality and conditions.

- The measured time parameters, deduced for each event from the single muon arrival time distributions registered with varying multiplicity, get scaled to a chosen reference value of the multiplicity by a correction according to predictions by simulation calculations (indicated for the case of the mean value $\Delta\tau_{mean}$ by a calibration curve in Fig. 3). The appearance of time profiles depends on the choice of the reference multiplicity. The correction procedure needs detailed simulation calculations of muon arrival time distributions of the kind shown in Fig. 2. The procedure has been successfully applied in recent KASCADE experiments (Antoni et al., 2001; Haeusler, 2000).

- The observation that for global time quantities the influences of the multiplicity and the time resolution are less pronounced, suggests to relate the muon arrival times to the arrival time of the shower centre by simulating the time difference between the arrival time τ_1 of the local foremost muon and the arrival τ_c of the EAS core. In this way (Badea, 2001) the local quantities are transformed into pseudo-global time parameters, which display the EAS time structure rather realistically, but invoke EAS simulations, specified in detail. While only the shape of the arrival time distributions enters in the above multiplicity calibration procedure, the transformation to pseudo-global quantities stresses also the absolute time difference $\tau_1 - \tau_c$.

Finally Fig. 6 presents a result of an experimental investigation (Haeusler, 2000) of EAS time profiles using the KASCADE detector. For different ranges of the truncated muon number N_μ^{tr} (used as approximate energy estimator) and with a consistent correction for the multiplicity dependence, the experimental results are compared with CORSIKA (Heck et

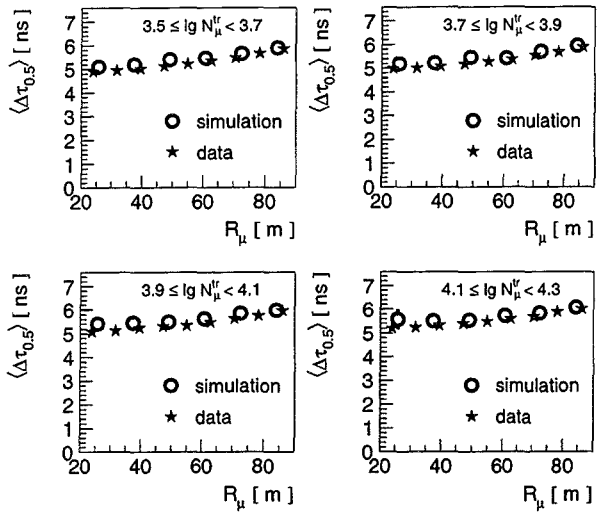

Fig. 6. Local EAS shower profiles ($\langle \Delta\tau_{0.5} \rangle$), corrected for the multiplicity dependence, as compared with predictions of EAS simulations using the Monte Carlo code CORSIKA (Heck et al., 1998), for different EAS muon sizes (corresponding to an energy range from $6 \cdot 10^{14}$ eV to $6.3 \cdot 10^{15}$ eV).

al., 1998) simulations, adopting a mass composition p:O:Fe = 1:1:1.

4 Conclusions

Measured muon arrival time distributions which refer to the arrival time τ_1 of the first locally registered muon, experience some distortions which arise from the superposition of different muon multiplicities spanning the observed distributions, entangled in an intricate way with the response of the experimental detector set-up. There are various procedures to correct for such effects and to display the measured results for a sensible comparison with theoretical predictions or other experiments. The procedures, weakly dependent on the used interaction model and adopted mass composition, invoke explicitely EAS Monte Carlo simulations.

Acknowledgements. The KASCADE experiment is supported by Forschungszentrum Karlsruhe and by collaborative WTZ projects in the frame of the scientific-technical cooperation between Germany and Romania (RUM 97/014), Poland (POL 99/005) and Armenia (ARM 98/002). The Polish group (Soltan Institute and University of Lodz) acknowledges the support by the Polish State Committee for Scientific Research (grant No. 5 P03B 133 20).

References

T. Antoni et al. - KASCADE collaboration, Astropart. Physics 15, 149 (2001).

A.F. Badea, FZKA Report 6579, Forschungszentrum Karlsruhe (2001).

I.M. Brancus et al.- KASCADE Collaboration, FZKA Report 6151, Forschungszentrum Karlsruhe (1998).

I.M. Brancus et al., Proceedings 27^{th} ICRC Hamburg (2001).

R. Haeusler, FZKA Report 6520, Forschungszentrum Karlsruhe (2000).

D.Heck et al. FZKA Report 6019, Forschungszentrum Karlsruhe (1998).

E.J. de Villiers et al., Journ. Phys G: Nucl. Phys.12, 547 (1986).

Proceedings of ICRC 2001: 153 © Copernicus Gesellschaft 2001

ICRC 2001

Production heights of muons determined with the Muon Tracking Detector of the KASCADE experiment

C. Büttner[1], T. Antoni[1], W.D. Apel[1], F. Badea[2], K. Bekk[1], A. Bercuci[1], H. Blümer[1,3], E. Bollmann[1], H. Bozdog[2], I.M. Brancus[2], A. Chilingarian[4], K. Daumiller[3], P. Doll[1], J. Engler[1], F. Feßler[1], H.J. Gils[1], R. Glasstetter[3], R. Haeusler[1], A. Haungs[1], D. Heck[1], J.R. Hörandel[3], T. Holst[1], A. Iwan[5,3], K-H. Kampert[1,3], J. Kempa[5,+], H.O. Klages[1], J. Knapp[3,¶], G. Maier[1], D. Martello[1,*], H.J. Mathes[1], H.J. Mayer[1], J. Milke[1], M. Müller[1], R. Obenland[1], J. Oehlschläger[1], M. Petcu[2], H. Rebel[1], M. Risse[1], M. Roth[1], G. Schatz[1], H. Schieler[1], J. Scholz[1], T. Thouw[1], H. Ulrich[3], B. Vulpescu[2], J.H. Weber[3], J. Wentz[1], J. Wochele[1], J. Zabierowski[6], and S. Zagromski[1]

[1]Institut für Kernphysik, Forschungszentrum Karlsruhe, 76021 Karlsruhe, Germany
[2]National Institute of Physics and Nuclear Engineering, 7690 Bucharest, Romania
[3]Institut für Experimentelle Kernphysik, University of Karlsruhe, 76021 Karlsruhe, Germany
[4]Cosmic Ray Division, Yerevan Physics Institute, Yerevan 36, Armenia
[5]Department of Experimental Physics, University of Lodz, 90236 Lodz, Poland
[6]Soltan Institute for Nuclear Studies, 90950 Lodz, Poland
[+]now at: Warsaw University of Technology, 09-400 Plock, Poland
[¶]now at: University of Leeds, Leeds LS2 9JT, U.K.
[*]now at: Department of Physics, University of Lecce, 73100 Lecce, Italy

Abstract. The capability of the Muon Tracking Detector to measure the radial and tangential angles of muons in extensive air showers, in combination with the shower direction as determined by the scintillator array of KASCADE experiment, has been investigated. Due to different characteristics in shower development of light and heavy primary particles the radial angle is sensitive to the mass of them. For estimating the displacement of the muon from the shower axis the tangential angle is used. The average radial angle and the muon production height have been studied as a function of shower core distance, muon number, and zenith angle. To check the consistency of the results, they have been compared to simulations, which have been done using the Monte Carlo program CORSIKA with the hadronic interaction model QGSJet.

1 Introduction

The direct measurement of the primary cosmic ray flux above the atmosphere is the most powerful method to determine the composition, but the fluxes of particles in the energy range of the knee and above are so small that it is difficult to build a detector large enough to collect a good statistical data sample of cosmic rays. A sufficient collecting sample can be easily supplied by indirect detection of the cosmic rays through measurements of the extensive air showers (EAS) produced in the atmosphere.

The KASCADE (**KA**rlsruhe **S**hower **C**ore and **A**rray **DE**tector) (Klages et al., 1997) experiment is built of different detectors that work in an independent way and can simultaneously measure many characteristics of EAS. A Muon Tracking Detector (MTD) (Atanasov et al., 2000; Zabierowski et al., 2001) is able to identify the direction of muons.

The measurement of angles of muons in EAS can be used for studying the mass composition of the primary cosmic rays (Linsley, 1986, 1992; Ambrosio et al., 1999), as the measured average radial angles are related to the longitudinal EAS development (Pentchev et al., 1999). These angles can be transformed into the Muon Production Height (MPH) taking into account the corresponding shower core distance. The derived MPH depends on the resolution of the shower core position (a function of the position within the scintillator array, the shower size, and the shower direction) and of the measured angles.

Correspondence to: C. Büttner (buettner@ik1.fzk.de)

2 The Muon Tracking Detector

The MTD is located within the KASCADE experiment in a tunnel beneath a shielding of 18 r.l., giving an 0.8 GeV energy threshold for vertical incoming muons. 16 muon telescopes (*detector towers*) are arranged in two rows. One detector tower consists of four detector modules (each 2×4 m^2), three of them positioned horizontally with a spacing of 82 cm and the fourth arranged vertically at the wall (fig. 1). The detector modules are instrumented with streamer tubes (ST) (Doll et al., 1995) which have been developed to fulfill the purpose of the MTD in the best way. Influence strips (pitch of 2 cm, width of 1.8 cm) are positioned below (angle of 60° to the ST wires) and above (perpendicular to the ST wires) the STs. A gas mixture of Ar-CO_2-C_4H_{10} 2:78:20 volume-

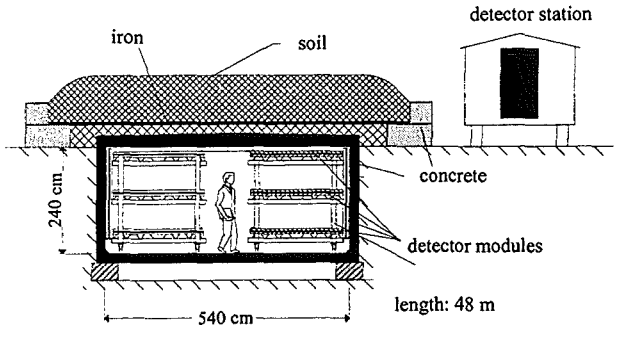

Fig. 1. Cross-section of the Muon Tracking Detector.

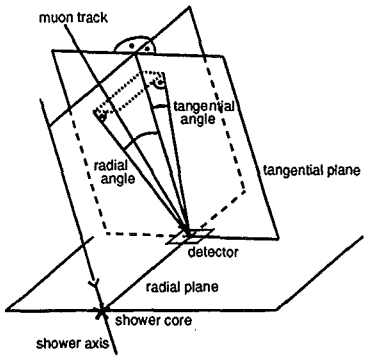

Fig. 2. Definition of radial and tangential angles.

% was used during the time of data taking from November 2000 to April 2001.

3 Definition of Radial and Tangential Angles

Due to the transverse momentum of the pions in EAS and multiple scattering in the atmosphere the muons form an angle in space with the shower axis. To describe the orientation of the muon track with respect to the shower axis radial and tangential angles are used (Bernlöhr, 1996).

The radial angle is defined as the angle between the direction of the shower axis and the projection of the muon track on the radial plane. The radial plane is subtended by the shower axis and the line connecting the shower core and the position, where the muon crosses the detector (fig. 2). The tangential plane is perpendicular to the radial plane, goes through the position of the muon and is parallel to the shower axis. The projection of the muon track on the tangential plane defines the tangential angle. The tangential angle gives a measure of transverse displacement of the muon direction with respect to the shower axis (Pentchev and Doll, 2001). Muons produced higher in the atmosphere may have a smaller transverse displacement (tangential angle) than those produced deeper, because of larger longitudinal momenta at the first interactions with the air nuclei.

4 Analysis

The *truncated muon number* (N_μ^{tr}), the shower direction, and the shower core postion are determined with the scintillator array of KASCADE. N_μ^{tr} is the muon size of the EAS measured by the scintillator array in the distance range from 40 to 200 m with respect to the centre. The reconstruction accuracy of the shower core position is around 3 m (depending on the shower size), of the shower angles it is better than 0.4°, and of $N_\mu^{tr} \approx 5\%$ (Weber, 1999).

For the present analysis the shower core has to be within a radial distance of 60 m around the centre of the scintillator array. As we want to investigate muons coming from high up in the atmosphere, which give some information about the place of the first interaction, the range of the tangential angle used for the analysis of the radial angle and the MPH is restricted to $\pm$ 0.7°, which corresponds to the average amount of scattering in the atmosphere and the absorber. To reconstruct radial and tangential angles with the parameters given by the scintillator array and the muon track of the MTD only such tracks have been used which hit the three horizontal modules of one tower (*3-hit tracks*).

4.1 Results from measured data

The radial angle has an asymmetric distribution (fig. 3(a)) with respect to the shower direction. Throughout this paper, a positive radial angle is assigned to a muon flying away from the shower axis. Due to the finite resolution of the detection system one should allow for some negative values. Here, radial angles down to -1° are taken into account. Most of the negative values correspond to muons which had been deflected inwards the shower axis due to multiple scattering.

Fig. 3(a) shows that for larger shower core distances the average radial angle exhibits larger values as for a fixed range of $3.25 < lg(N_\mu^{tr}) < 3.5$, muons can form larger angles originating from the same MPH.

Fig. 4 shows the median radial angle, determined including angle values starting from -1°, as a function of $\lg(N_\mu^{tr})$ for three ranges of shower core distances. With increasing $\lg(N_\mu^{tr})$ the median radial angle exhibits larger values. This behaviour is due to showers of higher energy which penetrate deeper in the atmosphere producing muons at larger average radial angles at fixed shower core distances. Another reason for the larger median radial angles with increasing $\lg(N_\mu^{tr})$ may be that it is more probable to find muons at larger shower core distances for larger $\lg(N_\mu^{tr})$. Also obvious in the different ranges of $\lg(N_\mu^{tr})$ are the larger median radial angles for larger shower core distances.

The tangential angle is symmetric around zero (fig. 3(b)), and the shape of its distribution is independent of the distance between shower core and muon. The spread of its distribution depends on the multiple scattering of the muons and on the resolution of the MTD and the scintillator array, as well

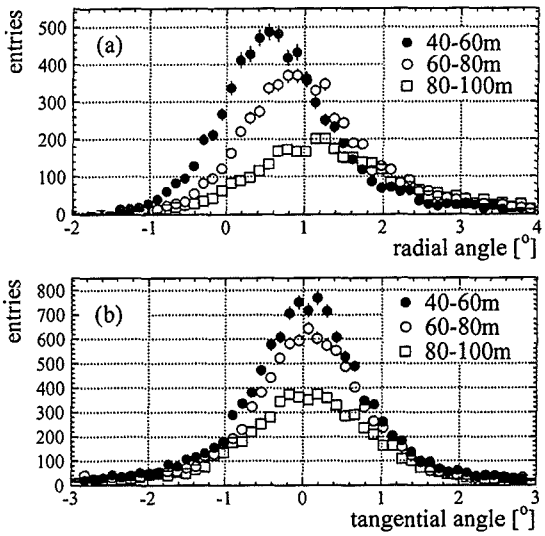

Fig. 3. Distributions of the radial angles (a) (tangential angles in the range from -0.7° to 0.7°) and the tangential angle (b) for three different ranges of shower core distance. Events with $3.25<\lg(N_\mu^{tr})<3.5$ and zenith angles of $0° < \Theta < 18°$ have been selected.

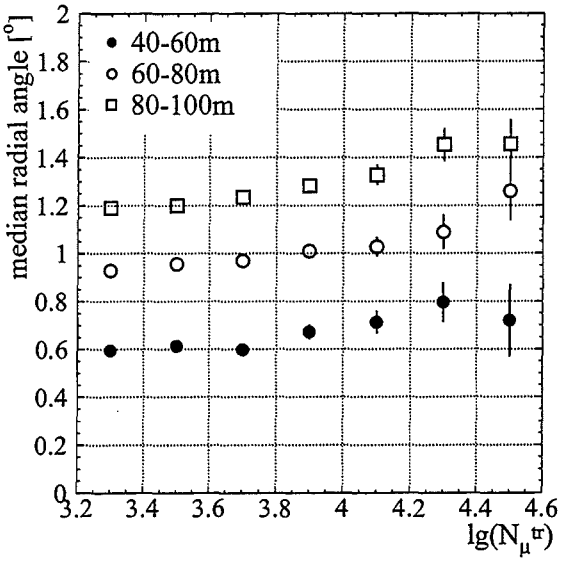

Fig. 4. Measured correlation between $\lg(N_\mu^{tr})$ and the median radial angle for three different ranges of core distance. Zenith angles of $0° < \Theta < 18°$ have been selected.

as on the transversal displacement of the muon origin (fig. 5 in (Zabierowski et al., 2001)). The angular resolution of the MTD will be improved in the future (Obenland et al., 2001).

5 Comparison with Monte Carlo Simulations

Shower simulations are based on the CORSIKA program (Heck et al., 1998) in the version 5.644 with the interaction model QGSJet (Kalmykov et al., 1997). Shower simulations are followed by simulations of the scintillator array and the MTD (GEANT package, 1993). In total about 64200 proton and iron showers have been simulated in the energy range of $1 \cdot 10^{14}$ eV to $1 \cdot 10^{17}$ eV with zenith angles up to 42°. All simulations were done with an $E^{-2.0}$ differential flux spectrum and appropriate event weights (eg. $\propto E^{-0.7}$) were applied to match a desired flux spectrum. For the analysis of the simulations the same cuts as for measured data were used.

In fig. 5 the comparison of measured data, pure proton and pure iron induced showers is shown for a range of shower core distances from 40-60 m and for three ranges of $\lg(N_\mu^{tr})$ (3.25-3.5, 3.75-4, 4-4.25). With larger $\lg(N_\mu^{tr})$, i.e. larger energy, the average radial angle moves to higher values. The statistics for the Monte Carlo simulations is very limited, therefore, the data have been scaled down, in order to check if the lower and upper tails of the data distribution can be compared to the proton and iron simulations (no conclusive superposition to fit the data distributions is shown).

The low radial angle values in the data may be associated to some iron component in the cosmic ray particle flux, the large radial angle values seem to be dominated by the penetrating proton component. There is some indication, that the radial angles of the data exhibit a more pronounced tail to larger values than the model calculations. This may indicate a deeper penetration of the cosmic ray particles than can be obtained with the model calculations.

Fig. 6 shows the distribution of slant MPH for the same shower core distances and ranges of $\lg(N_\mu^{tr})$ as in fig. 5. The MPH was determined by simple triangulation and is based on a relatively accurate shower core distance. Like in fig. 5 no conclusive superposition is shown. For this future task the model distributions, because of their limited statistics, will be fitted by analytical functions like those developed by (Wibig and Wolfendale, 2000) providing the spectral shape of proton and iron distributions as a function of zenith angle, N_μ^{tr}, and shower core distance.

6 Conclusions and Outlook

It has been shown that the radial angle of muons and the reconstructed MPH are sensitive to the mass of the primary cosmic ray particles. The distributions of radial angle and MPH are available in all core distance intervals from 20-120 m, and zenith angles from 0-40° and should provide enough material to evaluate interaction model features (available in CORSIKA) and cosmic ray composition estimates.

The KASCADE-Grande upgrade (Bertaina et al., 2001), re-using scintillator counters of the EAS-TOP experiment, will enable the study of radial angles and MPH for much larger shower core distances. This gives also the chance to investigate EAS with larger energies.

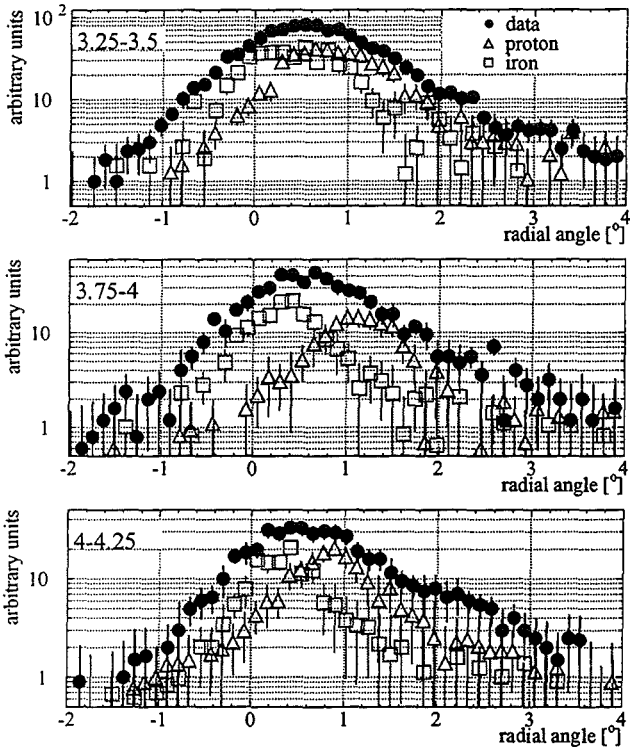

Fig. 5. Distribution of the radial angles for three different ranges of $\lg(N_\mu^{tr})$, shower core distances in the range of 40-60 m, zenith angles from 0-18°. Simulations are based on CORSIKA with hadron interaction model QGSJet.

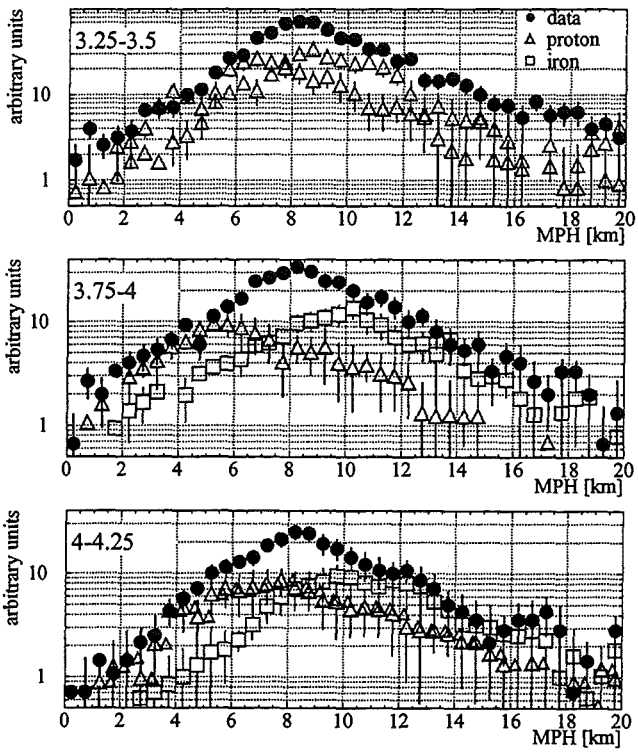

Fig. 6. Distribution of slant MPH for three different ranges of $\lg(N_\mu^{tr})$, shower core distances in the range of 40-60 m, zenith angles from 0-18°. Simulations are based on CORSIKA with hadron interaction model QGSJet.

Comparisons with other experiments which use for example the Cherenkov light (Arqueros et al., 2000) or try to derive information on the elemental composition of the primary particles from the depth of shower maximum in the atmosphere and the muon and electron sizes from the ground array (Swordy et al., 2000) have to be done.

Acknowledgements. The KASCADE experiment is supported by Forschungszentrum Karlsruhe and by collaborative WTZ projects in the frame of the scientific-technical cooperation between Germany and Romania (RUM 97/014, Poland (POL 99/005) and Armenia (ARM 98/002). The Polish group (Soltan Intitute and University of Lodz) acknowledges the support by the Polish State Committee for Scientific Research (grant No. 5 P03B 133 20).

References

Ambrosio, M. et al., Nucl. Phys. B (Proc.Suppl.) **75A** (1999) 312.

Arqueros, F. et al. (HEGRA Collaboration), Astron. and Astrophys., **359**, 682, 2000.

Atanasov, I. et al., Report **FZKA 6474**, Forschungszentrum Karlsruhe, 2000.

Bernlöhr, K., Astropart. Phys. **5** (1996) 139.

Bertaina, M. et al.(KASCADE Collaboration), Proc. 27^{th} Int. Cosmic Ray Conf., (Hamburg), Contribution HE 1.8.26, 2001.

Doll, P. et al., Nucl. Instr. and Meth. A367 (1995) 120.

GEANT, Application Software Group, Computing and Networks Division, GEANT-Detector Description and Simulation Tool, CERN, Program Library Office, Geneva, Switzerland, 1993.

Heck, D. et al., Report **FZKA 6019**, Forschungszentrum Karlsruhe, 1998.

Kalmykov, N. et al., Nucl. Phys. B (Proc.Suppl.) **52B** (1997) 17.

Klages, H.O. et al.(KASCADE Collaboration), Nucl. Phys. B (Proc.Suppl) **52B** (1997) 92.

Linsley, L., J. Phys. G: Part. Phys **12** (1986) 51.

Linsley, L., Nuovo Cim. **C15** (1992) 743.

Pentchev, L. et al., J. Phys. G: Part. Phys **25** (1999) 1235.

Pentchev, L. and Doll, P., J. Phys. G: Part. Phys. **27**,7(2001) in print.

Obenland, R. et al., (KASCADE Collaboration), Proc. 27^{th} Int. Cosmic Ray Conf., (Hamburg), Contribution HE 1.8.33, 2001.

Swordy, S.P. et al., Astropart. Phys. **13** (2000) 137.

Weber, J.H., Report **FZKA 6339**, Forschungszentrum Karlsruhe, 1999.

Wibig, T. and Wolfendale, A.W., J. Phys. G: Nucl. Part. Phys **26** (2000) 825.

Zabierowski, J. et al., (KASCADE Collaboration), Proc. 27^{th} Int. Cosmic Ray Conf., (Hamburg), Contribution HE 1.8.32, 2001.

Proceedings of ICRC 2001: 241 © Copernicus Gesellschaft 2001

ICRC 2001

Test of Hadronic Interaction Models with the KASCADE Hadron Calorimeter

J. Milke[1], T. Antoni[2], W. D. Apel[2], F. Badea[3], K. Bekk[2], A. Bercuci[2], H. Blümer[2,1], E. Bollmann[2], H. Bozdog[3], I.M. Brancus[3], C. Büttner[2], A. Chilingarian[4], K. Daumiller[1], P. Doll[2], J. Engler[2], F. Feßler[2], H. J. Gils[2], R. Glasstetter[1], R. Haeusler[2], A. Haungs[2], D. Heck[2], J. R. Hörandel[1], T. Holst[2], A. Iwan[1,5], K-H. Kampert[2,1], J. Kempa[5,+], H.O. Klages[2], J. Knapp[1,*], G. Maier[2], H. J. Mathes[2], H. J. Mayer[2], M. Müller[2], R. Obenland[2], J. Oehlschläger[2], M. Petcu[3], H. Rebel[2], M. Risse[2], M. Roth[2], G. Schatz[2], H. Schieler[2], J. Scholz[2], T. Thouw[2], H. Ulrich[1], B. Vulpescu[3], J. H. Weber[1], J. Wentz[2], J. Wochele[2], and J. Zabierowski[6]

[1]Institut für Experimentelle Kernphysik, University of Karlsruhe, 76021 Karlsruhe, Germany
[2]Institut für Kernphysik, Forschungszentrum Karlsruhe, 76021 Karlsruhe, Germany
[3]National Institute of Physics and Nuclear Engineering, 7690 Bucharest, Romania
[4]Cosmic Ray Division, Yerevan Physics Institute, Yerevan 36, Armenia
[5]Department of Experimental Physics, University of Lodz, 90236 Lodz, Poland
[6]Soltan Institute for Nuclear Studies, 90950 Lodz, Poland
[+]now at: Warsaw University of Technology, 09-400 Plock, Poland
[*]now at: University of Leeds, Leeds LS2 9JT, U.K.

Abstract. The interpretation of extensive air shower (EAS) measurements often requires the comparison with EAS simulations based on high-energy hadronic interaction models. These interaction models have to extrapolate into kinematical regions and energy ranges beyond the limit of present accelerators. Therefore, it is necessary to test whether these models are able to describe the EAS development in a consistent way. By measuring simultaneously the hadronic, electromagnetic, and muonic part of an EAS the experiment KASCADE offers best facilities for checking the models. For the EAS simulations the program CORSIKA with several hadronic event generators implemented is used. Different hadronic observables, e.g. hadron number, energy spectrum, lateral distribution, are investigated, as well as their correlations with the electromagnetic and muonic shower size. By comparing measurements and simulations the consistency of the description of the EAS development is checked. First results with the new interaction model NEXUS and the version II.5 of the model DPMJET, recently included in CORSIKA, are presented and compared with QGSJET simulations.

1 Introduction

At high energies ($> 10^{14}$ eV) the flux of cosmic rays becomes so low that direct measurements with balloon or satellite experiments run out of statistics. In this energy range only ground based experiments have been realized so far. These experiments cannot measure the primary particles directly, but the EAS induced by them in the atmosphere. Therefore, the interpretation of the measurements depends on the comparison with EAS simulations based on high-energy hadronic interaction models. To reduce uncertainties caused by these models it is mandatory to check the reliability of the used models. Vice versa, it is possible to obtain information about the hadronic interactions by comparing measured and simulated air showers.

When testing the interaction models in the energy range of 1 PeV–10 PeV, the problem arises that the flux and especially the mass composition of the primary cosmic rays are not well known. Therefore, in the following the measurements will be compared with the model predictions for the extreme assumption of a pure proton and a pure iron composition of the primaries. If the measured observable lies between the predictions, the corresponding model is compatible with the data, otherwise it is a hint at a problem of the model.

Recently the interaction model NEXUS and the version II.5 of the DPMJET model have been included in the CORSIKA program (Heck et al., 2001). In this analysis these models are compared with the "old" QGSJET model. An earlier comparison of QGSJET with the VENUS and the SIBYLL (Version 1.6) models has shown that QGSJET describes the measurements best (Antoni et al., 1999).

Correspondence to: J. Milke (milke@ik1.fzk.de)

2 Measurement and simulation

2.1 The experiment KASCADE

The experiment KASCADE, located on the site of the Forschungszentrum Karlsruhe (Germany), 110 m a.s.l., consists of several detector systems. A detailed description can be found in (Klages et al., 1997). The $200 \times 200\,\mathrm{m}^2$ large array of 252 detector stations, equipped with scintillation counters, measures the electromagnetic and muonic part of EAS.

In the center an iron sampling calorimeter (with an area of $16 \times 20\,\mathrm{m}^2$) detects the hadrons in the shower core. The calorimeter is equipped with 11 000 liquid ionization chambers in nine layers (Engler et al., 1999). Due to its fine segmentation ($25 \times 25\,\mathrm{cm}^2$) energy, position, and angle of incidence can be measured for individual hadrons.

2.2 Observables and event selection

From the array measurement the position of the shower core and the angle of incidence of the EAS are reconstructed (accuracy about 2 m at 1 PeV and better than 0.5 m at 10 PeV). By integrating the measured lateral distributions of electrons and muons the total particle numbers are determined. For the muons additionally the *truncated muon number* N_μ^{tr} in the distance range 40–200 m is calculated (details in (Antoni et al., 2001)). The hadrons in the calorimeter are reconstructed by a pattern recognition algorithm, which is optimized to separate the hadrons in the shower core. Hadrons at a distance of 40 cm are separated with a probability of 50% (Engler et al., 1999). The reconstruction efficiency is about 70% at 50 GeV and rises to nearly 100% at 100 GeV. The energy resolution varies from about 20% at 100 GeV to about 10% at 10 TeV. For all analyses an energy cut of 50 GeV is applied. For the hadron number N_h and the hadronic energy sum ΣE_h hadrons up to a distance of 10 m to the shower axis are taken into account. They are corrected for missing area beyond the boundaries of the calorimeter.

Events accepted for the analysis have to fulfill the following requirements: The shower core determined by the detector array is in the calorimeter, the zenith angle is less than 30°, the electron number N_e is larger than 10^4, the muon number N_μ^{tr} is larger than 10^3, and at least one hadron with an energy above 50 GeV is reconstructed in the calorimeter. After all cuts about 56 000 events, measured from May 1998 until April 2000, are left for the investigations.

2.3 Simulations

The EAS simulations were performed using the CORSIKA program (Heck et al., 1998). The interaction models chosen are QGSJET (version from 1997 (Kalmykov et al., 1997), CORSIKA version 5.644), NEXUS (version 2 (Drescher et al., 2000), CORSIKA version 5.946) and DPMJET (version II.5 (Ranft, 1999), CORSIKA version 6.001). For each of the models EAS simulations for primary protons and iron nuclei were performed in the energy range 10^{14}–10^{17} eV and zenith angles 0°–30°. The shower core positions were distributed uniformly over the calorimeter surface extended by 2 m beyond its boundary. For each combination of models and primaries about 46 000 showers with an overall spectral index of -2.0 were simulated. For the comparison with the measurements this spectral index was converted to a -2.7 slope.[1] To determine the detector response, all secondary particles at ground level are passed through a detector simulation program based on the GEANT package.

[1] Without a knee. This doesn't influence the results significantly.

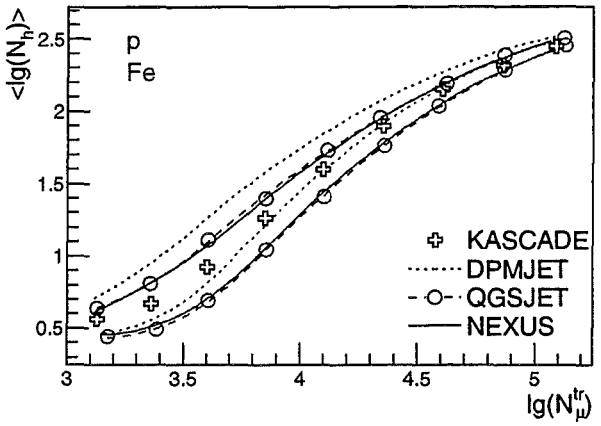

Fig. 1. Hadron number N_h versus muon number N_μ^{tr}. For reasons of better visibility for DPMJET and NEXUS only a parameterization is plotted. The muon number range $3.0 < \lg N_\mu^{\mathrm{tr}} < 5.25$ corresponds to a primary energy range 0.3–70 PeV.

3 Results

When comparing measurements and simulations, it is necessary to divide the data in intervals of shower sizes. In the following, examples of hadronic observables as functions of the electromagnetic (N_e) and muonic (N_μ^{tr}) shower sizes are discussed.

3.1 Shower Size Correlations

In figure 1 the correlation of the hadron number (N_h) and the muon number (N_μ^{tr}) is plotted. The measured data are compared with the prediction of all three models for primary protons and iron nuclei. Between the models QGSJET and NEXUS no difference can be found. Both models describe the measurements well (the measurements lie between the predictions of the models for proton and iron induced air showers). The model DPMJET however predicts a significantly larger hadron number than the other models. At large muon numbers (corresponding to high primary energies) the measured data do not lie between the model predictions. Therefore, the DPMJET model cannot describe the N_h–N_μ^{tr} correlation. In conjunction with other observables like the electron number (N_e) and the age parameter of the NKG fit to the electron lateral distribution it has to be concluded that showers simulated with DPMJET penetrate too deeply into the atmosphere.

Figure 2 shows the correlation of the hadronic energy sum (ΣE_h) and the electron number (N_e). When dividing the data in ranges of the electron number, within the individual bins proton induced showers are enriched because iron nuclei need a higher energy to yield the same electron number as proton induced showers. Hence, we expect that the measurements mainly follow the proton predictions. The QGSJET model fulfills this expectation. The deviation at higher electron numbers have not to be a hint at problems of the model. In this energy range it cannot be excluded that the primary

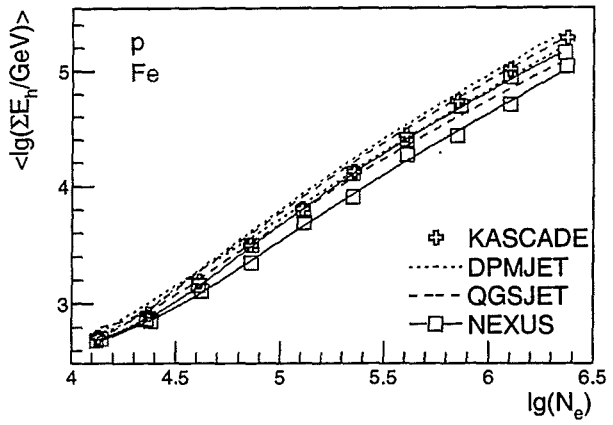

Fig. 2. Hadronic energy sum ΣE_h versus electron number N_e. For QGSJET and DPMJET only the parameterizations are plotted. The electron number range $4.0 < \lg N_e < 6.5$ corresponds to a primary energy range 0.3–20 PeV for proton and 0.5–40 PeV for iron induced showers.

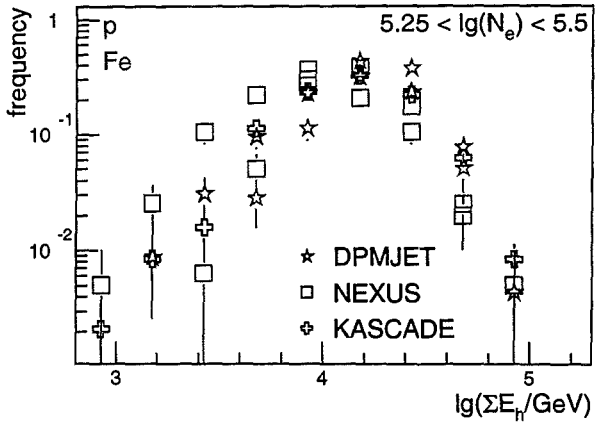

Fig. 4. Frequency distribution of the hadronic energy sum ΣE_h. The electron number bin corresponds to a primary energy of about 1.5 PeV for proton and 5 PeV for iron induced showers. The QGSJET distributions, not plotted here, are similar to DPMJET.

flux is dominated by iron nuclei, whereby the assumption of a proton enrichment is not longer valid. DPMJET also shows a relatively good agreement with the expectation. But, at low electron numbers the hadronic energy sum is overestimated by the model. The NEXUS model cannot describe the ΣE_h–N_e correlation at all. For all electron numbers the measurement lies on or even above the model predictions for iron induced showers. NEXUS predicts too few hadrons at constant electron numbers.

In addition to the mean values in figures 1 and 2 also the distributions of the hadron numbers and hadronic energy sums in the individual N_μ^{tr} and N_e intervals are investigated. Two examples are shown in figures 3 and 4. The shape of the distributions is, within the statistical errors, the same for all models and describes the measured data well. The main difference between the models is the shift of the mean values, as already seen in figures 1 and 2.

3.2 Lateral Distributions

Another model test concerns the lateral distribution of the hadrons in the core of the EAS. Figure 5 shows the energy density vs. the distance to the shower core in a muon number interval. All three models describe the shape of the measured lateral distribution quite well. But, the DPMJET prediction lies too high, as already seen in figure 1.

To point out the shape of the lateral distribution, the values are normalized to the integrals of the curves (see figure 6). Again, the models describe the measured values well. The differences between the models are rather small.

3.3 Energy Spectra

Not only the lateral distribution, but also the energy distribution of hadrons can be checked. Figure 7 shows two exam-

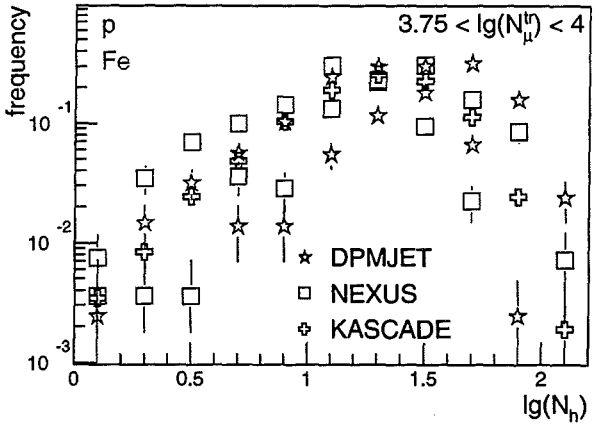

Fig. 3. Frequency distribution of the hadron number N_h. The muon number bin corresponds to a primary energy of about 2 PeV. The QGSJET distributions, not plotted here, are similar to NEXUS.

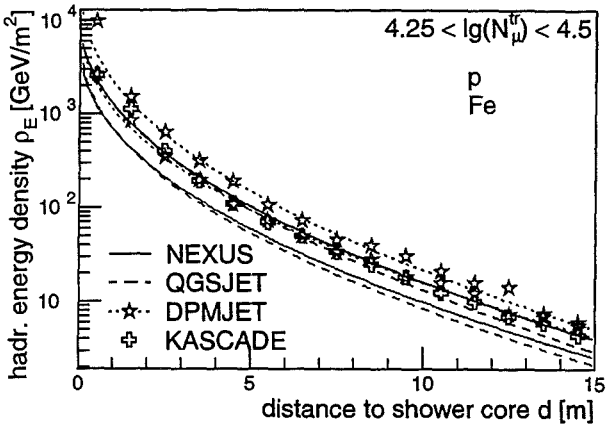

Fig. 5. Lateral distribution of the hadronic energy density. The muon number bin corresponds to a primary energy of 8 PeV.

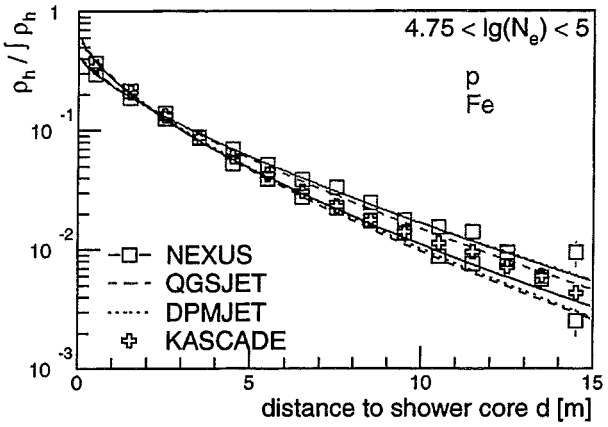

Fig. 6. Lateral hadron density.
To point out the shape of the lateral distributions, the curves are normalized to their integrals. The N_e bin corresponds to a primary energy of 0.7 PeV for proton and 2 PeV for iron induced showers.

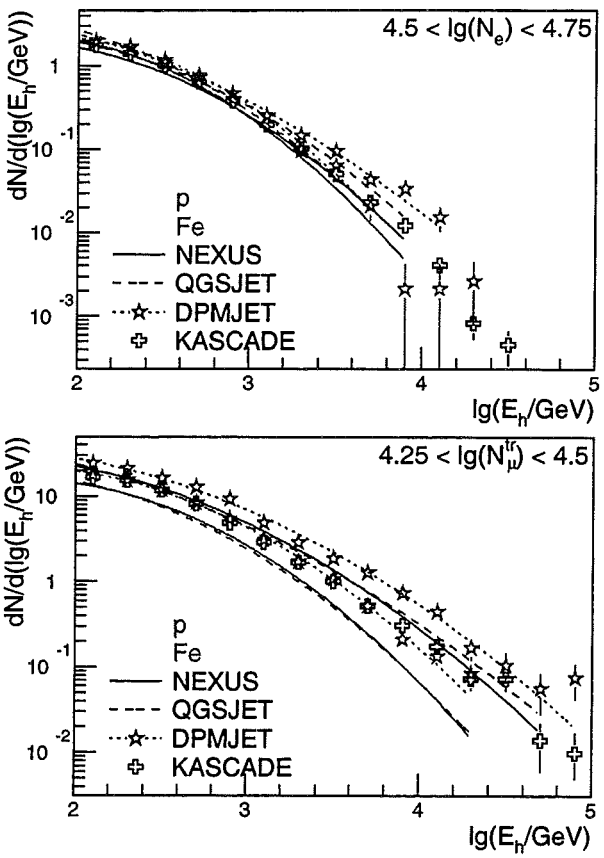

Fig. 7. Energy spectra of hadrons.
top: The N_e bin corresponds to a primary energy of 0.5 PeV for proton and 1.3 PeV for iron induced showers.
bottom: The N_μ^{tr} bin corresponds to 8 PeV.

ples. In the upper graph the spectra for an electron number interval are plotted. The models QGSJET and NEXUS describe the shape of the spectra quite well, the absolute values for NEXUS are again too low, whereas DPMJET overestimates the number of hadrons in the 10 TeV region for proton induced air showers. This effect was already seen in the correlation of hadronic energy sum and electron number (figure 2). At larger electron numbers this effect vanishes. In the bottom part of figure 7 the hadron energy spectra for a N_μ^{tr} interval is shown. All models describe the shape well, but DPMJET predicts a too large hadron number.

4 Conclusion

Using the hadronic shower core of EAS, measured by the KASCADE calorimeter, the interaction models NEXUS and DPMJET have been tested and compared with the QGSJET model. Several observables (number of hadrons, hadronic energy sum, frequency distributions of hadron number and energy sum, lateral distributions, and energy spectra) have been investigated as functions of the electromagnetic and muonic shower sizes. All three models describe the shapes of most distributions rather well. But, for the absolute values of hadron number and hadronic energy sum problems occur.

When dividing the data in intervals of the muon numbers, the model DPMJET overestimates hadron number and hadronic energy sum at ground level. Air showers simulated with DPMJET seem to penetrate too deeply into the atmosphere. Vice versa, when dividing the data in electron number bins, the model NEXUS predicts too small hadron numbers. There seems to be a problem in the balance between the hadronic and electromagnetic component of EAS. But, it should be stressed that both, NEXUS and DPMJET, are still under development and the problems might be specific to the used versions NEXUS 2 and DPMJET II.5.

Acknowledgements. The KASCADE experiment is supported by Forschungszentrum Karlsruhe and by collaborative WTZ projects in the frame of the scientific technical cooperation between Germany and Romania (RUM 97/014), Poland (POL 99/005) and Armenia (ARM 98/002). The Polish group (Soltan Institute and University of Lodz) acknowledges the support by the Polish State Committee for Scientific Research (grant No. 5 P03B 133 20).

References

Antoni, T. et al. (KASCADE Collaboration), J. Phys. G **25** (1999), 2161
Antoni, T. et al. (KASCADE Collaboration), Astroparticle Physics **14** (2001), 245
Drescher, H.J. et al., preprint hep-ph/0007198 (2000); Phys. Rep. (in print)
Engler, J. et al., Nucl. Inst. Meth. A **427** (1999), 528
Heck, D. et al., Report FZKA 6019, Forschungszentrum Karlsruhe (1998)
Heck, D. et al., Proc 27th Int. Cosmic Ray Conf., Hamburg (2001)
Kalmykov, N., Ostapchenko, S., and Pavlov, A.I., Nucl. Phys. B (Proc. Suppl.) **52B** (1997), 17
Klages, H.O. et al. (KASCADE Collaboration), Nucl. Phys. B (Proc. Suppl.) **52B** (1997), 92
Ranft, J., preprint hep-ph/9911213 (1999)

Proceedings of ICRC 2001: 1418 © Copernicus Gesellschaft 2001

ICRC 2001

Search for elongated spatial structures in hadronic shower cores with KASCADE

A. Iwan[1,5], T. Antoni[2], W. D. Apel[2], F. Badea[3], K. Bekk[2], A. Bercuci[2], H. Blümer[1,2], E. Bollmann[2], H. Bozdog[3], I. M. Brancus[3], C. Büttner[2], A. Chilingarian[4], K. Daumiller[1], P. Doll[2], J. Engler[2], F. Feßler[2], H. J. Gils[2], R. Glasstetter[1], R. Haeusler[2], A. Haungs[2], D. Heck[2], T. Holst[2], J. R. Hörandel[1], K-H. Kampert[1,2], J. Kempa[5,+], H.O. Klages[2], J. Knapp[1,*], G. Maier[2], H. J. Mathes[2], H. J. Mayer[2], J. Milke[2], M. Müller[2], R. Obenland[2], J. Oehlschläger[2], M. Petcu[3], H. Rebel[2], M. Risse[2], M. Roth[2], G. Schatz[2], H. Schieler[2], J. Scholz[2], T. Thouw[2], H. Ulrich[1], B. Vulpescu[3], J. H. Weber[1], J. Wentz[2], J. Wochele[2], and J. Zabierowski[6]

[1]Institut für Experimentelle Kernphysik, University of Karlsruhe, P.O. Box 3640, 76021 Karlsruhe, Germany
[2]Institut für Kernphysik, Forschungszentrum Karlsruhe, 76021 Karlsruhe, Germany
[3]National Institute of Physics and Nuclear Engineering, 7690 Bucharest, Romania
[4]Cosmic Ray Division, Yerevan Physics Institute, Yerevan 36, Armenia
[5]Department of Experimental Physics, University of Lodz, 90236 Lodz, Poland
[6]Soltan Institute for Nuclear Studies, 90950 Lodz, Poland
[+]now at: Warsaw University of Technology, 09-400 Plock, Poland
[*]now at: University of Leeds, Leeds LS2 9JT, U.K.

Abstract.

In this analysis the structure of hadronic shower cores is investigated with the KASCADE calorimeter. The energy, position, and direction of incidence for individual hadrons above 50 GeV are measured. In parallel, the spatial structure is studied using the simulation program CORSIKA with the hadronic interaction model QGSJET. First results are presented for the showers with primary energies above 5 PeV. Elongated cores are observed more frequently than expected from random coincidence. This proves that KASCADE is sensitive to hadronic interaction producing elongated structures. Alignment can be found in both data sets - measurements and simulation. No significant deviation between them or hints for new physics have been found so far.

1 Introduction

A finely segmented hadron calorimeter designed to study air shower cores is located in the center of the KASCADE EAS experiment (Klages et al. 1997). It is capable to measure energy, positions and direction of individual hadrons and, therefore, allows to search in hadronic cores for unusual structures. They could be signatures of certain properties of high-energy interactions of cosmic-ray particles with the air nuclei, and might allow to test hadronic interaction models. Structures of special interest are elongated hadronic cores. Experiments using X-ray emulsion chamber techniques at mountain altitudes, such as Pamir (Borisov et al., 1984, 2001), Kanbala (Xue et al., 1999) or in the stratosphere, like CONCORDE-ECHOS (Capdevielle, 1997, 2001) have reported on gamma hadron families showing strong geometrical alignment. Various interaction models have been tested in order to reproduce the observed phenomena and possible physics mechanisms were discussed (Mukhamedshin, 1994, 2001). The current status of these investigations is reflected in the following conclusion: "The alignment of superfamilies cannot be explained by the QCD-jet production but results from some new physical mechanism of coplanar emissions of particles in strong interactions" (Borisov et al., 2001). A search for elongated hadronic cores in the data registered by the KASCADE calorimeter and a comparison with simulated results may give some additional hints towards an explanation of the phenomena mentioned above.

Correspondence to: A. Iwan (iwan@ikl.fzk.de)

2 Experimental Set-up and Measurements

The KASCADE experiment, located at the Forschungszentrum Karlsruhe (Germany), measures with high precision all three components of an EAS. A large number of shower parameters is provided on event-by-event basis. An array of 252 scintillator stations, located on a 200×200 m^2 field, gives information about the electromagnetic and muonic (E_μ > 230 MeV) component. Three additional muon detectors (with thresholds of 0.49, 0.8 and 2.4 GeV) are operated in the Central Detector and the Muon Tunnel. The hadronic component is measured by a 16×20 m^2 iron calorimeter (Engler et al., 1999), being the main part of the Central Detector system (Fig. 1). The detector is equipped with 11 000 liquid

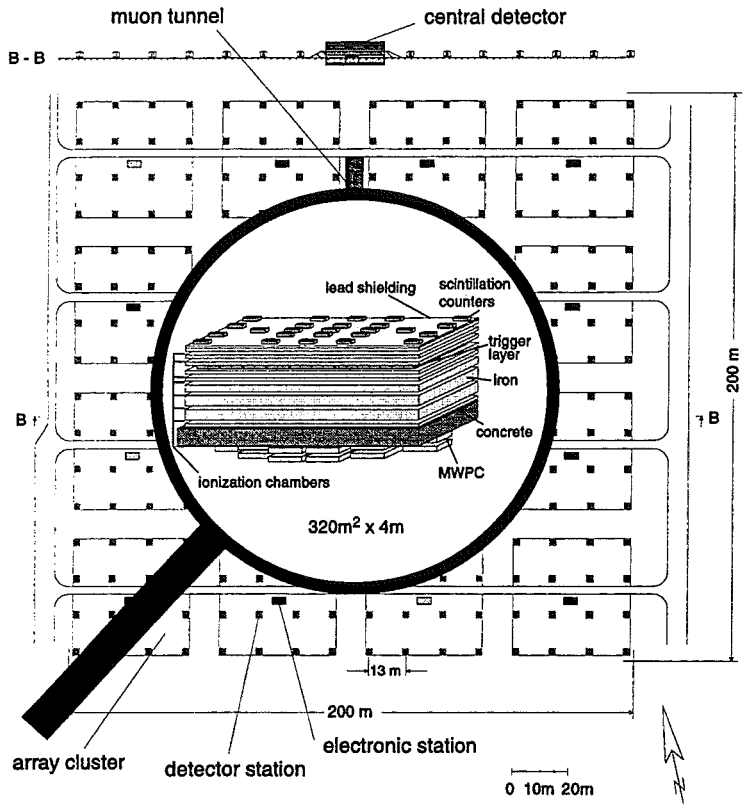

Fig. 1. Location of the hadron calorimeter within the KASCADE experiment.

ionization chambers, arranged in 9 layers above, between, and below the absorber. The latter consists of 4 000 t iron, concrete, and lead with a total thickness of 11.5 nuclear interaction lengths for vertical protons, ensuring a reasonable shower containment up to 25 TeV hadron energy. On average, 97.5 % of the energy is deposited in the calorimeter at this energy. Each chamber is read out by four 25×25 cm^2 pads.

The hadron energy reconstruction accuracy changes from 20 % at 100 GeV to 10 % at 10 TeV. The reconstruction efficiency approaches unity for hadrons of 100 GeV. The accuracy in position determination for hadrons of 100 GeV equals to 14 cm and reaches $\approx$ 10 cm for 1 TeV, and the hadron zenith angle accuracy improves from 12° at $E_H = 100$ GeV to 5° at $E_H = 1$ TeV.

3 Analysis

For the present analysis about 7.0 million showers with at least one reconstructed hadron have been considered. They have been registered between January 1997 and March 2000. The following cuts were applied to the data: The shower axis has been reconstructed in the center of the calorimeter with a distance of at least 3 m from its boundaries. Additionally, *truncated muon numbers* (Glasstetter et al., 1999) of $\log(N_\mu^{tr})$>3.5, zenith angles $\theta < 30°$ and at least four hadrons with an energy $E_H \geq$500 GeV are required. The muon number corresponds to a primary energy $E_0 > 10^{15}$ eV. 1417 events survived these cuts and are used for the following analysis. The hadron positions are transformed into a plane perpendicular to the shower direction.

3.1 Asymmetry parameter

Several quantities may be used to characterize the geometrical structure of high–energy hadronic shower cores. As an example, we apply the parameter λ, introduced by the Pamir Collaboration (Borisov et al., 1984):

$$\lambda_N = \frac{\Sigma_{i\neq k\neq j}^{N} cos2\phi_{ij}^{k}}{N(N-1)(N-2)} \quad (1)$$

where N is the number of hadrons, and ϕ_{ij}^k is the angle between straight lines connecting the i^{th} and j^{th} hadron with the k^{th}. The parameter λ_N equals 1 in the case of complete alignment of N hadrons along one straight line and tends to $-\frac{1}{N-1}$ for an isotropic distribution of hadrons in a plane.

3.2 Aligned events

For our data sample the parameter λ_4 was calculated, taking into account the 4 most energetic reconstructed hadrons. In Fig. 2. the example of a typical shower core with λ_4 = -0.11

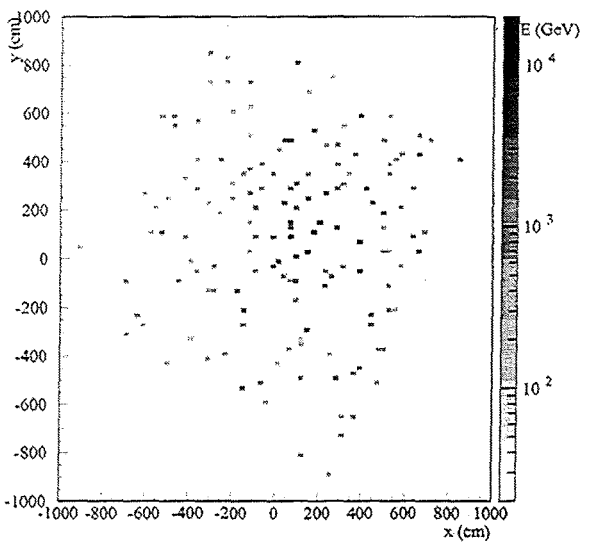

Fig. 2. Example of a measured, isotropic hadronic shower core with $\lambda_4 = -0.11$. Reconstructed primary energy is about $2 \cdot 10^{16}$ eV.

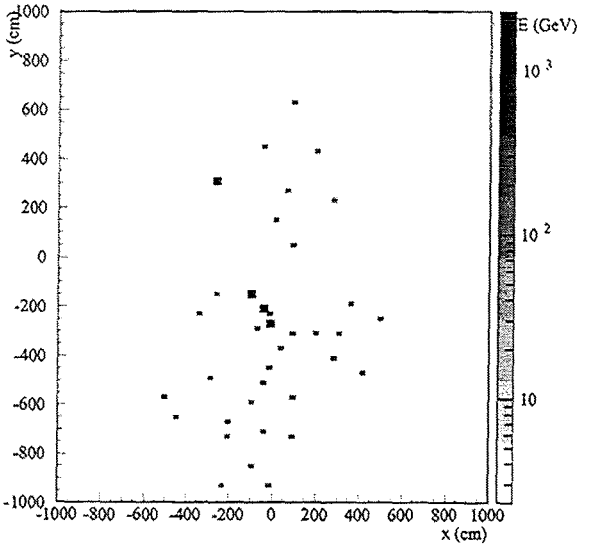

Fig. 3. Example of a measured, elongated hadronic shower core with λ_4 =0.82. Reconstructed primary energy is about $6 \cdot 10^{15}$ eV.

is shown. An example of an elongated event is given in Fig. 3 with $\lambda_4 = 0.82$.

The λ_4-distribution of the data together with results of two sets of random generated hadron positions are presented in Fig. 4. These tests show how the λ_4 parameter is distributed for isotropic events. In the first test (RANDOM1), four positions of hadrons within the fiducial area of the calorimeter are randomly chosen from a uniform distribution in x and y, then the parameter λ_4 is calculated. The second test was done taking into account the real lateral distribution of hadrons in a shower core. Starting from the measured configuration of the hadrons, their azimuthal angles are randomly varied around the geometrical center-of-gravity and again λ_4 is calculated (RANDOM2). Both tests are consistent with each other. The comparison with the KASCADE data shows, that for $\lambda_4 > 0.6$ the frequency of the data points exceeds by $\approx 60\%$ the results of both tests. The measured distribution is significantly shifted towards larger values of λ_4, i.e., to non-isotropic events. Thus, we can conclude, that the observed alignment tendency in hadronic EAS cores is not a pure-chance phenomenon.

4 Simulations

In order to check the physical relevance of the observed alignment in the data, we compare them with simulations. Showers with a primary energy $E_0 \geq 5$ PeV, initiated by protons and iron nuclei, with a spectral index of -2.7, have been simulated. The CORSIKA version 5.644 (Heck et al., 1998) with the hadronic interaction model QGSJET (Kalmykov et al., 1997) was used. A full detector simulation using GEANT3 (CERN, 1993) was performed and the events were reconstructed with the same software procedures as were used for the data. Finally, the parameter λ_4 was calculated and is plotted in Fig. 5 together with the data. As it is seen there, the simulations fully reproduce our data points.

Since KASCADE — in contrast to the emulsion chamber experiments — is located nearly at sea level, it has to be checked whether we would by sensitive to elongated structures generated in the first interactions. For this purpose spe-

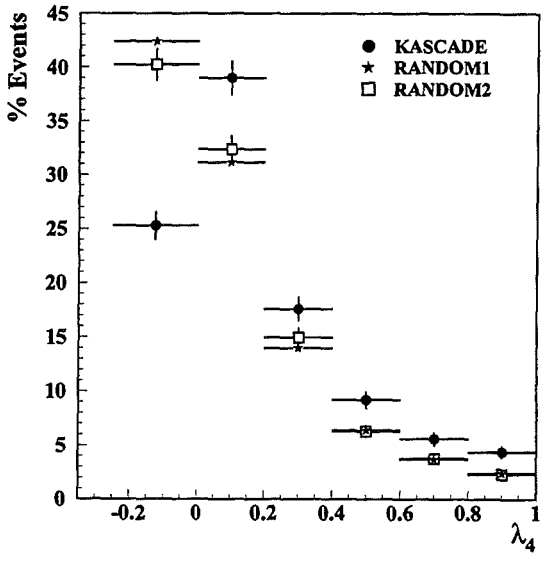

Fig. 4. Distribution of the parameter λ_4 for the KASCADE data and two random tests (see text).

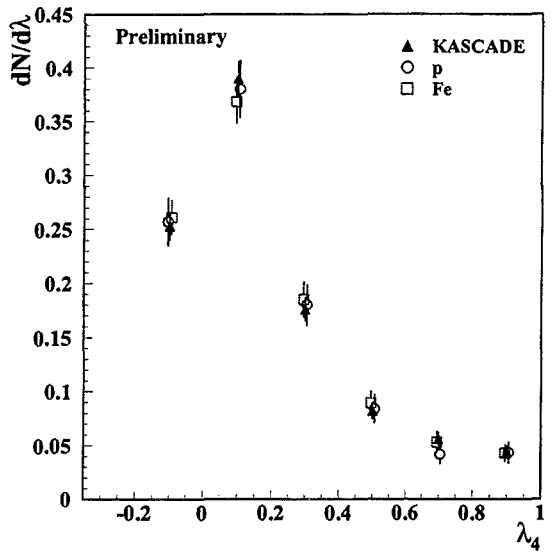

Fig. 5. Normalized distribution of a lambda parameter for KASCADE data and simulated showers with proton and iron primaries with $E_0 \geq 5$ PeV.

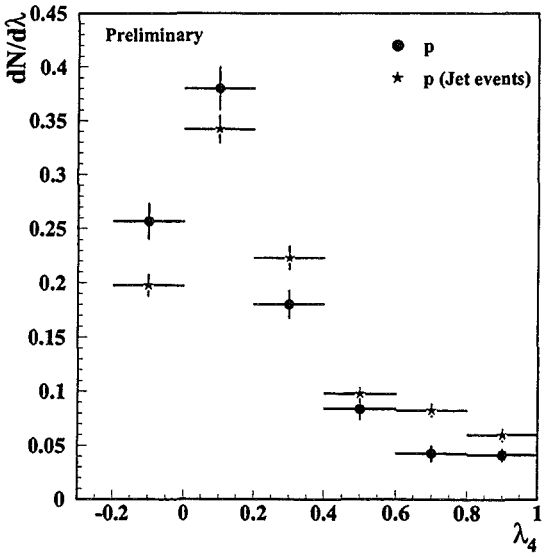

Fig. 6. Normalized distribution of a lambda parameter for simulated showers with a proton primary ($E_0 \geq 5$ PeV) for a standard QGSJet model and QGSJet where only events with jet production in the first interaction have been considered.

cially flagged showers were selected. *Grosso modo*, showers with a high-$\langle p_t \rangle$ jet (above a few GeV) of high-energetic hadrons in the first interaction are looked for. In Fig. 6 the corresponding λ_4 parameter of the flagged events is plotted together with the results obtained for all simulated events. A clear difference between those two distributions of the lambda parameter is seen. It signifies, that events with jet production exhibit a larger degree of hadron alignment, and that the method applied is sensitive to such interactions. This gives a hint towards further investigations of the role of QCD jet production and of elongated hadronic shower cores.

5 Conclusions

The preliminary study of the hadronic cores registered by the KASCADE calorimeter allows the following first conclusions:

1. Despite of its location nearly at the sea level, the KASCADE calorimeter is sensitive to hadron alignment phenomena generated in the first interactions.
2. To explain the observed elongation of events no necessity of new physics has been found so far. Instead, based on QGSJET simulations, normal QCD jet production seems to explain the observed degree of hadronic alignment.

Investigations using larger samples of data and simulated events are in progress. It is foreseen to include further observables in order to investigate the structure of the hadronic shower cores in coordinate and energy space.

Acknowledgements. The KASCADE experiment is supported by Forschungszentrum Karlsruhe and by collaborative WTZ projects in the frame of the scientific technical cooperation between Germany and Romania (RUM 97/014), Poland (POL 99/005) and Armenia (ARM 98/002). The Polish group (Soltan Institute and University of Lodz) acknowledges the support by the Polish State Committee for Scientific Research (grant No. 5 P03B 133 20).

A. I. is grateful for the support by a Marie Curie Training Site Grant "Physics at present and future colliders".

References

Borisov A.S. et al., *Proc. 3rd ISVHECRI*, Tokyo, 49, 1984.
Borisov A.S. et al., *Nucl. Phys. B (Proc. Suppl.)* **97**, 118, 2001.
Capdevielle J.N., *Proc. 25th Int. Cosmic Ray Conf.*, Durban **6**, 57, 1997.
Capdevielle J.N., *Nucl. Phys. B (Proc. Suppl.)* **97**, 126, 2001.
CERN GEANT 3.21, Detector Description and Simulation Tool, CERN Program Library Long Writeups W5015, 1993.
Engler J. et al., *Nucl.Inst. Meth. A* **427**, 528, 1999.
Glasstetter R. et al., (KASCADE Collaboration), *Nucl. Phys. B (Proc.Suppl.)* **75A**, 238, 1999.
Heck D. et al., Report **FZKA 6019**, Forschungszentrum Karlsruhe, 1998.
Kalmykov N.N., Ostapchenko S.S., and Pavlov A.I., *Nucl. Phys. B (Proc. Suppl.)* **52B**, 17, 1997.
Klages H.O. et al., (KASCADE Collaboration), *Nucl. Phys. B (Proc.Suppl.)* **52B**, 92, 1997.
Mukhamedshin R.A., *Proc. 7th ISVHECRI*, Tokyo, 57, 1994.
Mukhamedshin R.A., *Nucl. Phys. B (Proc. Suppl.)* **97**, 144, 2001.
Xue L. et al., *Proc. 26th Int. Cosmic Ray Conf.* Salt Lake City **1**, 127, 1999.

Proceedings of ICRC 2001: 806 © Copernicus Gesellschaft 2001

ICRC 2001

A layer of streamer tube detectors for the measurement of muons in the KASCADE central detector

T. Antoni[1], W. D. Apel[1], F. Badea[2], K. Bekk[1], A. Bercuci[1,2], H. Blümer[1,3], E. Bollmann[1], H. Bozdog[2], I. M. Brancus[2], C. Büttner[1], A. Chilingarian[4], K. Daumiller[3], P. Doll[1], J. Engler[1], F. Feßler[1], H. J. Gils[1], R. Glasstetter[3], R. Haeusler[1], A. Haungs[1], D. Heck[1], J. R. Hörandel[3], T. Holst[1], A. Iwan[3,5], K-H. Kampert[1,3], J. Kempa[5,+], H.O. Klages[1], J. Knapp[3,¶], G. Maier[1], H. J. Mathes[1], H. J. Mayer[1], J. Milke[1], M. Müller[1], R. Obenland[1], J. Oehlschläger[1], M. Petcu[2], H. Rebel[1], M. Risse[1], M. Roth[1], G. Schatz[1], H. Schieler[1], J. Scholz[1], T. Thouw[1], H. Ulrich[3], B. Vulpescu[2], J. H. Weber[3], J. Wentz[1], J. Wochele[1], J. Zabierowski[6], and S. Zagromski[1]

[1]Institut für Kernphysik, Forschungszentrum Karlsruhe, 76021 Karlsruhe, Germany
[2]National Institute of Physics and Nuclear Engineering, 7690 Bucharest, Romania
[3]Institut für Experimentelle Kernphysik, University of Karlsruhe, 76021 Karlsruhe, Germany
[4]Cosmic Ray Division, Yerevan Physics Institute, Yerevan 36, Armenia
[5]Department of Experimental Physics, University of Lodz, 90236 Lodz, Poland
[6]Soltan Institute for Nuclear Studies, 90950 Lodz, Poland
[+]now at: Warsaw University of Technology, 09-400 Plock, Poland
[¶]now at: University of Leeds, Leeds LS2 9JT, U.K.

Abstract. For an improved detection of cosmic ray muons with a threshold of 2.4 GeV, the KASCADE Central Detector has been upgraded with a new detector component built of limited streamer tubes. Combined with the operation of two layers of multiwire proportional chambers they enable studies of the muonic component of extensive air showers at higher particle densities. Due to the pad readout system of the streamer tubes, ambiguities in the muon track reconstruction, resulting from limitations of the readout system of the multiwire proportional chambers, can be resolved. Additionally the sensitive area for muon detection is increased from 40% to 82% of the area of the Central Detector by the new layer of streamer tubes, with a good spatial resolution in the parts not covered by the multiwire proportional chambers. The setup of the new detector system and the reconstruction procedures are described and demonstrated by first measurements.

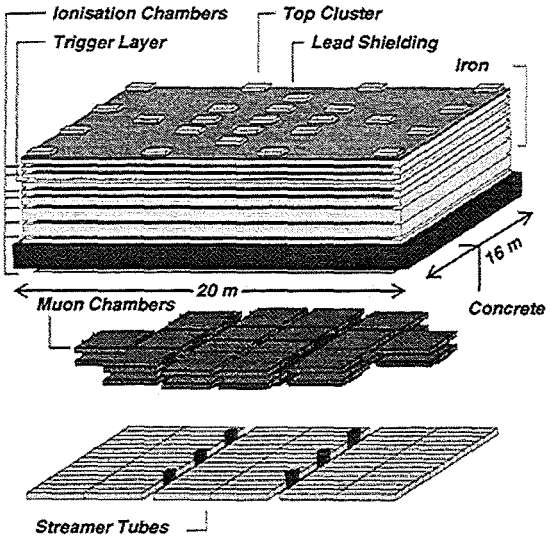

Fig. 1. Schematic view of the KASCADE Central Detector.

1 Introduction

The KASCADE experiment (Klages et al., 1997) at the site of the Forschungszentrum Karlsruhe aims at measuring extensive air showers (EAS) produced by the primary cosmic ray particles interacting with air nuclei in the earth's atmosphere. It consists of a 200 × 200 m^2 detector array built of scintillation counters for the measurement of the electromagnetic and muonic shower component. It also contains an underground muon tracking detector (Atanasov et al., 2000) that uses streamer tube detectors. In the middle of the detector array the Central Detector is placed which includes several components aiming at different observables of an EAS (Fig. 1). Its main component is an iron sampling calorimeter (Engler et al., 1999), which consists of eight layers of liquid ionisation chambers for the detection of the hadronic component of EAS. A ninth layer of the calorimeter detectors has been added on top of the iron shielding to investigate the electromagnetic shower component with a nearly full cover-

Correspondence to: T. Antoni (antoni@ik3.fzk.de)

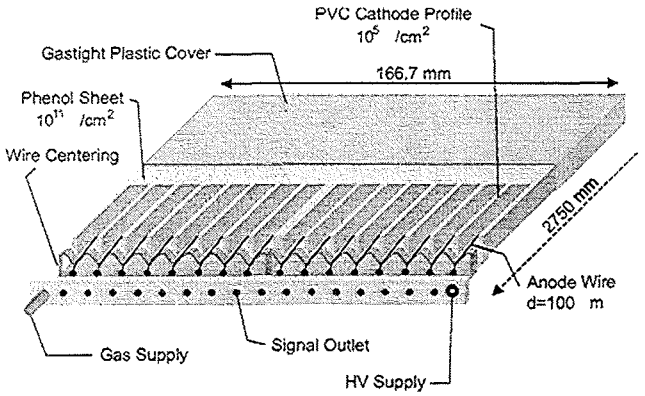

Fig. 2. Schematic view of one streamer tube.

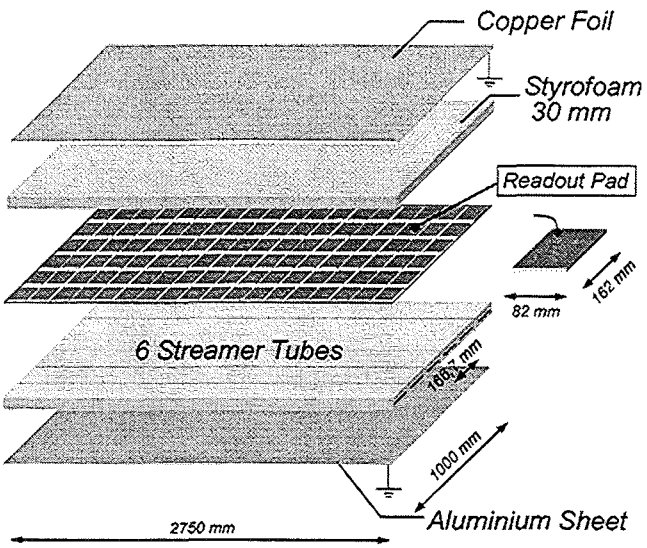

Fig. 3. Schematic view of a LST module with pad readout system.

age of the Central Detector area. On top of the calorimeter an array of 50 plastic scintillation detectors is installed. The purpose of this Top Cluster is the measurement of the electromagnetic component of EAS and to trigger the Central Detector for small shower sizes. In the third gap of the calorimeter a layer built of the same kind of scintillation counters is installed. This Trigger Plane consists of 456 detectors covering 64% of the area of the Central Detector. They are used to investigate the muonic shower component above a threshold of 490 MeV and to generate an additional trigger signal for the Central Detector. In the basement of the Central Detector two layers of multiwire proportional chambers (MWPC) are installed (Bozdog et al., 2000). They are used for investigating the muonic component of air showers above a threshold of 2.4 GeV for the muons, which is given by the iron shielding of the calorimeter. With these detectors the lateral distribution of muons (Haungs et al., 1996; Antoni et al., 2001) as well as muon density distributions (Haungs et al., 1999; Antoni et al., in press) have been studied. The investigations have been limited by the size of the detector system, as it covers only about 40% of the area of the Central Detector, and also by the ability to resolve multiple particle hits. Due to the layout of the MWPC detectors which consist of two layers of cathode stripes diagonal to each other and the anode wires, ambiguities occur above a particle density of 2 m^{-2}. As a result of these ambiguities only particle densities in a range of up to 4 m^{-2} can be measured. To improve this situation a third layer of detectors has been installed below the MWPC, increasing the detector area and the resolution of ambiguities of the hit reconstruction.

2 The streamer tubes

The new detector component for measuring muons in the basement of the Central Detector is built of Limited Streamer Tubes (LST). These are gas detectors making use of the self-quenching streamer mode (Doll et al., 1994) that is reached when, due to the very high voltage between the anode and cathode, the charge multiplication becomes so large that the electric field in the space charge equals the outer field. This causes the electrons to recombine with the ions. To prevent secondary charge avalanches, induced by photons produced in these processes, from sreading along the anode wire a quenching gas is used, thus keeping the signals localized.

2.1 Detector layout

In the streamer tubes employed here, CO_2 has been used as counting gas since it has good characteristics for producing signals and quenching and additionally can be used without safety regulations. All LST used in the KASCADE experiment are manufactured by WATECH, Vienna, Austria. The dimensions of one streamer tube are 2750 × 167 × 13 mm^3. The layout of one LST can be seen in Fig. 2. It consists of 16 anode wires of 100 μm that are positioned in a comb-like cathode profile with a cell size of 9 × 9 mm^2 made of conducting PVC. On the upper side this profile is closed with a sheet of conducting phenol paper. These components are located inside a gas tight plastic cover with a gas feed through on both ends and a signal outlet for each wire as well a high voltage supply on the front face. The cathode materials have a high resistivity which allows an electrostatic induction signal to be registered outside the streamer tube. This is done with a pad readout system to get a spatial resolution of the hits along the wires. The streamer tubes are installed in the basement of the Central Detector in modules containing six LST which are mechanically fastened together and are covered by a joint pad layer. The layout of these installation modules can be seen in Fig. 3. The pad layer consists of a styrofoam sheet of 30 mm thickness with copper foil glued to both sides. On the side facing the LST gaps are cut into the foil to produce the readout pads of a size of 162 × 82 mm^2. This amounts to 32 pads along one streamer tube and 192 on the whole module. The wires are grouped in pairs to reduce the number of electronic channels while still having a good spatial resolution.

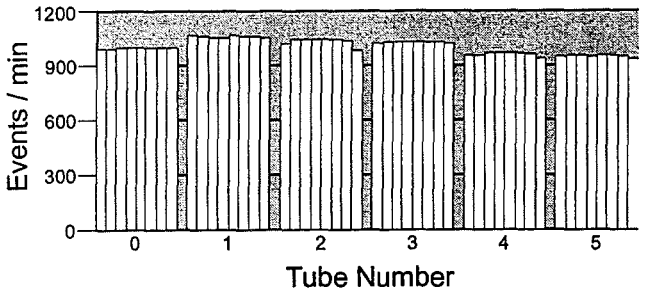

Fig. 4. Investigation of the homogeneity of the signals. The counting rate in the wire pairs of the six streamer tubes of the test module is shown here. The rate is homogeneous in each tube and there is a good agreement between the LST.

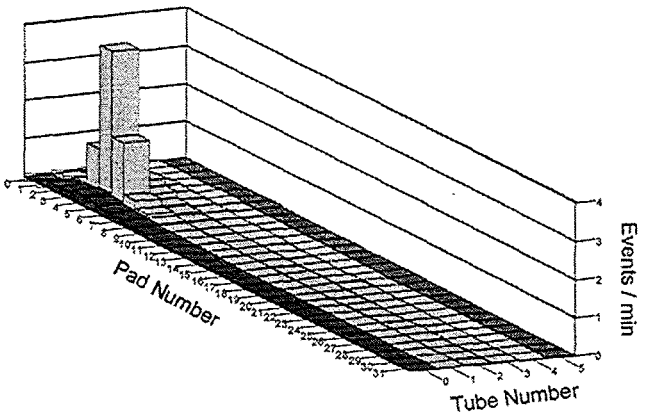

Fig. 5. Investigation of the crosstalk between the pads. The pad selected by the scintillator telescope shows the highest counting rate, but also the neighboring pads along the same tube show an increased rate. This is due to cross talk, geometry effects and the size of the charge cloud in the LST. Across the borders of the tubes there is almost no cross talk.

2.2 Readout electronics

The readout electronics for the LST detectors was developed at the Institut für Kernphysik of the Forschungszentrum Karlsruhe in co-operation with the Institute of Physics and Nuclear Engineering in Bucharest. It is a modified version of the electronics of the KASCADE Muon Tracking Detector (Zabierowski and Doll, 2001). The following basic conditions had to be fulfilled. The whole detector system consists of more than 22000 electronic channels which demands for a low price per channel. The signals of the LST are in the range of a few mV with a duration of several tens of ns, therefore special care has been taken in order to avoid noise and crosstalk between channels. A complete spatial separation between the analog and the digital parts of the electronics has been applied. The VME Streamer Tube Acquisition System (VME-STAS), that has been built, is a modular, VME controlled system. This VME-STAS consists of several modules. Two VME Streamer Tube Acquisition Modules (VME-STAM) each of which provides eight independent fast acquisition channels, which are fully controllable via VME bus. Each channel is receiving serial data (up to 2 Mbit/s sampling rate) coming from the acquisition boards of seven or eight streamer tube modules and saves them in a 512×8 bit FIFO memory. An external START signal commences the data acquisition with the internally chosen clock frequency. A splitter board controls the communication between the VME-STAM and the Acquisition Boards and collects the data from the acquisition chains. These readout chains consist of the Acquisition Boards that contain mainly the digital readout electronics to control the Amplifier/Discriminator Boards connected. The signals from either eight wires or eight pads are handled by one Amplifier/Discriminator Board. The delays and thresholds are adjustable via software controlled digital_to_analog converters.

3 Test measurements

As a first step in the study of the streamer tubes a test facility was built in the basement of the Central Detector. It consisted of one streamer tube module like they are in use in the final installation. This setup was equipped with a telescope of scintillation detectors to trigger on particles penetrating the module through one selected pad. The electronics used in this test facility was the prototype version of the electronics used later in the KASCADE system. Checks of its functioning showed the importance of a careful handling of the electric ground to minimize the noise disturbing the measurements. Two important results obtained with the test facility are shown in this paragraph. The homogeneity of the signals from the streamer tubes can can be seen in Fig. 4. The picture shows the free counting rate for each channel (wire pair). The rates of the channels belonging to the same tube are very homogeneous. The values for the different LST also show a good agreement, which is achieved by adjusting the thresholds. This result is also valid for the readout pads. Fig. 5 shows the result of a measurement triggered by the scintillator telescope that has been done to quantify the cross talk between the pads. It can be seen that there is almost no cross talk across the borders between different LST. In the direction of the wires the neighboring pads show an increased counting rate. This cross talk could be of electronic origin but also could be due to the extended space charge that can induce signals in more than one pad, since its size is roughly two thirds of the size of the pads, as a measurement with a finer segmentation showed. These effects are not distinguishable in this measurement. Summarizing, it can be said that the streamer tubes and the readout electronics seem to be working very well.

4 The streamer tubes in the KASCADE system

The LST have been installed in the basement of the KASCADE Central Detector 24 cm below the lower layer of the MWPC. The distance between the two layers of the MWPC is 38 cm. The streamer tubes cover approx. 80% of the area

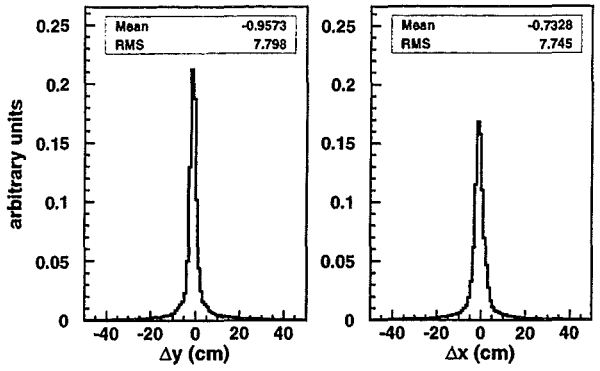

Fig. 6. Investigation of the agreement between the reconstruction of tracks in the multiwire proportional chambers and the hits in the streamer tubes. The pictures show the deviation in the x and y directions between the intersection of the MWCP tracks with the LST layer and the hits reconstructed in the LST.

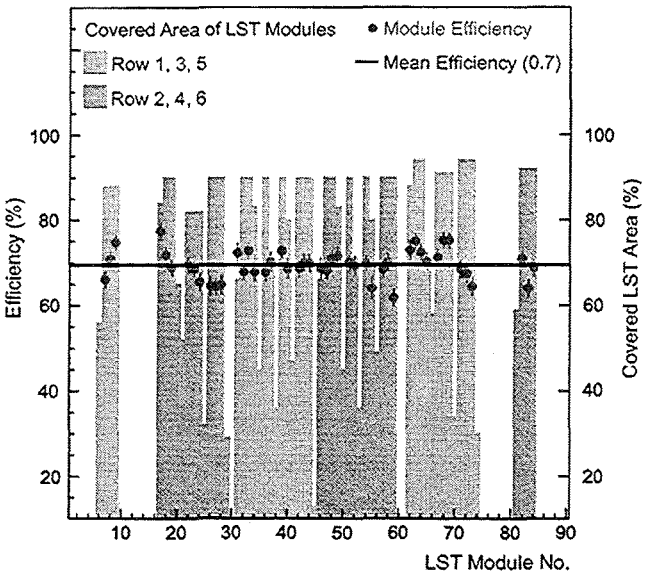

Fig. 7. Efficiency determination for the streamer tubes. The red dots show the efficiency for the modules that are covered by muon chambers to a large extend. The black line is the average over all these modules. The blue and green areas denote the percentage to which each LST module is covered with MWPC detection area.

of the Central Detector, which amounts to 16.5×15 m^2. The active area of the MWPC is only about 40%. As can be seen in Fig. 1 the LST layer is composed of six rows of 15 installation modules each. These 90 modules amount to 17280 pad channels and 4320 wire channels. After a period of stand alone measurements to test the functioning of the LST detectors and electronics, joint measurements and analyses of the MWPC and LST data have been started. As a first step the data of MWPC have been used to test the reconstruction algorithms for the LST data. The MWPC reconstruction offers two kinds of low level results. The hits in each of the two layers that have been reconstructed from the signals in corresponding anode wires and cathode stripes and the tracks calculated by correlating the hits in both MWPC layers. These MWPC tracks are intersected with the LST layer in order to check for matching hits in the streamer tube layer. Fig. 6 shows the distribution of the deviations between the expected and the measured hit positions in the LST. As expected the RMS of the distributions is about the size of the pads as can be seen in the two graphs that show the x and y directions. It can also be shown that there are no preferred directions in the deviations. With the same routines the efficiency of the LST can be investigated by checking the number of MWPC tracks that are intersected with the active area of the LST against the number of these tracks that have a matching LST hit. This procedure of course only is useful for LST modules that are for a large fraction covered by MWPC detectors. In Fig. 7 the blue and green areas denote the percentage to which each LST module is positioned below MWPC detectors. The efficiency of the LST for which this number is larger than 2/3 is displayed by the red dots. The black line gives the mean of these values which is approx. 70%. From these tests we deduce that our reconstruction algorithms work properly and we can start with more sophisticated analyses to reach into the particle densities the MWPC alone can not resolve.

5 Outlook

Based on the present tests it seems possible in the future to analyze muon distributions closer to the shower core on an event by event basis. The joint analysis of the MWPC and LST data has to be improved, in addition to the efficiency of the LST. To achieve this, pure CO_2 will be replaced by a mixture of *CO_2-Argon-Isobutane* or *Argon-Isobutane* only.

Acknowledgements. The KASCADE experiment is supported by the Forschungszentrum Karlsruhe and by collaborative WTZ projects in the frame of the scientific-technical cooperation between Germany and Romania (RUM 97/014), Poland (POL 99/005) and Armenia (ARM 98/002). The Polish group (Soltan Institute and University of Lodz) acknowledges the support by the Polish State Committee for Scientific Research (grant No. 5 P03B 133 20)

References

Antoni, T. et al., Astropart. Phys., 14, 245, 2001.
Antoni, T. et al., Astropart. Phys., in press 2001.
Atanasov, I. et al., FZKA Report 6474, Forschungszentrum Karlsruhe, 2000.
Bozdog, H. et al., FZKA Report 6580, Forschungszentrum Karlsruhe, 2000; Nucl. Instr. and Meth. A in press 2001.
Doll, P. et al., Nucl. Instr. and Meth., A 342, 495, 1994.
Engler, J. et al., Nucl. Instr. and Meth., A 427, 528, 1999.
Haungs, A. et al., Nucl. Instr. and Meth., A 372, 515, 1996.
Haungs, A. et al., FZKA Report 6262, Forschungszentrum Karlsruhe, 1999.
Klages, H. O. et al., Nucl. Phys. (Proc. Suppl.), 52B, 92, 1997.
Zabierowski, J. and Doll, P., submitted to Nucl. Instr. and Meth. A, 2001.

Proceedings of ICRC 2001: 810 © Copernicus Gesellschaft 2001

ICRC 2001

Large Muon Tracking Detector in the KASCADE EAS Experiment

J. Zabierowski[6], T. Antoni[1], W.D. Apel[1], F. Badea[2], K. Bekk[1], A. Bercuci[1,2], H. Blümer[1,3], E. Bollmann[1], H. Bozdog[2], I. M. Brancus[2], C. Büttner[1], A. Chilingarian[4], K. Daumiller[3], P. Doll[1], J. Engler[1], F. Feßler[1], H. J. Gils[1], R. Glasstetter[3], R. Haeusler[1], A. Haungs[1], D. Heck[1], J. R. Hörandel[3], T. Holst[1], A. Iwan[5,3], K-H. Kampert[1,3], J. Kempa[5,+], H. O. Klages[1], J. Knapp[3,¶], G. Maier[1], D. Martello[1,*], H. J. Mathes[1], H. J. Mayer[1], J. Milke[1], M. Müller[1], R. Obenland[1], J. Oehlschläger[1], M. Petcu[2], H. Rebel[1], M. Risse[1], M. Roth[1], G. Schatz[1], H. Schieler[1], J. Scholz[1], T. Thouw[1], H. Ulrich[3], B. Vulpescu[2], J. H. Weber[3], J. Wentz[1], J. Wochele[1], and S. Zagromski[1]

[1]Institut für Kernphysik, Forschungszentrum Karlsruhe, 76021 Karlsruhe, Germany
[2]National Institute of Physics and Nuclear Engineering, 7690 Bucharest, Romania
[3]Institut für Experimentelle Kernphysik, University of Karlsruhe, 76021 Karlsruhe, Germany
[4]Cosmic Ray Division, Yerevan Physics Institute, Yerevan 36, Armenia
[5]Department of Experimental Physics, University of Lodz, 90236 Lodz, Poland
[6]Soltan Institute for Nuclear Studies, 90950 Lodz, Poland
*now at: Department of Physics, University of Lecce, 73100 Lecce, Italy
+now at: Warsaw University of Technology, 09-400 Plock, Poland
¶now at: University of Leeds, Leeds LS2 9JT, U.K.

Abstract.

Accurate measurements of the muon component in EAS are particularily important for determination of the primary CR spectrum and composition. Multiparameter analysis possibilities in KASCADE have been recently enhanced by starting the operation of a large area streamer tube muon tracking detector. With its acceptance of about 500 $m^2 \cdot sr$ it identifies EAS muons with energy exceeding 0.8 GeV. The reconstruction of the mean muon production height, a parameter related to the nature of primary UHE particle, is a main goal of this detector. In addition, this detector is capable of independent determination of the shower direction, therefore, it can be used in combination with the scintillator array to improve the overall angular resolution of KASCADE. For the above-mentioned applications a good and well understood accuracy in determination of the angles of the muon tracks is of primary importance. The construction of the whole detector, as well as streamer tubes and electronics specially developed for it, allowed to reach high efficiency of muon track detection, on the level of 0.72. Various approaches to the concept of the angular resolution in track determination are discussed. The influence of the design and operation factors on the resolution, which can approach the level of 0.2°, is shown. Example of the detector performance in muon density measurements is given.

Correspondence to: J. Zabierowski (janzab@zpk.u.lodz.pl)

1 Introduction

Investigation of the UHE cosmic ray particles (with energy above 10^{15} eV), due to their very low flux (being much below $10^{-5} s^{-1} m^{-2}$), is possible only via indirect observations of extensive air showers (EAS), created as a result of interactions of those particles with nuclei of the atmosphere. Ground based experiments of large detection area have to measure precisely as many components of the cascade developing in the atmosphere as possible. Particularly important is the measurement of the muon component of the EAS, because some of the muons reaching the observation level carry information about the very first interactions at the top of the atmosphere. For large distances from the shower core individual muon tracks point to the muon production height (MPH) and help to identify the nature of the primary UHE particle. Monte Carlo calculations show, that by means of the mean MPH parameter, for a good statistics of showers, primary particles like iron nuclei (Fe) can be separated from light ones, like hydrogen (p).

As an extension to the KASCADE EAS experiment (Klages et al., 1997) a large area streamer tube (ST) Muon Tracking Detector (MTD) was put into operation. KASCADE at the *Forschungszentrum Karlsruhe* has been taking data since 1996, measuring various shower parameters with the 200 × 200 m^2 scintillator array and a central detector, consisting of a hadron calorimeter and muon detectors. The new MTD of about 500 $m^2 \cdot sr$ is intended to track the muons created in the EAS. In addition, it will enhance the capability of KASCADE in measurement of the muon multiplicities and their

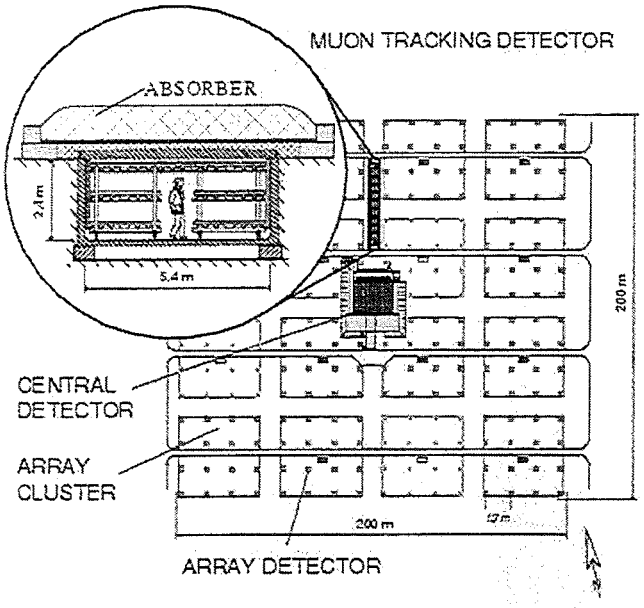

Fig. 1. Location of the MTD within the KASCADE experiment.

lateral distributions.

2 Detector and its components

The ST MTD is located within the KASCADE EAS experiment (fig.1) in the tunnel buried in the ground under a shielding of 18 r.l., made out of concrete, iron and soil. A multilayer of 6 iron plates of 3 cm thickness, separated each by 5 cm sand, provides a good absorber for a large fraction of low energy electromagnetic particles, thus enhancing the tracking capability and identification of the muons with an energy above 0.8 GeV. A cross section of the detector tunnel of $2.4 \times 5.4 \times 44$ m^3 and its location within the KASCADE experiment is shown in fig.1.

Table 1. Some ST design parameters.

PVC profile resistivity	100 kΩ/square
Bakelite cover resistivity	10^{11} Ω×cm
Anode wire diameter	100 μm
Anode wire tension	3 N at 20°C
Wire sagging between spacers	42 μm
ST chamber dimensions	13 × 166.6× 4000 mm^3

The MTD consists of 16 muon telescopes, called detector *towers*, arranged in two rows. A *tower* is built up of four detector *modules*: three positioned on horizontal planes and one arranged vertically. A detector *module*, of the size 2×4 m^2, consists of 12 ST chambers.

2.1 Streamer Tube chambers

As a result of intensive studies (Doll et al., 1992, 1994, 1995), of various commercial (Pol.Hi.Tech.; Hungerford et al., 1990)

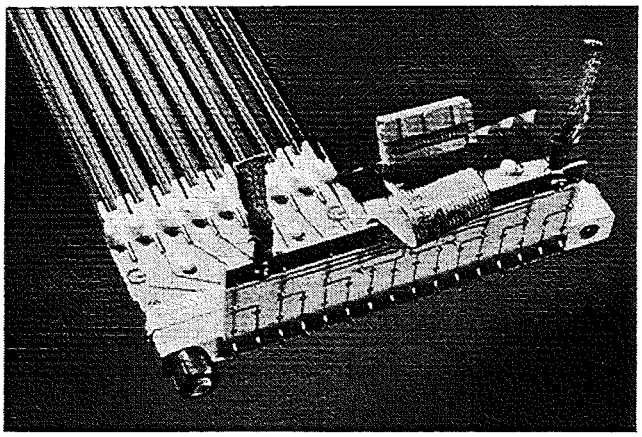

Fig. 2. Detailed view of opened ST chamber with adapter board. Anode wires connected in pairs and bakelite cover on one of the profiles are seen.

and custom made STs (Alekseev et al., 1986), (DeWulf et al., 1986), as well as several technological improvements, ST chambers of the Iarocci type (Iarocci, 1983) were built for KASCADE by a company (WATECH) from Vienna.

The chamber consist of two cathode comb profiles, being extruded out of conductive PVC for 8 parallel ST cells of 9×9 mm^2 cross section and 4000 mm length. High quality copper-beryllium wire, tempered and smoothed with 0.3 μm of silver has been used for anodes, being supported every 500 mm along the cells. A bakelite sheet closes the field around the anode wire very effectively (Pentchev et al., 1997) when applying negative HV to the cathode profiles. Profiles with wires and bakelite covers were slid into normal PVC envelopes and sealed off with endcaps, exhibiting connectors for anode wires, high voltage and gas. The details of the ST chamber construction can be viewed in fig. 2 and its basic design parameters are listed in Table 1.

2.2 Detector *modules* and electronics

Above the ST chambers in a detector *module* there is a layer of a rigid polyester foil of 75 μm thickness with evaporated aluminum strips of 20 mm pitch (18 mm width) and 2 m

Table 2. Operational parameters of MTD.

Detecting surface for vertical muons	128 m^2
Total detecting surface	512 m^2
Number of ST chambers	768
Number of readout channels	24 576
- wires	6 144
- strips	18 432
Number of readout boards	768
Gas mixture	70% isobutan + 30% argon
Gas flow rate	0.5 dm^3/h×16 towers
Full MTD gas volume	240×16 = 3840 dm^3

length, perpendicular to the wires. Another layer of such foil

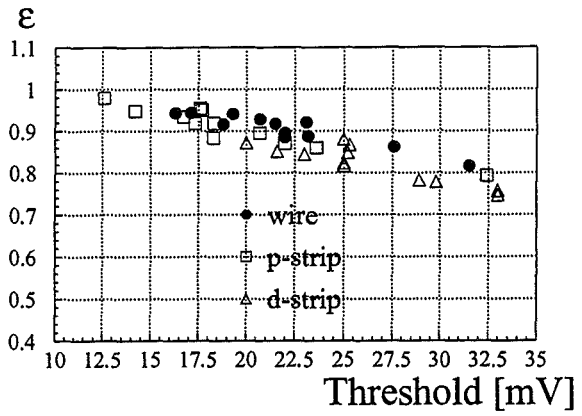

Fig. 3. Efficiency dependence on discriminator threshold for upper modules in all towers

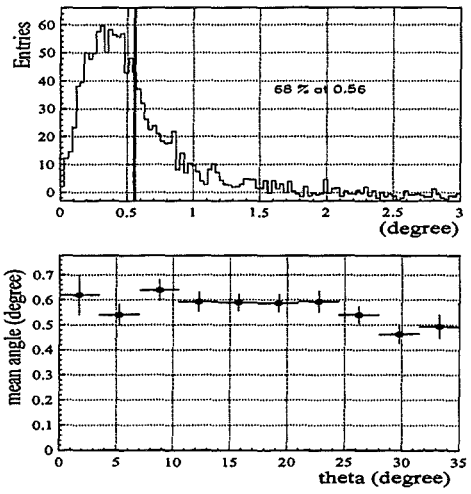

Fig. 4. Full intrinsic angular resolution of the MTD obtained with simulation (top) and its dependence on the zenith angle (bottom).

is mounted below the tubes but with strips oriented diagonally (60°). These *diagonal strips* are made out of the same strip material but 2 strips are combined at the readout side. Thus for the readout electronics every module is a source of 96 wire pairs signals, 192 perpendicular and 96 diagonal strip signals.

Our data readout system is of a chain type, commonly being used with the large scale ST detectors (e.g. Adams et al., 1999). Specially designed front-end boards (Zabierowski and Doll, 2001) are connected in series of 24 board long chains, which shift the data into CAMAC CAEN C267 STAS controllers. The MTD can be self triggered or receive triggers from other parts of KASCADE. Operational parameters of the MTD are listed in Table. 2.

3 The MTD efficiency

We define a *hit* in a *module* when a wire and corresponding perpendicular strip have data. The tracks are of two kinds. The *hits* found in three modules form *3-hit tracks* and, when data is found in two modules only, one has a *2-hit track.*

For the efficiency determination all tracks are used. Having a starting coordinate and the direction of each particle one checks for the wire and strip data in all modules along each track. The ratio of found to expected number of signals gives a measure of an efficiency in each wire or strip plane, which takes into account dead zones due to ST walls. This efficiency is also discriminator threshold dependent, as shown in fig. 3 for the upper module in all towers. As shown in the picture, for $\approx$ 17 mV threshold one has 95 % efficiency for wire and strips, what means $\approx$ 90% hit efficiency for a module and $\approx$ 72 % *3-hit track* efficiency for a MTD tower.

4 Angular resolution

The tracking detector has a *geometrical* angular resolution defined by its design and dimensions. With the 1640 mm separation of the top and bottom modules in towers, 20 mm strip widths and two 9 mm wide ST wire cells connected together the mean value of this parameter is $\approx$ 0.35° for vertical muons and improves with increasing zenith angle. However, this value can never be achieved, because of finite accuracy in the geometry determination and interactions of the particles in different materials that built up a detector, including tunnel shielding. We call *full intrinsic resolution* a parameter taking into account the above mentioned effects and showing how accurate a known muon direction above the tunnel can be reproduced with the MTD. In order to obtain this parameter a simulation study has been done, using the CRES (Cosmic Ray Event Simulation) Monte Carlo program, which is a GEANT3 based code developed for the KASCADE experiment. The sample of muons used as input particles reproduces the zenith and azimuth distributions of the showers reconstructed by the scintillator array with a realistic energy spectrum (Caso et al., 1998). In order to cover the uncertainty in the geometry of the detector two different *Geometry Data Bases* (DB) were used, one for the simulation of the reference track and another for the reconstruction of the track. The latter one was obtained starting from the former and smearing the positions of each module randomly with a sigma of 3 mm (assumed precision of our mechanical and optical measurements). The resulting distribution of true vs. reconstructed muon directions is plotted in top panel of fig. 4. The value, below which there is 68 % of all events, we call *full intrinsic angular resolution* of the MTD. In this case it is equal to 0.56°.

To lower this value one has to obtain better knowledge on detector geometry or/and improve *geometrical* resolution. The former is possible with various methods using cosmic muons, which allow to introduce corrections into DB. The latter requires some technical modifications such as single ST cell readout and utilizing drift time (Obenland et al., 2001).

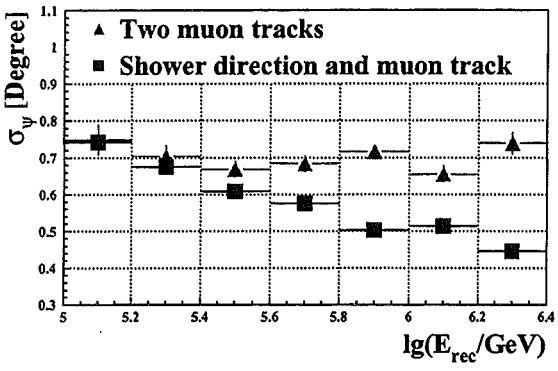

Fig. 5. Total angular resolution of the MTD as a function of reconstructed primary energy.

These techniques make it possible to obtain a *geometrical* resolution on the level of 0.2°.

In reality the true direction is not known and one is interested how accurate is the detector in pointing at the sky. This parameter, called *total angular resolution*, can be estimated by measuring the angle between two parallel muon tracks. High energy muons originating high in the atmosphere have to be used for this purpose. Tracks at large distance to the shower core are good candidates. They are not perfectly parallel, due to possible differences in production heights and due to multiple scattering in the atmosphere. But, since in real measurements we cannot avoid these two effects the value of resolution found this way includes these phenomena.

For the main application of the MTD, namely determination of the muon production height (Büttner et al., 2001), a resolution in determination of the angle between muon in MTD and the shower direction, determined from the array data, is an important parameter.

In fig. 5 the resulting *total angular resolution* as a function of reconstructed primary energy for the two cases mentionned above is given. We find that above 10^{14} eV one can measure the direction of a muon versus another muon with a precision of $\approx 0.7°$. This number contains *full intrinsic resolution* of the MTD and the mean value of muon scattering angle in the atmosphere, which, based on the CORSIKA (Heck et al., 1998) simulations, one can estimate to be $\approx 0.6°$. Measurements made with respect to the shower direction are more precise due to significantly better shower direction accuracy achieved by the scintillation array of KASCADE ($\leq 0.2°$ above 10^{15} eV).

As an example of the MTD capabilities muon lateral distributions are presented in fig. 6. It has to be noted, that the good agreement with the KASCADE array results confirms the proper understanding of the MTD efficiency.

Acknowledgements. The KASCADE experiment is supported by Forschungszentrum Karlsruhe and by collaborative WTZ projects in the frame of the scientific -technical cooperation between Germany and Romania (RUM 97/014, Poland (POL 99/005) and Armenia (ARM 98/002). The Polish group (Soltan Intitute and University of Lodz) acknowledges the support by the Polish State Committee for Scientific Research (grant No. 5 P03B 133 20).

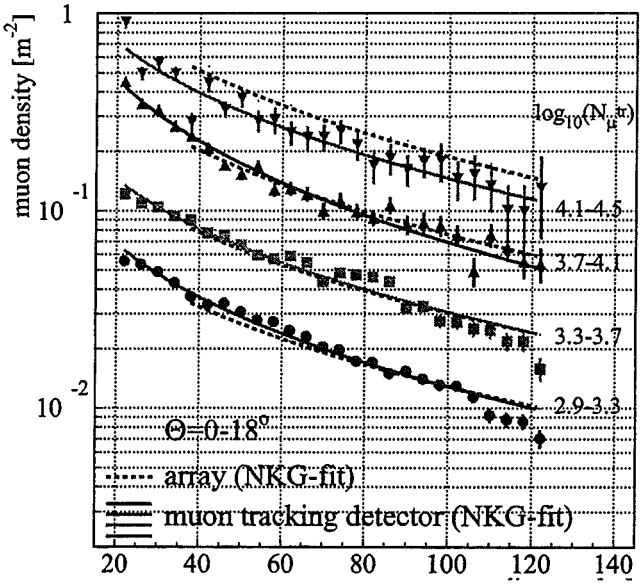

Fig. 6. Muon lateral density distributions for four different shower sizes $\lg(N_\mu^{tr})$ (Glasstetter et al., 1999) and zenith angles θ between 0° and 18°. Symbols represent data points from the MTD, and the solid lines fits to the data. The dashed lines are the fits to the data from the scintillation array (corrected for the threshold difference) for the same shower sample.

References

Adams D. et al., (SMC Collaboration), Nucl. Instr. and Meth. A435 (1999) 354.
Alekseev G.D. et al, Nucl.Instr. and Meth. A243 (1986) 385.
Büttner C. et al., (KASCADE Collaboration), Proceedings of the 27th ICRC, Hamburg (Germany) 2001, HE 1.2.30.
Caso C. et al.,(particle Data Group) The Eur.Phys.J. C3 (1998).
DeWulf J.P. et al., (CHARM II Collaboration), Nucl.Instr. and Meth. A252 (1986) 443.
Doll P. et al., Nucl.Instr. and Meth. A323 (1992) 327;
Nucl.Instr. and Meth. A342 (1994) 495;
Nucl.Instr. and Meth. A367 (1995) 120.
Glasstetter R. et al, (KASCADE Collaboration),
Nucl.Phys.B (Proc.Suppl) **75A** (1999) 238.
Heck D. et al., Report FZKA 6019, Forschungszentrum Karlsruhe, 1998.
Hungerford D. et al., Nucl. Instr. and Meth. A286 (1990) 155.
Iarocci E., Nucl. Instr. and Meth.A217 (1983) 30.
Klages H.O. et al., (KASCADE Collaboration),
Nucl.Phys.B (Proc.Suppl) **52B** (1997) 92.
Obenland R. et al., (KASCADE Collaboration), Proceedings of the 27th ICRC, Hamburg (Germany) 2001, HE 1.8.33.
Pentchev L. et al., Nucl.Instr. and Meth. A399 (1997) 275.
Pol.Hi.Tech., 67061 Carsoli (AQ), Italy.
WATECH, W. Bartl, Aslangasse 9, 1190 Wien, Austria.
Zabierowski J. and Doll P., submitted to Nucl. Instr. and Meth. A, (2001).

Proceedings of ICRC 2001: 814 © Copernicus Gesellschaft 2001

ICRC 2001

Improvement of the resolution of the muon tracking detector in the KASCADE experiment

R. Obenland[1], T. Antoni[1], W. D. Apel[1], F. Badea[2], K. Bekk[1], A. Bercuci[1], H. Blümer[1,3], E. Bollmann[1], H. Bozdog[2], I. M. Brancus[2], C. Büttner[1], A. Chilingarian[4], K. Daumiller[3], P. Doll[1], J. Engler[1], F. Feßler[1], H. J. Gils[1], R. Glasstetter[3], R. Haeusler[1], A. Haungs[1], D. Heck[1], J.R. Hörandel[3], T. Holst[1], A. Iwan[5,3], K-H. Kampert[1,3], J. Kempa[5,+], H.O. Klages[1], J. Knapp[3,¶], G. Maier[1], D. Martello[1,*], H. J. Mathes[1], H. J. Mayer[1], J. Milke[1], M. Müller[1], J. Oehlschläger[1], M. Petcu[2], H. Rebel[1], M. Risse[1], M. Roth[1], G. Schatz[1], H. Schieler[1], J. Scholz[1], T. Thouw[1], H. Ulrich[3], B. Vulpescu[2], J. H. Weber[3], J. Wentz[1], J. Wochele[1], J. Zabierowski[6], and S. Zagromski[1]

[1]Institut für Kernphysik, Forschungszentrum Karlsruhe, 76021 Karlsruhe, Germany
[2]National Institute of Physics and Nuclear Engineering, 7690 Bucharest, Romania
[3]Institut für Experimentelle Kernphysik, University of Karlsruhe, 76021 Karlsruhe, Germany
[4]Cosmic Ray Division, Yerevan Physics Institute, Yerevan 36, Armenia
[5]Department of Experimental Physics, University of Lodz, 90236 Lodz, Poland
[6]Soltan Institute for Nuclear Studies, 90950 Lodz, Poland
[+]now at: Warsaw University of Technology, 09-400 Plock, Poland
[¶]now at: University of Leeds, Leeds LS2 9JT, U.K.
[*]Department of Physics, University of Lecce, 73100 Lecce, Italy

Abstract. A Muon Tracking Detector has been built up in an underground tunnel north of the centre of the KASCADE experiment. It measures muons and their directions in EAS by using Limited Streamer Tubes. For that purpose tracks with hits in 2 and 3 modules are considered, each hit consisting of a signal from a wire pair and from influence strips perpendicular to them. Diagonal strips are used to reduce ambiguities. In order to get a good determination of the muon production height by means of triangulation, a good separation of multiple muon tracks close to the shower core and a good angular resolution is needed. Methods of improving the angular resolution of the detector system are presented. Investigations have been conducted to separate the wire pair signals and to include drift time measurements. Simulations of the electric field in a Streamer Tube cell ($9 \times 9\,mm^2$) and also the distance - drift time correlation are presented, as well as the resulting detector resolution. With respect to the KASCADE-Grande upgrade the improved resolution becomes very valuable, because of increasing muon densities at higher energies of the primary shower particles.

1 Introduction

The KASCADE experiment (Klages et al., 1997) measures the hadronic, electromagnetic and muonic component of extensive air showers (EAS) caused by cosmic ray particles in the energy region of the knee. Especially the muon component is very important as some high energetic muons originate from the very first interactions of the shower. Because of the fact, that muons are not very much scattered in the atmosphere, it is also possible to investigate the longitudinal development of an EAS. For this purpose a large muon tracking detector (MTD) was established (Doll et al., 1995; Atanasov et al., 2000) which, in combination with the shower core position determined by the KASCADE array, allows to reconstruct the muon production height by means of triangulation (Büttner et al., 2001).

The MTD (Fig. 1) has 16 towers in two rows, each consisting out of 3 horizontal and one vertical module, and is extending in geomagnetic north-south direction. The wire signals from the 12 streamer tubes (ST) give the x-position of a muon track along the short side of the towers, while the y-position is given by influence strips, perpendicular to the wires. To resolve ambiguities in case of two or more coincident tracks additional diagonal influence strips are used. The wire cells in the streamer tubes, formed by an extruded comb profile made out of conductive PVC (Bartl, 1991), have a cross section of 9×9 mm^2, and are 4000 mm long. Extensive studies have been conducted to find an appropriate cover for the open comb profile (Pentchev et al., 1997). To reduce the numbers of readout channels two wire cells are combined together on the adapter board (see Fig. 2 in Zabierowski et al. (2001)). For stable operation of the detectors the cluster sizes for the wire pairs and perpendicular influence strips amount to 1 and 2.4 respectively. For further information on the MTD read Zabierowski et al. (2001). The angular resolution of the MTD, taking into account the multi-

Correspondence to: R. Obenland (obenland@ik1.fzk.de)

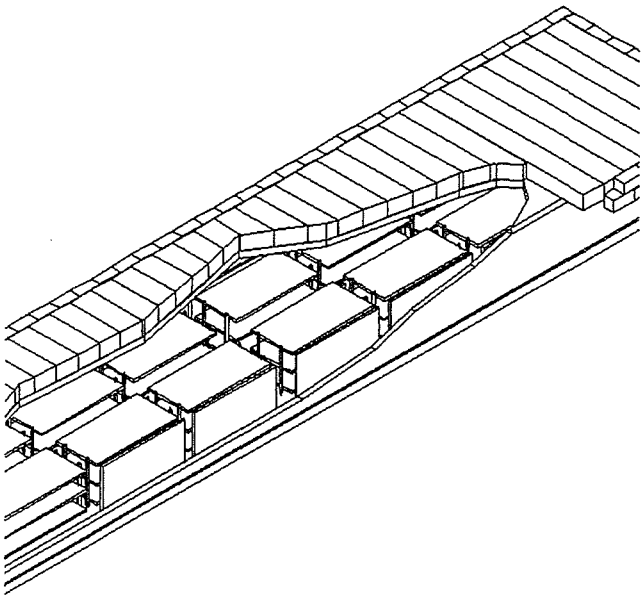

Fig. 1. Schematic view of the MTD of KASCADE. 48 m in y-direction, 5.4 m in x-direction and 2.5 m in z-direction.

ple scattering of the particles in the air, in the detector and in the absorber, the detector geometry and its precision is also discussed there.

2 Methods to improve the resolution

The angular resolution of a tracking detector, determined purely by its geometry, we call the *geometrical resolution*. This resolution of the MTD can be improved in two steps. First, by the separation of the wire pair signals and, as a next step, by using the drift time of the electrons from the point of ionization of the gas molecules to the anode wire in the centre of the streamer tube cell. The investigations presented below have been performed by using tracks with hits in every of the three horizontal modul planes. The experiment was carried out by starting readout of a test tower with a plastic scintillator telescope.

2.1 Wire pair separation

To distinguish which of the two combined wire cells in a ST is crossed by a muon the circuitry on the adapter boards was modified. The signal of one wire was attenuated with additional resistors. So the integrated charge signal from one wire

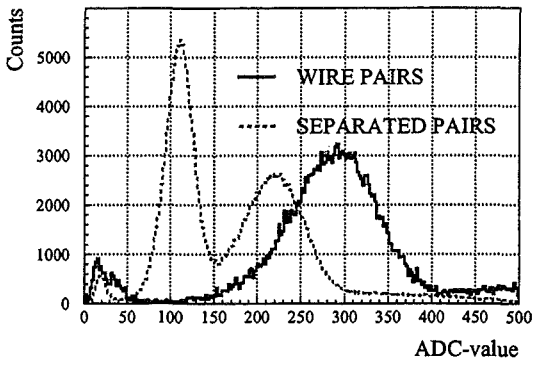

Fig. 2. ADC-spectra for combined (solid curve) and modified (dashed curve) wire pair coupling on the adapter boards.

becomes smaller than from the other one. Fig. 2 presents the resulting ADC-spectra which allow to distinguish the individual wire cell. In addition, a distribution of the ADC-values measured with the adapter boards in their original layout is shown. It can be seen that not only the signal of the wire cell with the modified readout is attenuated, but also the signal from the other wire cell. Although the forms of the distributions in height and width of the two wire cells are not the same anymore, their number of entries is still the same, so no loss of events occurs, since all signals remain above the threshold. Very inclined tracks can pass through two neighbouring cells and can exhibit additive adc-values. To treat the remaining overlap of the neighbouring wire cells the probability for a specific decision, for a specific wire cell, can be checked with the decisions which have been done in the other two modules for the considered track, because the single cells in the top, middle and bottom module should lie in a line as good as possible. Slightly different methods of signal separation will also be investigated in future.

2.2 Drift time

After the classification in the individual wire cells the drift time measurement can be used. Because of the square cross section of 9×9 mm^2 of the wire cells the drift velocity of the electrons in the gas depends very much on the position in the cell and the strength of the electric field there, as can be seen in Fig. 3, simulated with Garfield (7.03) program, for the used gas mixture with 20 % and 30 % of Isobutane respectively (-0.09 cm/μsec vol.%). The shoulder in the drift velocity at around 10^4 V/cm is due to the collision cross sections of the electrons for the various gas molecules. The drift velocity decreases with increasing pressure (-0.01 cm/μsec mb), because the mean free path between subsequent collisions of an electron with the gas molecules becomes shorter, while for temperature the drift velocity increases (+0.02 cm/μsec K). With high voltage of -4.7 kV at the cathode profile the strength of the electric field depends on the distance between wire and

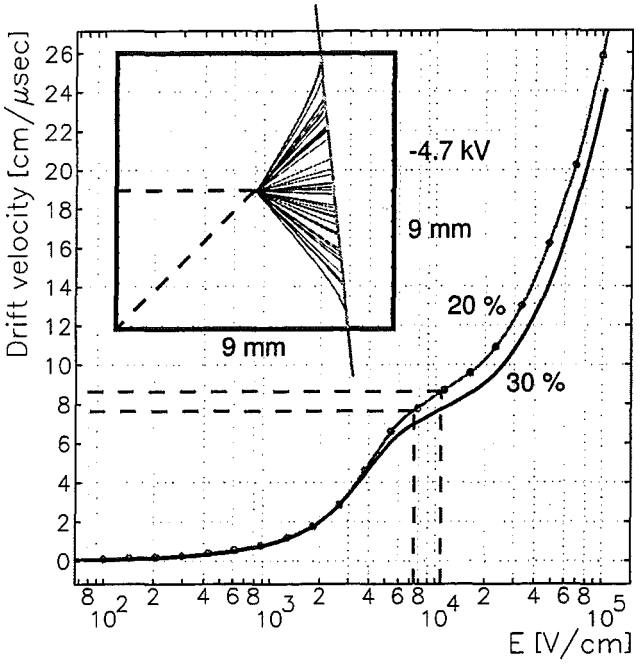

Fig. 3. Drift paths for about 60 primary electrons are shown and the dependence of the drift velocity of the electrons on the electric field for gas mixtures of 78:20:2 and 68:30:2 CO_2:Isobutane:Ar (vol.%) at 1 atm and 300 K. The square cross section of the wire cells leads to a smaller drift velocity out of the corners of the profile, due to a weaker field in these directions.

wall of the wire cell, which differs from 4.5 mm to $4.5\sqrt{2}$ mm into the corner of the cell. Therefore, a range of the electric field from 7.4 to 10.4 kV/cm at the edge of the profile is given. The electrons follow the field lines which leads to longer drift times out of the corners. The stability of the drift velocity also depends on the stability of the used gas mixture. If the fraction of isobutane increases the drift velocity becomes slower.

The measured drift time distribution ranges from 0 to 80 ns with an accumulation of shorter drift times. The population of smaller drift times in the experiment is partly due to earlier stop signals from neighbouring cells (in the case of combined cells) or can be explained with the simulated x(t)-correlation (Garfield, 7.03) in Fig. 4. There, the dependence of the drift time (for the fastest electron out of the ionization along the muon track) on the distance between the track, where it crosses the wire plane, and the wire is shown. This parabolic shape of the curve leads to shorter drift times. For inclined tracks the minimum distance between track and wire decreases, so the drift time becomes shorter than for vertical tracks - for tracks crossing the wire plane at the same distance from the wire. Corrections due to the distance in x, between the track and the wire, and the angle of a track still have to be included in the future analysis. Detailed investigations of the zenith and azimuth angle dependence of the shortest possible electron drift times are going on.

Another effect is the ambiguity on which side of the wire a

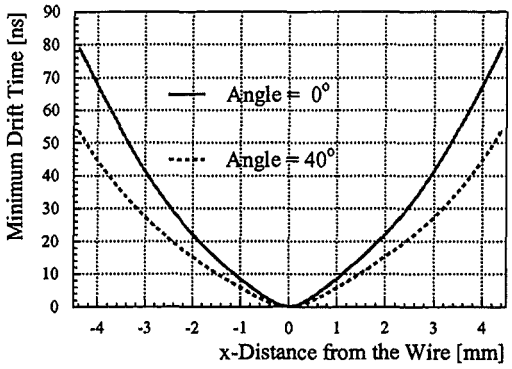

Fig. 4. x(t)-correlation depends from the distance between the track and the wire in the wire-plane and on the zenith angle of the track.

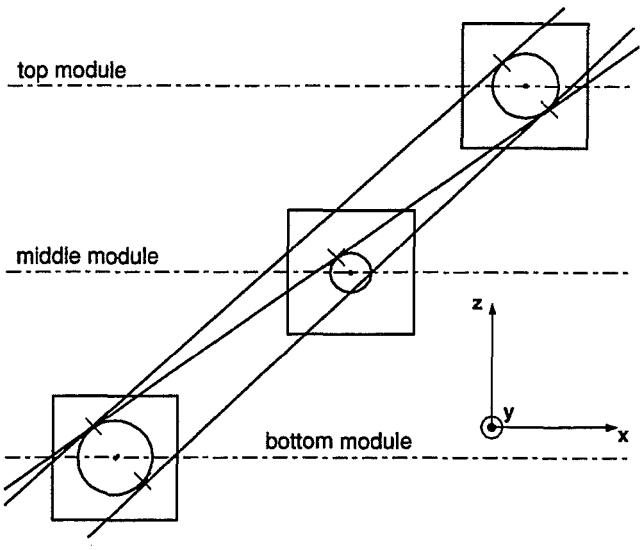

Fig. 5. The ambiguity on which side of the wire the muon crosses the cells is resolved with a least squares fit of all possible track solutions for the three modules.

track crosses the cells in each of the three module planes. The drift time measurements provide drift time circles around each wire with a precision of a few hundred micrometer, depending on the accuracy of the time measurement. An improved *constant fraction discriminator* should be employed in the future. Various possible muon tracks can be fitted to these circles (Fig. 5) in the x-z plane. The positions where the track tangents to the circles and the angle of the track can be derived from the x- and z-positions and the radii of the drift time circles of two modules, as described by Oh et al. (1991). Then, the obtained track solutions can be projected onto the third module and compared with the measured drift radius there. To resolve the ambiguity on which side of the wire a track has crossed the cell, the solution with the minimum mean square deviation out of a least square fit for all possible

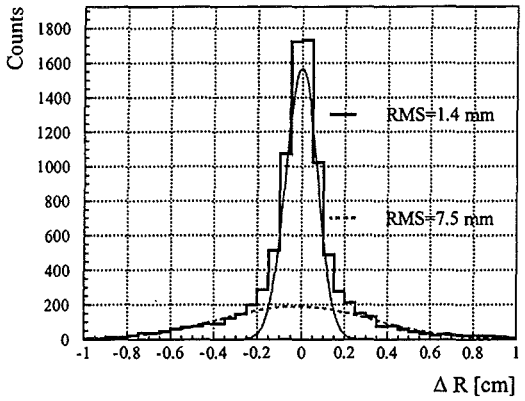

Fig. 6. The distance distribution between measured and projected positions in the middle module can be fitted by two Gaussians.

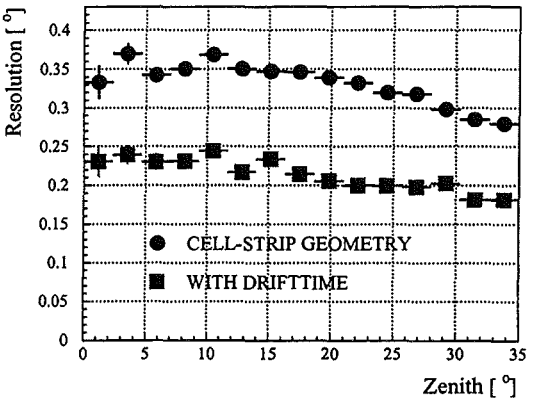

Fig. 7. Simulated geometrical resolution for using wire pairs and including drift time measurement for all azimuth angles.

tracks is employed. However not in all cases the fit results in a unique solution. For the future operation of the MTD one can consider to install additional ST modules shifted by half a cell width to the side with respect to the already installed modules to reduce this left-right ambiguity around the wires.

Fig. 6 presents a difference distribution which gives the deviation of the tracks, derived from the x- and z-positions and the drift times of the top and bottom module, from the measured positions in the middle module. The difference distribution is fitted by two Gaussians. The less correlated events can be attributed to limited ADC separation (see Fig. 2). The remaining RMS of 1.4 mm will be further improved by taking into account the fully parametrized - zenith and azimuth dependent - x(t)-correlation, either derived from simulation (Garfield) or from additional measurements, being considered for future upgrades.

3 Improved resolution

To investigate the influence of the improved track resolution on the geometric angular resolution (Zabierowski et al., 2001) a MC calculation was performed. This simulation starts with a muon track distribution in zenith and azimuth angles as observed in real showers. These tracks are propagated through the 3 detector modules where wire and strip hits are registered. Based on wire-strip cluster sizes of 1×1 that define a hit area of 20×20 mm^2 the difference angle between the incoming track and the reconstructed track is accumulated in a histogram. The solid points in Fig 7 give the mean value of this difference distribution as a function of the zenith angle. The slight improvement of the mean value for large zenith angles can be explained with the decreasing effective distances between two wires or strips and larger effective distances between the measured x and y module coordinates, for inclined muon tracks.

Taking into account the result, that from the measurement of the electron drift times in the wire cells an improved location of the muon track along the x-coordinate can be obtained, a similar MC simulation, based on a 1.4×20 mm^2 grid structure, leads to the mean values given by the squares. An improvement of about 40 % in the geometric angular resolution is observed.

For the future operation of the MTD in the environment of KASCADE-Grande (Bertaina et al., 2001) a MTD with improved resolution would be very helpful for tasks, like investigation of muon production heights close to the shower core or improved determination of muon densities and muon multiplicities.

Acknowledgements. The KASCADE experiment is supported by Forschungszentrum Karlsruhe and by collaborative WTZ projects in the frame of the scientific-technical cooperation between Germany and Romania (RUM 97/014, Poland (POL 99/005) and Armenia (ARM 98/002). The Polish group (Soltan Intitute and University of Lodz) acknowledges the support by the Polish State Committee for Scientific Research (grant No. 5 P03B 133 20).

References

Atanasov, I. et al., KASCADE, FZKA 6474, Forschungszentrum Karlsruhe.

Bartl, W., Nucl. Instr. and Meth. A305 (1991) 82.

Bertaina, M. et al., (KASCADE Collaboration), Proceedings of 27th ICRC, Hamburg (Germany) 2001, HE 1.8.26.

Büttner, C. et al., (KASCADE Collaboration), Proceedings of 27th ICRC, Hamburg (Germany) 2001, HE 1.2.30.

Doll, P. et al., Nucl.Instr. and Meth. A367 (1995) 120.

Garfield Version 7.03, CERN Software from Rob Veenhof, Reference W5050, http://consult.cern.ch/writeup/garfield/.

Klages, H.O. et al., (KASCADE Collaboration), Nucl.Phys.B (Proc.Suppl) **52B** (1997) 92.

Oh, S.H. et al., Nucl. Instr. and Meth. A303 (1991) 277.

Pentchev, L. et al., Nucl.Instr. and Meth. A399 (1997) 275.

Zabierowski, J. et al., (KASCADE Collaboration), Proceedings of 27th ICRC, Hamburg (Germany), HE 1.8.32.

Proceedings of ICRC 2001: 792 © Copernicus Gesellschaft 2001

ICRC 2001

KASCADE-Grande: a conclusive experiment on the knee

M. Bertaina[6], T. Antoni[1], W. D. Apel[1], F. Badea[2], K. Bekk[1], A. Bercuci[1], H. Blümer[1,3], H. Bozdog[2], I.M. Brancus[2], C. Büttner[1], A. Chiavassa[6], P. Doll[1], J. Engler[1], F. Feßler[1], P. L. Ghia[7], H. J. Gils[1], R. Haeusler[1], W. Hafemann[1], A. Haungs[1], D. Heck[1], J. R. Hörandel[3], A. Iwan[3,4], K-H. Kampert[3,1], J. Kempa[4,+], H.O. Klages[1], G. Maier[1], D. Martello[1,*], H. J. Mathes[1], H. J. Mayer[1], J. Milke[1], C. Morello[7], M. Müller[1], G. Navarra[6], R. Obenland[1], J. Oehlschläger[1], M. Petcu[2], H. Rebel[1], M. Roth[1], H. Schieler[1], J. Scholz[1], T. Thouw[1], G. C. Trinchero[7], H. Ulrich[3], B. Vulpescu[2], J. H. Weber[3], J. Wentz[1], J. Wochele[1], J. Zabierowski[5], and S. Zagromski[1]

[1]Institut für Kernphysik, Forschungszentrum Karlsruhe, 76021 Karlsruhe, Germany
[2]National Institute of Physics and Nuclear Engineering, 7690 Bucharest, Romania
[3]Institut für Experimentelle Kernphysik, University of Karlsruhe, 76021 Karlsruhe, Germany
[4]Department of Experimental Physics, University of Lodz, 90236 Lodz, Poland
[5]Soltan Institute for Nuclear Studies, 90950 Lodz, Poland
[6]Dipartimento di Fisica Generale dell'Università, 10125 Torino, Italy
[7]Istituto di Cosmo-Geofisica del CNR, 10133 Torino, Italy
[+]now at: Warsaw University of Technology, 09-400 Plock, Poland
[*]now at: Dipartimento di Fisica dell'Università, 73100 Lecce, Italy

Abstract. We present the status and capabilities of the Extensive Air Shower experiment (KASCADE-Grande) which is being realized at Forschungszentrum Karlsruhe through a large collecting area (0.5 km^2) electromagnetic array (Grande) that will operate jointly with the existing KASCADE detectors. KASCADE-Grande will cover the primary energy range 10^{16} eV $< E_0 <$ 10^{18} eV, overlapping with KASCADE around 10^{16} eV, thus providing a continuous information from $3 \cdot 10^{14}$ eV to 10^{18} eV. The main task of the experiment is the observation of the "iron knee" in the cosmic ray spectrum that is expected at $E_k^{Fe} \approx 10^{17}$ eV. This is expected following the increasing mass of the primaries observed between 10^{15} and 10^{16} eV (knee region for the light component), and the rigidity dependent breaks for the spectra of different primaries from the conventional acceleration models. Its observation will provide a definite proof of the knee structure.

1 Introduction

One of the main results so far obtained by the KASCADE (Glasstetter et al. (1999) ; Roth et al. (1999) ; Hörandel et al. (1999) and Weber et al. (1999)) and EAS-TOP (Aglietta et al. , 1999) experiments, is a picture of an increasingly heavier composition above the knee largely caused by a break in the spectrum of the light component. A change towards a heavier composition above the knee is expected in conventional acceleration models, where the knee is supposed to be rigidity dependent. A convincing verification of this type of model would be the observation of the knee in the heavy component in the primary energy region around $E_0 = Z_{Fe} \times E_k \approx 10^{17}$ eV. Such an uncovering requires the extension of the high quality data obtained in the energy range 10^{15} - 10^{16} eV by KASCADE and EAS-TOP, without loosing accuracy, significantly above E_0. For such purpose, a new Extensive Air Shower array (KASCADE-Grande) is being realized at the Forschungszentrum Karlsruhe (8° E, 49° N, 110 m a.s.l.) by means of 37 stations of 10 m^2 each of scintillator counters at a mutual distance of about 130 m and covering globally an area of about 0.5 km^2, next to the KASCADE site in order to operate jointly with the existing KASCADE detectors. In this configuration KASCADE-Grande will cover the primary energy range 10^{16}eV $<$ E$_0$ $<$ 10^{18}eV. The superposition with KASCADE will guarantee the cross calibration of the detectors, and provide a full coverage from $3 \cdot 10^{14}$ to 10^{18} eV. The detector will start operation in January 2002, and will reach its full statistics in 3-4 years of data taking. The present status of the array, its resolutions and capabilities in the reconstruction of average primary composition, and verification of the hadronic interaction models used for the analysis, in the energy range of operation, are discussed.

Correspondence to: bertaina@to.infn.it

2 The experiment

The basic layout of KASCADE-Grande is reported in fig. 1. It consists of three different arrays: KASCADE, Grande, and Piccolo.

The KASCADE experiment (Klages et al. , 1997) is made by three major components: an array of electron and muon detectors, a central detector mainly for hadron measurements but with substantial muon detection areas, and a tunnel with streamer tube muon telescopes. The e/γ and μ detectors cover an area of about 200 $\times$ 200 m^2 and consist of 252 detector stations located on a square grid of 13 m separation providing in total about 490 m^2 of e/γ and 622 m^2 of μ coverage. The detection thresholds for vertical incidence are $E_e > 5$ MeV and $E_\mu > 230$ MeV. The central detector system (320 m^2) consists of a highly-segmented hadronic

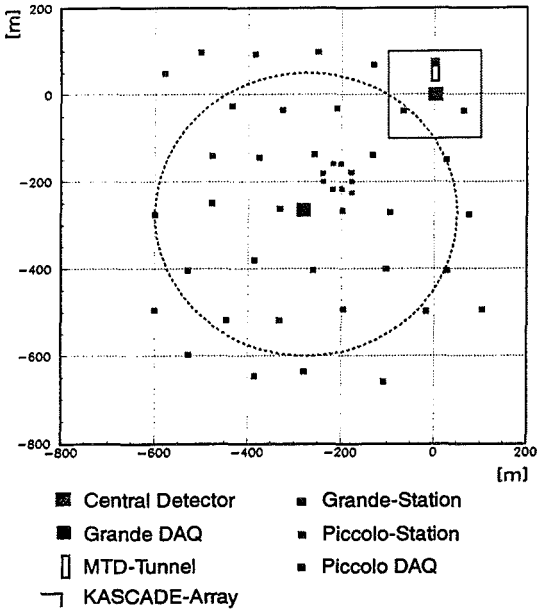

Fig. 1. Layout of KASCADE-Grande.

calorimeter read out by 55,000 channels of warm liquid ionization chambers, a layer of scintillation counters above the shielding, a trigger plane of scintillation counters in the third layer and, at the very bottom, 2 layers of positional sensitive MWPC's, and a streamer tube layer with pad read-out for muon tracking at $E_\mu \geq 2.4$ GeV. The muon tracking detector (Zabierowski et al. , 2001) is located in a 44 × 5.4 × 2.4 m^3 tunnel, close to the central detector. It houses three horizontal and two vertical layers of positional sensitive limited streamer tubes for muon tracking at $E_\mu \geq 0.8$ GeV. The accuracy in reconstructing the μ direction is $\sigma \approx 0.35^o$.

Grande consists of 37 stations of 10 m^2 each of scintillator counters - basically the electromagnetic detector of EAS-TOP (Aglietta et al. , 1989) - at a mutual distance of about 130 m and covering globally an area of about 0.5 km^2 next to the KASCADE site. Each of the 10 m^2 station is split into 16 individual scintillators (NE102A, 80 × 80 cm^2 area, 4 cm thick). Each scintillator is viewed by a photomultiplier XP3462B for timing and particle density measurements from $n_p \approx 0.3$ to ≈ 750 /10 m^{-2} (HG ch). The four central scintillators are equipped with an additional similar PM but with a maximum linearity divider, for large particle density measurements: from $n_p \approx 12$ to ≈ 30000 /10 m^{-2} (LG ch).

Piccolo consists of an array of 8 huts (10 m^2 each) equipped with 12 scintillator plates each, placed towards the center of Grande array. The main aim of Piccolo is to provide an external trigger to Grande and KASCADE for coincidence events allowing the recording of data from all the detectors of KASCADE-Grande. A triggering condition of ≈ 1 Hz will provide an efficiency $\epsilon > 0.6$ at 10^{16} eV, becoming $\epsilon \approx 1$ at $5 \cdot 10^{16}$ eV for all primaries in the fiducial area of 300 m radius around Piccolo (from CORSIKA-QGSJET).

A summary of the detector components together with their most relevant parameters is given in Table 1.

Piccolo, Grande and the cross triggering electronics are under construction, and the full array will start common data taking in January 2002.

3 Analysis.

The energy range of interest is shown in fig. 2. With three

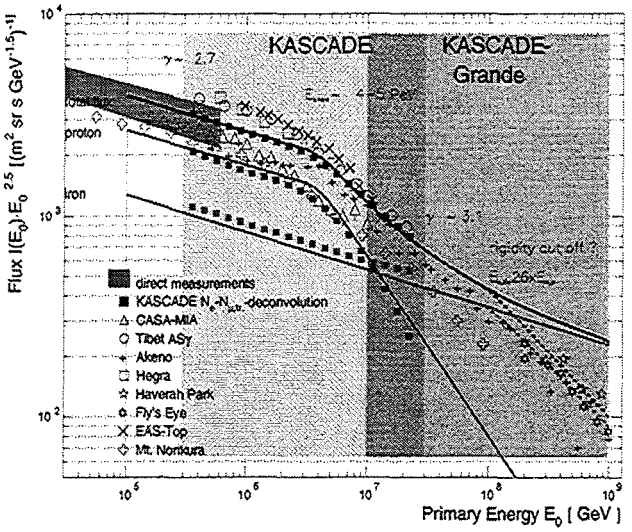

Fig. 2. Differential energy spectrum of CRs. The knee of the light component, the expectation for the heavy one, and the energy region covered by the KASCADE and KASCADE-Grande arrays are shown. The darker area represents the region of superposition of the two detectors.

years data taking, and collecting area $A \simeq 0.5$ km^2, the total exposure of KASCADE-Grande will be: $\Gamma \simeq 10^{14} m^2 srs$. This will correspond to a collected number of events (including the trigger efficiency of Piccolo): $n(> 10^{16} eV) \simeq 1.7 \cdot 10^6$, $n(> 3 \cdot 10^{16} eV) \simeq 2.8 \cdot 10^5$, $n(> 10^{17} eV) \simeq 2.5 \cdot 10^4$, $n(> 3 \cdot 10^{17} eV) \simeq 2.8 \cdot 10^3$, $n(> 10^{18} eV) \simeq 250$.
Up to about 10^{18} eV KASCADE-Grande will thus provide statistically significant physical information.

The basic observables will be: the muon density at core distance between 300 and 600 m (providing, together with the observed muon lateral distribution, the muon density at 600 m, $D_{\mu 600}$), their reconstructed production heights (h_μ) from the tracking modules (including timing information for the muons in the KASCADE central detector), and the shower size (N_e) and lateral electron density profile from the extended electromagnetic (e.m.) array.

For what concerns the reconstruction accuracies of the Grande array, the resolutions reported in table 2 have been estimated through a simulation based on CORSIKA-QGSJET model for near vertical events ($1.00 < \sec\theta < 1.05$) - left - and inclined showers ($1.15 < \sec\theta < 1.30$) - right. A good performance of the array is expected in all the simulated conditions (and that will be verified, at the lower energies, by the coincident data with the e/γ detector of KASCADE). Concerning the μ detectors, the same simulation gives a density

Detector	Channels	Separation(m)	Total area (m^2)	Threshold E_{kin}	Particle
Array e/γ	252	13	490	5 MeV	e
Array μ	192	13	622	230 MeV $\times$ sec θ	μ
Trigger	456	-	208	490 MeV $\times$ sec θ	μ
MWPCs	26080	-	129	2.4 GeV $\times$ sec θ	μ
Calorimeter	44000	-	304	50 GeV	Hadrons
Muon Tunnel	24576	-	128	800 MeV	μ
Grande	74	<130>	370	3 MeV	e,μ
Piccolo	16	<25>	80	5 MeV	e,μ

Table 1. Most relevant parameters of detector components. Detection thresholds refer to the particle energies above the absorber material of the detectors.

	$1.00 < sec\theta < 1.05$				$1.15 < sec\theta < 1.30$			
	p		Fe		p		Fe	
	10^{16} eV	10^{17} eV	10^{16} eV	10^{17} eV	10^{16} eV	10^{17} eV	10^{16} eV	10^{17} eV
$Log(Ne)$	6.15	7.26	5.85	7.08	5.73	6.82	5.42	6.65
ϵ	0.99 ± 0.02	1.00 ± 0.02	0.99 ± 0.02	1.00 ± 0.02	0.98 ± 0.02	1.00 ± 0.02	0.94 ± 0.02	1.00 ± 0.02
Δx	-0.07 (m)	0.06 (m)	-0.04 (m)	0.01 (m)	-0.04 (m)	0.02 (m)	-0.14 (m)	-0.16
$\sigma(x)$	9.08 (m)	5.32 (m)	11.2 (m)	5.39	9.08 (m)	5.32 (m)	11.2 (m)	5.39
Δy	0.14 (m)	0.04 (m)	-0.09 (m)	0.04 (m)	-0.05 (m)	-0.05 (m)	-0.19 (m)	0.02
$\sigma(y)$	6.1 (m)	4.69 (m)	7.13 (m)	4.54 (m)	8.60 (m)	5.27 (m)	10.6 (m)	5.23
Δs	-0.10	-0.03	-0.14	-0.04	-0.13	-0.04	-0.18	-0.05
$\sigma(s)$	0.09	0.07	0.10	0.08	0.10	0.07	0.11	0.07
$\Delta Ne\%$	0.6	1.3	-1.8	2.7	-13.1	-1.0	-28.4	-0.03
$\sigma(Ne\%)$	12.2	12.9	12.0	14.2	17.8	10.9	26.1	12.1

Table 2. Simulated reconstruction resolution (based on QGSJET) of the Grande array for near vertical events ($1.00 < \sec\theta < 1.05$) on the left and for inclined showers of $1.15 < \sec\theta < 1.30$ on the right. Numbers labelled Δ represent the average of (extracted - reconstructed) values. ϵ = efficiency, x and y = coordinates, s = age parameter and Ne = e.m. size.

of μ at 600 m from the core ($D_{\mu 600}$) of about 0.1 m^{-2} for a $E_0 = 10^{17}$eV proton. Considering a detection area of about 800 m^2 it implies an average of 80 μ detected on a event by event basis meaning a statistical fluctuation of about 12%.

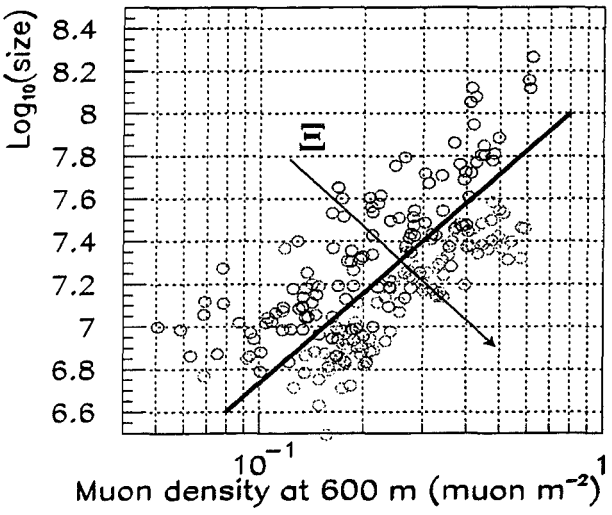

Fig. 3. QGSJET Simulations of proton and iron primaries in the energy range of $2 \cdot 10^{16} \leq E \leq 5 \cdot 10^{17}$ eV. The light symbols represent iron and the dark ones proton simulations. Both, shower fluctuations and experimental uncertainties are taken into account. The Ξ line is used as a guideline for the Ξ mass axis.

A Monte Carlo simulation, using the CORSIKA package, has been performed in order to check the experiment capabilities for testing the hadronic interaction models and reconstructing the mass of primary CRs through the three observables N_e, $D_{\mu 600}$, and h_μ. An example is presented in fig.3. Here, the primary composition is defined in terms of the mass parameter Ξ, whose definition through N_e and $D_{\mu 600}$ is shown in the same figure, in which N_e vs $D_{\mu 600}$ scatter plots obtained for protons and iron primaries obtained from QGSJET simulations are shown. The line separating p and Fe primaries best is indicated in the figure. The mass axis, Ξ is thus shown orthogonal to this line. $D_{\mu 600}$ is, as first approximation, used as energy estimator. The "iron knee" is identified as the saturation point ($D^{sat}_{\mu 600}$) of the mass parameter Ξ vs $D_{\mu 600}$, while the saturation level Ξ^{sat} depends on the low energy composition and the change in the spectrum of the individual components at the knee ($\Delta\gamma$). In figs. 4 and 5 the evolution of the mass parameter (Ξ) vs. primary energy ($D_{\mu 600}$) is shown for different interaction models (QGSJET and HDPM), for $\Delta\gamma = 0.5$ and $\Delta\gamma = 0.7$ (that are realistic values obtained from the interpretation of the data in the $10^{15} - 10^{16}$ eV energy range, assumed equal for all primaries) and a rigidity dependent knee (at $5 \cdot 10^{15}$ eV for primary protons). The statistic and reconstruction accuracies are sufficient to obtain the quoted measurements with uncertainties < 20%.

Concerning hadronic interaction models, their significant differences lead to different longitudinal developments. The average relation between h_μ and $D_{\mu 600}$ for the interaction models used (HDPM and QGSJET) are shown in Fig. 6.

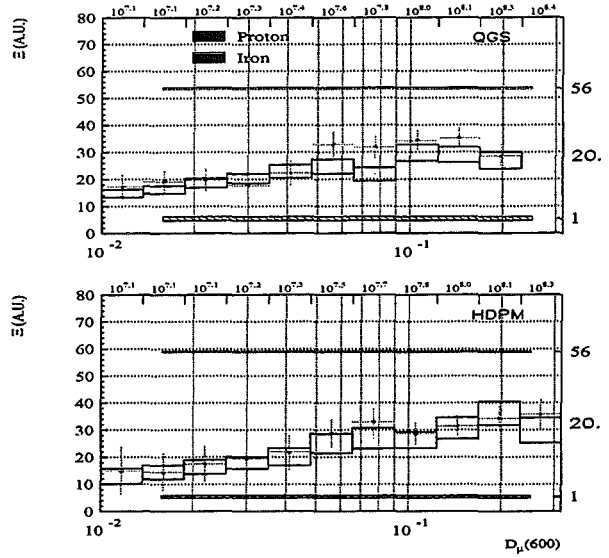

Fig. 4. Ξ vs μ density for a CMC composition model with a $\Delta\gamma = 0.5$. Cross and boxes represent the input and reconstructed values. The top scale is expressed in GeV, while the bottom one in m^{-2}.

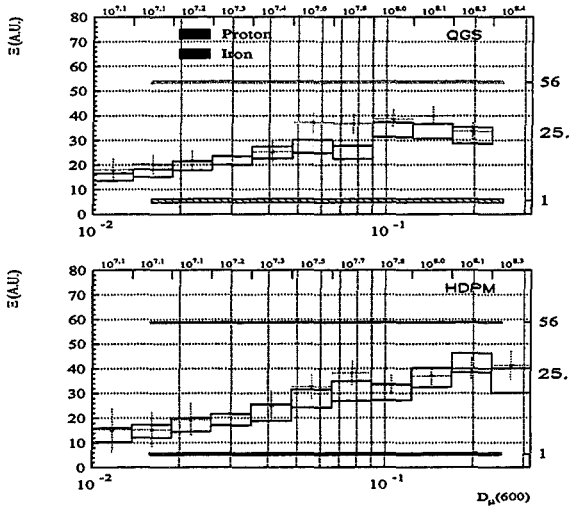

Fig. 5. Same as fig.4 but for $\Delta\gamma = 0.7$.

At $D_{\mu 600} \approx 0.1$ the accuracy $D_{\mu 600}$ on individual events is $\approx 15\%$, and on $h_\mu < 100$ gcm^{-2}, thus a separation can be performed from the clustering of the events in the regions corresponding the two models for the different masses.

4 Conclusions

The main characteristics of a new experiment (KASCADE-Grande) that is being realized at the Forschungszentrum Karlsruhe as a joint application of the KASCADE and EAS-TOP detectors, by employing well understood and proven experimental techniques already applied at lower energies, are discussed. The apparatus will be completed in 2001, data taking is planned from 2002 to 2005. In three years of effective data taking it will accumulate sufficient statistics up to 10^{18} eV ($\approx 10^3$ events above $5 \cdot 10^{17}$ eV). This experiment will cover an energy range that is poorly known, essentially from old AKENO (Nagano et al. , 1984) and the lower tail of FLY'S EYE (Bird et al. , 1994) data. The task of the experiment is to give a conclusive answer on the structure of the knee, testing the rigidity dependent model up to the energies of the "iron" group. Moreover it will allow to test different hadronic models in an energy range not accessible to accelerators but important for CRs physics. Finally it will provide a bridge to the measurement and interpretation of CRs for experiments working at much higher energies like the Pierre Auger, HIRES or OWL-Airwatch Projects.

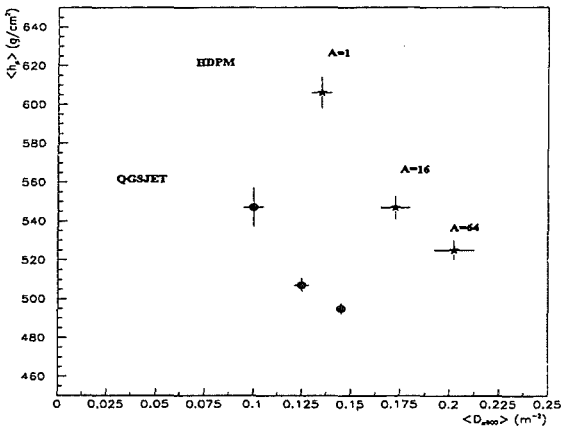

Fig. 6. Relation between $< h_\mu >$ and $D_{\mu 600}$ for different interaction models and primary mass nuclei for primary energy $E_0 = (1-2) \cdot 10^{17}$ eV and 600 m from the EAS core.

Acknowledgements. The KASCADE-Grande experiment is supported by Forschungszentrum Karlsruhe and by collaborative WTZ projects in the frame of the scientific-technical cooperation between Germany and Romania (RUM 97/014) and Poland (POL 99/005). The Polish group (Soltan Institute and University of Lodz) aknowledges the support by the Polish State Committee for Scientific Research (grant No. 5 P03B 133 20). Special thanks are due to INFN for allowing the use of the EAS-TOP equipment to build the Grande array.

References

Aglietta M. et al, Nucl. Instr. Meth. A, 277, 23, 1989.
Aglietta et al, Proc. 26th ICRC, HE-2.2.05, 1999.
Bird D.J. et al., Astrophys. J., 424, 491, 1994.
Glasstetter R. et al, Proc. 26th ICRC, HE-2.2.03, 1999.
Hörandel J.R. et al, Proc. 26th ICRC, HE-2.2.41, 1999.
Klages H.O. et al, KASCADE Collaboration, Nucl. Phys. B, Proc. Suppl. 52B, 92, 1997.
Nagano M. et al., J. Phys. G, 10, 1295, 1984.
Roth M. et al, Proc. 26th ICRC, HE-2.2.40, 1999.
Weber J.H. et al, Proc. 26th ICRC, HE-2.2.42, 1999.
Zabierowski J. et al, KASCADE Collaboration, Proc. 27th ICRC, HE-1.8.32, 2001.

Proceedings of ICRC 2001: 233 © Copernicus Gesellschaft 2001

ICRC 2001

Hadronic interaction models and the air shower simulation program *CORSIKA*

D. Heck[1], T. Antoni[1], W. D. Apel[1], F. Badea[2], K. Bekk[1], A. Bercuci[1,2], K. Bernlöhr[1,*], H. Blümer[1,3], E. Bollmann[1], H. Bozdog[2], I. M. Brancus[2], C. Büttner[1], A. Chilingarian[4], K. Daumiller[3], P. Doll[1], J. Engler[1], F. Feßler[1], H. J. Gils[1], R. Glasstetter[3], R. Haeusler[1], A. Haungs[1], J. R. Hörandel[3], T. Holst[1], A. Iwan[5,3], K-H. Kampert[1,3], J. Kempa[5,+], H. O. Klages[1], J. Knapp[1,¶], G. Maier[1], H. J. Mathes[1], H. J. Mayer[1], J. Milke[1], M. Müller[1], R. Obenland[1], J. Oehlschläger[1], S. Ostapchenko[1], M. Petcu[2], H. Rebel[1], M. Risse[1], M. Roth[1], G. Schatz[1], H. Schieler[1], J. Scholz[1], T. Thouw[1], H. Ulrich[3], B. Vulpescu[2], J. H. Weber[1], J. Wentz[1], J. Wochele[1], J. Zabierowski[6], and S. Zagromski[1]

[1]Institut für Kernphysik, Forschungszentrum Karlsruhe, 76021 Karlsruhe, Germany
[2]National Institute of Physics and Nuclear Engineering, 7690 Bucharest, Romania
[3]Institut für Experimentelle Kernphysik, University of Karlsruhe, 76021 Karlsruhe, Germany
[4]Cosmic Ray Division, Yerevan Physics Institute, Yerevan 36, Armenia
[5]Department of Experimental Physics, University of Lodz, 90236 Lodz, Poland
[6]Soltan Institute for Nuclear Studies, 90950 Lodz, Poland
[*]now at: Humboldt University, Berlin, Germany
[+]now at: Warsaw University of Technology, 09-400 Plock, Poland
[¶]now at: University of Leeds, Leeds LS2 9JT, U.K.

Abstract. The Monte Carlo program CORSIKA simulates the 4-dimensional evolution of extensive air showers in the atmosphere initiated by photons, hadrons or nuclei. It contains links to the hadronic interaction models DPMJET, HDPM, NEXUS, QGSJET, SIBYLL, and VENUS. These codes are employed to treat the hadronic interactions at energies above 80 GeV. Since their first implementation in 1996 the models DPMJET and SIBYLL have been revised to versions II.5 and 2.1, respectively. Also the treatment of diffractive interactions by QGSJET has been slightly modified. The models DPMJET, QGSJET and SIBYLL are able to simulate collisions even at the highest energies reaching up to 10^{20} eV, which are at the focus of present research. The recently added NEXUS 2 program uses a unified approach combining Gribov-Regge theory and perturbative QCD. This model is based on the universality hypothesis of the behavior of high-energy interactions and presently works up to 10^{17} eV. A comparison of simulations performed with different models gives an indication on the systematic uncertainties of simulated air shower properties, which arise from the extrapolations to energies, kinematic ranges, or projectile-target combinations not covered by man-made colliders. Results obtained with the most actual programs are presented.

1 Introduction

One of the reasons for the success of CORSIKA (**CO**smic **R**ay **SI**mulation for **KA**scade) (Heck et al., 1998) as the most-used air shower simulation program comes from the combination of the best programs available to describe the interactions of the various particles which appear in the development of Extensive Air Showers (EAS). E. g. the electromagnetic interactions of gammas, electrons and positrons are simulated by a tailor-made version of the Electron Gamma Shower code EGS4 (Nelson et al., 1985).

The largest uncertainties in numerical simulation of EAS with primary energies above some TeV are induced by the models which describe the hadronic interactions. Especially, when extrapolating to the highest energies, where the collision energies exceed those attainable with man-made accelerators, or to kinematic ranges not accessible with ordinary collider experiments one has to rely on theoretical guidelines to describe the interactions. Essential uncertainties stem from the fact that just those interaction products emitted at small angles into the extreme forward direction carry away the largest energy fraction, but in collider experiments those particles disappear in the beam pipe without being observable. In the development of EAS such particles are responsible for transporting the energy down into the atmosphere.

Six different hadronic interaction codes are presently coupled with the CORSIKA code: DPMJET (Ranft, 1995 & 1999), HDPM (Capdevielle et al., 1992; Heck et al., 1998), NEXUS (Drescher et al., 2000), QGSJET (Kalmykov et al., 1997), SIBYLL (Fletcher et al., 1994; Engel et al., 1999), and VENUS (Werner, 1993). These links offer the unique possibility to study how shower observables depend on different hadronic interaction models, thus deriving the systematic uncertainties of predictions from simulations.

Correspondence to: D. Heck (heck@ik3.fzk.de)

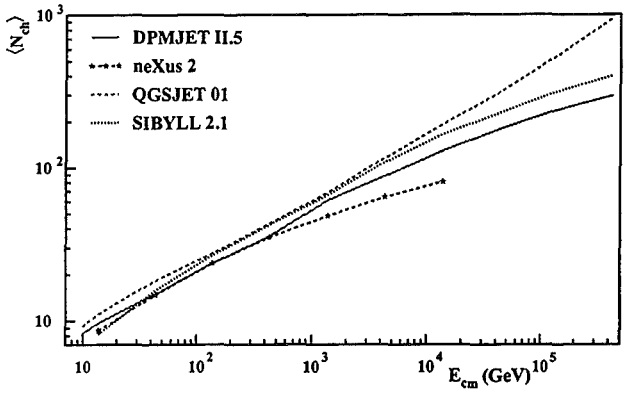

Fig. 1. Average charged particle multiplicity as function of energy for p-^{14}N-collisions.

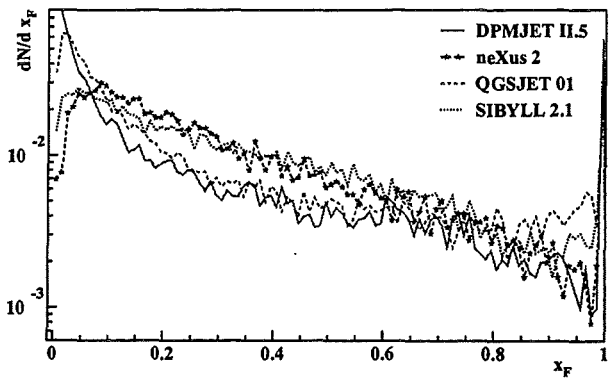

Fig. 2. Feynman-x distribution of most energetic baryon emerging from p-^{14}N-collisions at $E_{lab} = 10^7$ GeV.

2 Updated and new models

Since our first comparison of hadronic interaction models (Knapp et al., 1996) most of these models are replaced by revised versions. With NEXUS a completely new designed code is now available for air shower simulations.

2.1 DPMJET upgrade

Besides technical improvements DPMJET is upgraded to version II.5 by including new Dual-Parton-Model diagrams which lead to an enhanced baryon stopping power (Ranft, 1999) in nucleon-nucleon and nucleon-nucleus interactions.

2.2 NEXUS 2 features

The NEXUS model (Drescher et al., 2000) starts from the universality hypothesis stating that *the mechanisms of high energy interactions are identical in different reactions*. Thus, one can study the final state (s-channel) parton evolution and the subsequent hadronization on the basis of the e^+e^--reaction data, while the data on deep inelastic lepton-proton scattering allow to test the model description of the initial (t-channel) parton cascade. Proceeding in this way the modeling of the complicated mechanism of hadronic interaction is decomposed into separate 'building blocks' which are deduced from simpler systems. Also, fixing the relevant model parameters on the basis of data on different reactions allows to restrict considerably the parameter freedom of the model approach and to assure a more reliable extrapolation of the model to higher energies.

By construction NEXUS is a unified Gribov-Regge model of soft and hard interactions. While the former are described in the traditional way by the phenomenological soft Pomeron exchanges (Werner, 1993), the latter are treated using the perturbative QCD techniques, within the concept of the 'semi-hard Pomeron'. An important feature of NEXUS is the fully self-consistent treatment of the energy-momentum sharing between individual elementary scattering processes, including virtual rescatterings (Hladik et al., 2001). This is taken into account both in the cross-section calculations and in the particle production treatment. As demonstrated in Fig. 1 for p-^{14}N-interactions this leads to a rather moderate increase of the average charged particle multiplicity with energy.

2.3 QGSJET modifications

The modifications of QGSJET 01 concern a more correct treatment of diffractive processes in hadron-nucleus collisions. In the QGSJET treatment (quasi-eikonal approach), the diffraction acts essentially as a coherent process, which implies that the probability for *both* projectile and target diffraction should be calculated averaging over impact parameter of the interaction and over positions of the nucleons. In the previous version of the model the projectile diffraction had been simulated *after* sampling a particular impact parameter, thus violating to some extent the unitarity condition at small impact parameters. Now the diffraction processes are chosen according to the correct probability, without specifying a particular impact parameter in that case. On average the hadron-nucleus collisions show a slightly lower elasticity and the simulated EASs tend to a faster aging.

2.4 SIBYLL improvements

The old SIBYLL version 1.6 (Fletcher et al., 1994) is based on the minijet model and frequently used in combination with air-shower simulation programs like MOCCA (Hillas, 1997) or AIRES (Sciutto, 1999). Fundamental modifications (Engel et al., 1999) introduced the exchange of multiple soft Pomerons and an energy dependent transverse momentum cut-off of the minijets. These improvements revealed a considerably better agreement with experimental data. Though not released officially, for this analysis SIBYLL version 2.1 is used for comparisons. Further fine-tuning towards a settled version is ongoing (Engel, 2001).

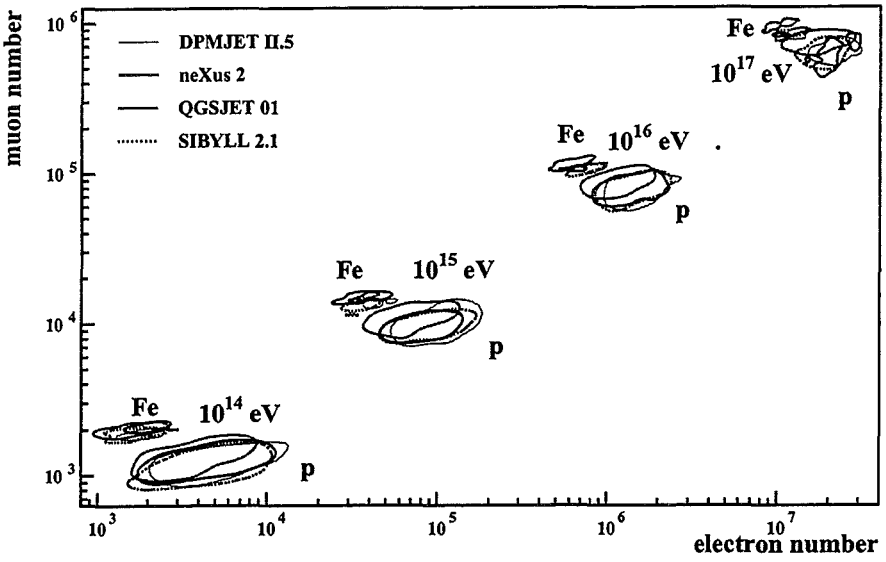

Fig. 3. Predicted number of muons vs. number of electrons at the KASCADE-Grande experiment (110 m a.s.l.) for vertical incident proton (p) and iron (Fe) primaries at various primary energies. The contour lines are drawn at half maximum of the respective two-dimensional distributions generated by 500 proton and 200 iron induced showers for each primary energy.

3 Comparison of actual models

^{14}N-nuclei are the most frequent targets of hadronic interactions in the EAS development, and therefore we compare such hadronic collisions. Fig. 2 shows the distribution of the longitudinal momentum fraction which is carried away by the most energetic baryon from p-^{14}N-collisions at E_{lab} = 10^{16} eV. For the development of EAS the most interesting portion is at $x_F > 0.8$ as particles in this range carry away the largest fraction of the collision energy, thus transporting the remainder of the projectile energy deeper into the atmosphere. But just in this range the different models exhibit larger differences. This plot should be compared with (Knapp, 1999) to see the improvements in the description of diffractive processes for the updated models.

Fig. 3 shows the scattering of muon numbers vs. electron numbers for vertical showers of different energies which might be observed by the KASCADE-Grande experiment (Bertaina et al., 2001). With increasing primary energy the relative fluctuations are reduced, but a separation between proton and iron induced showers is maintained.

To keep the CPU-times for these simulations at tolerable durations the *thin sampling* option available in CORSIKA has been used. This option does not treat in detail all secondary particles, rather below a selected energy threshold (here $E_{thin} = 10^{-5} \cdot E_0$) it samples 'representative' particles which are followed further on and weighted accordingly, while the remaining huge bulk of particles is skipped.

4 Highest energies

Presently three of the hadronic interaction models enable simulations of hadronic collisions with laboratory energies exceeding 10^{20} eV. Thus CORSIKA simulations of EAS induced by the most energetic primaries are possible (Risse et al., 2001) to predict in detail measurable shower parameters.

An interesting quantity is the atmospheric depth X_{max} of the shower maximum, which can be determined experimentally using fluorescence or Cherenkov techniques. It may be used to deduce the primary mass composition. Fig. 4 shows the predicted X_{max}-values of proton and iron induced showers with vertical incidence for primary energies between 10^{14} and 10^{20} eV together with experimental values.

Compared with the older SIBYLL 1.6 the X_{max}-values of version 2.1 are reduced by $\approx$ 20 g/cm^2 for proton showers and for iron showers with primary energies $\geq 10^{17}$ eV. Similarly, the evolution of QGSJET to version 01 accelerated the shower aging leading to X_{max}-values reduced by $\approx$ 12 g/cm^2 in the same range. It is remarkable that DPMJET II.5 reveals much larger X_{max}-values than the preceding version II.4, which unfortunately did not reach up to the highest energies. But the X_{max}-values of this older version agreed much better with those of NEXUS 2 and SIBYLL 2.1.

5 Outlook

A considerable progress in describing the inelastic hadron-air cross-sections up to 10^{15} eV can be stated during the last years. E.g. the variations in the inelastic p-air cross-sections adopted for the different interaction models have shrunk from 18 % in 1997 to today's 6 % around the average of 390 mb at 10^{15} eV. Similarly, the quality of predicted shower quantities has been improved. The differences of the average electron size at sea level for 10^{15} eV vertical proton induced EAS are reduced by a factor 3 from former 45 % to 15 % today (Knapp et al., 1996; Knapp, 1999) if we compare the results generated by the four modern models with those generated by the models available in 1996.

A further improvement of the hadronic interaction models may be expected in near future: DPMJET version 3 is announced (Roesler et al., 2000), works on NEXUS 3 succeeding version 2 are going on, and a more advanced version

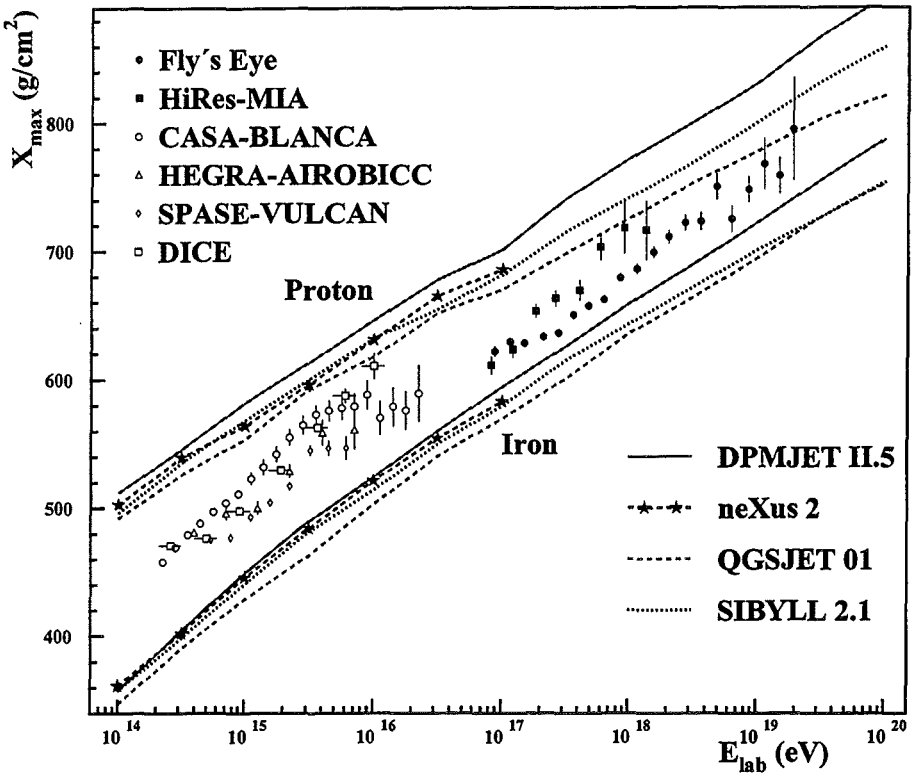

Fig. 4. Depth of shower maximum X_{max} of charged particles as function of primary energy for vertical showers as predicted by CORSIKA coupled with various models. The procedure to derive the X_{max}-values is similar to that described by (Pryke, 2001). A modified Gaisser-Hillas function (Gaisser and Hillas, 1977) has been fitted to the longitudinal distribution of each of the 500 proton or 200 iron induced showers at each of the 13 individual energies. Averaging the fitted X_{max}-parameters for each energy and primary particle gives the resulting X_{max}-values. Measurement points of fluorescence experiments (Bird el al., 1993; Abu-Zayyad et al., 2000) are indicated by filled symbols, those of Cherenkov experiments (Fowler et al., 2001; Arqueros et al., 2000; Dickinson et al., 1999; Swordy and Kieda, 2000) by open symbols.

of SIBYLL might become available soon (Engel, 2001).

6 Program distribution

The CORSIKA 6.00 program files including an up-to-date version of the User's Guide (Knapp and Heck, 1993) are available via anonymous ftp from **ftp-ik3.fzk.de**. Details for access to this anonymous account may be found on the web page **http://www-ik3.fzk.de/~heck/corsika/** .

Acknowledgements. Many thanks go to the authors of the hadronic interaction models for their help to get their programs running and for their advice in coupling the programs with CORSIKA. We are indebted to R. Engel for making available the SIBYLL version 2.1. The partial support of this work by the British German Academic Research Collaboration (Grant 313/ARC-lk) is acknowledged.

References

Abu-Zayyad, T. et al., preprint astro-ph/0010652, 2000 (submitted to *Astrophys. J.*).

Arqueros, F. et al. (HEGRA Coll.), *Astron. Astrophys.* **359**, 682, 2000.

Bertaina, M. et al. (KASCADE-Grande Coll.), *Proc. 27th Int. Cosmic Ray Conf.*, Hamburg (Germany), Contribution HE 1.8.26, 2001.

Bird, D. et al., *Phys. Rev. Lett.* **71**, 3401, 1993.

Capdevielle, J.N. et al., Report **KfK 4998**, Kernforschungszentrum Karlsruhe, 1992.

Dickinson, J.E. et al., *Proc. 26th Int. Cosmic Ray Conf.*, Salt Lake City (USA), **3**, 136, 1999.

Drescher, H.J. et al., preprint hep-ph/0007198, 2000; *Phys. Rep.* (in print).

Engel, R. et al., *Proc. 26th Int. Cosmic Ray Conf.*, Salt Lake City (USA), **1**, 415, 1999.

Engel, R., private communication, 2001.

Fletcher, R.S. et al., *Phys. Rev.* **D50**, 5710, 1994.

Fowler, J.W. et al., *Astropart. Phys.* **15**, 49, 2001.

Gaisser, T.K. and Hillas, A.M., *Proc. 15th Int. Cosmic Ray Conf.*, Plovdiv (Bulgaria), **8**, 353, 1977.

Heck, D. et al., Report **FZKA 6019**, Forschungszentrum Karlsruhe, 1998.

Hillas, A.M., *Nucl. Phys. B (Proc. Suppl.)* **52B**, 29, 1997.

Hladik, M. et al., *Phys. Rev. Lett* **86**, 3506, 2001.

Kalmykov, N., Ostapchenko, S., and Pavlov, A.I., *Nucl. Phys. B (Proc. Suppl.)* **52B**, 17, 1997.

Knapp, J. and Heck, D., Report **KfK 5196B**, Kernforschungszentrum Karlsruhe, 1993; for an up-to-date version see: http://www-ik3.fzk.de/~heck/corsika/ .

Knapp, J., Heck, D., and Schatz, G., Report **FZKA 5828**, Forschungszentrum Karlsruhe, 1996.

Knapp, J., *Nucl. Phys. B (Proc. Suppl.)* **75A**, 89, 1999.

Nelson, W.R., Hirayama, H. and Rogers, D.W.O., Report **SLAC 265**, Stanford Linear Accelerator Center, 1985.

Pryke, C.L., *Astropart. Phys.* **14**, 319, 2001.

Ranft, J., *Phys. Rev.* **D51**, 64, 1995.

Ranft, J., preprints hep-ph/9911213 and hep-ph/9911232, 1999.

Risse, M. et al., *Proc. 27th Int. Cosmic Ray Conf.*, Hamburg (Germany), Contribution HE 1.5.31, 2001.

Roesler, S., Engel, R., and Ranft, J., preprint hep-ph/0012252, 2000.

Sciutto, S., preprint astro-ph/9911331, 1999.

Swordy, S.P. and Kieda, D.B., *Astropart. Phys.* **13**, 137, 2000.

Werner, K., *Phys. Rep.* **232**, 87, 1993.

Proceedings of ICRC 2001: 522 © Copernicus Gesellschaft 2001

ICRC 2001

EAS simulations at Auger energies with CORSIKA

M. Risse[1], D. Heck[1], J. Knapp[2], and S. S. Ostapchenko[1,*]

[1]Institut für Kernphysik, Forschungszentrum Karlsruhe, 76021 Karlsruhe, Germany
[2]Department of Physics and Astronomy, University of Leeds, Leeds LS2 9JT, U.K.
[*]On leave of absence from the Moscow State University, Moscow, Russia

Abstract. The air shower simulation program CORSIKA is used to study the cascades initiated by the highest-energy cosmic rays. Due to different detection techniques of current experiments, the shower simulation should provide all necessary information on the production of fluorescence and Cherenkov photons during the cascade development and on the particle component reaching observation level. Additionally, the amount of CPU time and disk space should allow for the production of a large number of events to investigate shower fluctuations and the dependence on primary parameters. With respect to these requirements, the present CORSIKA usage is summarized with special focus on the application of particle thinning. A basic method to treat weighted particles in the detector simulation is proposed. Extensions concerning the fluorescence and Cherenkov light description are discussed. First results on the distribution of the energy deposit of charged particles in air showers, which is closely connected to the fluorescence light production, are given.

1 Introduction

The Auger experiment (Auger Collaboration, 1997) begins the exploration of the highest-energy cosmic rays with a prototype installation. Parallel to first measurements, a large data base of simulated extensive air showers (EAS) is prepared using the CORSIKA code (Heck et al., 1998). Since the detailed simulation of all produced secondary particles (of the order of 10^{13} secondaries in a 10^{20} eV shower) is impossible, thinning techniques are applied. Generation and transport of individual fluorescence and Cherenkov photons is also prohibited by the huge number of photons, exceeding the particle number by more than 3 orders of magnitude. Thus, to allow for a realistic simulation of fluorescence and Cherenkov light CORSIKA is being extended to enable a detailed mapping of the longitudinal cascade development.

In the first part of the paper, the current philosophy and experiences for preparing a CORSIKA shower library are described. Especially, aspects concerning the technique of particle thinning are discussed. In the second part, the status and first results of extracting information on fluorescence and Cherenkov light production are presented.

Correspondence to: M. Risse (risse@ik1.fzk.de)

2 Shower generation

2.1 CORSIKA

CORSIKA is an open program package for performing a complete 4-dimensional simulation of air showers with primary energies from sub-TeV to $>10^{20}$ eV. For the treatment of particle interactions, external state-of-the-art codes are employed. Electromagnetic interactions are simulated using a tailer-made version of the EGS4 code (Nelson et al., 1985). Due to the large theoretical uncertainties in the description of hadronic interactions, different high-energy and low-energy hadronic interaction models are to the user's disposal. For a recent model comparison, see Heck et al. (2001).

The usage of CORSIKA in connection with experiments of completely different detection techniques and simulation requests (e.g., arrays measuring the electromagnetic, muonic, and hadronic component, Cherenkov and neutrino telescopes, μ^+/μ^--charge ratio measurements) guarantees continuous critical checks, improvements, and extensions both of the simulation code itself and, by comparing with measurements, of the physics implemented. For the simulation of the highest-energy cosmic rays, the LPM effect (Landau and Pomeranchuk, 1953; Migdal, 1956) and techniques of particle thinning (see chapter 2.2) have been implemented (Heck and Knapp, 1998). Three hadronic interaction models reach to the highest energies: QGSJET 01 (Kalmykov et al., 1997; for the recent modifications, see Heck et al., 2001), DPMJET II.5 (Ranft, 1999), and SIBYLL (Fletcher et al., 1994; Engel et al., 1999). Cherenkov light production is possible. The energy deposit of charged particles is calculated for the subsequent modeling of the fluorescence light production.

2.2 Particle thinning

To keep the CPU times and particle output files in reasonable limits, for the simulation of highest primary energies the *thin sampling* option is available in CORSIKA. When activated, this option does not treat in detail all secondary particles, it

samples "representative" particles which are followed further on and weighted accordingly, while the bulk of particles is discarded (Hillas, 1997). This thinning starts at a selectable fraction of the primary energy. The additional use of an optimum weight limitation for the particles leads to a much better simulation performance (Kobal et al., 1999) in terms of decreased additional ("artificial") fluctuations, introduced by thinning, and computing time. Especially, optimal thinning includes different weight limits for the electromagnetic component compared to the muonic and hadronic ones.

For illustration, let's suppose a primary energy of $E_0 = 10^{19}$ eV and an optimized thinning of 10^{-6}. Then, a detailed simulation is performed down to particle energies of 10^{13} eV. Below this energy the thinning algorithm is employed until a weight limit is reached of $E_0/\mathrm{GeV} \cdot 10^{-6} = 10^4$ for electromagnetic particles and of 10^2 for muons and hadrons. Below these energies, i.e. about 10^9 eV (e/γ) and 10^{11} eV (μ/had), again the detailed simulation starts until simulation threshold.[1] Using instead a thinning of 10^{-7} *without* weight limits, particles with weights up to 10^7 (e/γ) and 10^4 (μ/had) are produced. The latter method will suffer from much larger artificial fluctuations. Also when comparing the data output, it is evident that the typical file size of $\simeq$350 MB (per shower!) with optimized 10^{-6} thinning yields a much better shower representation compared to $\simeq$20 MB using 10^{-7} thinning only.[2] Thus, for achieving best performance in terms of good data quality and small computing time, the use of optimized thinning is of crucial importance.

However, special care must be paid to control and perhaps *a posteriori* decrease the influence of artificial fluctuations introduced by thinning. Also, it is not evident how to treat weighted particles in a detector simulation. The statistical uncertainty in, e.g., the particle number in a given area is

$$\sigma_N = \sqrt{\langle N^2\rangle - \langle N\rangle^2} = \sqrt{\langle \left(\sum_{i=1}^{n} w_i\right)^2 \rangle - \langle \sum_{i=1}^{n} w_i\rangle^2} \quad (1)$$

for n particles with individual weights w_i which represent $N = \sum_i w_i$ particles. Denoting the average particle weight for an individual event as $W = \frac{1}{n}\sum_i w_i$, from (1) we gain

$$\sigma_N = \sqrt{\langle n^2W^2\rangle - \langle nW\rangle^2} \ . \quad (2)$$

This formula takes a very simple and easily understandable form when considering the particle weights to be constant, $W = \mathrm{const}$, and assuming that the fluctuations of the number of "thinned" particles n obey Poisson statistics, i.e. $\sigma_n = \sqrt{\langle n^2\rangle - \langle n\rangle^2} = \sqrt{\langle n\rangle}$. Then from (2) we obtain

$$\sigma_N = W\sqrt{\langle n\rangle} = \sqrt{W\langle N\rangle} \ . \quad (3)$$

Thus, large weights result in huge artificial fluctuations exceeding by far the "natural" ones, which consist both of shower-to-shower and of physical Poissonian fluctuations.[3]

[1] Usually 100 keV for e/γ and 100 MeV for μ/had.

[2] CPU times are only doubled for optimized 10^{-6} thinning.

[3] Natural and artificial fluctuations in the Auger surface detector are discussed in detail by Billoir (2001).

The artificial fluctuations reduce to the physical Poissonian of the "real" particle number N, $\sigma_N \to \sqrt{\langle N\rangle}$, only in the limit $W \to 1$.

To *a posteriori* decrease the artificial fluctuations, particles are collected from an area A_{coll} much larger than the detector area A_{det} (typically of the order of 10 m^2). The weights then are rescaled according to the ratio of both areas, $w_i^{new} = w_i \cdot (A_{det}/A_{coll})$. Limitations of this method are given by the effect of smoothing over the collecting area which contains both lateral gradients of densities, time delays etc. (which, to some extent, can be accounted for), larger-scale granularities and correlations of particles coming from the same subshower. To keep the collecting area and such effects small, again the use of optimal thinning is important, since larger particle weights require a larger collecting area. The approach used in the current Auger surface detector simulation and corresponding limitations are described by Billoir (2000).

To avoid rescaled weights $w_i^{new} > 1$ and duplication of (perhaps "fractional") particles for a detector simulation, the following method might be appropriate. The collecting area is chosen to be

$$A_{coll} = w_{max} \cdot A_{det} \Rightarrow w_i^{new} \leq 1 \quad \text{for all particles.} \quad (4)$$

Now, the interpretation of the weights $w_i^{new} \leq 1$ is the probability of the particle to be considered in the detector simulation. Optimal thinning with limited w_{max} could assure that A_{coll} is reasonably small. In the aforementioned case of optimal 10^{-6} thinning with $E_0 = 10^{19}$ eV, a collecting area of $10^4 \cdot A_{det}$ would be sufficient for e/γ, for μ/had even only $10^2 \cdot A_{det}$. Without optimal thinning the collecting areas typically are considerably larger even when particles with weights $w_i^{new} > 1$ are allowed (Billoir, 2000).

2.3 Shower Library

For the interpretation of the Auger data, a shower library is prepared at the computing center of IN2P3 in Lyon (France).[4] The typical production rate is 80–100 GB/week using simultaneously $\simeq$30 Linux 750 MHz Pentium Processors. This corresponds to roughly 2000 (200) highest-energy showers of optimized 10^{-5} (10^{-6}) thinning per week. The files are stored in a mass storage. Some shower information like the longitudinal energy deposit, are kept in small size files on local disk to allow conveniently some analyses.

Apart from simulation runs with specific parameter requirements, the current simulation strategy is twofold: Firstly, showers of (different) fixed primary energy and zenith angle are calculated with very good thinning quality of optimized 10^{-6} thinning. The energy - zenith angle combinations are chosen to cover in particular the parameter ranges important for the Auger Engineering Array. These showers, for instance, might be used to obtain shower parametrizations. Secondly, a non-discrete primary parameter distribution is chosen. The primary energies follow a power law (differential index of -2.0) with zenith angles out to 60°. To achieve

[4] See http://webcc.in2p3.fr/ for more information on CC-IN2P3.

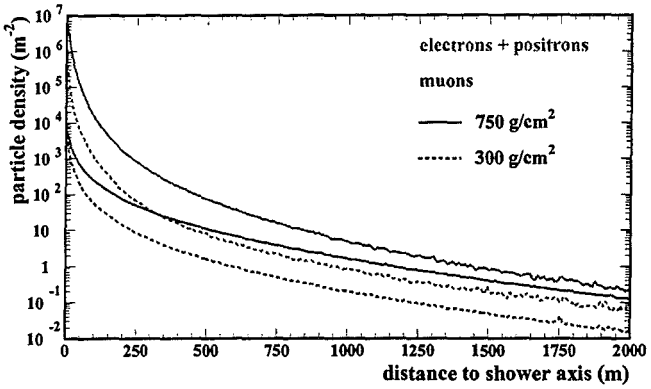

Fig. 1. Particle densities of $e^{\pm}$ and $\mu^{\pm}$ for proton primaries of $E_0 = 10^{19}$ eV at two different atmospheric levels.

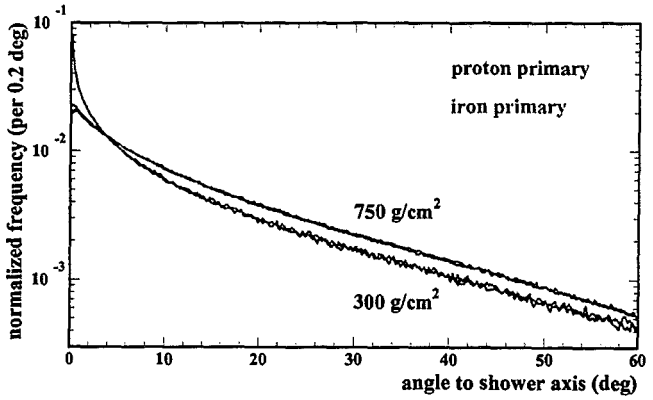

Fig. 2. Angular distribution (area normalized to one) of $e^{\pm}$ for proton and iron primaries of $E_0 = 10^{19}$ eV at two different atmospheric levels.

high statistics for these showers an optimized 10^{-5} thinning is used. For both strategies different primary particles as protons, iron nuclei, photons, etc. are simulated and the statistics is permanently increased.

As hadronic interaction model, QGSJET 01 is employed because analyses, though at smaller primary energies, have shown that this model provides the best overall description of EAS data (see, e.g., Antoni et al., 1999).

3 Fluorescence and Cherenkov light treatment

Two problems arise when treating fluorescence and Cherenkov light, observable by optical telescopes, in an air shower simulation: Firstly, a realistic transport description has to take atmospheric conditions as ozone or aerosol concentrations into account which vary with time. Thus, to allow a reuse of a (time-intensive!) air shower simulation, informations on the light production are given. The atmospheric transport is subject to a separate program. Secondly, the number of optical photons exceeds by orders of magnitudes the particle number and prohibits an individual consideration. A method to account for this is the extraction of detailed information for a limited number of levels of the cascade development (*longitudinal mapping*).

In the following, for vertical showers of $E_0 = 10^{19}$ eV, particle distributions are compared at atmospheric depths of 300 g/cm^2 and 750 g/cm^2 (close to shower maximum).[5] Insights into the light production can already be gained by investigating the emitting particles (chapter 3.1). More directly, the energy deposit of charged particles (for fluorescence, chapter 3.2) and the Cherenkov routines available in CORSIKA can be used (chapter 3.3). Apart from the possibility to study the shower physics of highest-energetic cascades in general, the technique of longitudinal mapping might help to look for suitable parametrizations and/or provide information in each single shower for a realistic fluorescence and Cherenkov light treatment.

[5] Optimal 10^{-6} thinning, average of 8 proton and 4 iron induced showers, respectively.

3.1 Emitting particles

In figure 1, particle lateral distributions are displayed. The particle number increase with X (atmospheric depth) can be seen. As expected, the muon lateral distribution is flat compared to that of $e^{\pm}$. The shape especially of the $e^{\pm}$ lateral distribution depends only weakly on X which is related to the smaller amount of matter per unit length at small X. The angular distributions of $e^{\pm}$ are given in figure 2. With increasing X, larger angles are more frequently. About 13.2 % (17.1 %) of the particles have angles $> 30°$ at 300 g/cm^2 (750 g/cm^2). The distributions for iron and proton primaries resemble each other. Finally, from the energy spectra shown in figure 3, the reduction of the average energy of $e^{\pm}$ and of the number of high-energy $e^{\pm}$ with increasing depth is visible. For iron primaries, the earlier development leads to a higher particle number at 300 g/cm^2, and the smaller energy per primary nucleon results in less high-energetic $e^{\pm}$.

3.2 Fluorescence light

The production of fluorescence photons is closely connected to the energy deposit of charged particles in air (Kakimoto et al., 1996). CORSIKA tabulates the energy deposit of the different particle components as a function of X, usually in layers of thickness 5 g/cm^2 (adjustable). In this approximation of a shower as a 1-dimensional line, the subsequent calculation of the fluorescence production is possible, taking into account temperature and pressure dependences etc. of the fluorescence yield (Kakimoto et al., 1996). To study the real size and the time-dependent signal of a shower as seen in the fluorescence light, figure 4 shows the development of the lateral energy deposit generated by $e^{\pm}$. Similar to the results of figure 1, the shapes do not depend significantly on the depth. While at smaller X, due to the earlier development, the energy deposits from iron primaries exceed on average those from protons, they resemble each other at larger depths for

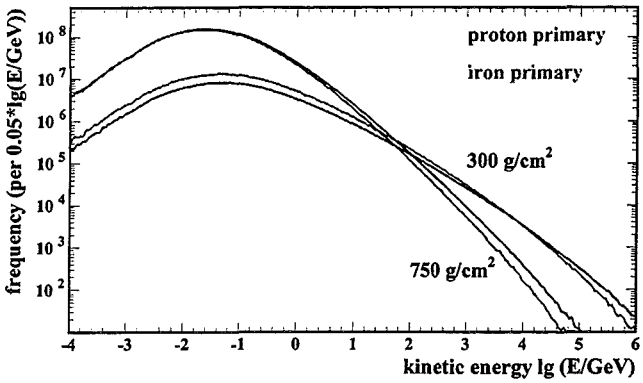

Fig. 3. Kinetic energy spectra of $e^{\pm}$ for proton and iron primaries of $E_0 = 10^{19}$ eV at two different atmospheric levels.

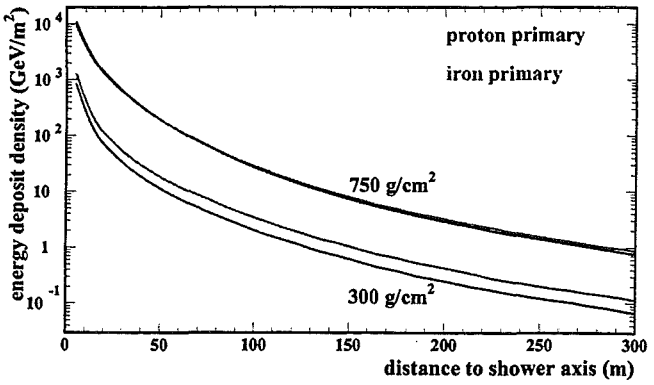

Fig. 4. Energy deposit density of $e^{\pm}$ vs. distance to shower axis, for proton and iron of $E_0 = 10^{19}$ eV at two different atmospheric levels.

distances out to a few 100 m.

3.3 Cherenkov light

With enabled Cherenkov option, CORSIKA calculates the number and emission direction of the Cherenkov photons in the chosen wavelength interval produced by the individual particles (which might have weights). The photons can be grouped to bunches of adjustable size (analogous to particle weights) with a common emission direction for the bunch. The idea currently followed is to activate the Cherenkov routines in CORSIKA for several small atmospheric layers (thickness of the order 1 g/cm^2). In these layers, correlated properties of the produced Cherenkov light are extracted, e.g. emission angles as a function of distance to shower axis.

4 Summary and outlook

The features of CORSIKA with respect to the simulation of the highest primary energies, and first experiences in preparing a mass production have been discussed. Special attention was paid to the question of particle thinning. Using weight limitation in terms of optimal thinning leads *a priori* to reduced artificial fluctuations. *A posteriori*, it is expected to allow a better reduction of artificial fluctuations and an elegant method to treat particle weights in a detector simulation. In this method, the rescaled weights are ≤ 1 and are interpreted as accepting probabilities. Further and more quantitative investigations are needed.

Currently, CORSIKA is extended to allow a detailed mapping of the longitudinal shower development. In particular, this aims to provide the necessary informations on fluorescence and Cherenkov light production. Thus, subsequently a realistic propagation of the light through the atmosphere and a detector simulation can be carried out.

Acknowledgements. We are indebted to W. Wojcik and colleagues of the IN2P3 and to J.N. Albert, A. Cordier, and E. Cormier for their continuous help and patient advice when preparing the mass production, and to many Auger Collaboration members for fruitful discussions. The partial support of this work by the British German Academic Research Collaboration from The British Council and the DAAD is acknowledged.

References

Antoni, T., et al., KASCADE Collaboration, *J. Phys. G: Nucl. Part. Phys.* **25**, 2161, 1999.

Auger Collaboration, *The Pierre Auger Observatory Design Report* (1997), http://www.auger.org/admin/DesignReport/index.html

Billoir, P., *Auger GAP note* 2000-025, 2000.

Billoir, P., *Auger GAP note* 2001-005, 2001.

Engel, R. et al., *Proc.* 26^{th} *Int. Cosmic Ray Conf.*, Salt Lake City (USA), **1**, 415, 1999.

Fletcher, R.S. et al., *Phys. Rev.* **D50**, 5710, 1994.

Heck, D. et al., Report **FZKA 6019**, Forschungszentrum Karlsruhe, 1998; see http://www-ik3.fzk.de/~heck/corsika .

Heck, D., and Knapp, J., Report **FZKA 6097**, Forschungszentrum Karlsruhe, 1998.

Heck, D. et al., *Proc.* 27^{th} *Int. Cosmic Ray Conf.*, Hamburg (Germany), Contribution HE 1.3.1, 2001.

Hillas, A.M., *Nucl. Phys. B (Proc. Suppl.)* **52B**, 29, 1997.

Kakimoto, F., et al., *Nucl. Instr. Meth.* **A 372**, 527, 1996.

Kalmykov, N., Ostapchenko, S., and Pavlov, A.I., *Nucl. Phys. B (Proc. Suppl.)* **52B**, 17, 1997.

Kobal, M., Filipčič, A., and Zavrtanik, D. for the Pierre Auger Collaboration, *Proc.* 26^{th} *Int. Cosmic Ray Conf.*, Salt Lake City (USA), **1**, 490, 1999.

Landau, L.D., and Pomeranchuk, I.Ya., *Dokl. Akad. Nauk SSSR* **92** 535 & 735, 1953.

Migdal A.B., *Phys. Rev.* **103** 1811, 1956.

Nelson, W.R., Hirayama, H. and Rogers, D.W.O., Report **SLAC 265**, Stanford Linear Accelerator Center, 1985.

Ranft, J., preprints hep-ph/9911213 and hep-ph/9911232, 1999.

Proceedings of ICRC 2001: 526 © Copernicus Gesellschaft 2001

ICRC 2001

Study of model dependence of EAS simulations at E $\geq 10^{19}$ eV

S. J. Sciutto[a1], J. Knapp[2], and D. Heck[3]

[1]Dept. de Fisica, Universidad Nacional de La Plata, Argentina
[2]Dept. of Physics and Astronomy, University of Leeds, Leeds LS2 9JT, United Kingdom
[3]Institut für Kernphysik, Forschungszentrum Karlsruhe, 76021 Karlsruhe, Germany

Abstract. Air shower simulation programs are essential tools for the analysis of data from present and future cosmic ray experiments, since estimates of energy and mass of the primary particle can only be obtained by comparison to model predictions, and the model uncertainties translate directly into systematic errors in the energy and mass determination. While the main uncertainty of contemporary models comes from our poor knowledge of the (soft) hadronic interactions at high energies, also electromagnetic interactions, low-energy hadronic interactions and the particle transport influence details of the shower development. We report here on a comparative analysis of simulations for 2×10^{19} eV protons, performed with the AIRES and CORSIKA air shower simulation programs. The model dependency of the main shower observables is discussed. We study also some aspects of the technical performance of both programs.

1 Introduction

Ultra high energy cosmic rays (UHECRs) pose some of the most exciting problems in modern astrophysics. It seems certain that cosmic rays with $E > 10^{20}$ eV exist and reach the Earth at a flux of about 1 per km^2 and century ($\approx$ 15 events in 35 years), yet no astrophysical object is known that could accelerate CRs to those energies. If the sources are distributed on cosmological distances one would expect to see a marked cut-off at about 6×10^{19} eV in the energy spectrum due to reactions of the UHECRs with the microwave background, but no such cut-off is seen by experiments so far. If the sources are nearby, as indicated by the absence of the cut-off, one could expect to see anisotropies in the arrival direction of the particles. At present, however, any investigation of this lacks statistics. Over the last few years many theorists have attempted to explain this enigma with new particles, new physics or exotic phenomena, such as decaying topological defects, or the violation of Lorentz invariance. A solution to the problem can only come from an increase in statistics at highest energies. The precise form of the energy spectrum, the whole-sky arrival direction distribution and the identification of the CR particles will allow to discriminate some of the proposed theories. For a recent review on UHECRs see (Nagano and Watson, 2000). The Auger Experiment (Auger Collaboration, 1997) aims to measure UHECRs with two detectors of 3000 km^2 each, positioned on the southern and northern hemisphere. However, only the secondaries are measured which the CR particles produce in the atmosphere. Particle detection at ground level is complemented with measurement of fluorescence light emitted in air. Arrival direction, energy, and identity of the primary particle have to be reconstructed from the air shower observables. For this purpose numerical models are employed that predict observable quantities as a function of the properties of the primary particle. Those models rely on experimental knowledge on hadronic and electromagnetic interactions, particle transport and decay and on theoretical ideas to extrapolate into kinematical and energy regimes not accessible in the lab. Analysis and interpretation of air shower data, therefore, always depends on the model used, and the larger the extrapolation from firm knowledge the bigger uncertainties become. Two models used within the Auger Collaboration are AIRES (Sciutto, 1999) and CORSIKA (Heck, 1998). In this paper we attempt a model comparison with emphasis on those quantities that will be measured by the Auger experiment and on which Auger physics results will likely rest.

Correspondence to: J. Knapp (j.knapp@leeds.ac.uk)
[a]Fellow of CONICET, Argentina

2 The Programs

AIRES and CORSIKA provide both fully 4-dimensional Monte Carlo simulations of proton, photon, and nucleus-induced air shower development in the atmosphere. Both simulate hadronic and electromagnetic interactions, propagate particles through the atmosphere, account for the Earth's magnetic field, for decays, energy loss and deflection (and many less important processes), and produce eventually a list of all particles reaching ground level.

AIRES is originally based on MOCCA (Hillas, 1997), but was significantly improved and extended. It uses its own set of routines for electromagnetic interactions (of $e^{\pm}$ and γ), decays and propagation. The additions comprise a link to the external high energy hadronic interaction models SIBYLL or QGSJET, muon pair production and bremsstrahlung, photonuclear reactions, the Landau-Pomerantchuk-Migdal (LPM) effect of high-energy γ and $e^{\pm}$, and the simulation of exotic primaries, (e.g. ν), (Bertou et al., 2001).

CORSIKA developed over the last 12 years to a standard analysis tool of the air shower community. CORSIKA attempts to model the individual processes of the shower development in as great detail as possible, to some extent irrespective of the computing effort needed. It employs proven solutions wherever available. So a variety of hadronic models have been linked to CORSIKA and are used and updated to the specifications of their respective authors. EGS4 (Nelson et al., 1985) is used for simulation of electromagnetic interactions, all two and three-body decays, with branching ratios down to 1%, are modelled kinematically correct and particle tracking and multiple scattering are done in great detail, even for strange and charmed particles. Also CORSIKA contains photonuclear reactions, muon pair production and bremsstrahlung, and the LPM effect.

Both programs use a statistical thinning algorithm (Hillas, 1981) to keep computing times and particle output at a manageable level. Particles are followed individually down to a chosen fraction of the primary energy, from then on only a subset of particles from each interaction is followed, while others are discarded. The particles followed acquire an appropriate weight to account for the energy of those discarded.

3 The Hadronic Models

The major source of uncertainty in air shower analysis stems from the hadronic interaction models. Soft hadronic interactions, i.e. those with low momentum transfer, are not calculable from first principles, and those are the interactions that are most important for the air shower development. The models, therefore, are always partially phenomenological. At present, high-energy interaction models based on Gribov-Regge theory (GRT) of multi-Pomeron exchange are favoured. They describe collider results rather well and provide a theoretical framework for extrapolation to higher energies. Many models are updated and new and more elaborate ones are formulated. At present, however, only two models reach up to 10^{20} eV. For a first test see, e.g., Heck et al. (2001). The model that seems to describe a variety of experimental findings from $10^{12} - 10^{16}$ eV best is QGSJET (Kalmykov et al., 1997). For this comparison both, AIRES and CORSIKA, use QGSJET for high energy interactions. However, at energies below $\approx$ 100 GeV the high-energy models start to get problems, since particle production is constrained by the small amount of energy available. At energies $\leq$ 10 GeV many measurements on hadron production exist. Cross-sections, multiplicities and particle fractions have been measured for many projectiles and targets. Still there is no detailed theory to model this from first principles, but phenomenological descriptions are fairly detailed. The low-energy model is of great importance, since all signals measured in an EAS experiment are produced by low-energy particles that come from low-energy interactions. Especially particle ratios and energies can be altered by those interactions.

AIRES uses an extension of the Hillas Splitting Algorithm (HSA) (Hillas, 1981) in which the initial energy is split at random into smaller and smaller portions. There are only two free parameters, one regulates the energy fraction at which the splitting occurs (usually uniformly distributed) and one determines the number N of subsequent splittings that are applied. Finally the energy portions are attributed to pions and nucleons. The HSA can be easily configured to approximately emulate the multiplicities and energy distributions of other models. However, cross-sections, transverse momenta distributions and composition of secondaries need to be inserted from outside. While the electromagnetic part of the shower seems to be rather insensitive to the setting of HSA parameters, the number of muons with $E_\mu < 10$ GeV varies by up to 40%.

CORSIKA uses GHEISHA (Fesefeldt, 1985), which was developed for detector simulations at collider experiments and is also used for hadronic interactions within GEANT. GHEISHA was tuned to experimental results over a variety of projectiles and targets in the few-GeV region and, consequently, reproduces cross-sections and particle production rather well. Although problems relating to energy and momentum conservation have been reported, GHEISHA is still a good choice to simulate the low energy portion of hadronic showers.

To cover the energies between the few-GeV range and the region where GRT models work comfortably, models on both sides have to be stretched to their limits. As a compromise, in both CORSIKA and AIRES, the low energy models are used below 80 GeV and the high energy model above. While in CORSIKA the transition between the two models shows a discontinuity at 80 GeV, the HSA in AIRES was tuned to reproduce a multiplicity as averaged over QGSJET and GHEISHA for $E < 80$ GeV. Hence, multiplicities are higher in AIRES by up to $\approx$ 30% as compared to CORSIKA.

4 Comparison and Results

The Auger experiment has two major observables: the longitudinal shower development as measured by the fluorescence light detectors, and the lateral energy density of ground particles as measured by the array of water-Cerenkov detectors. Therefore, the longitudinal shower development, and the ground particle distributions have been analysed. To perform a comparison between AIRES and CORSIKA, with each program 100 vertical proton-induced showers of 2×10^{19} eV have been simulated with thinning at a level of 10^{-7} E_0. Since both programs use the same hadronic interaction model for high energies, this comparison tests only differences due to the low energy hadronic interaction model, the electromagnetic part and the particle propagation.

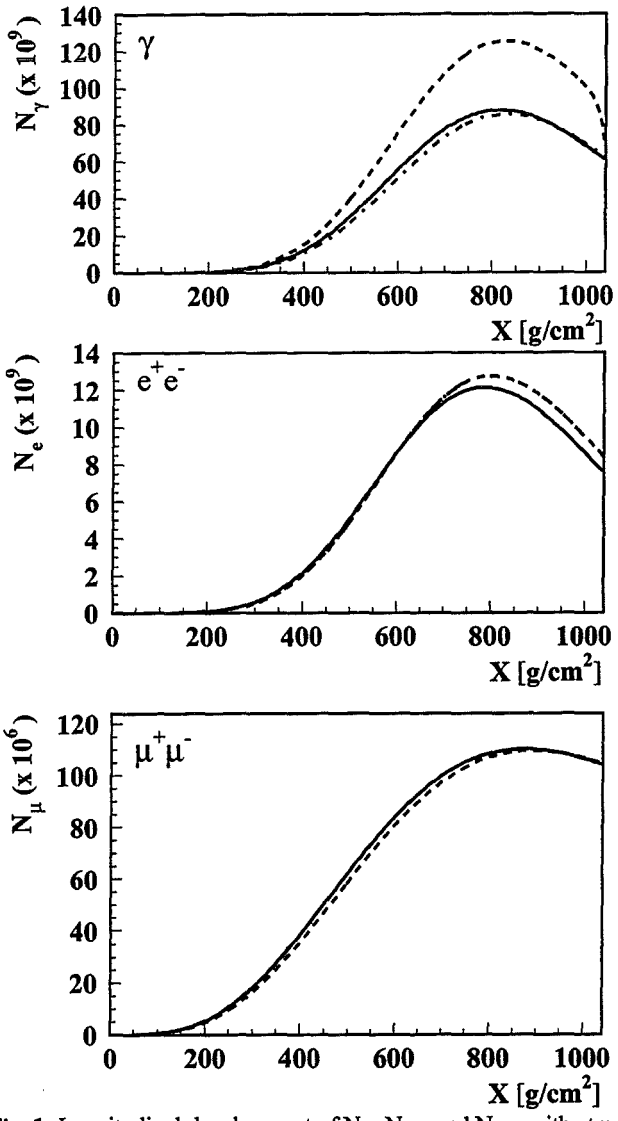

Fig. 1. Longitudinal development of N_γ, $N_{e\pm}$ and $N_{\mu\pm}$ with atmospheric depth. CORSIKA: solid line, AIRES including (excluding) upward going particles: dashed (dot-dashed) line

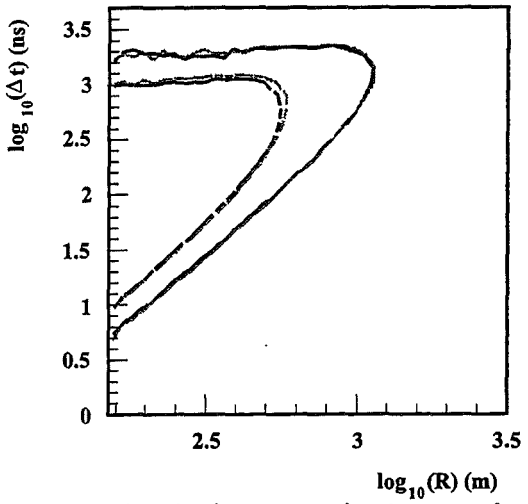

Fig. 2. Particle density contours for photons as function of core distance and arrival time. CORSIKA: black, AIRES: grey.

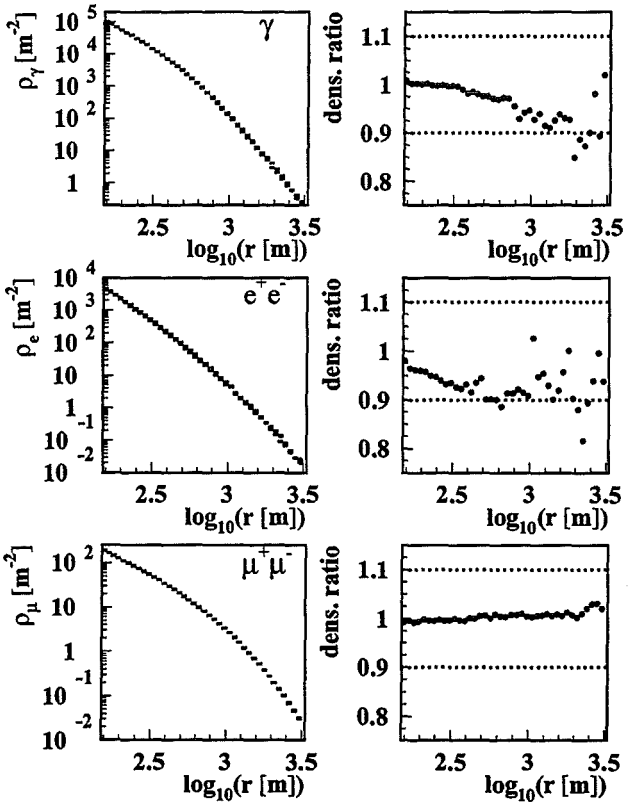

Fig. 3. Lateral particle densities for photons, electrons and muons. Left: particle densities. Right: relative difference between AIRES and CORSIKA as function of core distance.

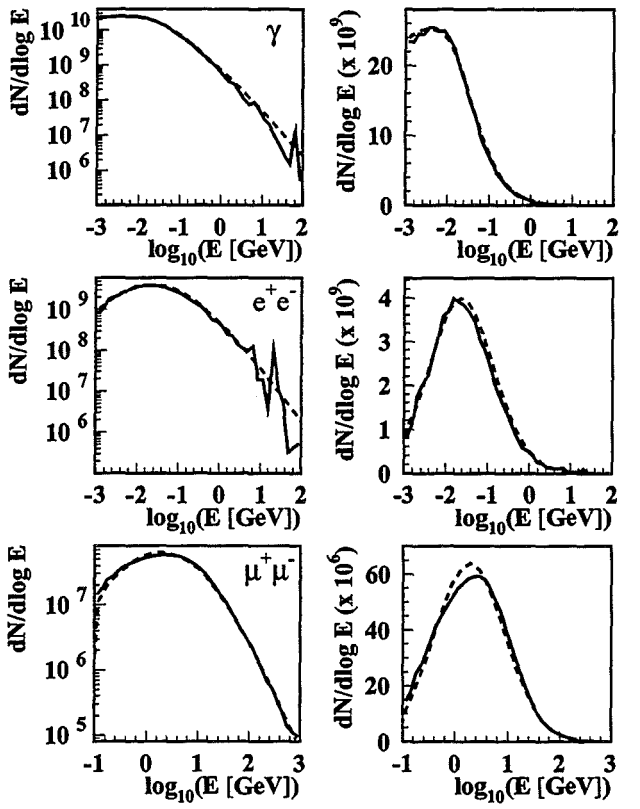

Fig. 4. Energy distributions for photons, electrons and muons. Left: logarithmic abscissa, Right: linear abscissa. CORSIKA: solid line, AIRES: dashed line.

Longitudinal shower development. The fluorescence light yield is determined by the energy deposit in the atmosphere, which, in turn, is dominated by the ionization due the numerous charged particles close to the shower axis. Thus, it relates well to the total number of electrons (and positrons) as a function of depth. This curve, however, is dominated by the high energy model and how it transfers the initial hadronic energy into the electromagnetic channel. The longitudinal shower development is crucially dependent on the inelastic cross-section and the inelasticity of interactions. Thus, low energy hadronic and electromagnetic models impose only second order effects on it. The evolution of $N_{e^+e^-}$ as a function of atmospheric depth agrees well between the two models, the electron numbers at the maximum of the shower development differ by less than 6% (see Fig. 1). The muon number as function of depth, which sensitively depends on details of the hadronic models, agrees even better. The differences at the shower maximum about 3%. There is a large difference apparent in N_γ as function of depth This is due to the fact, that in CORSIKA upward going particles are discarded. Those are predominantly very low energy (sub MeV) photons which contribute less than 2% to the energy deposit in the atmosphere. The disagreement in N_γ vanishes almost completely if AIRES discards the upward going particles (dot-dashed line). At ground level where no upward going particles exist the photon number agrees to about 10%.
Lateral distributions. The Auger array detectors measure the Cerenkov yield of shower particles in water. The array detectors are positioned on a hexagonal grid with 1.5 km distance. This means that rarely detectors will be close to the shower core. Typically, Cerenkov densities will be recorded in the range $r > 300$ m and this is what is checked by simulations. Fig. 3 shows the lateral densities of secondary photons, electrons and muons. The agreement is very good. The density ratios, 2(A-C)/(A+C), on the right emphasise the differences. With core distance CORSIKA tends to predict slightly higher densities, reaching $\approx$ 10% at km distances. The muon densities agree even better. Only at $r \approx 3$ km a deviation of about 3% is observed. Fig. 2 shows the photon distribution as function of core distance and arrival time. As expected, the larger the core distance the later the particles arrive on average. The agreement between AIRES and CORSIKA is excellent. The good agreement between the models, despite the differences on the microscopic level, demonstrates that particle densities at large core distances are mainly determined by $p_\perp$ at particle production and by multiple scattering, and less by details of the low energy models.
Energy distributions. The Cerenkov density in a water tank depends not only on the particle density but also on the energy the particles carry. Electrons and photons are basically absorbed in the water, i.e. deposit all their energy (typically 1-10 MeV), while muons usually penetrate the tank and release an energy of $\approx$ 2 MeV/cm $\times$ their tracklength (typically 240 MeV). Together with the fact that the muon density decreases slower with r than the electron and photon densities, this means that the muon component is dominant at large distances. Also the energy distribution has a more direct relation to the low energy hadronic model than longitudinal or lateral distributions, since the form of the shower is basically determined from the higher energy interactions. Fig. 4 shows the energy distributions for photons, electrons and muons in a linear and a logarithmic display. The general agreement between AIRES and CORSIKA distributions is quite good. The most obvious discrepancies (in AIRES with respect to CORSIKA) are a slight excess of photons and electrons with $E > 10$ GeV, and a deformation of the muon spectrum below 3 GeV, leading to a deficit for muons with $E < 0.5$ GeV and an excess for $0.5 < E < 3$ GeV. Rather likely both discrepancies stem from the low-energy hadronic model, e.g from the higher π yield in the HSA as compared to GHEISHA.
Runtime performance. The comparison showed that AIRES is about 3.5$\times$ faster than CORISKA. For simulations of highest energy showers with minimum thinning, computing time may be the limiting factor and this difference in speed may prove important. Also the particle output of AIRES is smaller than that of CORSIKA. Both programs store 8 words of output information per particle (i.e. particle id, p_x, p_y,p_z, x, y, t, weight). CORSIKA stores each word with 32 bits (4 bytes), while AIRES provides the output in its own compressed format with about 18 bits/word. Also this may be of advantage in case a large shower library is produced and the available disk space is limited.

5 Conclusion

The general agreement between AIRES and CORSIKA in longitudinal, lateral and energy distributions is very good. No discrepancies are found that are beyond the 10% level. The overall systematic uncertainty in EAS simulations is dominated by the high energy hadronic interaction models, which were not tested in this analysis. The main advantage of AIRES over CORSIKA is that it is faster and produces a smaller output. CORSIKA, however, offers a larger variety of elaborate models from specialist authors and, therefore does not need adjustment of model parameters.

Acknowledgements. We are indebted to the staff of the IN2P3 computing centre at Lyon, and to T. Dova for their support. JK and DH acknowledge support for a British-German Academic Research Collaboration from The British Council and DAAD.

References

Auger Collaboration, Auger Project Design Report, FNAL (1997)
Bertou, X., et al., preprint astro-ph/0104452 (2001)
Fesefeldt, H., **PITHA 85/02**, RWTH Aachen, (1985)
Heck, D. et al., **FZKA 6019**, Forschungszentrum Karlsruhe, (1998) see also http://www-ik3.fzk.de/heck/corsika
Heck, D. et al., Proc. 27th Int. Cosmic Ray Conf., Hamburg, Germany, Contribution HE 1.3.1, (2001)
Hillas, A.M., Proc. 17th Int. Cosmic Ray Conf., Paris **8** 193 (1981)
Hillas, A.M., Nucl. Phys. B (Proc. Suppl.) **52B** 29 (1997)
Kalmykov, N. et al., Nucl. Phys. B **52B** 17 (1997)
Nagano, M. and Watson, A.A., Rev. Mod. Phys. **72** 689 (2000)
Nelson, W.R. et al., **SLAC 265**, Stanford Linear Acc. Center (1985)
Sciutto, S.J. preprint astro-ph/9911331 (1999)

Proceedings of ICRC 2001: 741 © Copernicus Gesellschaft 2001

ICRC 2001

Calibration of the Auger Fluorescence Telescopes

H. O. Klages for the Pierre Auger Observatory Collaboration

Forschungszentrum Karlsruhe, Institut für Kernphysik, PO Box 3640, 76021 Karlsruhe, Germany

Observatorio Pierre Auger, Av. San Martin Norte 304, (5613) Malargüe, Argentina

Abstract. Thirty fluorescence telescopes in four stations will overlook the detector array of the southern hemisphere experiment of the Pierre Auger project. The main aim of these telescopes is tracking of EHE air showers, measurement of the longitudinal shower development (Xmax) and determination of the absolute energy of EHE events.

A telescope camera contains 440 PMTs - each covering a 1.5 x 1.5 degree pixel of the sky. The response of every pixel is converted into the number of charged particles at the observed part of the shower. This reconstruction includes the shower/observer geometry and the details of the atmospheric photon production and transport. The remaining experimental task is to convert the ADC counts of the camera pixel electronics into the light flux entering the Schmidt aperture.

Three types of calibration and control are necessary : a) Monitoring of time dependent variations has to be performed for all parts of the optics and for all pixels frequently. Common illumination for all pixels of a camera allows the detection of individual deviations. Properties of windows, filters and mirrors have to be measured separately. b) Differences in pixel-to-pixel efficiency are mainly due to PMT gain and to differences in effective area (camera shadow, mirror size limits). Homogeneous and isotropic illumination will enable cross calibration. c) An absolute calibration has to be performed once in a while using trusted light monitors.

The calibration methods used for the Pierre Auger FD telescopes in Argentina are discussed.

1 Introduction

The southern hemisphere experiment of the Pierre Auger Observatory will contain 1600 particle detectors on a hexagonal grid of 1.5 km spacing covering an area of nearly 60 km x 60 km. On the boundaries of this array observatory stations with optical telescopes are used to watch the atmosphere above the detector array for the fluorescence light from the interaction of the avalanche of secondary particles in the EHE extensive air showers with the Nitrogen molecules.

Simulations show that the number of charged particles produced in an air shower at the maximum of its development depends only slightly on the detailed knowledge of the interaction at extremely high energies, which is limited due to the low energies available at terrestrial accelerators. The determination of the differential energy loss of these particles in their passing through the atmosphere is realized by the measurement of the showers fluorescence light with high sensitivity telescopes. The fluorescence measurements offer the possibility to reconstruct the energy of the primary cosmic ray particle with less ambiguity than it is possible by the determination of the lateral and longitudinal distribution of secondary shower particles only. Hybrid operation with the ground array detector system will yield best accuracy and enable excellent cross calibration.

The determination of the shower/observer geometry is a rather simple first task in the FD reconstruction chain. A more severe problem is the precise knowledge of the fluorescence yield as function of particle type and energy, and of atmospheric density, temperature and composition. Dedicated laboratory measurements of the fluorescence yield have yet to be performed to reduce the existing errors. Another limiting factor is the uncertainty connected with the photon transport in the atmosphere which may depend strongly on the local weather conditions, height above ground, and other variables. Large effort is devoted to the precise determination of atmospheric conditions during the fluorescence measurements. These activities of the Pierre Auger Collaboration are presented in a separate contribution to this conference.

The remaining task is the thorough understanding of detector properties, which may be changing with time. An absolute detector calibration has to be performed in order to enable the conversion of the ADC counts in the data into the photon flux entering the detector. This calibration has to be checked frequently to detect any changes and individual deviations.

Correspondence to: H. O. Klages (klages@bk.fzk.de)

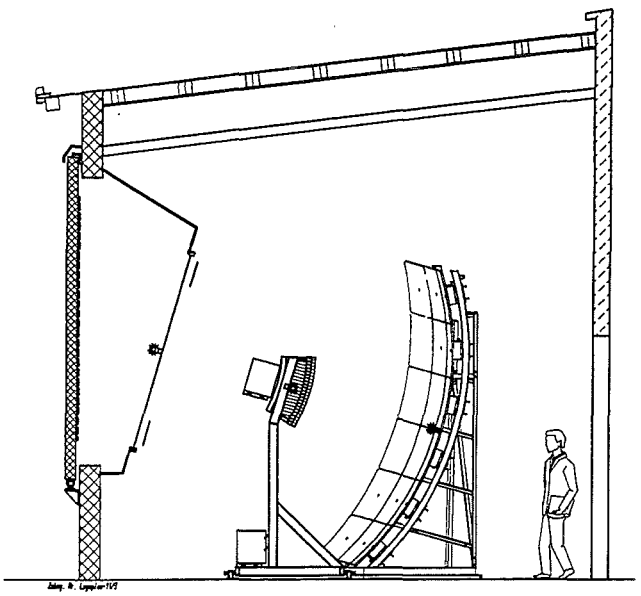

Fig. 1. Layout of the telescope system showing the Xenon flasher positions for 3 types of calibration procedures: a) at the centre of the mirror, b) on both sides of the camera body, and c) on both sides of the centre of the aperture box illuminating a Tyvek reflector on the shutter surface.

2 The telescope system

For the design of the fluorescence telescopes the principle of a wide angle Schmidt camera is adapted. The system contains a large spherical mirror with a radius of curvature of 3.4 m, a pixel camera with 440 PMTs in the focal surface, and a diaphragm with an entrance glass window and an opening of 1.7 m diameter, which can be enlarged to 2.2 m diameter in combination with an annular Schmidt corrector lens. This design is cost effective and combines a large field of view of 30 degree both in elevation and azimuth with a modest resolution which is dominated by spherical aberration. Due to the complete enclosure the telescopes are operated under controlled ambient conditions leading to an improved stability of the PMTs and the electronics. The entrance window will keep dust and moisture away from the optical elements. An external shutter protects the window against environmental influences between the periods of measurements.

Figure 1 shows the principal layout of the telescope system with the external shutter, the aperture box holding the window, UV filter, and corrector ring, the 440 PMT pixel camera, and the large spherical mirror with its central line-of-sight pointing 16 degrees above the horizon.

3 Sources of variations

In the telescope system, pixel-to-pixel differences are present which have to be determined experimentally with high accuracy. In addition, time dependent changes may occur for the overall system or in individual channels. Some sources of these possible variations are listed here.

The UV light transmission through the window, the UV filter, the corrector lens, and the PMT windows as well as the reflectivity of the mirrors and the PMT light guides may decrease slowly with a growing deposit of dust and other dirt on the surfaces and may be much higher again after cleaning.

The transmission through the optical elements depends slightly on the angle of incidence of the photon beam, i.e. on the pixels individual direction of view. The effective area illuminated on the mirror shows this angular dependence to a larger extent. The variation is mainly due to the geometrical acceptance and to the shadow of the camera body and support structure which varies substantially from the center to the corners of the field of view. In addition, at the mirror gaps and edges, a small part of the light may be missing due to the limited mirror size. These effects are of the order of a few percent only and can be simulated quite accurately but should be determined experimentally in any case.

The individual PMTs are slightly different in gain, naturally. 22 phototubes (selected for similar gain) are using a common HV power supply. PMTs are subject to aging effects of the photocathode, the dynodes and the anode structure. These effects on the gain can be dependent on the wavelength of the detected light. Gain changes from HV instabilities or varying load (background light) are reduced considerably by a well designed supply chain. Temperature effects may also occur, but will probably be small due the controlled ambient room temperature.

The conversion factor for the PMT current signal into ADC counts through the electronics chain can be tested completely using an internal test pulse system. However, the full chain should also be checked frequently with calibrated light pulses.

4 Central calibration system

For frequent tests of the detector properties a central light pulse system with fiber optic distribution is used. The light source system consists of a Xenon flash tube with appropriate beam optics, a beam splitter with source monitor, spectral filters for the selection of certain wavelengths, neutral density filters for intensity variation, and a 1:7 optical splitter. It is located in a central calibration room of the observatory building. The computer controlled light source is connected to the Slow Control system of the building. Remote control is the normal way of operation.

Six UV transmitting optical fibers are used for the supply of the 6 telescope systems in the building. The 7th fiber goes to an output light monitor with a calibrated radiometer. In the telescope bays the light is split again to be used with different Teflon diffusers as can be seen in figure 1.

The first diffuser is positioned at the center of the mirrors. It is used to illuminate the full camera. By this method the individual PMTs are tested for stability only. An example of raw data from such full camera test is shown in figure 2. The measurement was made at Rome university during the functionality test of the first PMT camera in March 2001.

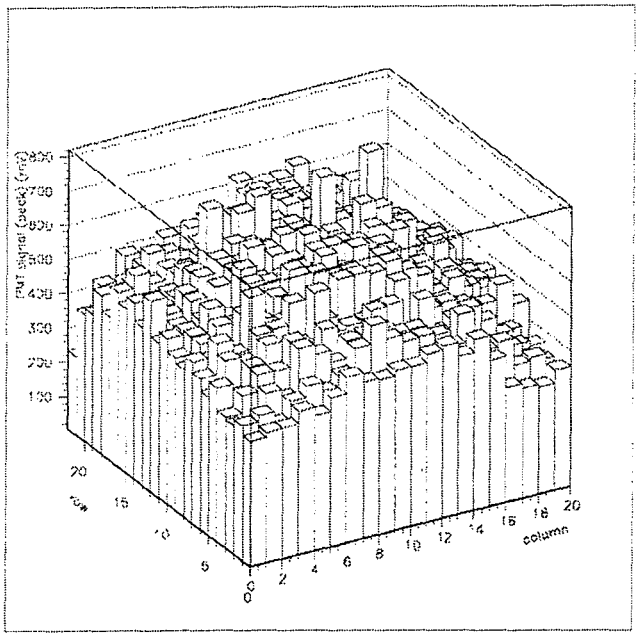

Fig. 2. Test results of illumination of the full PMT camera with a Xenon flasher plus Teflon diffuser at 1.7 m distance. The raw data show the response of the individual PMTs.

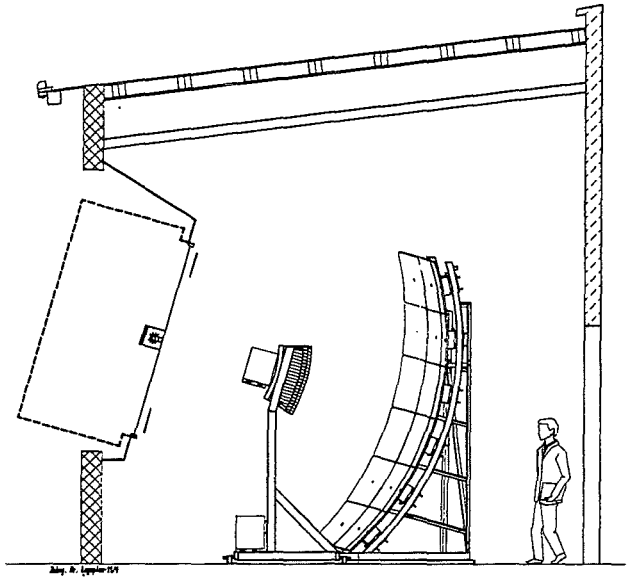

Fig. 3. Absolute calibration of the entire telescope system is performed using a Tyvek/Teflon diffuse reflector outside the entrance window with a stabilized UV light source (LED) and a calibrated light sensor.

Two Teflon diffusers are located at the camera, one on each side, pointing towards both halves of the mirror area. With these diffuse light sources a different illumination of the pixels is achieved and, in addition, also changes of mirror reflectivity can be detected.

Two additional light diffusers are mounted at the sides of the aperture box pointing out towards a large sheet of Tyvek reflector on the inside of the shutter doors. The Tyvek acts as a rather uniform and diffuse reflector for the Xenon light pulses. This third type of camera illumination enables tests of the full light transport through the aperture window, filter and corrector lens, including the effects of the mirrors and the PMT light guides. However, also these will be relative measurements and stability checks only.

In addition to the Xenon flash tubes in special measurements UV emitting LEDs will be used which are commercially available with a narrow line width around 375nm and higher intensity compared to the flasher/fiber system. These LEDs have the advantage of an easily variable pulse length for detailed tests of the camera trigger system. Simultaneous pulsed and DC illumination of the PMTs is possible to study the effects of increasing background light quantitatively.

5 Absolute calibration

To achieve an absolute conversion factor for ADC counts into photon flux for each pixel it is necessary to use a precisely known light source and a stable detection system with calibrated and trusted light sensors. For this purpose at present two different approaches are investigated intensively. The first method is using bright stars as external light sources, well measured by astronomers and the second method relies mainly on the highly accurate absolute calibration of stable and trusted light sensors.

5.1 Star monitor telescope

Bright stars with a well known photon flux in the UV can be used to determine the absolute efficiency of a 10 inch star telescope when the position of the star is nearly vertical and atmospheric uncertainties are rather small. Pointing the telescope immediately to another star in the field of view of a camera pixel enables a comparison of pixel response and star monitor sensitivity. This is quantitatively possible when the effective aperture is known precisely enough for both detectors. A remaining problem is a possible difference in the pixel response to DC and pulsed light which has to be studied carefully with the calibration system. In addition, if the brightness of the star in the field of view is also well known by astronomers, its apparent brightness in the UV at low elevation enables a cross check on the atmospheric monitoring data measured by other means.

5.2 Calibration dome

A sufficiently homogeneous and isotropic local light source has been developed for the absolute calibration of all pixels of the PMT camera. The light output of this device is monitored by trusted light sensors during the measurements and calibrated routinely in a separate experimental set up using light sensors with NIST certification. It consists of a lightweight frame covered with a Tyvek laminate reflector bag. The shape of this "light dome" resembles a large pillbox with about 2.6 m diameter and 1.4 m height. During the

calibration runs (about once every month) it is brought to a telescope bay and mounted outside the aperture window on a support ring in the aperture box as indicated in figure 3. This method of absolute calibration is enabled only by the use of a Schmidt camera design with a well defined optical aperture.

The bottom of the box is closed by a thin Teflon diffuser sheet. The primary light source is a stabilized UV emitting LED with a small Teflon sphere as first diffuser. The forward angles are partly blocked by the monitor detector for the LED, a NIST calibrated Silicon sensor. Trusted PMTs are used for the monitoring of the output of reflected light from the dome. Each time before the dome is brought into operation, an absolute calibration of its photon flux is performed in a separate room and the response of the monitor detectors is determined. By this chain of procedures a total error of less than 5% for the absolute calibration parameters can be achieved.

Relative differences in pixel-to-pixel efficiency can be measured with much better accuracy by several different methods including the dome illumination. Time dependent variations of the full system between the calibration runs and deviations of individual pixels will be determined on the 1% level by the Xenon flasher/fiber system.

Acknowledgements. The systems and methods described in this article were designed and realized by the hard and excellent work of the FD calibration subtask group of the Pierre Auger Collaboration.

Proceedings of ICRC 2001: 760 © Copernicus Gesellschaft 2001

ICRC 2001

Acceptance of the Pierre Auger Southern Observatory fluorescence detector to neutrino-like air showers

C. Kj. Guérard

IEKP-Universitaet Karlsruhe Postfach 3640, D-76021 Karlsruhe, Germany

Abstract. We compute the acceptance of the Southern Pierre Auger Fluorescence Detectors to neutrino-like showers with zenith angles greater than 80° and, based on modern neutrino flux models, estimate that the rate for detection of showers arising from $(\nu_e + \bar{\nu}_e)N$ via charged-current interactions will be $\sim 2/y$ at best above 10 EeV.

1 Introduction

The Pierre Auger Observatory (PAO) will be able to detect EAS originated by 10 EeV and higher energy primaries with zenith angles ranging from 0° to 60°. For more inclined primaries the electromagnetic component becomes dramatically reduced due to the increase in slant atmospheric depth. The column depth encountered by a vertical primary is $\sim$ 1030 g/cm^2 while a primary reaching Earth tangentially will encounter an equivalent column depth of $\sim$ 36,000 g/cm^2. This means that strongly interacting primaries entering Earth's atmosphere with large zenithal angles will have their shower development phase at higher altitudes than vertical or near vertical ones where the lower density encountered will translate into larger hadron mean free path, allowing the mesons from the hadronic cascade to decay at higher energies, resulting in a narrow muon beam reaching ground. On the other hand, EAS initiated by weakly interacting particles or neutrinos (ν-like showers) will occur, if at all, at lower altitudes where the atmospheric density is higher resulting in both direct electromagnetic and muonic components reaching Earth. Despite the fact that neutrino interaction lengths above 10 EeV are still a few orders of magnitude larger than the path length encountered by primaries reaching Earth tangentially it is possible that cosmic ray observatories with $km^3 \cdot sr$ water equivalent acceptances may detect some of these ν-like showers.

For the case of the PAO particle-detector, surface array acceptances have been estimated to be (in units of $km^3 \cdot sr$) 2.3 at 0.1 EeV, 17.2 at 1 EeV, and 43.2 at 10 EeV (see Billoir (1997)) where ν-like showers have been approximated by highly inclined proton showers injected at low altitudes with a fraction of the neutrino energy (for neutral and charged currents giving a non-decaying heavy lepton), or a mixture of proton and photon showers with the full energy of the neutrino (charged currents supplying an electron). Gandhi et al. (1998) have calculated event rates using a variety of models for neutrino fluxes from AGNs, gamma-ray bursters, topological defects, and cosmic-ray interactions in the atmosphere (see figure 1) and have found that for the PAO surface array the highest rates arise from $(\nu_e,\bar{\nu}_e)N$ charged-current interactions in the AGN-M95 model of Mannheim (1995) and AGN-P96 model of Protheroe (1996). These estimates are listed in table 1. (Note that the $\nu_e+\bar{\nu}_e$ flux from the $\pi \rightarrow \mu \rightarrow$ e decay chain is $\sim$ half of the $\nu_\mu+\bar{\nu}_\mu$ flux).

Surface detectors face, however, the great difficulty of discriminating the few ν-like showers from abundant muonic-tale background originating from very inclined hadronic showers (see Ave et al. (2000)).

Model	$E_{sh} \geq 10^8\ GeV$	$E_{sh} \geq 10^9\ GeV$
AGN-M95	6.1	3.3
AGN-P96	8.9	2.6

Table 1. Predicted PAO surface array annual event rates for nearly horizontal air showers induced by $(\nu_e,\bar{\nu}_e)N$ charged-current interactions taken from Gandhi et al. (1998). (The CTEQ4-DIS in this reference has been used).

In this paper we present a study of the PAO Fluorescence Detector (FD) acceptance to deep penetrating exotic primaries. This paper is divided as follows: Firstly we present a review of the Fluorescence technique followed by a brief discussion of hadron initiated HAS, and conclude presenting acceptance and event rates of the Southern Auger FD to ν-like EAS.

Correspondence to: C. Kj. Guérard (guerard@ik1.fzk.de)

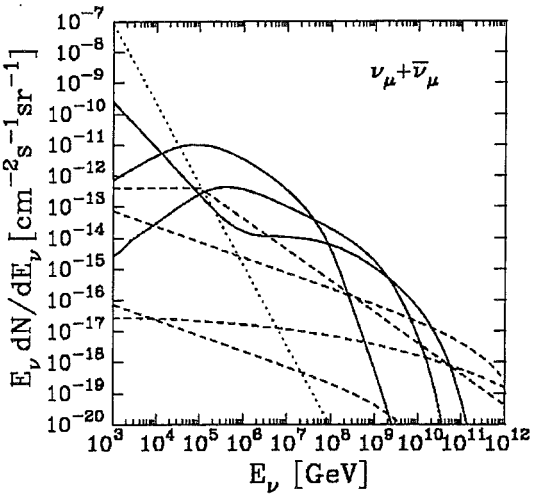

Fig. 1. $\nu_\mu+\bar{\nu}_\mu$ fluxes on Earth's surface. AGN model predictions are in solid lines. At 1 TeV neutrino energy and decreasing in magnitude these are: the pγ model of Mannheim (1995) (AGN-M95), of Stecker et al. (1991) (escaled by 0.3), and of Protheroe (1996) (AGN-P96). Following the same convention, the dash lines correspond to the models of: Waxman and Bachall (1997), Wichoski et al. (1998)(denoted TD-WMB12 and TD-WMB16), and of Sigl et al. (1997). The angle-averaged atmospheric neutrino flux is represented by the dotted line.

2 Fluorescence Technique Review

Fluorescence telescopes detect the optical fluorescence from the ionization of air N_2 molecules when cosmic rays shoot through the atmosphere.

The fluorescence yield has proven to be proportional to charged-particle energy deposit (see Kakimoto et al. (1996)) and can vary from 3 to 5.6 photons/m/charged-particle depending on altitude and temperature, isotropically emmitted, with a spectrum ranging from $\sim$ 280 to 450 nm.

The amount of fluorescence light generated per shower electron is small. However, EHE cosmic rays showering through the atmosphere produce enough electrons that the isotropically emitted fluorescence light can be detected by photomultiplier tubes (PMTs) many km away from its point of emission. As an illustrative example, a 10 EeV primary will produce an EAS with $\sim 6 \cdot 10^9\ e^-$ near shower maximun and will dissipate more than 0.1 J in $\sim 30\mu s$.

After subtracting for atmospheric transmision, camera obscuration, mirror reflectivity, filter transmittance, and PMT quantum efficiency, only a small fraction of fluorescence photons that were within the PMT's FOV at emission, $(3-5)\%$ in average, will be converted into photoelectrons (pes).

The main source of background light comes from the night sky. The HiRes experiment has measured this number to be (filters included) 40 photons/$m^2/deg^2/\mu s$ (27.1 $pe/\mu s$) in the frequency range of interest for fluorescence detection (see Bird et al. (1993)). These numbers can be better understood by saying that fluorescence light can be detected, in average, as far as 30 km or 50 km when produced by 10 EeV or 100 EeV primaries, respectively, with zenith angles up to 60 degrees.

3 HAS induced from strongly interacting particles

Monte Carlo simulations of EAS have shown that for 10^{19} eV primaries and depths exceeding $3,000$ g/cm^2 (equivalent to 70° slant depths) the electromagnetic component is highly attenuated (see Ave et al. (2000)). Thus, depending upon the geometry of a particular shower with respect to the viewing Fluorescence Eyes, we can subdivide very inclined hadronic showers into two categories: showers viewed way past shower maximum, and showers viewed near shower maximum. A complete characterization of both will require a Monte Carlo which is in progress at the moment. However, in what follows, we make some observations.

3.1 Near-horizontal hadronic EAS past shower maximum

Simulations of a 10 EeV proton primary by Ave et al. (2000) have shown that at depths exceeding 70° the N_e is $\sim 7 \cdot 10^6\ e^-$, which is almost three orders of magnitude smaller than the number at shower maximum, and arises mainly from μ-decay. We can make a simple calculation and find out up to what distances will the fluorescence due to the previous electron size trigger a FD PMT. In the case of the PAO-FD a single PMT triggers when the sum of any 10 consecutive ADC (10 MHz) readings gives a total photoelectron (pe) count greater or equal to 48 pe (equivalent to 4σ, with $\sigma = \sqrt{27.1}$ since the PMT anode is AC-coupled). A simple calculation shows that if the camera-shower distance is greater than $\sim$ 1 km there will be no PMT trigger. This will result in short pmt pulses, making such showers difficult to reconstruct. Given that the PAO-FD will look only up to $\sim$ 32° above horizon, these showers will have to pass at a height above gound smaller than $\sim$ 500 m in order to trigger enough PMTs so as to produce a mirror trigger. Aerosol scattering's intrincic difficulty to model shall, in addition, contribute to the difficulty in analysis of any such data.

For higher energy primaries with zenith angles greater than 70° we assume that N_e arises from μ-decay, and that it scales with muon number. Ave et al. (2000) have calculated the number of muons (N_μ) produced by 10 EeV proton and Iron primaries, and have found that N_μ has a power law dependance on primary energy with exponent close to 0.9 (depending on primary composition). If we take an interme-

diate case (mixture of proton and Iron) then we find that very inclined 100 EeV primaries will produce $\sim$ 8.2 times more N_e than a 10 EeV primary. In this case fluorescence light reaching the FD from distances smaller than $\sim$ 3.5 km will trigger pixels (at the 4σ level). The same difficulty to analyze such data applies as in the previous case.

We conclude saying that detecting fluorescence light from highly inclined hadronic primaries (viewed way past maximum) having energies below $\sim$ 100 EeV would be a cumbersome task.

3.2 Near horizontal hadronic EAS near shower maximum

In principle, and depending upon primary energy, combinations of zenith angles and heights above ground -amounting to a $\sim 1,000\ g/cm^2$ equivalent column depth of traversed atmosphere- may produce mirror triggers. Two examples are: 1) horizontal hadrons whose projected trajectory overpasses ground at 30 km height, and 2) hadrons entering earth's atmosphere with a zenith angle of 80 degrees whose projected trajectory would overpass ground at $\sim$ 14 km height. In both cases it is possible that hadrons carrying an energy barely greater than 10 EeV may trigger a mirror. These showers will be very interesting since their observed profiles could be very different from the non highly-inclined ones.

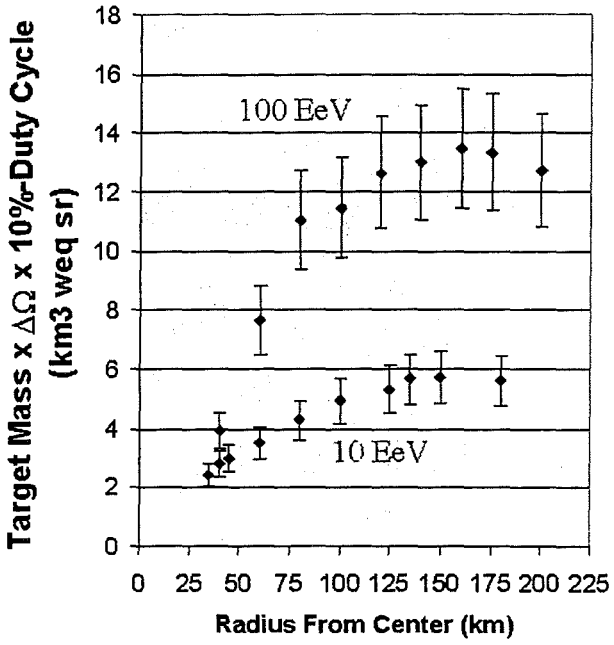

Fig. 2. Acceptance at 10 and 100 EeV shower energy to neutrinos incident in the Earth's atmosphere with zenith angles above 80 degrees.

4 Neutrino-like Showers: Acceptance and Rates

We have performed a Monte Carlo calculation of the Southern Auger FD acceptance to HAS. We have approximated neutrino EAS by proton showers interacting deep in the atmosphere using the Gaisser-Hillas function. In this simulation Cerenkov emission was not taken into account.

We have thrown neutrinos with zenith angles equal or greater than 80 degrees, and have allowed the primary to have its first interaction anywhere within a cylindrical volumen centered directly above the Central Eye. We have varied this volumen and have found that the acceptance (product of target volume and detection efficiency) reaches a maximum (which depends on primary energy) and then falls down (see figure 2).

The fluorescence technique has the great advantage that fluorescence light can be detected very far away from its point of emission, unlike the surface array which is constrained to lateral distances (vertical in the case of HAS) of a few km maximum, (3-5) km, from ground level. Two effects contribute to this: 1. that the atmosphere becomes thinner with altitude making the EAS longitudinal development extend over a larger distance enhancing the probability of detection by an -otherwise- distant eye; and 2) that the horizontal Rayleigh photon mean free path increases greatly with height (from $\sim$ (10$-$20) at ground level km to $\sim$ (100$-$200) km at 15 km a.s.l.). Therefore, the acceptance will largely increase with increasing shower energy. In figure 3 we plot the ground-projected trayectories of all 10 and 100 EeV EAS detected by the PAO central eye.

In figure 4 we plot the fluorescence exposure (Acceptance times duty cycle, taken to be 0.1) calculated in this work, as well as that calculated for the Telescope Array (see The Telescope Array Design Report (2000)). Calculated values are, in units of $km^3\ weq \cdot sr$: 6 and 13 at 10 EeV and 100 EeV, respectively. Despite the increase in acceptance with increasing primary energy, actual detection rates are, however, limited by the FD duty cycle which is $\sim$ 10%. At 100 EeV the calculated FD acceptance still falls below that of the surface array acceptance. For comparison, also shown in figure 2 are the acceptances calculated by Billoir (1997) for the Surface Array. We may note that at 10 EeV the Telescope Array exposure reaches a value of $\sim$ 30 $km^3\ w.eq. \cdot sr$, which is a factor of 5 times larger than that of Auger-South at the same energy. This is in principle, and making a very rough comparison, in accordance with the fact that Telescope Array will employ $\sim$ 5 times as many telescopes as Auger.

We have followed Gandhi et al. (1998) in order to make predictions for the PAO-FD ν-like events. We take their cross sections for $(\nu_e,\bar{\nu}_e)N$ charged-current interactions according to the CTEQ4-DIS parton distribution functions. We find that at 10 EeV the FD will be most sensitive to neutrinos and antineutrinos arising in the AGN-M95 model of Mannheim (1995). At 100 EeV, however, the FD will be more sensitive to neutrinos arising from decays of topological defects in the TD-WM16 model of Wichoski et al. (1998). In either case, the estimated differential event rate is $(1-2)/y$ at best. Predicted are rates summarized on table 2.

Finally, let us mention that random fluctuations of the dark

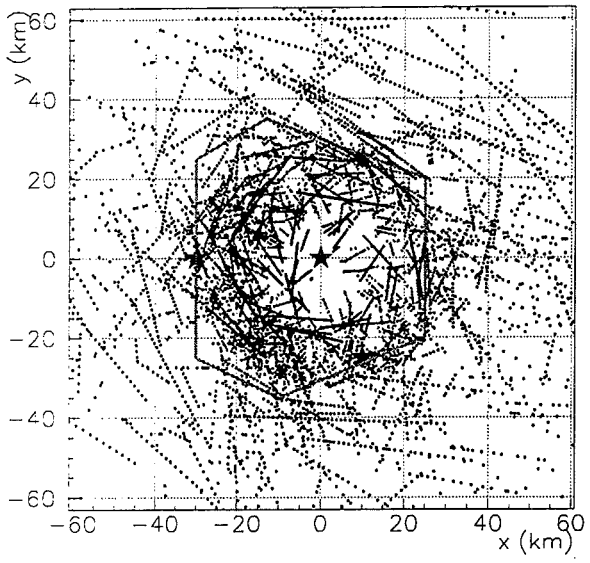

Fig. 3. Central eye sensitivity to ν-like EAS. Ground-projected trayectories of showers triggering the PAO central Fluorescence detector. Black and red dots refer to 100 EeV and 10 EeV primaries, respectively. The position of the 4 Fluorescence detectors are marked with a star. The polygon marks the boundary of the $3,000 km^2$ surface array.

Model	$E_{sh} = 10^{19}\ eV$	$E_{sh} = 10^{20}\ eV$
AGN-M95	≤ 1	
TD-WMB12		≤ 2

Table 2. Estimated PAO-FD annual event rates for horizontal air showers induced by $(\nu_e,\bar{\nu}_e)N$ charged-current interactions. The CTEQ4-DIS was taken form Gandhi et al. (1998)

night background giving rise to fake near-horizontal showers can be discriminated easily: For a pixel trigger threshold set at 4σ (100 Hz pixel trigger rate) and a 4-pixel-fold-coincidence time window of 50 μs the rate of randoms is of the order of 10^{-4} Hz (or one every 3 hours) which is very high. However, if we demand a pixel count of 24 pe above background (4.6 σ) this will lower the rate of random single pixel triggers to 10 Hz, and the rate of 4-fold random coincidences to 10^{-8} Hz (or less than 1 per every 3 years!).

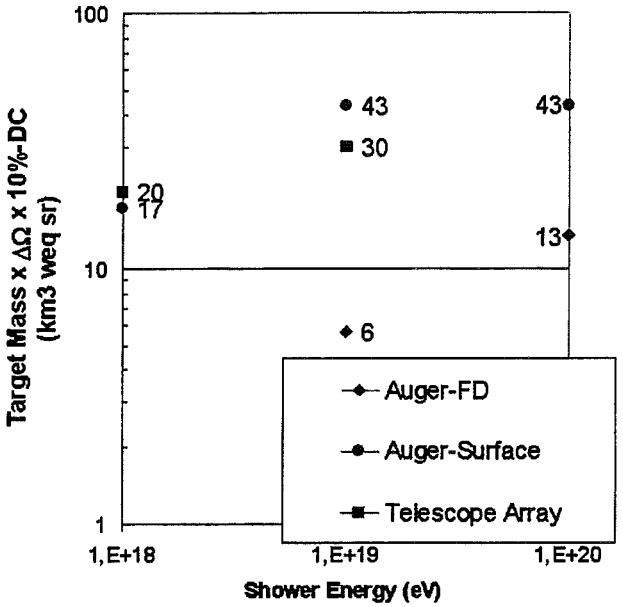

Fig. 4. Acceptance of ground surface array and exposure of Fluorescence detectors to ν-like showers. In the case of the fluorescence detectors, the predicted Telescope Array exposure at 1 EeV and 10 EeV is also shown.

References

M. Ave, R.A. Vázquez, E.Zas, J.A. Hinton and A.A. Watson, In press.

Pierre Billoir "Estimation of the acceptance of the Auger ground detector to quasi horizontal showers induced deeply in the atmosphere", Pierre Auger project note GAP-97-049, available at http://www.auger.org/admin.

K.S. Capelle, J.W. Cronin, G. Parente, and E. Zas, "On the detection of ultrahigh-energy neutrinos with the Auger observatory", Astropart. Phys. 8, 321 (1998) (also as astro-ph/9801313).

R. Gandhi, C. Quigg, M.H. Reno and I. Sarcevic. hep-ph/9807264 6Jul 1998.

D.J. Bird et al., 23rd ICRC (Calgary) 2 (1993) 450.

F. Kakimoto, E.C. Loh, M. Nagano, H. Okuno, M. Teshima and S. Ueno. Nucl. Instr. Meth A 372 (1996) 527-533.

K. Mannheim, Astropart. Phys. 3, 295 (1995).

R. J. Protheroe, astro-ph/9607165.

G. Sigl, S. Lee, D. N. Schramm and P. Coppi, Phys. Lett. B392, 129 (1997).

F. W. Stecker, C. Done, M. H. Salamon, and P. Sommers, Phys. Rev. Lett. 66, 2697 (1991); ibid. 69, 2738E (1992).

The Telescope Array Collaboration Design Report, 19 July 2000.

E. Waxman and J. Bachall, Phys. Rev. Lett. 78, 2292(1997).

U.F. Wichoski, J.H. MacGibbon, and R.H. Brandenberger, "High Energy Neutrinos, Photons and Cosmic Rays from Non-Scaling Cosmic Strings", BROWN-HET-1115 (also as hep-ph/9805419).

Proceedings of ICRC 2001: 443 © Copernicus Gesellschaft 2001

ICRC 2001

Results of EAS characteristics calculations in the framework of the universal hadronic interaction model NEXUS

N. N. Kalmykov[1], S. S. Ostapchenko[2,1], and K. Werner[3]

[1] Skobeltsyn Institute of Nuclear Physics, Moscow State University, Moscow, Russia
[2]Institute fur Kernphysics, Forschungszentrum Karlsruhe, Karlsruhe, Germany
[3]SUBATECH, Universite de Nantes IN2P3/CNRS Ecole des Mines, Nantes, France

Abstract. An extensive air shower (EAS) calculation scheme based on cascade equations and some EAS characteristics for energies 10^{14}–10^{17} eV are presented. The universal hadronic interaction model NEXUS is employed to provide the necessary data concerning hadron-air collisions. The influence of model assumptions on the longitudinal EAS development is discussed in the framework of the NEXUS and QGSJET models. Applied to EAS simulations, perspectives of combined Monte Carlo and numerical methods are considered.

1 Introduction

The simulation of the extensive air shower development and the reliability of model predictions are of prime importance in studies of super-high ($> 10^{15}$ eV) energy cosmic rays. Indeed, the reconstruction of primary particle characteristics by measuring EAS characterictics implies the knowledge of the interaction model whereas the models used are phenomenological ones and their validity is open to question above the energy range attained by modern colliders (about 10^{15} eV for equivalent fixed target energy). It should be noted that a considerable gap exists between this upper limit and the energy region 10^{20}–10^{21} eV which is presently the object of much attention (see AUGER Collaboration (1999)).

It would not be an overestimation to say that the most popular technique to provide necessary theoretical predictions of EAS characteristics is the Monte Carlo (MC) method which may be realized in two main variants. The first one (employed in the program CORSIKA (Heck et al., 1998)) uses the direct MC simulation down to the lowest particle energies under consideration. Such an approach produces results that can be easily compared with experimental data including not only average EAS characteristics but their fluctuations as well. But it proves to be very time-consuming and this serious drawback prevented to use the direct MC above 10^{17} eV. Even at lower energies there are difficulties with simulation of sufficient number of events. The alternative is to use so-called "thinning" (Hillas, 1981) – multilevel sampling of secondary branches of the cascade where one ignores the majority of secondary particles and follows the fate of a few of them introducing proper weights. Reducing greatly the simulation time, this procedure distorts fluctuations and comes up with some other problems (Kobal et al., 1999).

But there exist effective methods to calculate EAS development using the combination of MC and numerical techniques. As all essential contributions to EAS fluctuations come from the initial part of the cascade process i. e. from the fluctuations due to the behaviour of the most energetic particles, it is sufficient to employ explicit MC simulations only for particles with energies above some cutoff $E_{\rm thr} = kE_0$ ($k \approx 10^{-2}$–10^{-3}, E_0 is the primary energy). Contributions of secondary particle cascades of smaller energies may be accounted for in average using numerical solutions of corresponding cascade equations. This approach was, for example, successfully used in (Kalmykov et al., 1997) as well as by many other researchers in the last few decades.

Recently a new hadronic interaction model NEXUS has been proposed (Drescher, 2001) which has much more solid theoretical basis than presently used models such as VENUS (Werner, 1989) or QGSGET (Kalmykov et al., 1997). This new model enables one to obtain more reliable predictions at super-high energies but it is more complicated and therefore more time-consuming. So the problem of the EAS simulation strategy assumes a greater importance.

In this paper we consider the calculations of EAS characteristics in the framework of the NEXUS model and discuss the EAS simulation strategy.

2 Solving cascade equations in the framework of the NEXUS model

The NEXUS model treats cross-section and particle production calculations consistently considering energy conserva-

Correspondence to: kalm@eas10.eas.npi.msu.ru

tion strictly in both cases. Hard processes are introduced in a natural way without any unphysical dependencies. The set of model parameters is adjusted so as to fit basic data in proton-proton and lepton-nucleon scattering as well as in electron-positron annihilation. All that ensures a much safer extrapolation to super-high energies when compared to other models but at the same time the necessity to accelerate EAS simulations becomes more pronounced.

Calculations of average EAS characteristics in the framework of the NEXUS model were carried out in (Bossard et al., 2001). Using the system of hadronic cascade equations (see Gaisser (1990)) one describes average hadronic cascades by the differential energy spectra $h_n(E, X)$ of hadrons of type n with energy E at depth X. The corresponding system of integro-differential equations for $h_n(E, X)$ may be reduced (after discretizing over energy) to the system of linear differential equations that can be solved by standard methods. Our approach is based on the same ideas as in (Dedenko, 1965; Hillas, 1965) but with some improvements (Kalmykov and Motova, 1986) which enable to avoid too small steps when integrating over the depth. The system used incorporates nucleons (and anti-nucleons), pions and kaons. The inclusive spectra of secondaries of type n produced in interactions of primaries of type m were calculated using the MC technique and a special smoothing procedure was applied to eliminate the influence of statistical fluctuations. Other EAS characteristics (electron and muon numbers) were computed as functionals from $h_n(E, X)$ (see Bossard et al. (2001)). The method employed enables to obtain average EAS characteristics within $\sim$ 1% accuracy. As the number of discretized energies is propotional to $\ln E$ the computing time appears to be quite negligible when compared to the direct MC approach. It is worth noting that in some cases the knowledge of the average EAS behavior is quite sufficient to analyze experimental data or to compare predictions of different models. Thus calculated shower maximum depthes were compared with experimental data to obtain the information on the primary mass composition near the knee (see Bossard et al. (2001)).

3 Comparison of NEXUS and QGSJET predictions

Some dependencies of EAS characteristics on the depth for a set of primary energies were presented in (Bossard et al., 2001). It is also of interest to compare the predictions of the NEXUS and QGSJET models as the latter one was frequently used in calculations at super-high energies. The results of this comparison are shown in Fig. 1 for electron and muon ($E_\mu > 1$ GeV) numbers at sea level and in Fig. 2 for shower maxima. Label 1 corresponds to the assumption that only inclusive spectra of hadrons are different whereas cross-sections are the same as in the QGSJET model (see Kalmykov et al. (1997)). Label 2 marks results obtained with different cross-sections. (The NEXUS model predicts higher values of cross-sections at energies above 10^{14} eV.) As there is no essential discrepancy between QGSJET and NEXUS predictions at 10^{14}–10^{17} eV it is hardly possible to expect any significant divergence in conclusions derived if one replaces one model by another. It follows from Fig. 1 that the exponent $\alpha_{e(\mu)}$ in the traditional fit

$$\overline{N}_{e(\mu)} = K_{e(\mu)} E^{\alpha_{e(\mu)}}$$

does not differ more than by 0.02 for these two models. Calculations have shown that only for hadron numbers (in case of different cross-sections) expected deviations reach 0.03–0.04.

But variations discussed may increase as energy increases above 10^{17} eV.

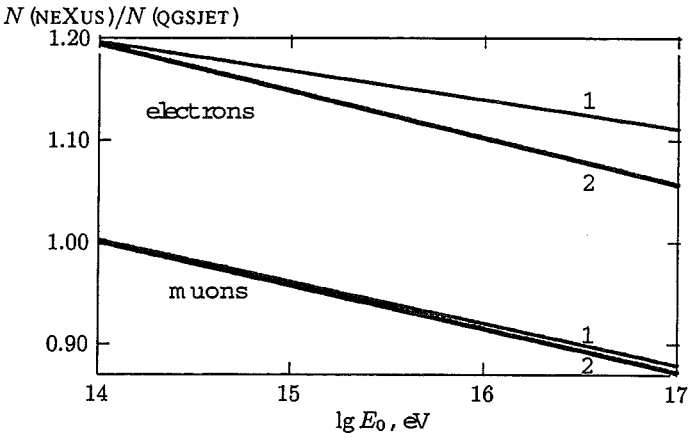

Fig. 1. NEXUS to QGSJET ratio for electron and muon numbers at sea level vs. primary energy. 1—cross-sections are identical, 2—cross-sections are different.

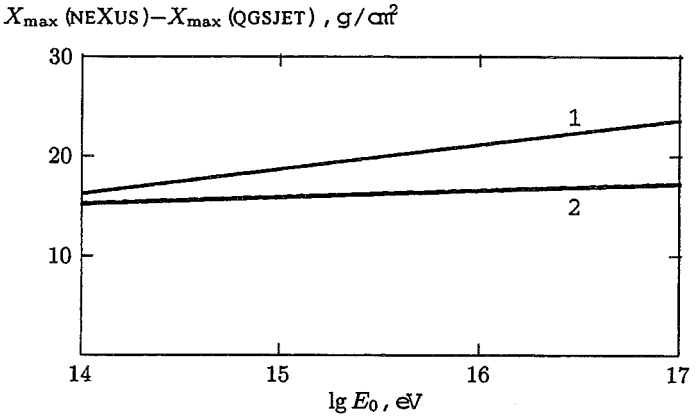

Fig. 2. Difference of NEXUS and QGSJET shower maxima vs. primary energy. 1—cross-sections are identical, 2—cross-sections are different.

It may be also of interest to explore how the distribution of the projectile energy between hadrons and gammas influences on EAS characteristics. Fig. 3 demonstrates NEXUS model predictions for some EAS characteristics at sea level. The value of K_γ incorporates results of π^0 and η decays

and also some minor contributions. The influence of K_γ enhancement is rather well pronounced for hadrons ($E_h >$ 50 GeV) and muons but may be neglected for electrons. It is essential to note that there are practically no variations of shower maxima due to K_γ enhancement.

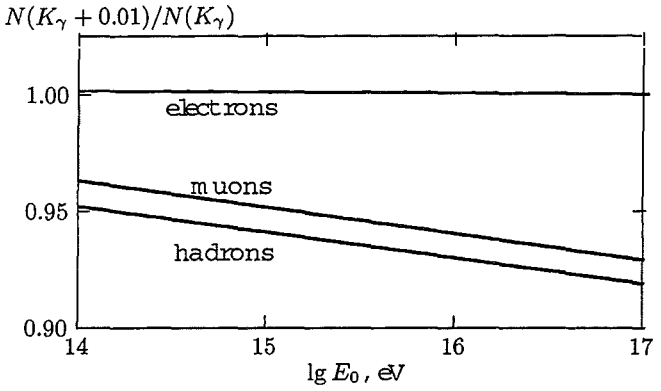

Fig. 3. Infuence of K_γ enhancement on electron, muon, and hadron numbers at sea level.

4 Perspectives of simulation strategy

Although calculations of average EAS characteristics can provide valuable information it is highly desirable to have at hand a sufficiently fast procedure which accounts for EAS fluctuations properly. It is possible to split such a procedure into well separated blocks.

The first one is the solution of the cascade equations for different initial conditions. This block should produce spectra of shower particles at given observation levels as function of their types, energies, angles, transverse displacements and time delays. The results must be tabulated. It is essential to generalize cascade equations and their solutions from one-dimensional case described in (Bossard et al., 2001) to full three-dimensional cascades. In doing so one can employ the results of the standard ajoint equation approach (see Lagutin (1993)) to treat electron-photon cascades.

The second block is the explicit MC simulation of the high energy part of the cascade (for particles with energies $E_{\rm thr} < E < E_0$) using the NEXUS model. It is important that one may neglect scattering angles and employ one-dimensional procedure as $E_{\rm thr}$ is sufficiently high. The calculation of EAS components for individual showers is realized by summing up all partial contributions. As a rule these contributions should be obtained by interpolation from the tables but, in principle, it is possible to solve cascade equations for random initial conditions representing individual showers.

It is also possible to employ pretabulated MC results for low energy cascades (below some value $E_{\rm min} \ll E_{\rm thr}$). These cascades should be simulated as in the CORSIKA program. The comparatively small time needed for simulations of low energy cascades could ensure necessary statistics of individual histories and thus achieve precise enough description of the distribution tails.

A number of additional blocks may be introduced to provide calculations of necessary EAS characteristics (e. g. fluorescence and cherenkov light).

Acknowledgements. This work was partly supported by the Federal Scientific–Technical Program for 2001 year "Research and design in the most important directions of the science and technique of the civil applications", subprogram "High energy physics" and RFBR grant 99-02-16250.

References

AUGER Collaboration, The Pierre Auger Observatory Design Report, 1999, http:/www.auger.org

Bossard, G. et al., Phys. Rev. D, 63, 054030, 2001.

Dedenko, L.G., in Proc. 9-th Int. Cos. Ray Conf., London, Vol. 2, p. 622, 1965.

Drescher, H.J. et al., Phys. Rep. (in print), hep-th/0007198.

Gaisser, T.K., Cosmic Rays and Particle Physics, Cambridge University Press, Cambridge, England, 1990.

Heck, D. et al., FZKA 6019, Forschungszentrum Karlsruhe GmbH, 1998.

Hillas, A.M., in Proc. 9-th Int. Cos. Ray Conf., London, Vol. 2, p. 758, 1965.

Hillas, A.M., in Proc. 17-th Int. Cos. Ray Conf., Paris, Vol. 8, p. 193, 1981.

Kalmykov, N.N. and Motova, M.V., Yadernaya Fizika (Rus), 43, 630, 1986.

Kalmykov, N.N., Ostapchenko, S.S., and Pavlov, A.I., Nucl. Phys. B, (Proc. Suppl.)52B, 17, 1997.

Kobal, M. et al., in Proc. 26-th Int. Cos. Ray Conf., Salt Lake City, Vol. 1, p. 490, 1999.

Lagutin, A.A., in Proc. of RIKEN Int. Workshop on Electromagnetic and Nuclear Cascade Phenomena in High and Extremely High Energies, RIKEN, Nishima Hall, Japan, p. 309, 1993.

Werner, K., Phys. Rev. D, 39, 780, 1989.

Proceedings of ICRC 2001: 446 © Copernicus Gesellschaft 2001

ICRC 2001

Very high energy hadronic interactions - solution of the main puzzle

S. Ostapchenko[1,2], T. Pierog[3], and K. Werner[3]

[1]Forschungszentrum Karlsruhe, Institut für Kernphysik, Karlsruhe, D-76021 Germany
[2]Moscow State University, Institute of Nuclear Physics, Moscow, 119899 Russia
[3]SUBATECH, Université de Nantes – IN2P3/CNRS – Ecole des Mines, Nantes, France

Abstract. A consistent treatment of hadronic and nuclear interactions at high energies is developed. A special attention is paid to the correct description of energy-momentum sharing processes in multiple scattering collisions. Also we stress the necessity to consider contributions of so-called enhanced Pomeron diagrams, which provide important screening corrections to the interaction mechanism. The latter ones appear to dominate the interaction process at very high energies and allow to solve many consistency problems of present hadronic interaction models, in particular, the seeming contradiction between the realistic parton structure functions, measured in deep inelastic scattering experiments, and the energy behavior of hadronic cross sections.

1 Introduction

Nowadays nobody would question the importance of reliable hadronic interaction models in the physics of high energy cosmic rays. Currently they are used to project new air shower arrays, to make interpretations of experimental data, to analyze different astrophysical hypothesises. All those topics significantly wenf forward since microscopic Monte Carlo models, developed in the Gribov-Regge framework, like VENUS (Werner, 1993), QGSJET (Kalmykov and Ostapchenko, 1993; Kalmykov *et al.*, 1994, 1997), DPMJET (Ranft, 1995), as well as the alternative approaches – HDPM (Capdevielle, 1992), MOCCA (Hillas, 1995), and SIBYLL (Fletcher *et al.*, 1994) – have become available for applications in cosmic ray physics and went into a common use, mainly due to their implementation in the CORSIKA air shower simulation program (Heck, 1998), and later on – in the AIRES code (Sciutto, 1999).

Naturally arises a question on the reliability of the available models in the region of extremely high interaction energies. The analysis showed that calibrating the models on the hadronic collider data along does not provide a unique possibility for their extrapolation towards very high energies (Kalmykov *et al.*, 1999), which explains to a great extent the existing differences between model predictions (Heck, 2001). On the other hand, there exist serious theoretical inconsistences in the very construction of presently available models.

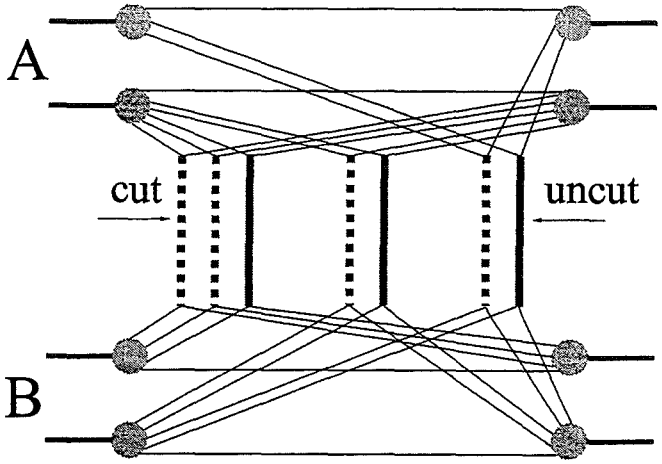

Fig. 1. Typical contribution to the nucleus A – nucleus B interaction cross section; cut and uncut Pomerons are shown as dashed and smooth thick lines correspondingly.

Recently we have developed a principally new universal model NEXUS (Drescher *et al.*, 2001). The universality of the model allowed to test its main algorithms and to tune reliably its parameters on the basis of a combined description of different reactions, including hadronic and nuclear collisions as well as electron-positron annihilation and deep inelastic lepton-proton scattering processes (Drescher *et al.*, 1999). This ensured much more reliable model extrapolation towards very high energies. Besides that, we have found for the first time satisfactory solutions for many severe consistency problems of the present models, like the correct treatment of the energy-momentum sharing mechanism in multiple scattering processes (Hladik *et al.*, 2001) as well as the

Correspondence to: S. Ostapchenko (serguei@ik3.fzk.de)

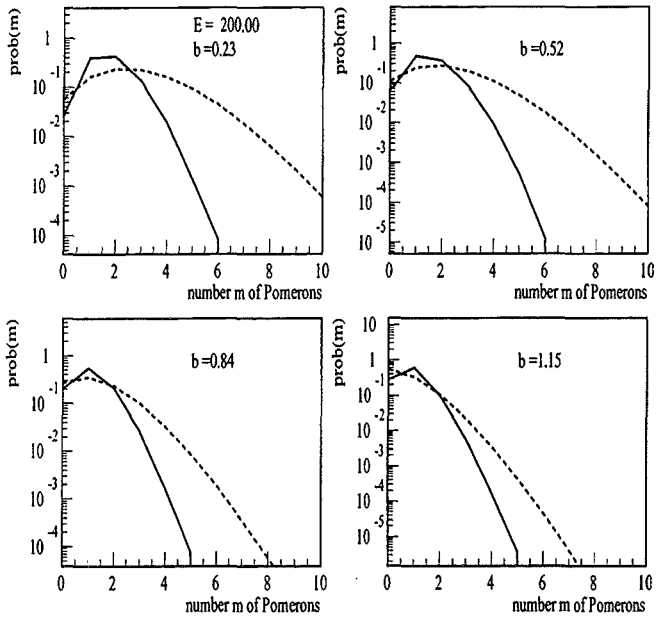

Fig. 2. Distribution of the number of Pomerons in proton-proton scattering at c.m. energy $\sqrt{s} = 200$ GeV/c for different impact parameters b. We show the results of a full simulation (solid curves) as well as the Poissonian distribution obtained by ignoring the energy conservation (dashed curves).

account for the contributions of Pomeron-Pomeron interactions (Drescher *et al.*, 2001; Ostapchenko *et al.*, 2001). The latter provide very important screening corrections to the interaction mechanism and appear to be of crucial importance for model applications at very high energies. In the current work we discuss some of these most recent developments and present the obtained preliminary results which illustrate their effect on the important interaction characteristics.

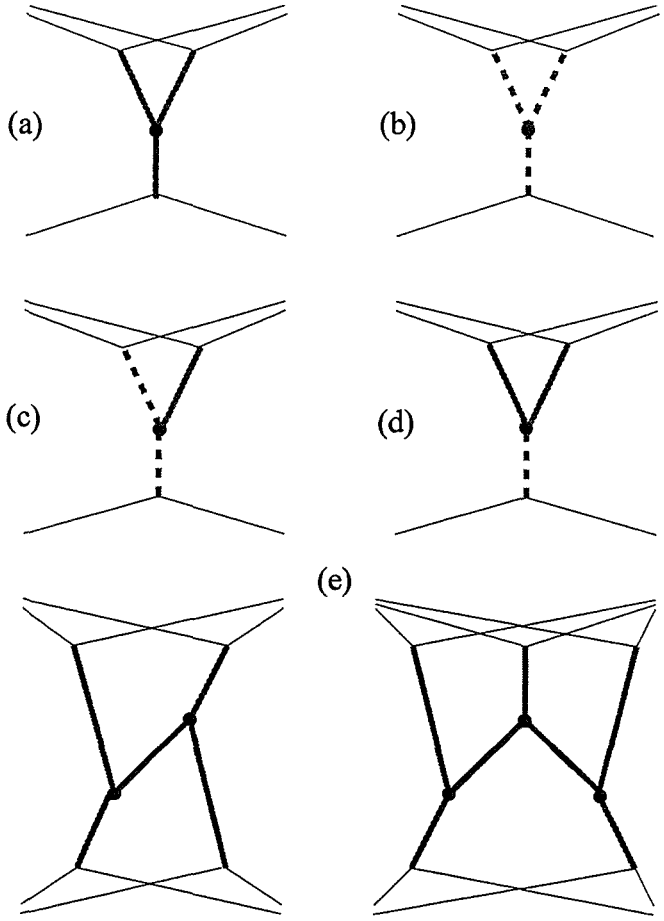

Fig. 3. The lowest order Pomeron-Pomeron interaction diagram – (a) and its different cuts: cut Pomeron "fusion" – (b), screening correction to one-cut-Pomeron process – (c), and high mass diffraction process – (d). Also shown some contributions of higher orders – (e). Cut and uncut Pomerons are represented by dashed and smooth thick lines correspondingly.

2 The model

In NEXUS model (Drescher *et al.*, 2001) high energy hadron-hadron (hadron-nucleus, nucleus-nucleus) interactions are treated within the Gribov-Regge framework (Gribov, 1968, 1969) as multiple scattering processes consisting of many individual elementary interactions happening in parallel, as shown schematically in Fig. 1. Each individual interaction is represented by a long microscopic parton cascade which mediates the scattering of parton constituents (quarks and antiquarks) of the interacting hadrons (nuclei) on each other. Correspondingly, one has to consider two main contributions to these elementary interactions: the nonperturbative "soft" scattering - when all the partons in the cascade are characterized by small virtualities $Q_i^2 < Q_0^2$, with $Q_0^2 \simeq 2$ GeV^2 being a reasonable scale for the perturbative quantum chromodynamics (QCD) being applicable, and the "semihard" interaction - when at least a part of this cascade develops in the perturbative region $Q_i^2 \geq Q_0^2$.

The first contribution is described phenomenologically as the soft Pomeron exchange (Werner, 1993), whereas in the second case we use the soft Pomeron description for the nonperturbative part of the parton evolution ($Q_i^2 < Q_0^2$) and treat the "hard" part ($Q_i^2 > Q_0^2$) using the QCD techniques - thus arriving to the concept of the "semihard Pomeron" (Ostapchenko *et al.*, 1997; Drescher *et al.*, 2001). The sum of the two contributions constitutes the "generalized Pomeron" which works as the basic ingredient for the construction of a general Gribov-Regge scheme.

An important feature of the Gribov's approach is that in each hadronic collision one has to consider both real elementary interactions, which result in the production of secondary particles and which are described as so-called cut Pomerons [1], shown symbolically as the dashed thick lines in Fig. 1, and virtual interactions, shown as the smooth thick lines in the Figure, when hadron constituents scatter elastically on each

[1] Cutting procedure amounts to replace the Pomeron exchange amplitude by its absorptive part, as the sum of contributions of any number of intermediate on-shell hadrons.

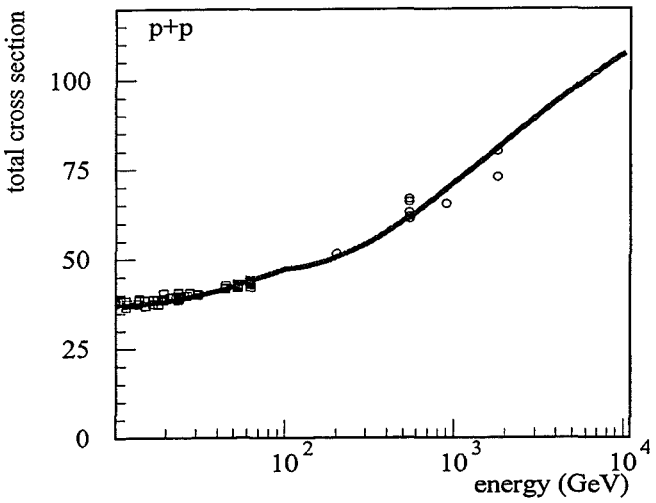

Fig. 4. The calculated total proton-proton interaction cross section as a function of the c.m. energy $\sqrt{s}$ – full curve; the points represent experimental data (Caso *et al.*, 1998).

other and the intermediate parton cascades recombine back to the initial hadrons. Those virtual contributions provide important screening corrections to the process and finally assure the unitarity of the scheme.

2.1 Energy-momentum sharing

To calculate both the interaction cross sections and the probabilities for different configurations of the hadronic (nuclear) collisions, as well as to simulate individual interaction events, down to the production of final secondary hadrons, one has to account for the sharing of the initial energy-momentum between many elementary scattering processes, both real and virtual, so that each process disposes only a part of the total initial energy (Braun, 1990; Abramovskii and Leptoukh, 1992). The solution of this problem has been provided for the first time in our work (Hladik *et al.*, 2001), allowing to develop a fully self-consistent treatment of the reactions, both concerning cross section calculations and particle production simulation. At high energies, the account for this mechanism results in a dramatic reduction of the average number of elementary interactions per hadronic (nuclear) collision – Fig. 2. This effect is especially strong in central nucleus-nucleus interactions.

2.2 Enhanced Pomeron diagrams

One of the most recent and very important developments in NEXUS model is the treatment of Pomeron-Pomeron interactions (Ostapchenko *et al.*, 2001), described by so-called enhanced Pomeron diagrams, with the lowest order graph depicted in Fig. 3a. One naturally encounters such contributions at high energies, when the number of elementary interactions, happening in hadron-hadron and, especially, nucleus-nucleus collisions, becomes large and the corresponding microscopic parton cascades start to overlap and to interact with each other.

Table 1. The calculated diffractive proton structure function, $x_{\mathrm{P}} F_2^{D(3)}\left(x_{\mathrm{P}}, \beta, Q^2\right)$, for diffractive scattering via $\gamma^* p \rightarrow XN$ for $Q^2 = 8$ GeV^2 and for the mass of the nucleonic system N $M_N < 5.5$ GeV. Experimental data are from ZEUS collaboration (Breitweg *et al.*, 1999).

x_{P}	β	$x_{\mathrm{P}} F_2^{D(3)}$ (NEXUS)	$x_{\mathrm{P}} F_2^{D(3)}$ (exp.)
0.00871	0.062	0.0304	0.0288±0.0018
0.00580	0.062	0.0318	0.0312±0.0018
0.00391	0.062	0.0324	0.0328±0.0020

There, one has to take into account not only interactions of real cascades - cut Pomerons, shown in Fig. 3b and generally known as string fusion, but also an important process of elastic interaction between a real and a virtual cascades - Fig. 3c, which provides screening corrections of a new type and modifies considerably the final spectra of secondary hadrons, as well as the contribution of high mass diffraction dissociation, represented by the diagram of Fig. 3d.

Naturally, one can not restrict himself with just lowest order graphs discussed above and has to include all important diagrams of higher orders for a given interaction energy of interest, with some examples shown in Fig. 3e. For example, considering diagrams with four Pomeron-Pomeron vertexes, we had to deal with nearly a hundred contributions of that type.

The main parameter which controls the magnitude of those contributions is the value of the Pomeron-Pomeron interaction vertex, the so-called triple-Pomeron coupling, $r_{3\mathrm{P}}$. It is remarkable that one can reliably fix this coupling using the information on the diffractive structure function of the proton $F_2^{D(3)}\left(x_{\mathrm{P}}, \beta, Q^2\right)$ [2], measured by ZEUS collaboration (Breitweg *et al.*, 1999) – see Table 1.

The main effects of the described mechanism are:

- suppression of hadron-hadron interaction cross sections at high energies;
- suppression of secondary hadron multiplicity, especially, in central nucleus-nucleus collisions;
- serious modifications of final particle spectra, especially, for central collisions of asymmetric systems;
- significant increase of fluctuations of secondary hadron multiplicity.

[2] In the standard interpretation of the diffractive process by means of the Pomeron exchange x_{P} corresponds to the momentum fraction of the proton carried by the hadronic system X into which the virtual photon dissociated and β is the momentum fraction of the struck quark within this system.

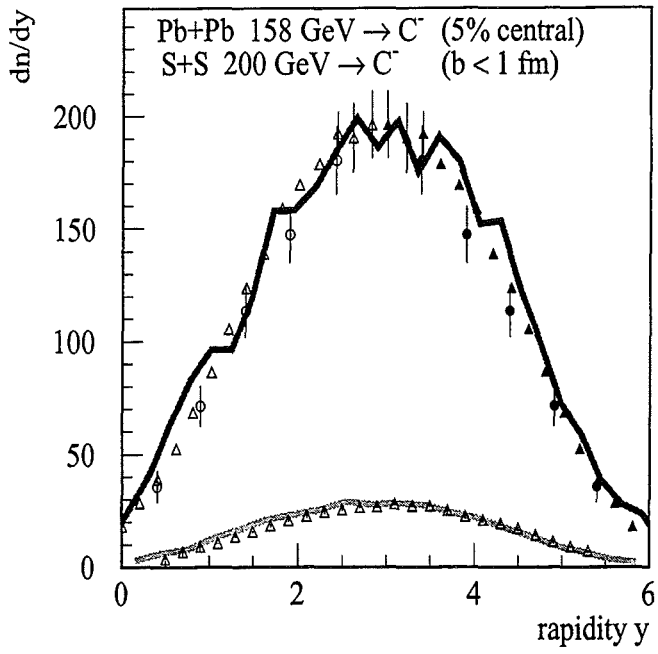

Fig. 5. The calculated rapidity distributions of negatively charged particles for $Pb - Pb$ collision at $\sqrt{s}$=158 GeV/c and for $S - S$ collision at $\sqrt{s}$=200 GeV/c – full curves; the points represent experimental data (Alber *et al.*, 1998; Appelshauser *et al.*, 1999).

The first point needs a special stressing. Our approach allows to obtain a consistent description of hadron-hadron interaction cross sections - Fig.4, while being in consistency with the realistic proton structure functions, measured in deep inelastic scattering experiments. Thus, we can avoid the invention of any artificial energy-dependent cutoff for the QCD evolution (see, for example, Bopp *et al.*, 1994) - the recipe which would rule out any predictive power of the perturbative QCD for high energy hadronic interactions. The key point here is that the inclusion of enhanced diagrams affects hadronic cross sections to much greater extent than it does for partonic distributions. This can be illustrated, for example, by the contributions of diagrams shown in Fig. 3e, which appear to be the dominant ones in hadron-hadron interactions at high energies but which do not give any contribution to the structure functions (Ostapchenko *et al.*, 2001).

Both the suppression of secondary hadron multiplicity and the modifications of final particle spectra come from the interplay between different cuts of the enhanced diagrams, known as the violation of Abramovskii-Gribov-Kancheli cancellations (Abramovskii *et al.*, 1974) for the secondary hadron spectra (Kaidalov, 1991). In particular, our scheme allows to obtain a consistent description of secondary hadron multiplicity in central heavy ion collisions - Fig. 5, which was a severe problem for the most of currently available models.

3 Conclusions

We presented the new hadronic interaction model NEXUS and discussed its most important features as well as illustrated their importance for the main characteristics of hadronic and nuclear interactions. The theoretical approach realized in this model is currently the only one which takes systematically into account all important microscopic interaction mechanisms and allows to obtain a self-consistent description of hadron-hadron, hadron-nucleus, and nucleus-nucleus collisions. In particular, we showed that the consistent treatment of Pomeron-Pomeron interactions is of crucial importance for the correct description of high energy hadronic and nuclear reactions.

The extension of the model validity till the highest cosmic ray energies should provide a reliable tool for the investigation of the composition of Ultra High Energy Cosmic Rays.

Acknowledgements. One of the authors (SO) would like to thank H. Blüemer, D. Heck, and T. Thouw for fruitful discussions and interest to the work.

References

Abramovskii, V. A., Gribov, V. N. and Kancheli, O. V., Sov. J. Nucl. Phys., 18, 308-317, 1974.
Abramovskii, V. A. and Leptoukh, G. G., Sov. J. Nucl. Phys., 55, 903-905, 1992.
Alber, T. *et al.*, NA35, Eur. Phys. J. C, 2, 643-659, 1998.
Appelshauser, H. *et al.*, NA49, Phys. Rev. Lett., 82, 2471-2475, 1999.
Bopp, F. W. *et al.*,Phys. Rev. D, 49, 3236-3247, 1994.
Braun, M.A., Sov. J. Nucl. Phys., 52, 164-171, 1990.
Breitweg, J. *et al.*, ZEUS, Eur. Phys. J. C, 6, 43-66, 1999.
Caso, C. *et al.*, Particle Data Group, Eur. Phys. J. C, 3, 1-794, 1998.
Drescher, H. J. *et al.*, Phys. Rep., 2001, *in press*; Preprint hep-ph/0007198.
Drescher, H. J. *et al.*, J. Phys. G, 25, L91-L96, 1999.
Fletcher, R. S. *et al.*, Phys. Rev. D, 50, 5710-5731, 1994.
Gribov, V. N., Sov. Phys. JETP, 26, 414-422, 1968.
Gribov, V. N., Sov. Phys. JETP, 29, 483-487, 1969.
Hillas, A. M., *Proc. 24th Int. Cosmic Ray Conf.*, Rome, 1, 270, 1995.
Hladik, M. *et al.*, Phys. Rev. Lett., 86, 3506-3509, 2001.
Capdevielle, J. N. *et al.*, Report KfK 4998, 1992.
Heck, D. *et al.*, Forschungszentrum Karlsruhe, Report FZKA 60198, 1998.
Heck, D. *et al.*, these proceedings.
Kaidalov, A., Nucl. Phys. A, 525, 39-58, 1991.
Kalmykov, N. N. and Ostapchenko, S. S., Phys. Atom. Nucl., 56, 346-353, 1993.
Kalmykov, N. N., Ostapchenko, S. S. and Pavlov, A. I., Bull. Russ. Acad. Sci., Phys. Ser., 58, 1966-1969, 1994.
Kalmykov, N. N., Ostapchenko, S. S. and Pavlov, A. I., Nucl. Phys. B (Proc. Suppl.), 52, 17-28, 1997.
Kalmykov, N. N., Ostapchenko, S. S. and Pavlov, A. I., Nucl. Phys. (Proc. Suppl.), 75A, 293-295, 1999.
Ostapchenko, S., Thouw, T. and Werner, K., Nucl. Phys. B (Proc. Suppl.), 52, 3-7, 1997.
Ostapchenko, S., Pierog, T. and Werner, K., 2001, *in preparation.*
Ranft, J., Phys. Rev. D, 51, 64-84, 1995.
Sciutto, S. J., AIRES: A system for air shower simulations (version 2.2.0), Preprint astro-ph/9911331, 1999.
Werner, K., Phys. Rep., 232, 87-299, 1993.

Proceedings of ICRC 2001: 567 © Copernicus Gesellschaft 2001

ICRC 2001

A mystery of Uhecron - any connection to UHECR?

V. Berezinsky[1,2], M. Kachelrieß[3], and S. Ostapchenko[4,5]

[1]INFN, Laboratory Nazionale del Gran Sasso, Assergi (AQ), I-67010 Italy
[2]Institute for Nuclear Research, Moscow, Russia
[3]TH Division, CERN, CH-1211 Geneva 23, Switzerland
[4]Forschungszentrum Karlsruhe, Institut für Kernphysik, Karlsruhe, D-76021 Germany
[5]Moscow State University, Institute of Nuclear Physics, Moscow, 119899 Russia

Abstract. The interaction properties of hadronic bound states of a light supersymmetric particle, gluino, are studied in the framework of the QGSJET Monte Carlo model. All important contributions to the interaction mechanism are taken into account. In particular, it is found that direct hard interaction of the valence gluino plays an important role in the process. The formalism is applied to the investigation of the properties of extensive air showers, initiated by such particles. Comparing the results with existing cosmic ray data, we were able to set the new limit on the gluino mass, $m_{\tilde{g}} < 5$ GeV, for gluino-hadrons to be the carriers of ultra high energy cosmic ray signal.

1 Introduction

The existence of Ultra High Energy Cosmic Rays (UHE CR) with the energies above the so-called Greisen-Zatsepin-Kuzmin cutoff (Greisen, 1966; Zatsepin and Kuzmin, 1966) is now well established experimentally (for a recent review see Nagano and Watson, 2000). There exist a wide-spread opinion that such very energetic particles have an extragalactic origin. On the other hand, usual cosmic ray primaries, protons and nuclei, emitted from distant sources have little chances to reach the earth with energies above the GZK-cutoff because of their energy losses in the interactions with the cosmic microwave background radiation. As a possible alternative one may consider stable hadronic bound states of the gluino $\tilde{g}$ in supersymmetric models in which the gluino is the lightest supersymmetric particle (Farrar, 1996; Raby, 1998). Such exotic hadrons, referred below as gluino-hadrons, could successfully mimic usual proton-induced Extensive Air Showers (EAS) and would allow to postpone the GZK-cutoff to higher energies.

The bound state of the gluino and the gluon, the so-called glueballino $\tilde{G} = \tilde{g}g$, has been discussed as a possible UHE primary already in the 80's in connection with Cyg-X3 (Berezinsky and Ioffe, 1986). More recently, the S^0, a $uds\tilde{g}$ bound-state, has been proposed as the carrier of the UHE CR signal (Farrar, 1996). A detailed investigation of S^0-induced EAS has been performed by Albuquerque *et al.* (1999), using a modified version of the SIBYLL model (Fletcher *et al.*, 1994). The authors of that work came to the conclusion that gluino masses as large as 50 GeV are consistent with current cosmic ray data. However, their analysis was not self-consistent as they neglected the contribution of minijet production in the model while assuming large cross sections for S^0-nucleus interactions. This appears to be in contradiction with the philosophy of the SIBYLL model, where the "soft" nonperturbative physics is considered to be of scaling type and very high energy hadronic interactions are dominated by hard parton processes (Fletcher *et al.*, 1994).

In our recent work (Berezinsky *et al.*, 2001), the interactions of gluino-hadrons have been studied in the framework of the QGSJET Monte Carlo model (Kalmykov and Ostapchenko, 1993; Kalmykov *et al.*, 1994, 1997), known to describe successfully a great variety of existing cosmic

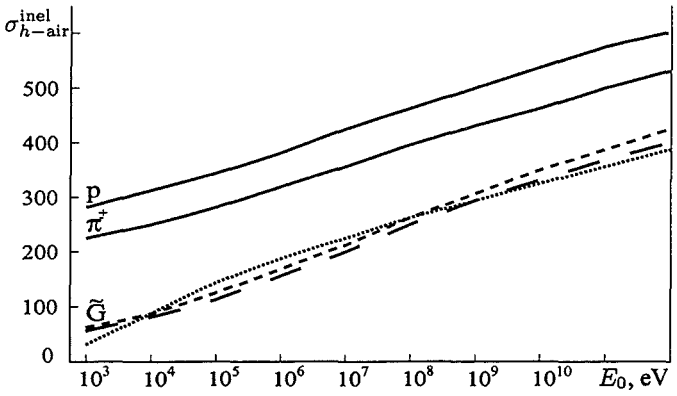

Fig. 1. Inelastic hadron-air cross section/mbarn as a function of the interaction energy for proton - p, pion - $\pi^{\pm}$, and glueballino - $\tilde{G}$; the different choices for the gluino mass are shown as dashed, long-dashed, and dotted curves for $m_{\tilde{g}} = 2, 5, 50$ GeV correspondingly.

Correspondence to: S. Ostapchenko (serguei@ik3.fzk.de)

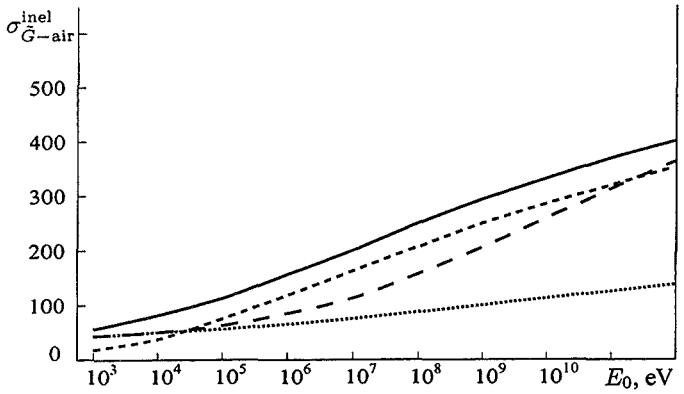

Fig. 2. Inelastic $\tilde{G}$-air cross section/mbarn for $m_{\tilde{g}} = 5$ GeV; the curves correspond to different assumptions concerning the interaction mechanism ("total" – smooth, "direct hard" – dashed, "semihard" – long-dashed, "soft" – dotted), as explained in the text.

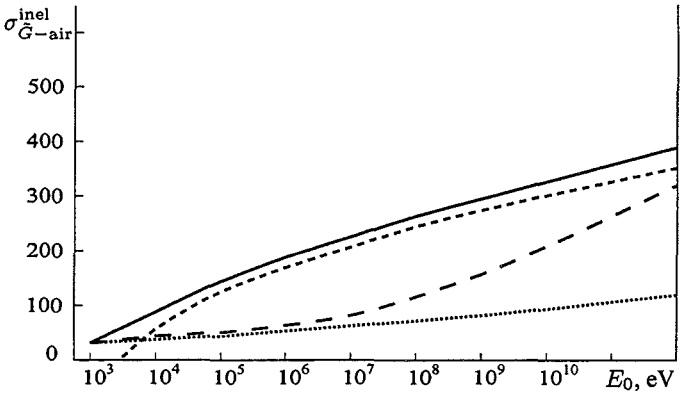

Fig. 3. The same as in Fig. 2 for $m_{\tilde{g}} = 50$ GeV.

ray data. The suitable modification of the model allowed to take into account all essential contributions to the interaction mechanism, to obtain a self-consistent description of interactions of gluino-containing particles with protons and nuclei, and to perform Monte-Carlo simulations of extensive air showers, initiated by gluino-particles in the atmosphere. In the current work we discuss in some detail the important features of interactions of $\tilde{g}$-hadrons as well as their impact on the calculated characteristics of air showers induced by such particles. In particular, we shall demonstrate that for the gluino mass being larger than 5 GeV the calculated longitudinal development of such showers appears to be in strong disagreement with the experimental observations, thus rejecting these particles as the UHE CR primaries.

2 QGSJET formalism for the interactions of $\tilde{g}$-hadrons

The QGSJET model, developed in the Gribov-Regge framework, treats hadronic interactions as multiple scattering processes, with different elementary scattering contributions corresponding either to pure "soft" nonperturbative dynamics, described phenomenologically as "soft" Pomeron exchanges, or to so-called "semihard" interactions. In the latter case at least a part of the underlying parton cascade develops in the region of large parton virtualities. This allows to apply the methods of perturbative QCD and leads to the concept of the "semihard" Pomeron (Kalmykov *et al.*, 1994; Ostapchenko *et al.*, 1997).

To include the new hadrons into this scheme one has to fix the value of the Pomeron-hadron coupling $\gamma_{h\rm P}$ and to define the momentum distribution of the constituent partons in the hadron. As the Pomeron couping is essentially proportional to the effective transverse size of the hadron $\gamma_{h\rm P} \sim R_h^2$, with the hadron h radius R_h being inverse proportional to its reduced mass $\tilde{M}_h$ (Berezinsky and Ioffe, 1986), in the particular case of the glueballino one can use simple scaling arguments to derive this parameter from that of the pion as

$$\gamma_{\tilde{G}\rm P} = \gamma_{\pi\rm P} \left(\frac{\tilde{M}_\pi}{\tilde{M}_{\tilde{G}}} \right)^2 . \tag{1}$$

Here for the reduced mass of the glueballino, we use $\tilde{M}_{\tilde{G}} = m_{\tilde{g}} m_g/(m_{\tilde{g}}+m_g)$, with $m_{\tilde{g}}$ being the gluino mass and $m_g \simeq 0.7$ GeV is the constituent mass of the gluon. Similarly, for the pion we use $\tilde{M}_\pi = m_q/2$ with $m_q \simeq 0.35$ GeV as the quark constituent mass.

For the momentum distribution $\rho^{\tilde{G}}_{\tilde{g}}$ of the valence gluino in the glueballino we use the traditional Regge-inspired ansatz of the QGSJET model

$$\rho^{\tilde{G}}_{\tilde{g}}\,(x_{\tilde{g}}) \sim x_{\tilde{g}}^{\beta_{\tilde{g}}}\,(1-x_{\tilde{g}})^{\beta_g} , \tag{2}$$

with $\beta_g \simeq 0$. The unknown parameter $\beta_{\tilde{g}}$ can be fixed assuming that the energy is shared between the valence gluon and the valence gluino according to their constituent masses:

$$\langle x_{\tilde{g}} \rangle = \frac{m_{\tilde{g}}}{m_g + m_{\tilde{g}}} , \tag{3}$$

where the average gluino momentum share is obtained from eq. (2) as $\langle x_{\tilde{g}} \rangle = (\beta_{\tilde{g}}+1)/(\beta_g+\beta_{\tilde{g}}+2)$.

In the case of gluino-hadrons, one has to account also for the contribution of the so-called "direct hard" process, where the valence gluino interacts perturbatively with some parton from the target hadron (nucleus). The specific feature of this interaction is that it results in very small energy losses of the valence gluino as a large longitudinal momentum transfer $z \simeq \frac{\Delta E_{\tilde{g}}}{E_{\tilde{g}}}$ is suppressed by the process kinematics, with the virtuality scale for the reaction increasing quadratically with z:

$$Q^2 = \frac{p_\perp^2}{1-z} + \frac{z^2 m_{\tilde{g}}^2}{1-z} , \tag{4}$$

with $p_\perp$ and z being the transverse momentum and the light cone momentum fraction for the gluon emitted of the initial valence gluino (Berezinsky and Ioffe, 1986; Berezinsky and Kachelrieß, 1998).

To treat such interactions, the standard QGSJET procedure for the description of QCD parton evolution has been

Table 1. Inelasticity coefficient K^{inel}_{h-air} for hadron-air interactions at different energies E_0.

Reaction type	E_0, eV			
	10^{12}	10^{15}	10^{18}	10^{21}
p-air	0.65	0.74	0.79	0.83
$\tilde{G}$–air ($M_{\tilde{g}} = 2$ GeV)	0.26	0.28	0.29	0.29
$\tilde{G}$–air ($M_{\tilde{g}} = 5$ GeV)	0.15	0.15	0.16	0.16
$\tilde{G}$–air ($M_{\tilde{g}} = 50$ GeV)	0.02	0.02	0.02	0.02

generalized to include relevant processes for a supersymmetric parton (gluino). As the result, we developed the universal description of the interaction process, which allowed us both to calculate the interaction cross sections and to perform an explicit Monte Carlo modeling of glueballino-hadron (nucleus) collisions (Berezinsky *et al.*, 2001). Finally, we made simulations of $\tilde{G}$-induced air showers, using the traditional method based on the combination of numerical and Monte-Carlo techniques (Kalmykov *et al.*, 1997).

3 Numerical results

3.1 Interaction characteristics

In Fig. 1 we show the calculated cross sections σ^{inel}_{h-air} for inelastic interactions of protons, pions, and glueballinos with the nitrogen nucleus as the typical representative of the earth atmosphere. One can see from the figure that at high energies the glueballino cross sections $\sigma^{inel}_{\tilde{G}-air}$ are rather independent on the gluino mass and are comparable in magnitude with the corresponding cross sections for usual hadrons.

To investigate this result in more detail we plot in Fig. 2,3 the cross sections $\sigma^{inel}_{\tilde{G}-air}$ for $M_{\tilde{g}} = 5$ GeV and $M_{\tilde{g}} = 50$ GeV as calculated within different assumptions concerning the interaction mechanism: taking into account only pure "soft" nonperturbative contributions to the interaction process [1] – "soft"; accounting for both "soft" and "semihard" interactions but neglecting the contribution of the "direct hard" process – "semihard"; considering only the "direct hard" contribution – "hard"; and including all the mechanisms – "total". It is easy to see that, like in the case of usual hadrons, pure "soft" processes give a small contribution at very high energies compared to the "semihard" ones, characterized by a much steeper energy dependence. On the other hand, the "direct hard" contribution is very essential in high energy glueballino interactions and even becomes the dominant one for large gluino masses – see Fig. 3, with the interaction process being essentially perturbative on the glueballino side. This important difference from the usual hadron case is due

[1] This option essentially corresponds to the basic assumptions of Albuquerque *et al.* (1999).

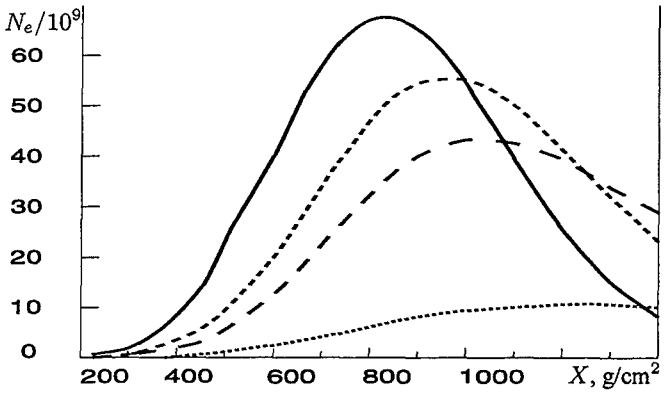

Fig. 4. Average shower profiles for proton- (smooth curve) and $\tilde{G}$-induced EAS ($m_{\tilde{g}} = 2$ GeV – dashed curve, $m_{\tilde{g}} = 5$ GeV – long-dashed, $m_{\tilde{g}} = 50$ GeV – dotted) of energy $E_0 = 10^{20}$ eV.

to the very asymmetric energy partition between parton constituents of the glueballino, with the valence gluino carrying almost the whole initial energy of the particle: 88% for $M_{\tilde{g}} = 5$ GeV and 99% for $M_{\tilde{g}} = 50$ GeV – see eq. (3).

In Table 1 we present another important characteristics of $\tilde{G}$-air interaction, the so-called inelasticity coefficient, i.e. the relative energy loss of the glueballino in the process. It is compared with the corresponding quantity for proton-air interaction, defined as the relative energy difference between the initial proton and the fastest secondary baryon. Here one can see that the glueballino inelasticity, contrary to the proton case, remains essentially energy-independent and falls down rapidly with increasing gluino mass. The reason for this effect is twofold. On one side, as discussed above, gluinos of larger masses carry a larger fraction of the initial particle energy, leaving a smaller part of it for the sea constituents ((anti-)quarks and gluons) and thus reducing the average number of multiple interactions in $\tilde{G}$-air collisions. On the other hand, for heavier gluinos increases the relative weight of the "direct hard" process, characterized by very small energy loss of the valence gluino.

3.2 Glueballino-induced extensive air showers

The two main features of the interaction – sufficiently large cross sections and small energy losses – result in a specific development of $\tilde{G}$-induced EAS: Contrary to the proton case, where the leading proton releases most of its energy in very few initial interactions at large heights, glueballino continues ejecting the energy in small portions into electromagnetic cascade throughout the atmosphere, resulting in a rather delayed EAS development and giving rise to a much wider shower profile compared to the one for the primary proton – Fig. 4.

We also compared the shape of the calculated profiles for individual p- and $\tilde{G}$-induced EAS of energy $E_0 = 3 \cdot 10^{20}$ eV with the corresponding measurements of the Fly's Eye collaboration (Bird *et al.*, 1995) – Fig. 5. In doing so we choose only those showers which reach their maxima in the vicinity

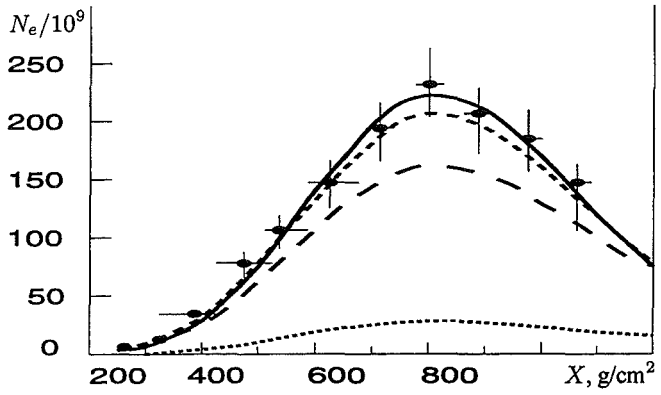

Fig. 5. "Individual" shower profiles for proton- and $\tilde{G}$-induced EAS of energy $E_0 = 3 \cdot 10^{20}$ eV. The abbreviations for the curves are the same as in Fig. 4. The Fly's Eye data (Bird *et al.*, 1995) are shown as filled circles.

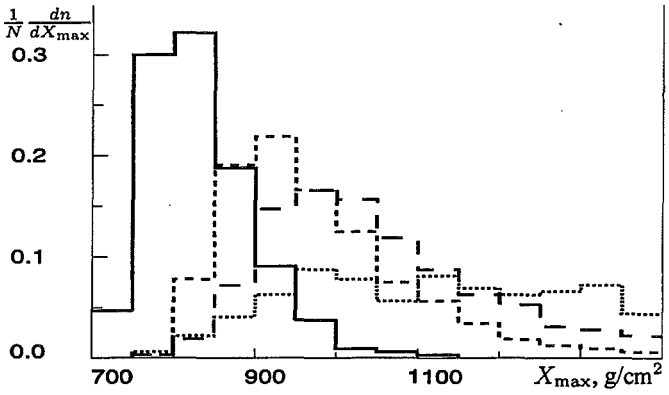

Fig. 6. Normalized distribution of the shower maxima for proton- (smooth histogram) and $\tilde{G}$-induced EAS ($m_{\tilde{g}} = 2$ GeV – dashed histogram, $m_{\tilde{g}} = 5$ GeV – long-dashed, $m_{\tilde{g}} = 50$ GeV – dotted) of energy $E_0 = 10^{20}$ eV.

of the measured value $X_{\max} = 815 \pm 50$ g/cm^2 and average the obtained profiles when shifting them to the same position of the shower maximum, $X_{\max} = 815$ g/cm^2. For gluino masses larger than 5 GeV the shape of the calculated profile strongly disagrees with the experimental observations, thus rejecting the corresponding particle as the cosmic ray primary. The account for the LPM effect results in only 5% reduction of the electron number in the shower maximum for proton-induced EAS (Kalmykov *et al.*, 1995) and has an even smaller influence on the $\tilde{G}$-induced showers due to much softer π^0-spectrum in the glueballino interactions.

In the case of the gluino mass being smaller than 5 GeV one can discriminate primary protons and primary gluino-hadrons analyzing the distributions of shower maxima – see Fig. 6. Such a possibility may be provided by the future data of the HIRES and AUGER installations.

4 Conclusions

We have analyzed the interactions of gluino-hadrons within the self-consistent Gribov-Regge framework, taking into account the contributions of both soft and semihard processes to the interaction mechanism. In particular, we have shown that the direct hard interaction of the valence gluino constitutes a substantial part of the total interaction cross section for such particles.

Comparing the calculated longitudinal development of extensive air showers, initiated by gluino-hadrons, with available experimental data we were able to obtain a new limit on the gluino mass, $m_{\tilde{g}} < 5$ GeV, for such particles to be initiators of very high energy cosmic ray events. Although our analysis was explicitly performed for the particular case of the glueballino as the test particle, our main results remain also valid for other hadronic states of the gluino as they are based on the general properties of hadronic systems containing a comparatively heavy gluino: i) small effective size of the system; ii) very asymmetric energy partition between parton constituents of gluino-hadrons; iii) significant interaction contribution of the "direct hard" gluino process, characterized by a small energy loss of the valence gluino. For sufficiently large gluino masses the whole interaction process becomes essentially perturbative on the gluino-hadron side, thus making our conclusions model-independent in this limit.

In the case of the gluino mass being smaller than 5 GeV one can finally confirm or reject the hypothesis of gluino-hadrons as the carriers of UHE CR signal on the basis of future measurements of ultra high energy extensive air showers with the HIRES and AUGER detectors.

References

Albuquerque, I. F., Farrar, G. R. and Kolb, E. W., Phys. Rev. D, 59, 015021, 1999.

Berezinsky, V. S. and Ioffe, B. L., Sov. Phys. JETP, 63, 920-925, 1986.

Berezinsky, V. and Kachelrieß, M., Phys. Lett. B, 422, 163-170, 1998.

Berezinsky, V., Kachelrieß, M. and Ostapchenko, S., In "Les Arcs 2001, Very High Energy Phenomena in the Universe", *in press*; paper in preparation.

Bird, D. J. *et al.*, Astrophys. J., 441, 144-150, 1995.

Farrar, G. R., Phys. Rev. Lett., 76, 4111-4114, 1996.

Fletcher, R. S. *et al.*, Phys. Rev. D, 50, 5710-5731, 1994.

Greisen, K., Phys. Rev. Lett., 16, 748-750, 1966.

Kalmykov, N. N. and Ostapchenko, S. S., Phys. Atom. Nucl., 56, 346-353, 1993.

Kalmykov, N. N., Ostapchenko, S. S. and Pavlov, A. I., Bull. Russ. Acad. Sci., Phys. Ser., 58, 1966-1969, 1994.

Kalmykov, N. N., Ostapchenko, S. S. and Pavlov, A. I., Phys. Atom. Nucl., 58, 1728-1731, 1995.

Kalmykov, N. N., Ostapchenko, S. S. and Pavlov, A. I., Nucl. Phys. B (Proc. Suppl.), 52, 17-28, 1997.

Nagano, M. and Watson, A. A., Rev. Mod. Phys., 72, 689-732, 2000.

Ostapchenko, S., Thouw, T. and Werner, K., Nucl. Phys. B (Proc. Suppl.), 52, 3-7, 1997.

Raby, S., Phys. Lett. B, 422, 158-162, 1998.

Zatsepin, G.T. and Kuzmin, V.A., JETP Lett., 4, 78-80, 1966.

Proceedings of ICRC 2001: 302 © Copernicus Gesellschaft 2001

ICRC 2001

Simulation studies of the information content of muon arrival time observations of high energy extensive air showers

I. M. Brancus[1], H. Rebel[2], M. Duma[1], A. F. Badea[1], C. Aiftimiei[1], and J. Oehlschlaeger[2]

[1]IFIN-HH Bucharest, P.O.B.MG-6, 76900 Bucharest, Romania
[2]Forschungszentrum Karlsruhe, Institut f. Kernphysik, Postfach 3640, 76021 Karlsruhe, Germany

Abstract. On basis of detailed Monte Carlo simulations of high energy Extensive Air Showers, using the EAS simulation code CORSIKA, the information potential of muon arrival time studies has been explored. Muon arrival time distributions and EAS time profiles have been analysed up to 320 m distances from the EAS centre for proton, oxygen and iron induced showers. Special attention is focussed to the model dependence and mass discriminating features, scrutinized for three energies ranges, (1.-1.78) 10^{15} eV, (1.-1.78) 10^{16} eV and (1.78-3.16) 10^{16} eV. Non-parametric statistical inference methods have been applied in the analysis of multidimensional distributions and of the correlations of the EAS time parameters with different other EAS observables. Local muon arrival times referring to the first registered muon indicate a good mass separation when correlated with the local muon density and the shower age, especially at larger distances from the shower core. Global muon arrival times, which refer to the arrival of the shower core and represent also the curvature of the EAS disk, exhibit a slightly improved mass separation quality.

1 Introduction

The temporal structure of the muon component of Extended Air Showers (EAS) is of great interest for a detailed understanding of the EAS structure, since it reflects the longitudinal EAS development (Linsley et al., 1961; Rebel et al., 1995). Muon arrival distributions, observed in particular at large distances from the shower axis map the distributions of the production heights via the time-of-flight of the muons from the decay loci of the charged pions which are produced by hadronic collisions along the shower axis. Arrival times $\tau_\mu^1, \tau_\mu^2, \tau_\mu^3, \ldots$ of muons, registered by timing detectors at a distance R_μ from the shower centre have to refer to a well defined zero-time, usually the arrival time τ_c of the shower core *("global" arrival times)*:

$$\Delta\tau_\mu^n = \tau_\mu^n(R_\mu) - \tau_c \quad (1)$$

When the arrival time τ_c is difficult to determine with sufficient precision, *"local" times* are considered, which refer to the foremost muon, locally registered by the detector:

$$\Delta\tau^n(R_\mu) = \tau_\mu^n(R_\mu) - \tau_\mu^1(R_\mu) \quad (2)$$

The single relative arrival time distributions can be characterised by the mean values $\Delta\tau_{mean}$, and by quantles $\Delta\tau_q$ like the median $\Delta\tau_{0.50}$, the first quartile $\Delta\tau_{0.25}$ and the third quartile $\Delta\tau_{0.75}$ (Antoni et al., 2001). Their mean values and dispersion (standard deviations) represent the time profile of the EAS muon component. Recently the temporal EAS structure has been studied in dependence on the shower size N_e, the muon number N_μ, or the truncated muon number N_μ^{tr} in KASCADE experiment (Antoni et al., 2001). The present analysis, based on simulations neglecting the detector response, explores the basic information which is provided by the time observables and their correlations with other EAS observables, in view of the discrimination of the primaries mass and of the hadronic interaction model.

2 Time profiles of the EAS muon component

For calculating the time profiles the EAS development has been simulated by the Monte Carlo program CORSIKA (Heck et al., 1998), invoking different models for the hadronic interaction, QGSJET, VENUS, and SIBYLL, and using the NKG approximation for the electron-photon component and the full Monte Carlo EGS simulations (Antoni et al., 2001). 500 proton and 500 iron induced EAS of the primary energy of 10^{15} eV and of vertical incidence have been analysed for a radial range up to 150 m, and the muon arrival time distributions and time profiles (bins with $\Delta R_\mu = 10$ m) of the muon component ($E_\mu \geq 2.4$ GeV) have been constructed.

Fig.1 displays the time profiles for the median distributions and for median divided by the average density $\rho_\mu(R_\mu)$

Correspondence to: I. M. Brancus (iliana@ifin.nipne.ro)

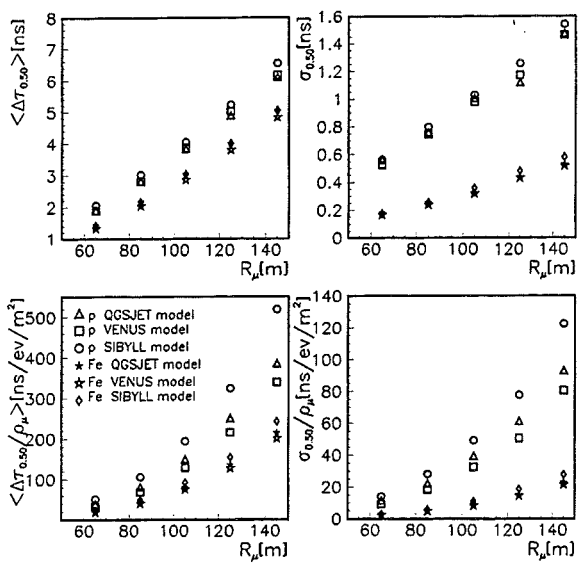

Fig. 1. Simulated muon profiles for the time distributions and the standard deviations by $\Delta\tau_{0.50}$ and $\Delta\tau_{0.50}/\rho_\mu$, for two primaries p and Fe and for three models, QGSJET, VENUS, and SIBYLL.

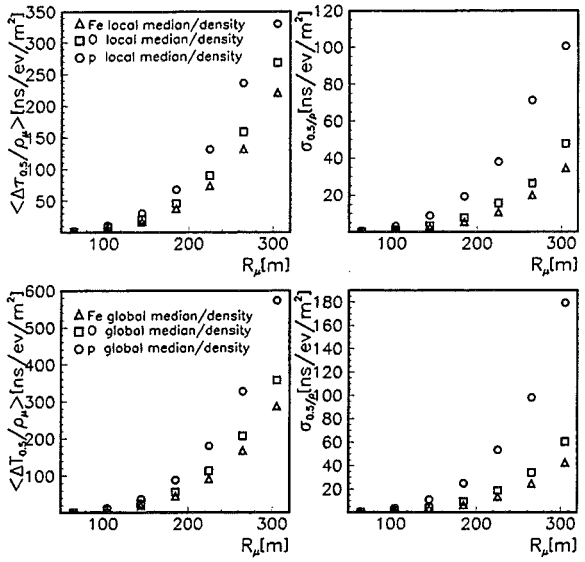

Fig. 2. Simulated muon profiles for the $\Delta\tau_q/\rho_\mu$ distributions and the standard deviations of the local and global median values, for the three primaries p, O, Fe.

of muons in the corresponding R_μ-bin, for the two different primaries p and Fe of the energy 10^{15} eV and comparing three different hadronic interaction models The use of the observables $\Delta\tau_q(R_\mu)/\rho_\mu(R_\mu)$ results in some improvement of the mass discrimination, but especially for the discrimination of different models, the lateral distribution of the muons is contributing to the discriminative power.

For higher energies, (1.78-3.16) 10^{16} eV, and for each class of primaries, p, O, and Fe, 50 showers have been generated for QGSJET model on extended radial ranges up to 310 m.

Fig.2 displays the profiles of $\Delta\tau_q/\rho_\mu$, resulting in a similar behaviour for both local and global times with a better separation of primaries with increasing distance from the shower core.

3 Non-parametric statistical analysis

The non-parametric statistical methods enable the study of multidimensional observables-distributions to associate the single observed events to different classes (in our case to proton, oxygen or iron primaries) by comparing the observed events with the model distributions without using a prechosen parameterisation (Chilingarian, 1989). For each class of primaries, p, O and Fe, 200 showers with energies in the range (1.-1.78) 10^{15} eV, 100 showers with energies in the range (1.-1.78) 10^{16} eV and 50 showers with energies in the range (1.78-3.16) 10^{16} eV have been generated for QGSJET and VENUS models, and the multidimensional distributions of various EAS observables have been analysed using the Bayesian approach.

Fig.3 displays the probability distribution for $\Delta\tau_{0.50}(R_\mu)/\rho_\mu(R_\mu)$ for median local times, at 3 different radial distances, whose overlaps indicate the expected improved separation by the combination time/density.

The values of the classification and misclassification probabilities of an EAS event to be associated to a particular class are presented in Figs. 4, 5 and listed in the tables.

The notation is: $\Delta\tau_{0.50}(R_x)$ is the median arrival time in the range R_x, x=A,B,C, where 90 m $\leq R_A <$ 100 m, 180 m $\leq R_B <$ 190 m, and 260 m $\leq R_C <$ 270 m; $\rho_\mu(R_x)$ is the density in the radial range R_x.

Fig.4 shows the classification and misclassification probabilities for various combinations of EAS observables for QGSJET model at incident energy (1.78 -3.16) 10^{16} eV. The quantity muon arrival time/muon density gives a better discrimination than each separated quantities, similar by taking the correlations of two observables, muon arrival time and muon density. The use of muon *global* times instead of *local* times brings a slightly improved classification. For better mass discrimination we have to look for correlations of muon arrival times with N_e, N_μ^{tr}, and the shower age.

Fig.5 displays the comparison of the classification and misclassification probabilities using the correlation of the observation of the third quantile with other shower observables; the best result is given by correlating $\Delta\tau_{0.75}$ with the age and N_μ^{tr}.

Tab. 1 presents the classification and misclassification probabilities for various combinations of EAS observables at high energies, 50 showers for each class: p, O, Fe, (1.78-3.16) 10^{16}eV.

The comparison of the muon arrival times at different radial distances indicates an improved mass discrimination for larger distances.

Tab. 2 gives the classification and misclassification prob-

Mode	P ↓			O ↓			Fe ↓		
	P	O	Fe	P	O	Fe	P	O	Fe
N_e	.56	.34	.10	.19	.44	.37	.00	.17	.83
$N_e - \Delta\tau^A_{0.50}/\rho^A_\mu$	.73	.23	.04	.09	.63	.28	.00	.19	.81
$N_e - \Delta\tau^A_{0.50}/\rho^A_\mu - \Delta\tau^C_{0.50}/\rho^C_\mu$	.72	.24	.04	.10	.64	.26	.00	.15	.85
$N_e - \Delta\tau^A_{0.50}/\rho^A_\mu - \Delta\tau^B_{0.50}/\rho^B_\mu - \Delta\tau^C_{0.50}/\rho^C_\mu$	.77	.20	.03	.08	.66	.26	.00	.15	.85
N^{tr}_μ	.43	.31	.26	.10	.35	.55	.00	.28	.72
$N^{tr}_\mu - \Delta\tau^A_{0.50}/\rho^A_\mu$	.69	.28	.03	.05	.63	.32	.00	.13	.87
$N^{tr}_\mu - \Delta\tau^A_{0.50}/\rho^A_\mu - \Delta\tau^C_{0.50}/\rho^C_\mu$	.70	.26	.04	.06	.65	.29	.00	.13	.87
$N^{tr}_\mu - \Delta\tau^A_{0.50}/\rho^A_\mu - \Delta\tau^B_{0.50}/\rho^B_\mu - \Delta\tau^C_{0.50}/\rho^C_\mu$	.73	.23	.04	.05	.68	.27	.00	.17	.83

Table 1. The classification and misclassification probabilities inferred from different combinations of shower observables: N_e and N^{tr}_μ and correlating with $\Delta\tau_{0.50}/\rho_\mu$ at different radial distances for the modes: only one observable, N_e, respectively N^{tr}_μ; two observables by adding $\Delta\tau_{0.50}(R_A)/\rho_\mu(R_A)$; three observables by adding $\Delta\tau_{0.50}(R_C)/\rho_\mu(R_C)$; four observables by adding $\Delta\tau_{0.50}(R_B)/\rho_\mu(R_B)$.

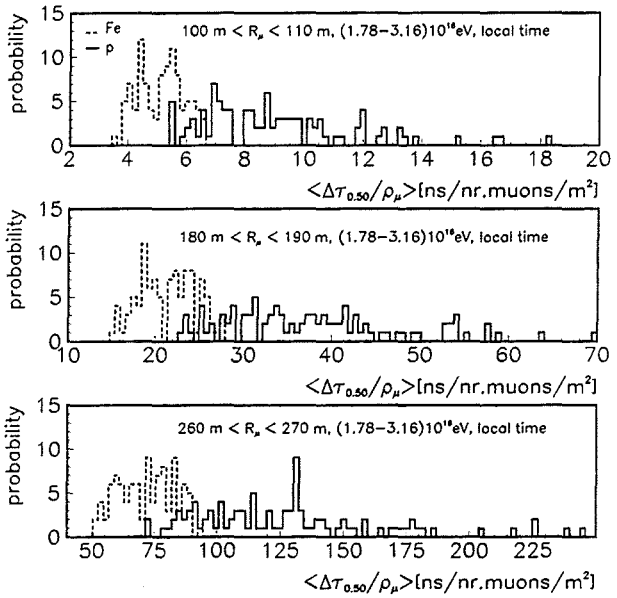

Fig. 3. The probability density distributions for $\Delta\tau_q/\rho_\mu$ corresponding to proton and iron EAS primaries, for three different radial distances from the shower core.

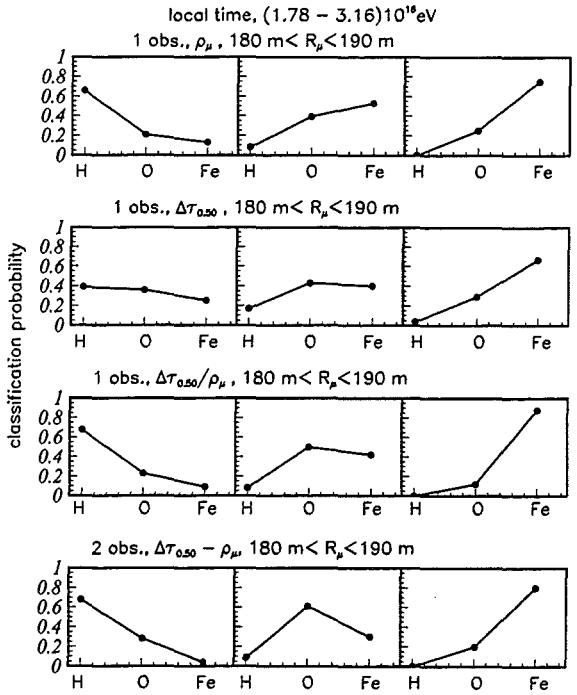

Fig. 4. The classification and misclassification probabilities for different observation modes.

abilities at different incident energies, by correlating the shower age $\Delta\tau_{0.50}(R_A)/\rho_\mu(R_A)$ displaying an improved discrimination for higher energies.

Energy	P ↓			O ↓			Fe ↓		
	P	O	Fe	P	O	Fe	P	O	Fe
$1.\ 10^{15}$	.70	.28	.01	.14	.56	.30	.00	.19	.81
$1.\ 10^{16}$	.73	.25	.02	.09	.71	.20	.00	.21	.79
$1.78\ 10^{16}$	.73	.24	.03	.06	.72	.22	.00	.07	.93

Table 2. The classification and misclassification probabilities by correlating age, $\Delta\tau_{0.50}(R_A)/\rho_\mu(R_A)$ for different energy ranges, (1.-1.78) 10^{15} eV, (1.-1.78) 10^{16} eV, and (1.78-3.16) 10^{16} eV.

Tab. 3 compares the classification and misclassification probabilities using QGSJET and VENUS model, by correlating the age, $N_e - \Delta\tau_{0.50}(R_A)/\rho_\mu(R_A)$.

Model	P ↓			O ↓			Fe ↓		
	P	O	Fe	P	O	Fe	P	O	Fe
QGS	.75	.23	.01	.08	.68	.23	.00	.15	.84
VEN	.80	.18	.01	.08	.70	.22	.00	.12	.88

Table 3. The classsification and misclassification probabilities by correlating age $N_e - \Delta\tau_{0.50}(R_A)/\rho_\mu(R_A)$ for the primary energy (1.-1.78)10^{16} eV with the two different interaction models QGSJET and VENUS.

4 Conclusions

The present studies have been focussed to explore the information carried by EAS time observables and their correlations in view of features discriminating the mass of the cos-

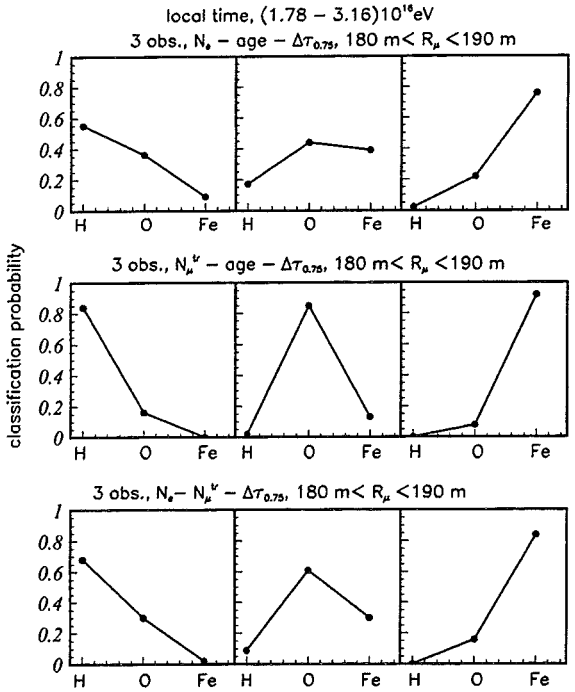

Fig. 5. The classification and misclassification probabilities correlating the observation of muon arrival times with N_e, N_μ^{tr} and the shower age.

mic primary and different hadronic interaction models. Advanced non-parametrical statistical methods based on Bayesian decision rules have been applied to scrutinise the EAS observables and to specify quantitatively the results:

1. The correlations of the local muon arrival time variables with the local muon density improves the true classification rate and discrimination features. It turns out that the correlation can be replaced by a single parameter: $\Delta\tau_q/\rho_\mu$. The classification gets improved by the correlation with the shower age, the shower size N_e, and N_μ^{tr}.
2. Correlating the observation of $\Delta\tau_q/\rho_\mu$ for different radial distances, the mass discrimination of the primaries is only slightly improved, different from our previous result (Brancus et al., 1997) analysing the (global) arrival times of the foremost muon.
3. Comparing the classification rates for different muon arrival time quantities, the VENUS model leads to better results than the QGSJET one.

From the present results an enhancement of the discriminative features may be expected at larger distances from the shower core (> 150 m) and to higher primary energies ($> 10^{16}$ eV). The finding is of actual interest in view of the current efforts of the KASCADE collaboration to extend the detector array to a larger area: KASCADE GRANDE.

Acknowledgements. One author (I.B.) acknowledges the support by a grant from the Deutsche Forschungsgemeinschaft and the Forschungszentrum Karlsruhe for the hospitality, providing the possibility to perform detailed analyses of the information carried by muon arrival times observations.

References

Antoni, T., et al., KASCADE Collaboration, Astropart. Phys. 14, 245, 2001.
Antoni, T., et al., KASCADE Collaboration, Astropart. Phys. 15, 149, 2001.
Brancus, I.M., et al., Astropart. Phys. 7, 343, 1997.
Chilingarian, A.A., Comp. Phys. Comm. 54, 381, 1989; Chilingarian, A.A., ANI Reference Manual, 1999.
Heck, D., et al., Report FZKA 6019, Forschungszentrum Karlsruhe, 1998.
Linsley, J., et al., Phys. Rev. 92, 485, 1961.
Rebel, H., et al., Journ. Phys. G: Nucl. Part. Phys. 21, 451, 1995.

Proceedings of ICRC 2001: 71 © Copernicus Gesellschaft 2001

ICRC 2001

On the knee in the energy spectrum of cosmic rays

J. R. Hörandel

Institut für Experimentelle Kernphysik, University of Karlsruhe, P.O. Box 3640, 76021 Karlsruhe, Germany

Abstract. The enigma of the *knee* in the cosmic–ray energy spectrum is scrutinized with an empirical model, comparing results from direct and indirect measurements. The energy spectra of individual elements, as obtained by direct observations, are extrapolated to high energies and compared to a compilation of all–particle energy spectra from air shower measurements. A model, assuming a cut-off for each species proportional to its charge Z is adopted. The fine structure of the energy spectrum with changes of the spectral index at 2.5 PeV and 300 PeV are explained by cut-offs of the proton component and of the stable elements (Z=92). The *knee* in the all–particle energy spectrum results from a charge dependent cut-off for each individual element of the galactic component. No additional cosmic ray component is required in the *knee* region to describe the observed spectrum. The model allows a prediction of the mass composition of cosmic rays at high energies, which is in agreement with experimental results from air shower experiments.

1 Introduction

The cosmic–ray energy spectrum extends over many orders of magnitude from GeV energies up to at least 10^{20} eV as a steep falling spectrum roughly following a power law $dN/dE \propto E^{-\gamma}$ with almost no special features. A closer look exhibits some fine structures, most prominent is a change in the spectral index from $\gamma_1 \approx -2.7$ to $\gamma_2 \approx -3.0$ at about 3 PeV, generally called *the knee*. Its origin is still under discussion and is generally assumed to be a corner stone in the understanding of the origin of cosmic rays.

The energy spectra of cosmic rays are measured directly up to several 10^{14} eV for individual elements with satellite and balloon–borne experiments at the top of the atmosphere. Due to the steep falling spectrum, measurements at higher energies require large detection areas or long exposure times, at present only realized in ground–based detector systems. These experiments measure extensive air showers, generated by interactions of high–energetic cosmic rays in the atmosphere.

In this work the fluxes obtained by direct measurements are extrapolated to high energies and compared to results of indirect measurements.

Theories for cosmic ray acceleration (see for example (Wiebel98) (Gaisser99)) propose acceleration processes becoming inefficient at an energy $E_C \propto Z$ where Z is the nuclear charge of the particle, and a complete cut-off is expected at higher energies, also proportional to Z. Therefore, we expect a cut-off or at least a change of the spectral index in the spectrum for the individual species at an energy E_C^Z. Inspired by these theories, we adopt an empirical model to explain the fluxes of high–energy cosmic rays.

Above about $Z \cdot 10$ GeV energy/nucleon, where the modulation due to the solar magnetic field is negligible, the energy spectra of cosmic–ray nuclei can be described by a power law. We chose the ansatz

$$\frac{d\Phi_Z}{dE}(E) = \Phi_Z^0 \cdot E^{\gamma_Z} \left[1 + \left(\frac{E}{Z \cdot E_C^p}\right)^{\epsilon}\right]^{\frac{\gamma_C - \gamma_Z}{\epsilon}} , \quad (1)$$

γ_C and ϵ characterize the change in the spectrum at the cut-off energy $Z \cdot E_C^p$, with the cut-off energy E_C^p for protons.

Summing up the flux of all elements, the all–particle spectrum is obtained. We have two parameters Φ_Z^0 and γ_Z for each element and three common parameters E_C^p, γ_C, and ϵ to describe the end of the single element spectra. Φ_Z^0 and γ_Z are deduced from direct measurements of individual nuclei, the remaining 3 parameters will be derived from indirect measurements of the all–particle spectrum.

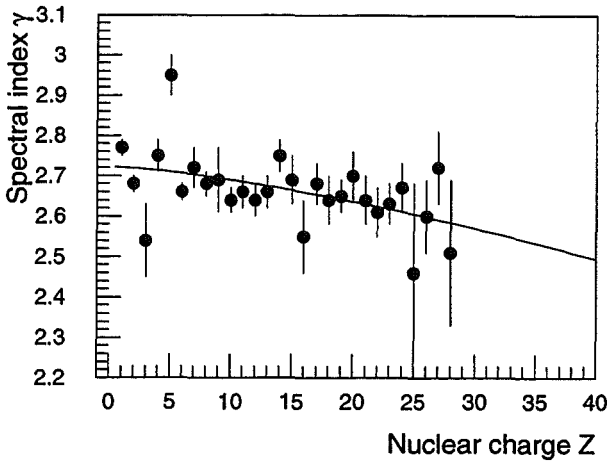

Fig. 1. Spectral indices (Wiebel98) versus nuclear charge.

Correspondence to: J. R. Hörandel (joerg@ik1.fzk.de)

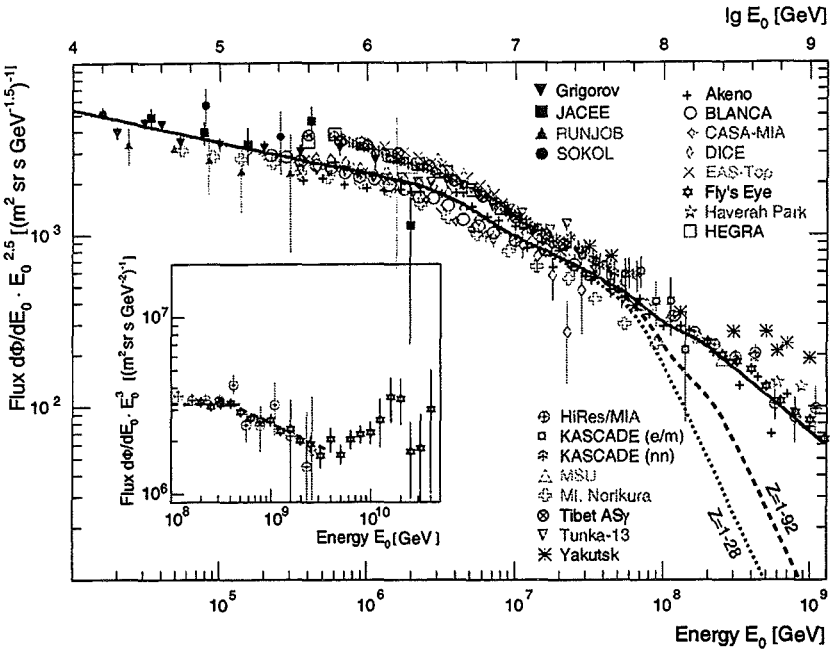

Fig. 2. All–particle energy spectrum obtained from direct observations by Grigorov (Shibata99), JACEE (Tominaga93), RUNJOB (Apanasenko98), SOKOL (Ivanenko93), and indirect measurements by AKENO (Nagano84), BLANCA (Fowler01), CASA-MIA (Glasmacher99), DICE (Swordy00), EAS-Top (Aglietta99), Fly's Eye (Bird94), Haverah Park (Lawrence91), HEGRA (Arqueros00), HiRes/MIA (Abu–Zayyad00), KASCADE parametric (electrons + muons) (Ulrich01) and neural network analysis (Roth01) (Antoni01), MSU (Fomin91), Mt. Norikura (Ito97), Tibet ASγ (Amenomori96), Tunka–13 (Gress97), and Yakutsk (Dyakonov91). The lines represent sum spectra for elements with Z=1-28 and Z=1-92. The insert shows the high–energy end of the spectrum, as measured by Fly's Eye and HiRes/MIA. The dashed line represents a fit by Bird et al. (Bird94).

2 Direct Measurements

Many direct measurements of individual nuclei have been performed using balloon–borne detectors at the top of the atmosphere and instruments on spacecrafts. A compilation by Wiebel–Sooth et al. (Wiebel98) summarizes results for energy spectra from hydrogen to nickel and gives abundance values at 1 TeV. The abundance of ultra-heavy elements ($Z > 28$) at energies just above the geomagnetic cut–off has been measured by the experiments ARIEL 6 (Fowler87) and HEAO 3 (Binns89). All stable elements of the periodic table from hydrogen up to the actinides have been found in cosmic rays. For ultra–heavy elements only the abundance is measured, no spectral information is available. Hence, the spectral indices for these elements shall be estimated.

The spectral indices for the elements from hydrogen to nickel, taken from (Wiebel98), are shown in figure 1 versus the nuclear charge. Theories using a nonlinear model of Fermi acceleration in supernovae remnants predict a more efficient acceleration for elements with large mass to charge ratios compared to elements with a smaller A/Z ratio, see for example (Ellison93). Consequently, it is expected that elements with higher A/Z have a flatter spectrum. Such a trend is visible in figure 1.

In our model we assume the relation $\gamma(Z) = A + B \cdot Z^C$ to describe the Z dependence of the spectral indices. The three parameters are determined by fits to the values in figure 1 as well as to the all–particle spectrum as described below. The curve in figure 1 represents the best fit, exhibiting a decreasing spectral index with the nuclear charge:

$$\gamma(Z) = 2.72 - 0.130 \cdot 10^{-2} \cdot Z^{1.4} \quad . \tag{2}$$

This expression is applied to estimate the spectral indices for ultra–heavy elements ($Z > 28$) in order to extrapolate the flux obtained by ARIEL 6 and HEAO 3.

Even if the abundance of ultra–heavy elements is small at low energies, their relative number will increase due to their assumed flatter energy spectrum. In our model they become more and more important for the all–particle spectrum at high energies, since all lighter elements have already reached their cut-off energy $E_C^Z \propto Z$.

3 Indirect Measurements

Many groups published results on the all–particle energy spectrum from indirect measurements, recent results are compiled in figure 2. The overall agreement between the experiments is quite good, the differential fluxes multiplied by $E^{2.5}$ agree within a factor of two.

Typical uncertainties of air shower experiments in the absolute energy calibration are quoted to be in the order of 10% to 20%. The spectra can be normalized by slightly changing the energy scale in order to fit the flux given by direct measurements around 10^5 GeV. The result is presented in figure 3 together with the normalization factors. They are in agreement with the above quoted energy uncertainties. The mean normalization factor is $-5.4\% \pm 1.5\%$, i.e. most experiments slightly overestimate the primary energy. A fact which could exhibit a systematic effect in the hadronic interaction models used to interpret the air shower data. The similar shape obtained by the different experiments is obvious in this representation, an interesting observation, since the energy scaling does not change the shape of the spectra.

A *knee* at about 3 PeV is clearly visible in the figure. Assuming this bend is caused by the cut-off of the proton com-

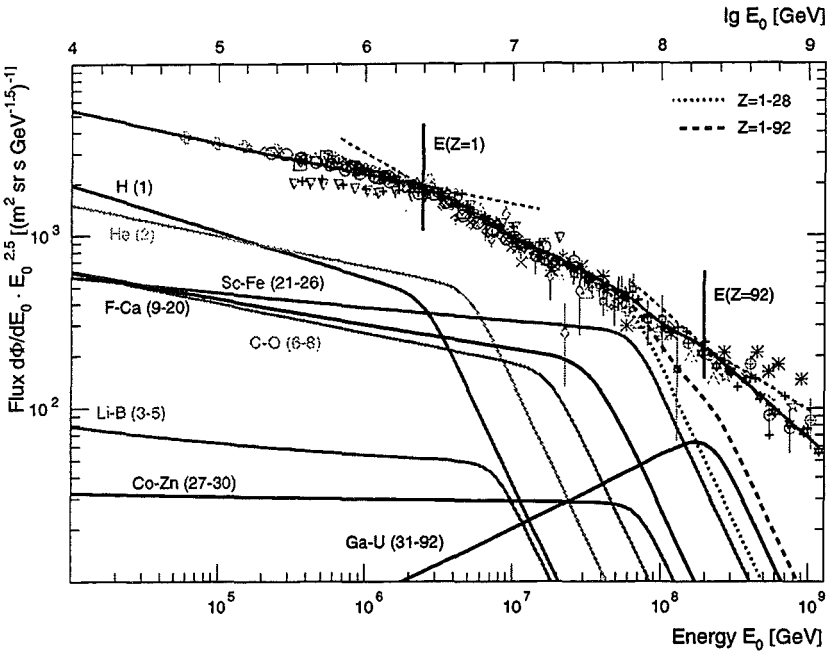

Fig. 3. Normalized all–particle energy spectrum. The normalization factors for the energy scales are:

Experiment	Norm. Factor
AKENO	0%
BLANCA	2%
CASA–MIA	2%
DICE	0%
EAS–Top	−13%
Fly's Eye	−5%
Haverah Park	−9%
HEGRA	−11%
HiRes	−5%
KASCADE (e/m)	−9%
KASCADE (nn)	−9%
MSU	−9%
Mt. Norikura	8%
Tibet	−11%
Tunka–13	−7%
Yakutsk	−10%

The solid curves (H to Ga-U) represent extrapolated spectra for groups of elements according to our assumptions.

ponent, the galactic component should extend up to about $92 \cdot 3$ PeV$\approx$ 0.3 EeV. A change in the spectral slope around 3 to $4 \cdot 10^8$ GeV is visible in figure 2, especially in the insert — the dashed line represents a fit taken from (Bird94). This observation is confirmed by results from AKENO and Haverah Park (Bird94). The change in slope coincidences well with the proposed cut-off of the heaviest nuclei of the galactic component.

4 All–Particle Energy Spectrum

The parameters E_C^p, ϵ, and γ_C are determined from indirect measurements using the data as presented in figure 3. A least–square fit to the all–particle spectrum, using the parameters Φ_Z^0 and γ_Z for elements up to nickel results in the blue, dotted graph in figure 3. The parameters describing the shape of the cut-off for the individual element spectra are $\epsilon = 7$ and $\gamma_C = 4.3$. The proton *knee* is found to be at $E_C^p = 2.5$ PeV.

Next, the coefficients for the $\gamma(Z)$ dependence shall be determined. The values influence the all–particle spectrum and must fit the values in figure 1. A combined fit of figure 1 and the all–particle spectrum yields the coefficients in equation 2. The resulting sum spectrum for elements with Z=1 to 92 is plotted in figure 3 as dashed curve. The contribution of ultra–heavy elements causes a change in the spectral index around 0.3 EeV, as has been observed by the Fly's Eye and HiRes experiments.

Above this energy, a new (extragalactic) component takes over and dominates the spectrum at the highest energies. This component is introduced into the model *ad hoc*, adding the required flux to the galactic component to match the measured flux values. This flux difference as function of energy is needed to calculate the mass composition in the next section. The resulting all–particle spectrum, including the *ad hoc* component is shown as a red, solid curve in figures 2 and 3. One notices that the empirical model consistently describes the cosmic–ray energy spectrum from several 10 GeV up to 10^9 GeV.

5 Mass Composition

All parameters in equation 1 being defined, the spectrum for each species can be deduced. To avoid confusion, only the spectra of groups of elements are shown in figure 3.

It is now possible to calculate the mass composition of cosmic rays for a given energy using for example the mean logarithmic mass, defined as

$$\langle \ln A \rangle = \sum_i r_i \ln A_i \qquad (3)$$

where r_i is the relative fraction of component i with mass A_i. One difficulty in deriving a value for $\langle \ln A \rangle$ is the unknown composition of the "extragalactic component" which has been introduced *ad hoc* to describe the observed all–particle spectrum. Several theories predict an extragalactic component consisting of proton and helium nuclei only, see for example (Biermann93). We, therefore, assume a mixture of protons and helium. The predicted mean logarithmic mass is presented in figure 4 as function of the particle energy. The values for the galactic component increase up to pure uranium, since all other species already reached their cut-off energies (dotted, red line). Assuming pure protons and pure helium nuclei for the extragalactic component, the dashed, red lines are obtained, respectively.

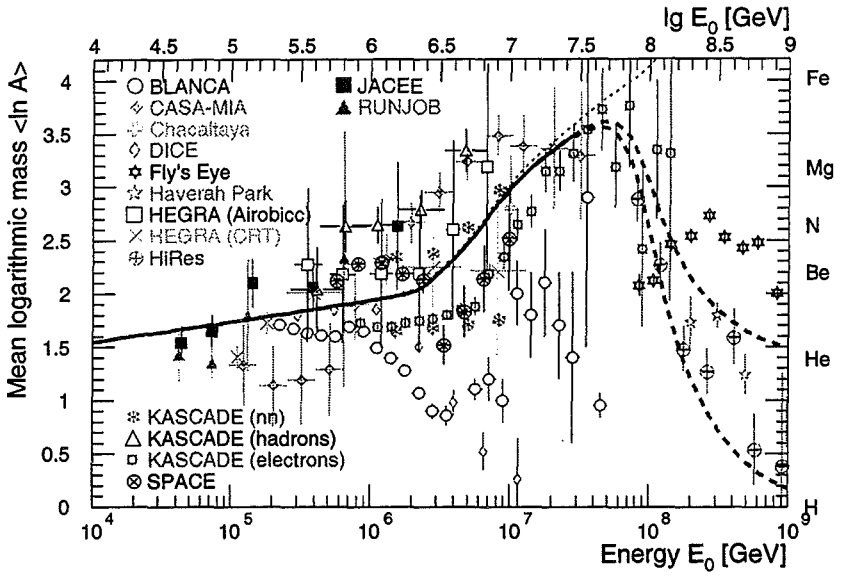

Fig. 4. Mean logarithmic mass vs. particle energy from JACEE, RUNJOB (Shibata99); CASA–MIA (Glasmacher99); Chacaltaya (Aguirre00); DICE (Swordy00); Haverah Park (Watson00); HEGRA Airobicc (Arqueros00), CRT (Bernlöhr98); HiRes (Abu–Zayyad00); KASCADE neural network (two extreme results from different observables) (Roth01) (Antoni01), parametric analysis using electrons + muons (Ulrich01), hadrons + muons (Hörandel98); BLANCA, Fly's Eye, and SPACE taken from (Fowler01) with QGSJET interpretation. Some papers quote results for several interaction models used to interpret the data, in such a case only QGSJET results are shown. The curves show the mass function according to the empirical model.

In the figure the calculated $\langle \ln A \rangle$ values are compared with results from several experiments. The measurements exhibit a wide scattering of the $\langle \ln A \rangle$ values, which is mainly caused by different interpretations of the data due to uncertainties in the interaction models used. Different models lead to different mass compositions for the same measurement and the same interaction model leads to different values of $\langle \ln A \rangle$ for different observables. For example, KASCADE uses several models and observables and obtains different results (Hörandel98) (Antoni01). Two extreme results in a neural network analysis when using different observables (Antoni01) are shown in the figure to illustrate the effect.

Despite of the discrepancies in the measurements or their interpretation, the general trend of the predicted mass function is supported by most experiments.

6 Conclusion

Adopting an empirical model with a cut-off for individual element spectra at an energy $E_C^Z = Z \cdot E_C^p$, and extrapolating the energy spectra of individual nuclei obtained by direct measurements to high energies, the energy spectrum of cosmic rays in the range from 10 GeV up to almost 1 EeV can be described consistently, and the fine structure of the spectrum can be explained. The all–particle energy spectrum compiled from many air shower experiments shows two changes in spectral slope at $E_C^p = 2.5$ PeV and 0.3 EeV ($\approx 92 \cdot E_C^p$), which can be correlated to the cut–off energies of protons (Z=1) and the heaviest stable nuclei (Z=92). Within the model ultra–heavy nuclei (Z=30-92) with spectral indices $\gamma(Z) \propto Z^{1.4}$ are important to describe the energy spectrum around 100 PeV. The predicted mass composition is in agreement with results from air shower experiments.

Acknowledgements. The author would like to thank Joachim Engler and Karl–Heinz Kampert for helpful comments on this work.

References

Abu–Zayyad, T. et al., 2000, astro-ph/0010652
Aglietta, M. et al., 1999, Astropart. Phys. **10**, 1
Aguirre, C. et al., 2000, Phys. Rev. D **62**, 032003
Amenomori, M. et al., 1996, Ap. J. **461**, 408
Antoni, T. et al., 2001, accepted by Astropart. Phys.
A.V. Apanasenko et al., 1998, ISAS–report No. 37
Arqueros, F. et al., 2000, Astron. Astrophys. **359**, 682
Bernlöhr, K, et al., 1998, Astropart. Phys. **8**, 253
Biermann, B.L., 1993, Astron. Astrophys. **271**, 649
Binns, W.R. et al., 1989, Ap. J. **346**, 997
Bird, D.J. et al., 1994, Ap. J. **424**, 491
Dyakonov, M.N. et al., 1991, Proc. 22^{nd} ICRC, Dublin **2**, 93
Ellison, D.C., 1993, Proc. 23^{rd} ICRC, Calgary **2**, 219
Fomin, Y.A. et al., 1991, Proc. 22^{nd} ICRC, Dublin **2**, 85
Fowler, P.H. et al., 1987, Ap. J. **314**, 739
Fowler, J.W. et al., 2001, Astropart. Phys. **15**, 49
Gaisser, T.K., 1999, Cosmic Rays and Particle Physics, Cambridge
Glasmacher, M.A.K. et al., 1999, Astropart. Phys. **10**, 291
Gress, O.A. et al., 1997, Proc. 25^{th} ICRC, Durban **4**, 129
Hörandel, J.R. et al., 1998, Proc. 16^{th} ECRS, Alcala, 579; and Engler, J. et al., 1999, Proc. 26^{th} ICRC, Salt Lake City **1**, 349
Ito, N. et al., 1997, Proc. 25^{th} ICRC, Durban **4**, 117
I.P. Ivanenko et al., 1993, Proc. $23rd$ ICRC, Calgary **2**, 17
Lawrence, M.A. et al., 1991, J. Phys. G: Nucl. Part. Phys. **17**, 733
Nagano, M. et al., 1984, J. Phys. G: Nucl. Part. Phys. **10**, 1295
Roth, M. et al., 2001, Proc. 27^{th} ICRC, Hamburg
Shibata T., 1999, Nucl. Phys. B (Proc. Suppl.) **75A**, 22
Swordy, S.P., Kieda, D.B., 2000, Astropart. Phys. **13**, 137
Tominaga, T. et al., 1993, Proc. 23^{rd} ICRC, Calgary **2**, 21
Ulrich, H. et al., 2001, Proc. 27^{th} ICRC, Hamburg
Watson, A.A., 2000, Physics Reports **333-334**, 309
Wiebel–Soth, B. et al., 1998, Astron. Astroph. **330** , 389

Proceedings of ICRC 2001: 1608 © Copernicus Gesellschaft 2001

ICRC 2001

A new measurement of the energy spectra of cosmic-ray nuclei

J. R. Hörandel[1,2], J. W. Britton[1], F. Gahbauer[1], G. Hermann[1,3], D. Müller[1], S. P. Swordy[1], and S. P. Wakely[1]

[1]The Enrico Fermi Institute, The University of Chicago, Chicago, IL 60637, USA
[2]Institut für Experimentelle Kernphysik, University of Karlsruhe, Postfach 3640, 76021 Karlsruhe, Germany
[3]Max Planck Institut für Kernphysik, 69029 Heidelberg, Germany

Abstract. A new large-area detector system was constructed at the University of Chicago for direct measurements of heavy cosmic ray nuclei (oxygen to iron) up to about 10 TeV/nucleon. TRACER ("Transition Radiation Array for Cosmic Energetic Radiation") uses plastic scintillators to measure charge and a proportional tube array to measure energy via specific ionization and transition radiation. While TRACER is designed for circumglobal long-duration balloon flights, an initial 28-hour flight was conducted in Autumn 1999 from Ft. Sumner, New Mexico. We will discuss the performance of the detector and present first data from the balloon flight.

1 Introduction

While the overall energy spectrum of cosmic rays extends beyond 10^{20} eV/particle, present data on composition and spectra of the individual components are scarce at energies above several 10^{13} eV/particle. Consequently, current ideas about particle acceleration and propagation lack some important constraints over much of the high–energy region, including the *knee* around $3 \cdot 10^{15}$ eV/particle. New observations with large–area detectors and long exposure times are required to improve this situation. The TRACER program ("Transition Radiation Array for Cosmic Energetic Radiation") attempts to address this need. The TRACER instrument has been flown in a conventional balloon flight in autumn 1999, and is presently prepared for a long–duration flight in 2002. TRACER also serves as a prototype for a detector that could eventually be used as an attached payload on the Space Station. Here we shall report on the performance of the instrument and on the data obtained in the first balloon flight in 1999.

Correspondence to: J. R. Hörandel (joerg@ik1.fzk.de)

2 Description of the Instrument

In order to obtain a detector with a favorable weight to area ratio, we employ gaseous detectors that determine the particle energy via the logarithmic dependence of the specific ionization on the Lorentz factor $\gamma = E/mc^2$ of the particle, or via the detection of transition radiation (TR) at the highest energies. In this fashion, the Lorentz factor range from less than 10 to at least 10^4 can be covered for nuclei with charge $Z > 3$. Protons and helium are not included since the statistical fluctuations become too large as to permit a reliable measurement of γ for these low–Z elements with this technique. The TR measurement follows a concept first developed for the CRN instrument flown on the Space Shuttle in 1985 (L'Heureux et al. 1990), and the accelerator calibrations originally performed for CRN are also applicable for TRACER. However, the TR detector of CRN consisted of thin–window multiwire proportional chambers at atmospheric pressure, and the instrument had to be enclosed in a pressurized shell. For TRACER, the wire chambers are replaced by layers of single wire–proportional tubes which easily withstand external vacuum. Hence, a pressurized container is not needed.

TRACER is shown schematically in figure 1. The main elements are:

1. Two square scintillators, each 2 m × 2 m in area, on top and bottom of the instrument. These serve as coincidence triggers and determine the nuclear charge Z of cosmic–ray particles. Each scintillator sheet is just 5 mm thick and is viewed by 12 photomultiplier tubes (PMT) via wavelengthshifter bars.

2. An acrylic Cherenkov counter, 2 m × 2 m in area, located below the bottom scintillator, to reject sub–relativistic nuclei.

3. An array of eight layers of proportional tubes, each tube 2 cm in diameter and 200 cm long, to measure the specific ionization of traversing cosmic rays.

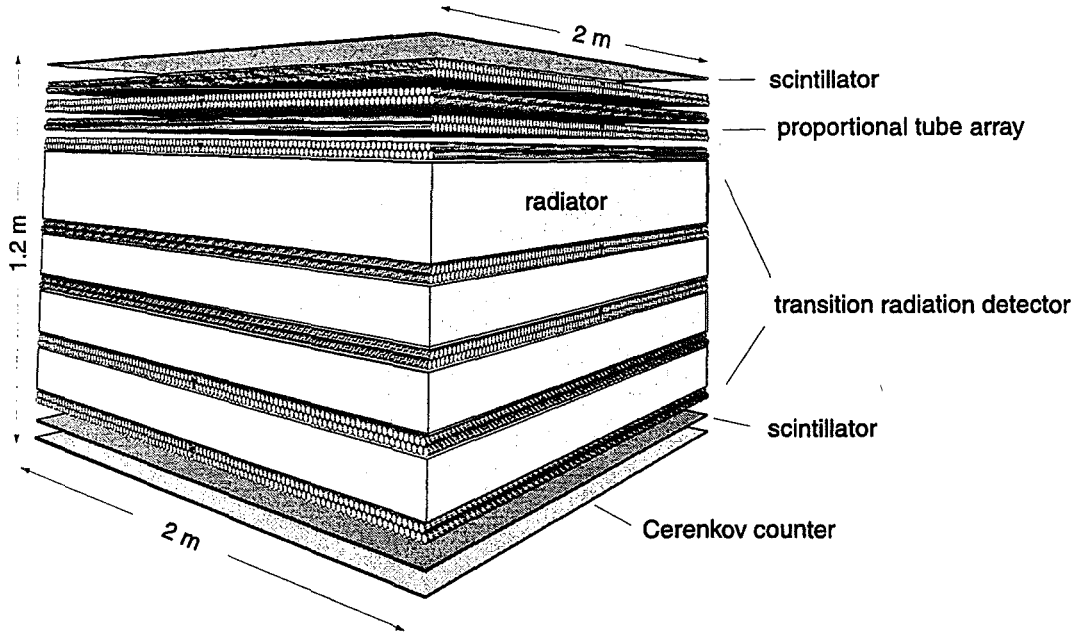

Fig. 1. Schematic view of the TRACER detector system.

4. A transition radiation detector (TRD) consisting of a stack of four radiator detector combinations: The radiators are battings of polyolefin fibers, identical to those of CRN (L'Heureux et al. 1990), and each detector comprises a double layer of proportional tubes. All tubes are filled with a Xe/CH_4 mixture.

The signal read–out is accomplished by analyzing each of the 64 PMT signals with 12 bit resolution, and by analyzing each of the 1600 proportional tubes with 8 bit resolution, using VLSI electronics. Limitations in the dynamic range of the electronics available to us when TRACER was constructed, restrict the range to $7 < Z < 28$ for the first TRACER flight.

3 Balloon Flight

The first balloon flight of TRACER was conducted from Ft. Sumner, N.M., on September 20/21 1999. The instrument floated at an altitude corresponding to 4 to 6 g/cm^2 of residual atmosphere for a duration of 28 hours, and was safely recovered by parachute. The average geomagnetic cutoff rigidity was 4.5 GV. During the flight, the instrument detected a total of 1.3 million events, corresponding to about 500 MByte of raw data which were recorded on board and simultaneously received by telemetry on ground.

4 Data Analysis and Results

The data analysis proceeds in the following steps:

4.1 Charge measurement and trajectory information

The elemental charge Z is determined primarily from the signals of the two plastic scintillators. The specific ionization is proportional to Z^2, but for iron (Z=26), the density effect reduces the measured signal by 29% from proportionality to Z^2. However, light collection from the scintillator exhibits spatial non–uniformities of about a factor of 2. Hence response maps for the scintillators, generated with cosmic–ray muons on ground, and confirmed by the flight data, are used to normalize the scintillator signals. Therefore, the trajectory of each particle must be determined first. This is obtained in two steps. First, the positions of all tubes with signals above threshold provide 16 measurements, each with 2 cm resolution. A least–square fit to the center positions of these tubes determines the trajectory with a lateral accuracy of about 5 mm. Second, we use the fact that the magnitude of the signal in each tube is proportional to the path length of the particle through the tube, within statistical fluctuations. Taking this into account in the fitting procedure, we improve the lateral accuracy to 1 mm for oxygen and 0.25 mm for iron (Hörandel et al. 2001).

Figure 2 shows a charge spectrum obtained from the corrected signals of the scintillators and of the Cherenkov counter, with the additional requirement that the signals in the top and in the bottom scintillators are consistent with each other within resolution limits. This requirement rejects nuclei that may have undergone a nuclear interaction in the instrument. The charge resolution is about 0.22 charge units for oxygen. Note that the charge resolution around iron will further improve when the data are corrected for some distortions due to occasional PMT–saturation.

4.2 Determination of the Energy Spectrum

After assignment of nuclear charge Z, we investigate the signals from the proportional tubes. The upper 8 layers measure the specific ionization, which increases logarithmically with γ. The lower eight layers again measure the ionization sig-

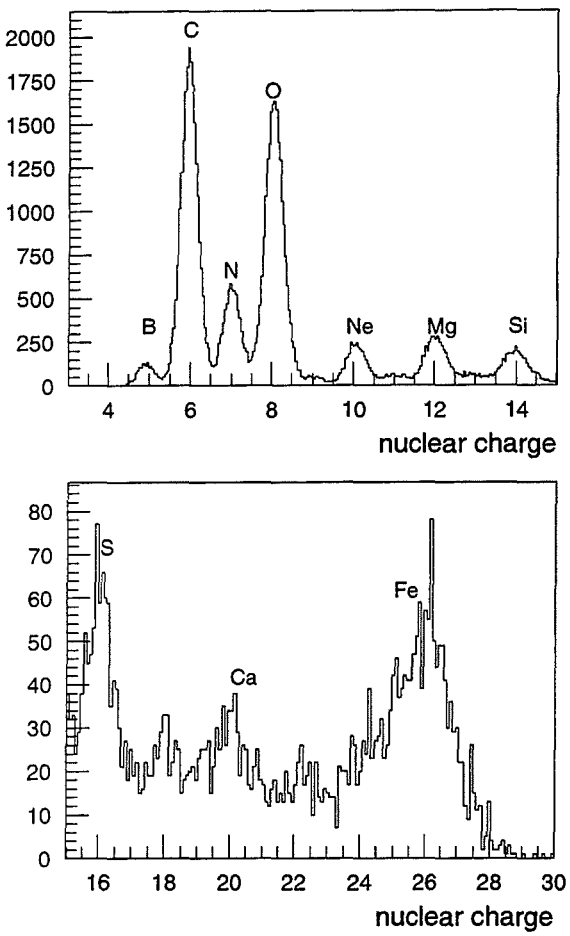

Fig. 2. Measured charge distribution for relativistic cosmic–ray nuclei.

nal, but for large energies ($\gamma > 500$), transition radiation signals are superimposed. As the signals depend on the pathlength through the tube, knowledge of the trajectory again is important for the analysis. For each set of double layers, we determine the total signal, normalized to the total pathlength and use this number for further analysis.

For the analysis, we make extensive use of the GEANT 4 code (CERN 2001), which simulates both ionization loss and transition radiation. We first verify that the code properly reproduces the data obtained in accelerator calibrations (L'Heureux et al. 1990) (Swordy et al. 1990). We than generate simulated data: We subject a realistic model of the TRACER instrument, which includes the actual detector geometry, mass distribution, etc. to an isotropic flux of simulated cosmic rays with an assumed primary energy spectrum with a spectral index of -2.7 and a geomagnetic cut–off of 4.5 GV. The simulation takes all interactions, including nuclear fragmentation, δ–ray production, TR generation, etc., into account, including realistic statistical fluctuations. Each particle and each X–ray photon is followed, and simulated proportional tube signals are obtained.

In figure 3 we illustrate the procedure by showing a scatter plot for simulated signals for oxygen nuclei ($Z = 8$) versus

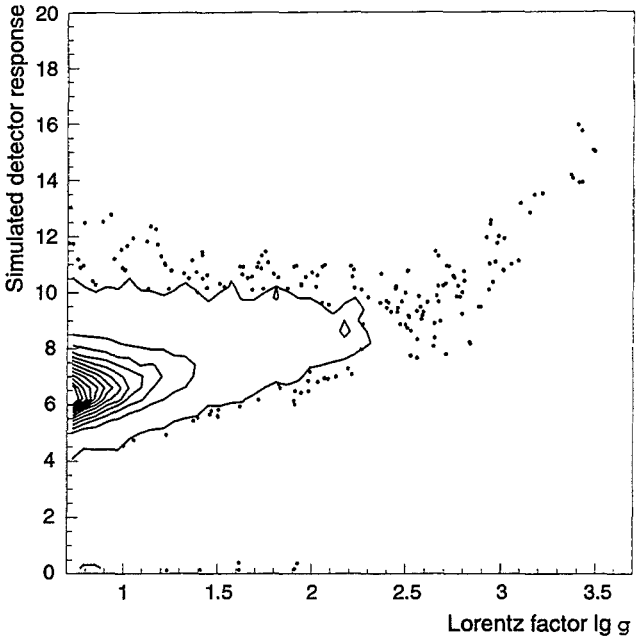

Fig. 3. The simulated detector response vs. Lorentz factor for oxygen nuclei as detected by the TRD.

their Lorentz factor γ. A primary spectrum $\propto \gamma^{-2.7}$ is assumed. The simulated data in the figure are the signals just from the TRD part of the detector system. The trend of the data is characterized by a slow increase in spezific ionization up to a Lorentz factor $\gamma \approx 500$, followed by a stronger

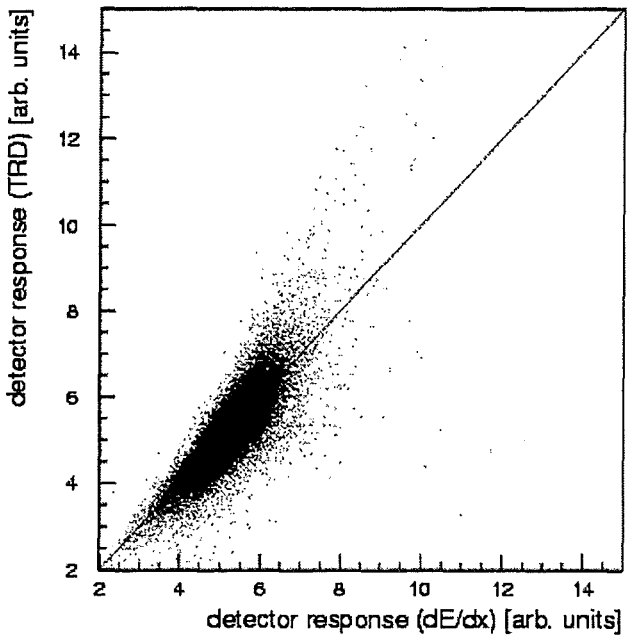

Fig. 4. Measured detector response of the TRD versus the proportional tube array. Raw data for oxygen nuclei, as taken during the balloon flight are shown.

increase due to TR. The figure also illustrates the spread of the data due to fluctuations in detector response. The possibility that such fluctuations will cause a low–energy particle to mimic a high–γ event, can be strongly reduced if one requires consistency between the signals of the TRD and of the proportional tube array that estimates the particle energy from the relativistic rise in ionization loss only.

The correlation between TRD signals and ionization loss measurements are shown in figure 4, using oxygen data, taken during the balloon flight. While for low Lorentz factors the signals of both detectors are proportional to each other, for higher energies we see a systematic enhancement in the TRD signals over those of the ionization detectors.

A formal analysis to extract the shape of the energy spectra for the different nuclear cosmic ray species from the measured data is presently in progress. We will present the resulting spectra at the time of the conference.

5 Conclusion

A successful standard balloon flight with the TRACER system shows that the instrument is working as expected. A analysis procedure to reconstruct the energy spectra of cosmic–ray nuclei has been developed using a detailed detector simulation. Energy spectra for individual elements will be presented at the conference.

Acknowledgements. This work has been supported by NASA grant NAG 5–5072 and NAG 5–5305.

References

CERN program library, http://wwwinfo.cern.ch/asd/geant4/
L'Heureux, J. et al., Nucl. Instr. and Meth. A **295** (1990) 246
Hörandel, J.R. et al., Nucl. Phys. B (Proc. Suppl.) **97** (2001) 142
Swordy, S.P. et al., Phys. Rev. **D 42** (1990) 3197

Proceedings of ICRC 2001: 1612 © Copernicus Gesellschaft 2001

ICRC 2001

Cosmic ray nuclei at high energies: recent results from TRACER and future prospects

F. Gahbauer[1], G. Hermann[1,2], J. Hörandel[1,3], D. Müller[1], S. P. Swordy[1], and S. P. Wakely[1]

[1]The Enrico Fermi Institute, The University of Chicago, Chicago, IL 60637, USA
[2]Max Planck Insitut für Kernphysik, 69029 Heidelberg, Germany
[3]Institut für Kernphysik, Forschungszentrum und Universität Karlruhe, 76021 Karlsruhe, Germany

Abstract.

The first balloon flight of the TRACER instrument in 1999 led to a new measurement of the energy spectra of cosmic ray nuclei from Z=8 to Z=26 at energies from a few GeV/nucleon to several TeV/nucleon. We will present and discuss the results, compare them with other recent measurements and examine the implications for current cosmic ray propagation and acceleration models. Finally, we will comment on the prospects of planned flights of the TRACER instrument on long duration balloons, and on the adaptation of the measurement technique to anticipated space missions.

1 Introduction

The TRACER instrument ("Transition Radiation Array for Cosmic Energetic Radiation") was flown for the first time in September 1999 in a 28-hour balloon flight from Fort Sumner, New Mexico. The instrument was designed to measure the energy spectra of the heavy cosmic ray nuclei from oxygen (Z=8) to iron (Z=28). The measurement technique makes use of the relativistic rise with energy of the specific ionization generated by cosmic rays in gaseous detectors, and of the energy dependence of the yield of transition radiation. Some details about the technique and the data analysis approach are given by Hörandel at al (2001).

2 Energy Spectra of Cosmic Ray Nuclei

A unique feature of TRACER is the capability of deriving with a single instrument, the energy spectra of cosmic ray nuclei over three decades, from geomagnetic cutoff (~4.5 GV) to several TeV/nucleon. At the time of this writing, the analysis is still in progress, but the energy spectra for individual elements resulting from this work, will be presented at the conference. Our work will concentrate on the major primary elements oxygen, neon, magnesium, silicon, and iron, and our results will be compared with those from other investigations, including those obtained by our group with the CRN detector on the Space Shuttle (Müller et al, 1991). It will be very instructive to compare the shape of the measured energy spectra with what might be expected in the context of galactic propagation model. It is now well known, at least up to energies around 100 GeV/n, that the propagation path length Λ_p of cosmic rays decreases with energy, as $E^{-\delta}$ with $\delta \approx 0.6$. In simple diffusion models without reacceleration in interstellar space, the effective path length Λ of cosmic rays is then determined by competition between diffusive propagation and loss by nuclear spallation:

$$\frac{1}{\Lambda} = \left(\frac{1}{\Lambda_s} + \frac{1}{\Lambda_p(E)} \right) \quad (1)$$

For relativistic nuclei, the spallation path length Λ_s is essentially independent of energy, but is commensurate with typical values of Λ_p, for instance, for iron $\Lambda_s = 2.3 g/cm^2$. If the cosmic ray energy spectrum at the source is a pure power law with index γ_0, one would expect the observed spectrum to exhibit a gradual steepening, reaching a spectral index $\gamma = \gamma_0 + \delta$ at high energies. For heavy elements like iron, this asymptotic slope would be obtained at higher energies than for the lighter elements, due to the dependence of Λ_s on the mass of the nucleus. Previous analysis of the energy spectra obtained with the CRN instrument, indicated qualitative agreement between the data and this model (Swordy et al, 1993), with the possible exception of the element Silicon (Z= 14). The present data from TRACER will permit a much more sensitive test of the model, because of the larger energy coverage and improved counting statistics. We will present and discuss the results of such an analysis.

3 Future Prospects

The 1999 balloon flight of TRACER provided significant data, and successfully tested a new detector concept. To fully

Correspondence to: F. Gahbauer
(f-gahbauer@uchicago.edu)

exploit the technique, longer exposures are desirable. We therefore plan to use the instrument in a long duration balloon flight from Fairbanks, Alaska, in early summer 2002. This will be a circumglobal flight along the Arctic Circle, with an anticipated duration of about two weeks. If successful, this flight will improve the counting statistics by more than an order of magnitude.

Finally, instruments like TRACER should be used in space for durations of the order of years. This is especially important for measurements of interstellar secondary nuclei with good statistics, and without contamination by spallation produced nuclides in the atmosphere. Such elements, notably Li, Be, and B, are essential for determining the interstellar propagation path length.

Acknowledgements. This work has been supported by NASA grants NAG 5-5072 and NAG 5-5305.

References

Hörandel, J. et al. 2001, Proc. 27th ICRC (Hamburg, 2001)
Müller, D. et al. 1991, Ap. J. 374, 356.
Swordy, S. et al. 1993, Ap. J. 403, 658.

Proceedings of ICRC 2001: 22 © Copernicus Gesellschaft 2001

ICRC 2001

Comparisons of measured and simulated energy spectra of electromagnetic particles at the Pamir emulsion experiment

A. Haungs[1] and J. Kempa[2]

[1]Institut für Kernphysik, Forschungszentrum Karlsruhe, 76021 Karlsruhe, Germany
[2]Warsaw University of Technology, 09-400 Plock, Poland

Abstract. The reconstructed energy spectrum of electromagnetic particles, measured at high-altitude is compared with spectra obtained by Monte Carlo simulations. The extensive air shower simulations are based on the CORSIKA program including different high energy interaction models, e.g. QGSJET, VENUS or neXus. Additionally the Monte Carlo includes a detailed simulation of the detector response for the particles based on the GEANT code. From the obtained optical density the energy of the particles is reconstructed with the same algorithms like at the Pamir experiment. These procedures enables to discuss in details resolution and threshold effects of the Pamir emulsion calorimeter at both, the optical density and the energy of the electromagnetic particles.

1 Introduction

Experiments at high mountain altitudes on Pamir or Mt. Chacaltaya measure electrons, gammas and hadrons with high particle energy thresholds in the TeV region by emulsions or X-ray films (Baradzei et al.,1992). Besides the reconstruction of the cores of extensive air-showers in the knee region by the so called particle families, integral measurements of single hadrons and electrons/gammas are performed. At high altitudes these particles stem mainly from primary cosmic rays of energies below 1 PeV and were produced in extremely forward direction. This explains the special suitability of these measurements for comparisons with expectations by high-energy hadronic interaction models: in the primary energy region of 10-100 TeV the elemental composition and flux of the cosmic rays are approximately known from direct measurements on balloons or satellites. The sensitivity of the emulsion experiments to the extreme forward direction of the interaction has complementary information to the data of accelerator experiments to which the cross sections of the interaction models are adjusted. Hence the measurement can be used for a test of these models (Haungs et al., 2001).

Correspondence to: A.Haungs (haungs@ik3.fzk.de)

In the present paper we compare the expected inclusive flux of e/γ for the Pamir experiment for seven different high-energy interaction models, all embedded in the air-shower simulation program CORSIKA (Heck et al., 1998). The measured distribution of the electromagnetic component with the e/γ-block of the Pamir experiment is compared with the expectations of the simulations including detailed detector simulations. The considered observable is the so-called optical density of spots displayed in X-ray films. The optical densities are then converted into the energy of the secondary particles and the resulting "reconstructed" spectra are discussed. Finally the results are compared with a measured spectrum: $I(>E) = (1.63 \pm 0.13) \cdot 10^{-6} \cdot (E/5TeV)^{-1.93\pm0.12}$ [$m^{-2}s^{-1}sr^{-1}$] (Bialawska, 1999).

2 CORSIKA air shower simulations

Air-shower events are generated for three different nuclei (H, He, Fe), using seven different interaction model codes: VENUS vers.4.12 (Werner, 1993), QGSJET vers. of CORSIKA 5.62 (Kalmykov et al., 1997), SIBYLL vers.1.6 (Engel et al., 1992), HDPM (Heck et al., 1998), DPMJET vers.2.4 (Ranft, 1995), SIBYLL vers.2.1 (Engel, 1999), and neXus vers.2β (Drescher et al., 1999), implemented in CORSIKA (basically vers. 5.62). For each primary and model 500,000 events were generated, except for the DPMJET and neXus models, where somewhat fewer events were simulated in view of the long computing time required for these codes. In the case of primary protons the simulations cover the energy range of 10^{13} eV - 10^{16} eV with slope $\gamma_H = 2.75$ and isotropic incidence up to 40° . In the case of primary helium (iron) the slope used is $\gamma_{He} = 2.62$ ($\gamma_{Fe} = 2.60$) in the energy range $2 \cdot 10^{13}$ eV - 10^{16} eV (10^{14} eV - 10^{16} eV). The slopes were taken from the compilation of direct measurements (Wiebel-Sooth et al., 1998). All secondary particles with energies larger than 1 TeV at the observation level of the Pamir experiment (4370 m) are taken into account.

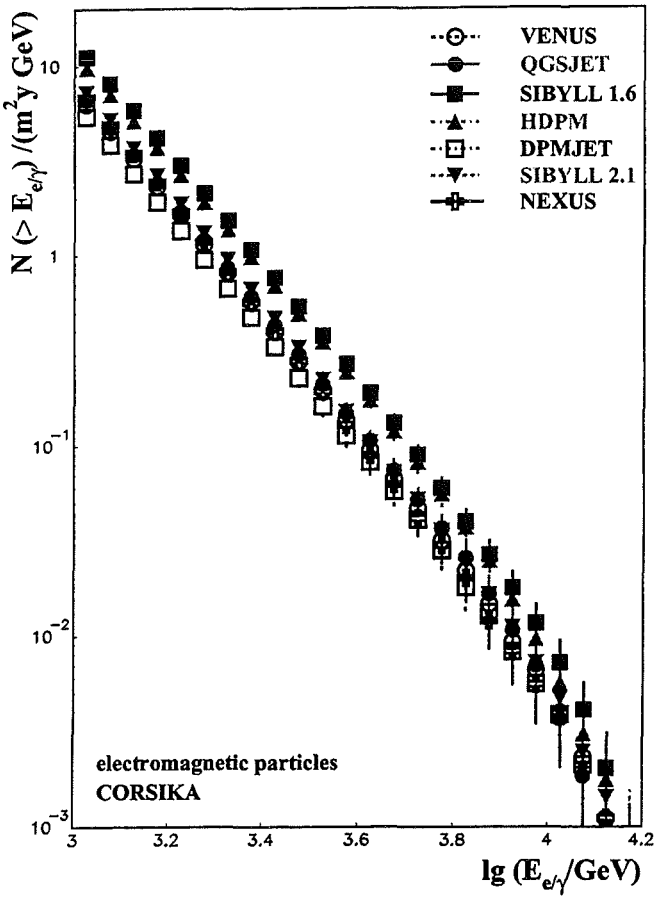

Fig. 1. The energy spectra of electromagnetic secondary shower particles above 1 TeV as expected for the Pamir observation level for different interaction models. The spectra are displayed in integral form and normalised to one m^2 and year. The error bars denote the statistical uncertainties of the simulations, which affect the high-energy tail of the spectra.

Figure 1 compares the integral energy spectra of electromagnetic particles for all interaction models. The spectra are reconstructed by the sum of the different progenitors weighted with the relative fluxes as estimated by a compilation of direct measurements (Wiebel-Sooth et al., 1998). It could be shown (Haungs et al., 1999, 1998) that heavy primaries give a nonsignificant contribution to such integral measurements. The contribution of heavy primaries is not only reduced owing to the assumed fluxes, but also by the faster development by showers induced by heavy particles. Primaries with larger energies do not compensate for this effect, due to the steeply decreasing primary spectrum.

Obviously the spectra shown in Figure 1 reflect somehow the primary energy spectra with their power law distribution. Above 10 TeV the spectra show a cut-off which is due to the missing ultra-high primary energies above 10^{16} eV at the simulations. The differences between the slopes from the different models are within statistical uncertainties, but the absolute scales of the predictions differ by a factor of 2-2.5.

With a fit of a power law in the energy region 1–10 TeV we calculate the slope and the expected flux of particles above 5 TeV. The results are listed in Table 1. The SIBYLL 1.6 and HDPM produce significantly more and DPMJET significantly fewer particles than the other models. (This also holds for the hadronic secondary particles, see Haungs et al., 2000.)

Table 1. Fit results for the integral spectra of electromagnetic particles for different interaction models. The values are the parameters of the functional form $I(> E) = c \cdot (E/5TeV)^{\gamma}\,\mathrm{m}^{-2}\mathrm{s}^{-1}\mathrm{sr}^{-1}$. The statistical errors of the parameters are in the order of 5-10%.

	coefficient c	slope γ
VENUS	$1.42 \cdot 10^{-6}$	-1.94
QGSJET	$1.57 \cdot 10^{-6}$	-1.93
SIBYLL 1.6	$2.72 \cdot 10^{-6}$	-1.87
HDPM	$2.50 \cdot 10^{-6}$	-1.83
DPMJET	$1.24 \cdot 10^{-6}$	-2.02
NEXUS	$1.26 \cdot 10^{-6}$	-2.05
SIBYLL 2.1	$1.57 \cdot 10^{-6}$	-1.95

3 Detector response

For electromagnetic particles the optical densities in the X-ray films were calculated for photons and electrons of different energies and angles of incidence by a detailed detector simulation using the GEANT tool (Haungs and Kempa, 1997). The optical density is the energy measure of such experiments. The results were then parameterised. An optical density is then calculated for each e.m. particle (of the CORSIKA simulations) with given energy and angle of incidence by interpolating the density distributions (Haungs and Kempa, 1998). These procedures account for the response of the detector, including its fluctuations, and for the efficiency and threshold effects of the Pamir experiment.

Figure 2 compares the expected density distribution for different interaction models with a typical data set of the Pamir experiment (Bialobrzeska et al., 1998). Above the large threshold region (the Pamir collaboration quote the threshold to be $\approx$ 4 TeV) a power law distribution is given. Again deviations from the power law behaviour is seen at high energies (large optical densities) due to the missing simulations for primary energies above 10^{16} eV. The behaviour and slope of the simulated distributions closely agree with the measurements, but the differences between the models in the absolute flux still hold. The differences in particle numbers as discussed for Fig. 1 are still evident after the detector simulation and conversion into the measured observable. That means the SIBYLL (version 1.6) and HDPM models predict the largest numbers and their particle fluxes are far off the measurements (note the integral form of the displayed spectra). They seems to produce too many electromagnetic particles above TeV energies at the observation level of Pamir. All the other models agree with the data within the statistical uncertainties of simulations and measurements. The DPMJET

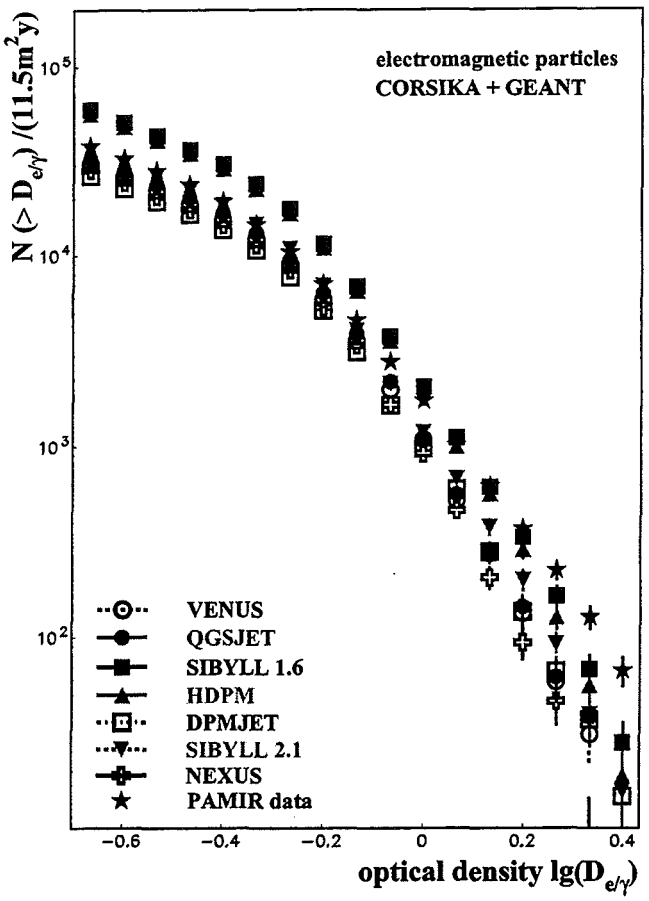

Fig. 2. The integral spectra of the optical density as expected for the Pamir observation level for different interaction models and for a typical data set of the Pamir experiment.

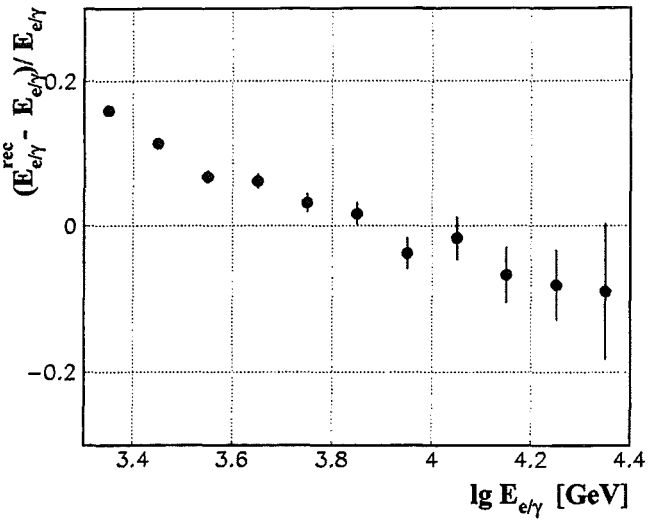

Fig. 3. The energy resolution of the reconstruction procedures of the Pamir experiment for electromagnetic secondary shower particles.

model tends to underestimate the total number of particles. In general the QGSJET and VENUS simulations match the data satisfactorily. This is confirmed by using various measured data samples of the same observable for the comparisons.

4 Energy reconstruction

After the simulation of the optical density the primary energy of the single particle can be reconstructed using the reconstruction procedures of the Pamir experiment. For each particle the energy is reconstructed from the optical density for the $r = 48\,\mu$m diaphragm according to the functions of Roganova and Ivanenko 1987 including the zenith angle of the particle. Figure 3 shows the quality of the energy reconstruction of this procedure for all particles with an integral optical density larger than 0.2. In spite of the high fluctuations in average the reconstruction quality is quite good with a relative error of less than 20% and nearly independent of the species of the particle (gamma or electron), but the resolution is energy dependent. At low energies near the threshold the reconstructed energy is larger than the true one. This could be due to systematic effects at the threshold of the Pamir experiment which may not be included in the calibration procedure. At energies above 10 TeV a tendency to an underestimation of the energy is obvious.

Figure 4 shows the reconstructed energy spectra for different interaction models as expected for the Pamir experiment including the detector response and the reconstruction procedures. The influence of the detection efficiency and threshold effects are visible up to 5 TeV. Again, for energies above 10 TeV the limited Monte Carlo statistics especially for ultra-high primary energies are affecting the spectra. The small energy region and poor statistics does not allow a power law fit to the reconstructed spectra. But the general features of the different interaction models still persist: the expected slopes are not very different, but the total flux varies for the different interaction models more than the uncertainty of the measurements. Nevertheless the reconstructed energy spectra reproduce the initial spectra (i.e. obtained by pure air-shower simulation without detector response and reconstruction efficiencies, Fig. 1) surprisingly well in the energy region between 5 and 10 TeV. A direct comparison in the case of the QGSJET model is shown in Figure 5. Therefore the slope and flux values of the initial spectra (see Table 1) can be compared with the measured energy spectrum (Bialawska, 1999):
$I(> E) = (1.63 \pm 0.13) \cdot 10^{-6} \cdot (E/5TeV)^{-1.93 \pm 0.12}$
given in $[\mathrm{m}^{-2}\mathrm{s}^{-1}\mathrm{sr}^{-1}]$.

The hadronic interaction models VENUS, SIBYLL 2.1, and QGSJET show the best agreement with the measurements. All models reproduce the slope of the integral spectrum within the statistical uncertainty of the measurements, but for the expected flux for particles above 5 TeV some of the models deviate by a factor which is much larger than the uncertainties.

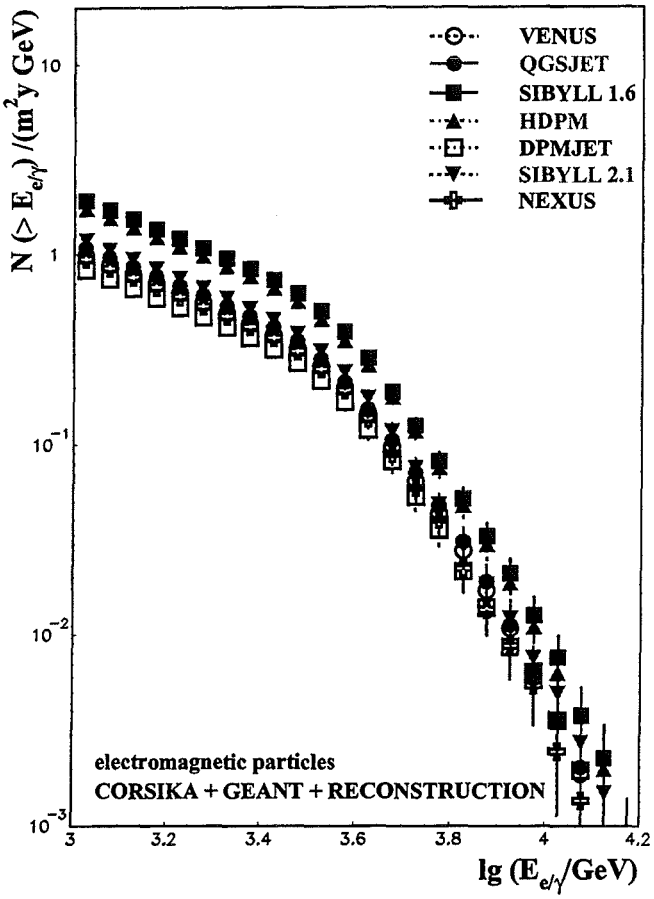

Fig. 4. The energy spectra of electromagnetic secondary shower particles including detector response and reconstruction procedures as expected for the Pamir observation level for different interaction models. The spectra are displayed in integral form and normalised to the measurement of one m^2 and year.

5 Conclusions

The combination of the air shower simulation in the atmosphere (CORSIKA with different high-energy interaction models) and the simulation of the detector response (GEANT) leads to a reasonable reconstruction of the measured energy spectrum of secondary electromagnetic particles. In spite of the excellent agreement of the measurements with expectations using QGSJET or VENUS as high-energy interaction models, the other models cannot be ruled out in general due to the large systematic uncertainties of the analyses. Main sources of systematic effects are the correction of hadronic particles producing spots in the emulsion chambers, which was accounted for up to 20%, and the uncertainty of the chemical composition of the cosmic rays, which is of the same order. Nevertheless the present investigations show a reasonable understanding of the detector response and reconstruction procedures of the Pamir emulsion experiment. Additionally the present results can be used as hints for the interpretation of the various interaction features in the models, especially for the extremely forward direction at relatively low primary energies of 50-1000 TeV.

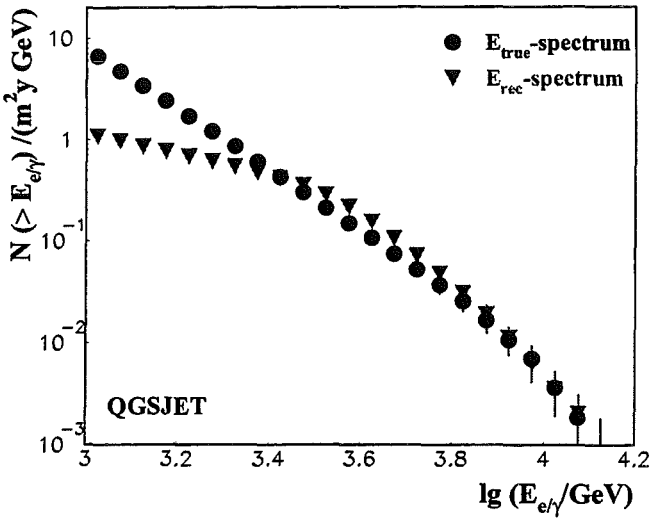

Fig. 5. The energy spectra of electromagnetic secondary shower particles as expected for the Pamir observation level with the interaction model QGSJET. The spectra are displayed in integral form and normalised to the measurement of one m^2 and year for both, the expectation of the pure air-shower development (CORSIKA) and with including detector response and energy reconstruction.

Acknowledgements. We would like to thank Dieter Heck for embedding the models in CORSIKA, and Janek Malinowski for valuable discussion concerning the energy reconstruction.

References

Bialawska, H., 25th Pamir - Chacaltaya Int. Symp., Lodz, 1999.
Bialobrzeska H., et al., Nucl. Phys. B (Proc. Suppl.) 75A, 162, 1998.
Baradzei, L.T., et al.-Chacaltaya and Pamir collaboration, Nucl. Phys. B 370, 365, 1992.
Drescher, H.J., et al., preprint hep-ph/9903296, March 1999.
Engel, J., et al., Phys. Rev. D46, 5013, 1992.
Engel, R., Proc.26th ICRC, Salt Lake City, HE 2.5.03, 1999.
Haungs, A. and Kempa, J., Proc.25th ICRC, Durban, 1, 101, 1997.
Haungs, A. and Kempa, J., Proc.16th ECRS, Alcala, Spain, Ed. J.Medina, p.583, 1998.
Haungs, A., et al., Proc.26th ICRC, Salt Lake City, HE 1.2.23, 1999.
Haungs, A., et al., Nucl. Phys. B (Proc. Suppl.) 97, 134, 2001.
Heck, D., et al., FZKA 6019, Forschungszentrum Karlsruhe, 1998.
Kalmykov, S.S., et al., Nucl. Phys. B (Proc. Suppl.) 52B, 17, 1997.
Ranft, J., Phys. Rev. D51, 64, 1995.
Roganova, T., and Ivanenko, I.P., private communication, 1987.
Werner, K., Phys. Rep. 232, 87, 1993.
Wiebel-Sooth, B., et al., Astron. Astroph. 330, 389, 1998.

Proceedings of ICRC 2001: 315 © Copernicus Gesellschaft 2001

ICRC 2001

Feasibility study of cosmic ray composition measurements with Cherenkov Telescopes using fractal image parameterization

A. Haungs[1,2] and J. Knapp[2]

[1]Institut für Kernphysik, Forschungszentrum Karlsruhe, 76021 Karlsruhe, Germany
[2]Department of Physics and Astronomy, University of Leeds, Leeds LS2 9JT, UK

Abstract. In Earth-bound γ-ray astronomy cosmic rays of 5-500 TeV form the major background. At this energy reliable results on elemental composition of cosmic rays are rare. Direct measurements with balloons or satellites and air shower observations mainly with arrays of particle detectors are stretched to their limits to cover this energy range. An independent measurement of the elemental composition using Cherenkov telescopes promises a better understanding of the composition and provides a test of the simulation programs underlying all the indirect composition estimates. With the air shower simulation program CORSIKA and a detailed simulation of the detector response, Cherenkov images of the Whipple telescope are generated for the cosmic ray (CR) background. The images are parameterized with the well-known Hillas parameterization as well as by fractal and wavelet methods. Special emphasis is given to the recognition of the mass of individual particles.

1 Introduction

Irrespective of ninety years of measurements and the more and more sophisticated experiments and analysis methods the knowledge about the CR elemental composition for primary energies of 10 TeV and above is still poor. The problems are manifold: The low flux of particles limits the statistical accuracy of direct measurements with balloon-borne detectors. Also the estimation and correction of detector efficiencies is increasingly difficult. For indirect measurements via extensive air showers (EASs) the mass resolution is worse due to large intrinsic fluctuations of the showers observables. The conversion of measured observables to primary energy and mass needs indispensably Monte Carlo simulations of the shower development. Here high-energetic hadronic interactions play the key-role in understanding the results. Although for energies close to those in direct measurements accelerator data are available for a calibration of the interaction models, extrapolations to the unknown kinematic region of the extreme forward direction is necessary. Investigations of different observables at the same event or of various independent experiments are necessary to reconstruct the elemental composition and at the same time to understand the interaction mechanisms in more detail.

γ-ray experiments using the atmospheric Cherenkov imaging technique measure as background charged cosmic rays in the interesting energy region of TeV to PeV. The usual method of image parameterization is optimized to separate γ's and hadrons efficiently, irrespective of the masses of the hadrons (Hillas, 1985). Nevertheless there might be a sensitivity of the image parameters to the CR mass. It was shown recently (Haungs et al., 1999), that an alternative parameterization based on fractal and wavelet methods results also in mass sensitive observables. A combination of the parameters may give an alternative measure of the cosmic ray composition in the energy region connecting direct measurements with the results of particle arrays. Additionally, such results would help to advance the understanding of the development of air showers.

Correspondence to: A. Haungs (haungs@ik3.fzk.de)

2 Simulations and image parameterizations

2.1 EAS and telescope simulations

For this analysis sets of simulated images for four CR mass groups were generated. These simulations are performed for the present 10 m-Whipple telescope with a 490 pixel camera (Finley et al., 1999). CORSIKA (v6.0, Heck et al., 1998) is used for the simulation of the shower development and the production of the Cherenkov photons in the atmosphere. High-energy interactions are handled with QGSJET (vers.01, Kalmykov et al., 1997), the low energy part with GHEISHA (Fesefeldt 1985), and the electromagnetic part of the showers is treated by EGS4 (Nelson et al., 1985). 3000 EAS were generated for each primary protons ($E_0 = 0.7 - 200$ TeV), helium nuclei ($E_0 = 0.8 - 300$ TeV), oxygen nuclei ($E_0 =$

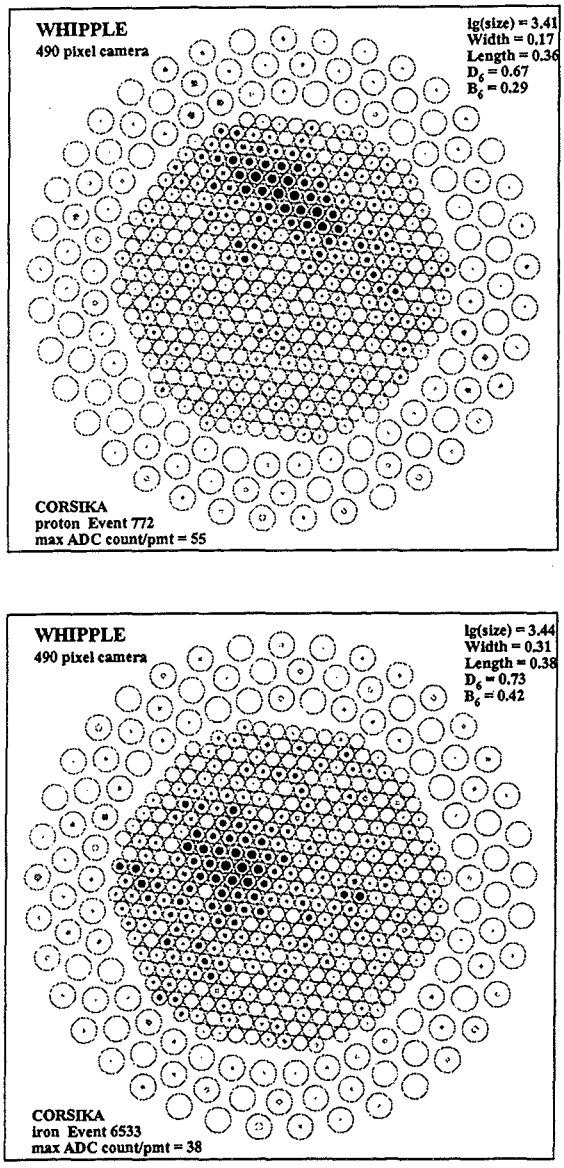

Fig. 1. Examples of simulated Whipple images with the 490 pixel camera. Some of the parameterization results are also given.

$1 - 400\,\mathrm{TeV}$), and iron nuclei ($E_0 = 2 - 500\,\mathrm{TeV}$). The energy ranges were chosen that the resulting sizes cover the range of the Whipple measurements. The energy distribution follows a power law with slope -2.7. The showers arrive uniformly from zenith angles of $18.5° - 21.5°$ and azimuth angles of $179.5° - 181.5°$, i.e. covering the field of view of the Whipple telescope pointing to the south with a zenith angle of 20°. Cherenkov photons reaching the observation level of 2300 m a.s.l. are stored for fifteen virtual Whipple telescopes arranged on a 5×3 rectangular grid with 80/2 m and $80\sqrt{3/4}$ m spacing, such that some of the telescopes form the planned VERITAS configuration. The position of the shower core is scattered from event to event within the telescope array up to 80 m resulting in maximum impact points of up to 180 m. A detailed simulation of the atmosphere, mirror and camera response to the Cherenkov photons is included, as well as a realistic simulation of the night sky background (NSB) (Haungs et al., 2001). For each image the ADC counts of each pixel are stored, and data and simulations are parameterized with the same algorithms. For the parameterization described below, only signals of the smaller inner tubes are taken into account. Fig. 1 shows examples of simulated images from proton and iron showers as seen by the Whipple camera.

2.2 Hillas parameterisation

For the parameterization in terms of first and second order moments only pixels with a signal of $> 4.25\sigma$ of the night sky background (NSB) and neighboring pixels with a signal of $> 2.25\sigma \cdot$ NSB are taken into account. The resulting Hillas parameters can be generally classified into either shape parameters such as *length* and *width* which characterize the extension of the image, or into orientation parameters such as *alpha*, which is the angle of the image length with the direction of the source location within the field of view of the camera. Hadron induced events do not point to a definite source on the sky, hence only the shape parameters can be used. Cherenkov images of showers are mainly elliptical in shape, this is well represented by the *width* and the *length* of the image. Deviations from the ideal elliptical form depending on primary mass might still modify the *width* to *length* ratio.

The *size* of the image is defined as the sum of the ADC counts of those pixels belonging to the image by the definition above. If by chance a pixel exceeds the 4.25σ level, but its position is far away from the image center, it will not change the *size* dramatically, but it will distort the *width* and *length* parameters. On the other hand Cherenkov photons hitting pixels with small entries close to the image center will not be taken into account. The *sum* of the image represents the total content of ADC counts at all inner tubes.

2.3 Fractal and wavelet parameterisation

The development of air showers in the atmosphere varies with primary mass. Different heights of the shower maximum or number of relativistic electrons and muons should be reflected in slightly different distributions and number of Cherenkov photons reaching the telescope. Hence we expect differences in the structure of the images. Pattern recognition tools are for example fractal or wavelet analyses, which result in parameters (multifractal and wavelet dimensions) characterizing the structure of the image of each single event. The idea is to analyse the image on different scale-lengths to reveal deeper structures which may be hidden in a single scale by superimposed Poissonian or Gaussian background fluctuations (Haungs et al., 1999).

For this we divide the image into M = 8, 10, 20, 80, and 320 (with $\nu = log_2\, M$ as fractal scale-length) equally sized, non overlapping cells and calculate the number of ADC counts in each cell. The multifractal moments $G_q(M) = \sum_{j=1}^{M} (k_j/N)^q$

have been computed, with N the total number of ADC counts, k_j the counts in the j^{th} cell and q=2,3,4,5,6 defines the order of the fractal moment. The wavelet moments are $W_q(M) = \sum_{j=1}^{M-1}(\frac{|k_{j+1}-k_j|}{N})^q$, where here the difference of the signals in each scale $(k_{j+1} - k_j)$ defines the moment. G_q and W_q show a proportionality to the length-scale of the form $G_q \propto M^{\tau_q}$ and $W_q \propto M^{\beta_q}$. The exponents lead to the fractal dimensions $D_q = \tau_q/(q-1)$ and wavelet dimensions $B_q = \beta_q/(q-1)$, respectively. Whereas the fractal dimensions characterize more the global structure of the photon distribution in the camera, the wavelet dimensions are more sensitive to local structures.

3 The parameters and their mass sensitivity

Following image parameters are considered for their mass sensitivity: the Hillas parameters *width* and *length*, the fractal parameters D_2 and D_6 and the wavelet dimensions B_2 and B_6. For equal primary energy showers of different masses are expected to have different shapes of the ellipse (*width* to *length* ratio) reflecting the different height of maximum of the shower development in the atmosphere. The fractal dimensions are sensitive to the largest amplitude in the image and how the peak appears on the different length scales. Hence D_2 and D_6 will distinguish between images containing a single large peak in the center and images with several similar sized peaks or smooth distributions. Wavelet parameters examine the differences of neighboring pixels (cells) and how these appear on different length scales. Here light produced by muons or produced at higher altitudes will disperse the image, leading to larger differences from cell to cell and therefore larger wavelet parameters (as example see the right panel in Fig.2).

Heavier primary masses produce less light at observation level for fixed primary energy (Fig.2 left). As the energy is unknown for the recorded images, they have to be classified with the *size* or *sum* of the image. It was found that the mass sensitivity of all the parameters shrinks with *size* or *sum* instead of primary energy (Fig.3). If primary hadrons of different masses produce equal amount of light in the atmosphere, roughly the same shape of the image is expected, but with a flatter and smoother density distribution of the pixels for the heavier primaries (see also Fig. 1). But the *width* increases for heavier primaries due to additional pixels with large amplitudes, presumably from the higher number of muons (Fig.3 left). These additional pixels also change the wavelet parameters (Fig.3 right), but here also smaller amplitudes are taken into account. The fractal parameters, i.e. the overall structure of the image, which are very sensitive parameters for the γ/hadron separation of images (see Haungs et al., 2001) show only poor mass separation for images of same *size*. For both, the fractal and wavelet parameters, the separation improves slightly if they are compared for images of same *sum* instead of *size*. This is understandable, as the *size* does not count the small amplitudes outside the ellipse which influence these parameters.

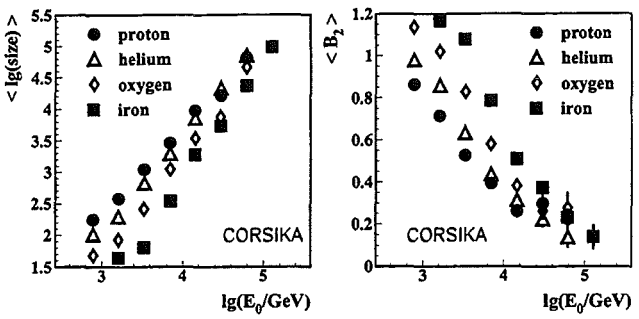

Fig. 2. Mean values of the image parameters *size* and B_2 vs. the primary energy for the different primary particles.

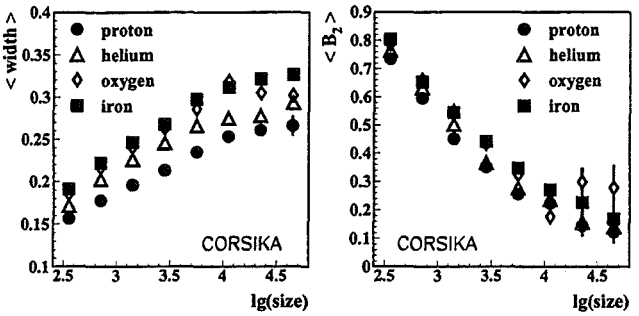

Fig. 3. Mean values of the image parameters *width* and B_2 vs. the *size* of the images for the different primary particles.

The larger the *size*, the better the separation (Fig. 3). This is due to the decreasing event-to-event fluctuation with increasing primary energy (*size* or *sum*). Fig.3 shows the expected mass sensitivity of single parameters. A separation in more than two or three mass groups seems prohibited by the relatively poor mass resolution. Especially for distinguishing between heavier nuclei (e.g. oxygen and iron) the differences at the reconstructed observables are to small. This holds at least for the present Whipple telescope.

4 Neural Net Investigations

We have examined the classification potential of the parameters more quantitatively by an application of an artificial neural net (Lönnblad et al., 1994). The philosophy is that the net is trained with one set and generalized with another independent set of simulated events. The network can then be applied to the measured events, and the events are classified by the network output value. This procedure requires a large set of Monte Carlo generated events, and the number increases about quadratically with the number of input parameters, and with the number of classes. The whole kinematic and geometric range of possibly triggering events have to be covered by simulations. This is fulfilled with the simulations used for this analysis. In a first attempt five input parameters were used and we optimize the net to classify the events in two groups only. For expanding the net to more input parameters or output classes a larger Monte Carlo statistics would be required. We use the inputs: *width*, *length*, D_2, B_2, and

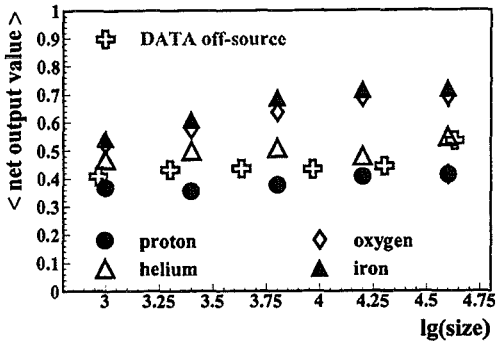

Fig. 4. Average net output values vs. *size* of simulated events for different primary masses and for the measured events.

Table 1. Misclassification matrix: probability that an proton, helium, oxygen, or iron initiated EAS is classified for the light or heavy group. All EAS are taken into account.

	proton	helium	oxygen	iron
light	0.71	0.52	0.36	0.29
heavy	0.29	0.48	0.64	0.71

the *sum*, which are the most independent ones, i.e. with the lowest correlations. In addition to some general cuts (i.e. the Hillas parameterisation was successful and the pixel with the largest ADC count is not at the edge of the inner field of PMTs) we restrict the events to *size* > 500 to be far away from threshold problems for the different primary masses and to cut off most of the images which are produced by single high-energy muons. The net is trained with 2/3 of the simulated proton-sample with output value of zero and 2/3 of the oxygen and iron samples with 1 as output value. After optimizing the net, it is applied to the full Monte Carlo sample and to 3 runs of Crab off-source data. These runs were chosen to have an average zenith angle close to the simulated 20° and to be recorded at good seeing conditions. Fig. 4 shows the average net output value dependent on *size* for the different primaries and the real data set. The separation quality increases with increasing *size*. The training of the net does not use helium nuclei, nevertheless applying the net to helium yields values between the proton and the heavy ones. Table 1 lists the classification probabilities of the trained neural net. The two groups light and heavy are separated with a cut in the neural net output value of 0.5.

With help of calculated classification probabilities the fractions of light and heavy induced primaries of a certain *size* range can be deduced by correcting the numbers of misclassified events. Assuming that only proton and iron primaries exist in the data sample, the fraction of the light sample in a *size* range of 4000 to 16000 ADC counts amounts to $\approx 84\%$. With a more realistic assumption that the light group consists of protons and helium nuclei (1.5:1) and the heavy group consists of oxygen and iron nuclei (1:1) the light part increases to $\approx 98\%$. This increase is only due to changes of the classification probabilities used for the correction procedure. For the range of larger *sizes* the light part decrease slightly to $\approx 94\%$.

These results are estimated for ranges of shower *sizes*. Because of the steeply falling primary energy spectrum of the primaries (of all masses) a natural enhancement of the light primaries occurs. A conversion of the results to an elemental composition in terms of primary energy requires a finer binning in ranges of the size and an examination of the energy dependent trigger and reconstruction efficiency of the different masses. This in turn needs a much higher statistics of Monte Carlo events carefully tuned with the observation conditions of the data set to be analysed. Additionally an improvement of the classification probabilities and the number of classification groups should also be possible with increased statistics.

The whole procedure relies on the Monte Carlo model, especially on the modelling of the high-energy hadronic interactions. By comparing results obtained from different models and with results of direct measurements, systematic uncertainties and differences due to these models can be estimated.

5 Summary

In the present study the principal possibility of composition measurements with existing data of imaging Cherenkov telescopes on an event-by-event basis was demonstrated. First applications to data of the Whipple telescope show a large part of light primaries in the energy range of 10 to 100 TeV. This is expected from an extrapolation of the direct measured single mass group spectra. In addition the light induced showers are enhanced by classifying the sample with the shower size, which decreases for fixed energy with the primary mass. A more detailed investigation of the composition with improved statistics is in preparation.

Acknowledgements. A.H. would like to acknowledge the Royal Society of U.K. and the Whipple collaboration for supporting the presented studies at the Leeds University. Special thanks are given to H.Rebel and H.Blümer that they plead for the possibility of these studies within the framework of the Forschungszentrum Karlsruhe.

References

Fesefeldt, H., PITHA-85/02, RWTH Aachen, 1985.
Finley, J.P., et al., AIP Conf.Proc. 515, 301, 1999.
Haungs, A., et al., Astrop.Phys., 12, 145, 1999.
Haungs, A., et al., Proc. of the 27th ICRC, Hamburg, OG 2.4, 2001.
Heck, D., et al., FZKA 6019, Forschungszentrum Karlsruhe, 1998.
Hillas, A.M., Proc. 19th ICRC, La Jolla, Vol.3, 445, 1985.
Kalmykov, N., et al., Nucl. Phys. B (Proc. Suppl.), 52B, 17, 1997.
Lönnblad, L., et al., CERN Preprint, CERN-TH. 7135/94, 1994.
Nelson, W.R., et al., SLAC 265, Stanford Linear Accelerator, 1985.

Proceedings of ICRC 2001: 2910 © Copernicus Gesellschaft 2001

ICRC 2001

Application of fractal and wavelet analysis to Cherenkov images of the Whipple Telescope

A. Haungs[1,2], J. Knapp[2], I. Bond[2], and R. Pallassini[2]

[1]Institut für Kernphysik, Forschungszentrum Karlsruhe, 76021 Karlsruhe, Germany
[2]Department of Physics and Astronomy, University of Leeds, Leeds LS2 9JT, UK

Abstract. Multifractal and wavelet methods are mathematical tools used in pattern recognition and image parameterisation. Their application to images of Cerenkov light from air showers as obtained in the high-resolution camera of the Whipple telescope promises improved gamma/hadron separation over the whole energy range of interest. Using recent data of on/off-source measurements for the Crab nebula and Mrk421 the performance of fractal and wavelet parameters are tested and compared with that of the conventional Hillas parameterisation. The new parameters are independent of the image orientation and depend only on the shape, i.e. on the density distribution, of the image. Hence the methods are of special interest for the search of faint, extended, or diffuse sources of TeV gamma emission. The benefit of fractal and wavelet analyses to Cherenkov image analysis is discussed for the Whipple telescope as well as for an array of telescopes like VERITAS.

1 Introduction

One of the main aims of experiments measuring high-energy cosmic γ-rays using the atmospheric Cherenkov imaging technique is the reconstruction of the energy spectrum of galactic or extragalactic sources. Starting from the raw data several steps are needed to evaluate the spectrum, all depending more or less on Monte Carlo simulations. Strongly model dependent are the selection of γ induced images, the estimation of the telescopes collecting area, and the energy reconstruction (see e.g. Mohanty et al., 1998). Hence it is important to check each step either with different Monte Carlo calculations and/or an independent methodological approach.
In this paper we compare the standard image parameterisation (for γ-selection) in terms of first and second-order moments resulting in the so-called Hillas parameters (Hillas, 1985) with a fractal and wavelet based parameterisation method (Haungs et al., 1999). The latter one uses tools well known from image or pattern recognition applications and is based on the idea that γ-induced Cherenkov light produces a different image than hadron-induced Cherenkov light. In parallel we compare two different Monte Carlo packages for the simulation of the air shower cascades: The KASCADE system (Kertzman and Sembroski, 1994) and the CORSIKA program (Heck et al., 1998).

Correspondence to: A. Haungs (haungs@ik3.fzk.de)

2 Data and simulation base

The following investigation uses a part of the Whipple observatory database on the Crab Nebula recorded with a focal plane detector (Finley et al., 1999) consisting of 379 densely packed 1/2" photomultiplier tubes (PMT) in an inner region and 111 1" tubes in three outer rings (Fig. 1). For the present analysis only the inner PMTs are used. Data of 6 hours of

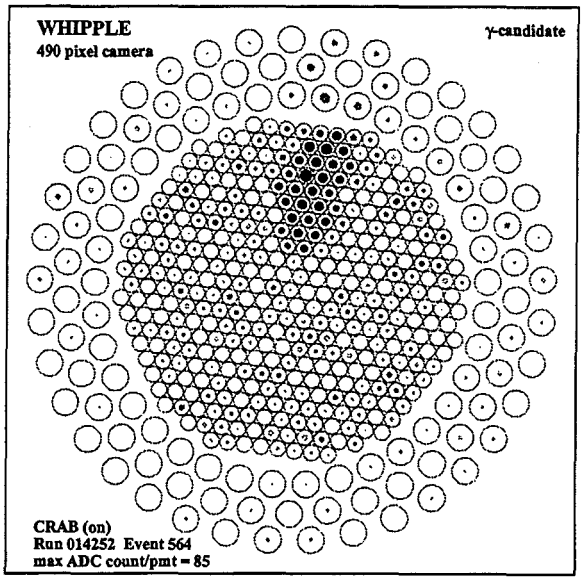

Fig. 1. Example of an recorded Whipple image with the 490 pixel camera, most probable a photon induced event.

on/off Crab observations and of 4 hours on-source measurements of Mrk 421 from the January 2001 flare are analysed. The raw data are calibrated and the ADC values of each pixel for each event are stored for the subsequent image parameterisation.

CORSIKA shower development were performed for primary photons in the energy range of 50 GeV to 30 TeV with a power law (slope of -2.6) energy dependence. High-energy hadronic interactions are simulated with the QGSJET option (Kalmykov et al., 1997). Cherenkov photons reaching the observation level are stored for fifteen virtual Whipple telescopes arranged on a 5×3 rectangular grid with 80/2 m and $80\sqrt{3/4}$ m spacing, such that some of the telescopes form the planned VERITAS configuration. The position of the shower core is scattered from event to event within the telescope array resulting in a uniform core distance distribution up to 80 m and with maximum impact points of up to 180 m. A detailed simulation of the mirror and camera response is performed, including wavelength-dependent light absorption within the atmosphere, mirror reflectivity and quantum efficiency of the PMTs. Noise and night sky background (NSB) are added to each pixel according to measured distributions, i.e. with an asymmetric tail to large ADC values, which can be described, e.g., by a double Gaussian function.

The same NSB was added to a set of Cherenkov images (in photoelectrons/pixel) which were generated by KASCADE simulations, also including a detector response function. This set (provided by Vassiliev, 2001) comprises γ-induced events with fixed energies from 178 GeV to 31 TeV distributed over core distances up to 200 m. The abundances within individual energy bins follow a power law with index ≈ -2.5. More than half a million simulated images are at disposal for further investigations. Both, data and simulated showers are selected for zenith angles of about 20°.

3 Image parameterisation

In addition to the standard parameterisation in terms of first and second order moments, resulting in the well known Hillas parameters, each simulated and recorded image is parameterised in terms of fractal and wavelet moments. The aim is to quantify hidden characteristic structures of the density distributions of the images, invisible by second-order moments but revealed by viewing the image on different scale-lengths. The mathematical procedures described in (Haungs et al., 1999) are applied to the innermost 320 pixels of the camera. Whereas for the Hillas parameterisation only pixels with a signal $\geq 4.25\sigma$ of the NSB (or $\geq 2.25\sigma$ of the NSB if there is a signal in neighbouring pixels) the fractal analysis takes all pixels into account which, after subtraction of the pedestals, have a positive signal. The *size* of an image is defined as the sum of the ADC counts of all pixels used for the Hillas parameterisation.

Fractals: Fractals are structures which display a self-similar behaviour, and the fractal nature of an object is quantified by its fractal dimension. We have calculated multifractal (and wavelet) moments of each image by dividing the image into M = 8, 10, 20, 80, and 320 equally sized, non overlapping parts and by calculating the sum k of ADC counts in each part. The fractal scale-length ν is defined by $\nu = \log_2 M$. The multifractal moments of order q are computed by the following expression $G_q(M) = \sum_{j=1}^{M}(k_j/N)^q$, where N is the total number of ADC counts in the image, k_j is the counts in the j^{th} cell and $q = 2, 3, 4, 5, 6$. If the fractal moments G_q show a power law relation to the parameter M, i.e. $G_q \propto M^{\tau_q}$, then the Cherenkov images exhibit a self-similar structure, i.e. they are fractals. The exponent τ_q is determined from G_q by using the formula $\tau_q = \frac{1}{\ln 2}\frac{d\ln G_q}{d\nu}$. This exponent τ_q is related to the generalized multifractal dimension, D_q, by $D_q = \tau_q/(q-1)$. Using the total signal of each pixel including the NSB, even small images behave like fractals, moreover, an image containing only noise can be regarded as an ideal fractal as it contains only Gaussian or Poissonian parts.

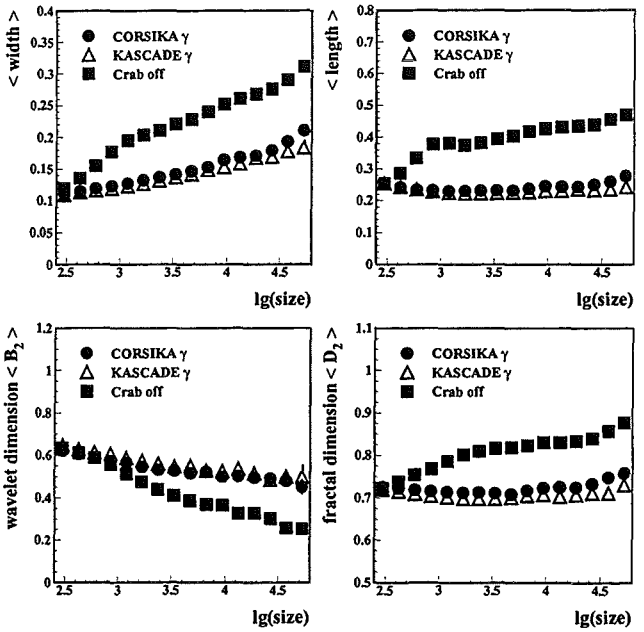

Fig. 2. Mean values of various image parameters vs. the image size in ADC counts for two different simulation programs and for Crab off-source data.

Wavelets: A pattern analysis in terms of wavelets can be regarded as a sequence of filtering processes to examine the presence of local structures on different scale-lengths. When applied to the images, the wavelet moment W_q is calculated, given by: $W_q(M) = \sum_{j=1}^{M-1}(\frac{|k_{j+1}-k_j|}{N})^q$; k_j denotes the ADC count in the j^{th} cell on a particular scale. The wavelet moment is a measure of differences of signals from one scale to the next. Again, a proportionality $W_q \propto M^{\beta_q}$ holds. The slope β of the best-fit regression line to the function $\log W_q$ vs. $\log M$ leads to the wavelet dimension $B_q = \beta_q/(q-1)$ of order q. The wavelet dimensions are sensitive to differences in the average counts in neighboring pixels on different length scales. With vanishing differences β gets smaller.

Photon induced images are more compact and have a smoother change of content from pixel to pixel. Hadron induced images are more jagged, leading to smaller wavelet dimensions and larger fractal dimensions (Fig. 2).

4 Correlations of the parameters

Investigations of the correlations between the different parameters can be used as a measure for their sensitivity, i.e. a measure for the gain on γ/hadron separation by the new parameters. The correlation coefficient c between two variables x and y, is defined as
$c = \sum_{i=1}^{n}(x_i - \overline{x})(y_i - \overline{y}) \,/\, \sqrt{(\sum_{i=1}^{n}(x_i - \overline{x})^2)(\sum_{i=1}^{n}(y_i - \overline{y})^2)}$
and is a measure of the linear association between the two variables. $c \equiv \pm 1$ means a perfect, positive or negative, correlation between x and y, and $c \equiv 0$ means no correlation at all. The four image shape parameters in Table 1 are correlated to each other with roughly the same strength, and the coefficients are clearly < 1. Hence we expect on average a gain in γ/hadron separation sensitivity with the new observables, especially wavelet parameters correlate least with width and length. The correlation between fractal and wavelet parameters of different q are larger than those shown in Tab. 1, but lowest for B_2 with B_6 and D_2 with D_6, respectively. Therefore we use B_2, B_6, D_2, and D_6, to examine the structure of the Cherenkov images. It is important to note the low correlation of all shape parameters with the size of the image, which entails a uniform efficiency over the whole energy range if selection cuts are applied.

Table 1. Correlation coefficients for image parameters calculated with the whole set of simulations. Below the diagonal are the values for the KASCADE simulations, above those for CORSIKA generated showers.

	Width	Length	D_6	B_6	Size
Width		0.807	0.840	0.707	0.339
Length	0.802		0.836	0.747	0.199
D_6	0.843	0.816		0.878	0.224
B_6	0.705	0.718	0.870		0.148
Size	0.290	0.168	0.199	0.135	

5 Comparisons of the Monte Carlo models

In general the images for primary photons agree very well between the two different Monte Carlo models. Fig. 2 and Table 1 show that, for a given size, the image parameters differ only slightly. But there are differences in the lateral distribution of the Cherenkov photons: CORSIKA produces a few more photons than the KASCADE model (Fig. 3). Furthermore CORSIKA has larger fluctuations in the size distribution from shower to shower displayed in Fig. 3 (right panel). Hence the simulated size-to-energy relation, which is an important factor for the energy reconstruction, seems to

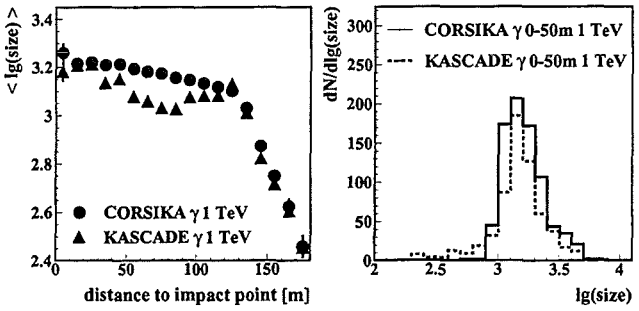

Fig. 3. Comparison of the size distributions of CORSIKA and KASCADE for fixed primary energy. Left: size as function of core distance; right: size distribution for a range of core distances.

be more sensitive to differences of Monte Carlo generators than the parameterisation of the image shapes.

6 Quality of γ/hadron separation

The quality of the γ/hadron separation achieved with different image parameters is estimated by looking at the significance of the photon excess of the standard γ-source, the Crab Nebula. After some general cuts (i.e. that the Hillas parameterisation was successful and the pixel with the largest ADC count is not at the edge of the inner field of PMTs) the significance is calculated from the number of excess events in the range of the orientation parameter $\alpha < 15°$, according to the likelihood ratio method described by Li and Ma, (1983). Without any further cuts the significance of the on/off data used is determined to be 3.9σ. The standard cuts of the Whipple Collaboration (Mohanty et al., 1998), the so-called supercuts, lead for the same data set to a significance of 10.7σ, but with the relatively small number of 346 excess events. These supercuts use the fact that the photons are coming directly from the source (shape and orientation parameters). For the detection of extended or diffuse sources only shape parameters can be used. Here the new observables which are pure shape parameters allow for improvement. To check this, the standard cuts were weakened and only the shape parameters width and length have been used, resulting

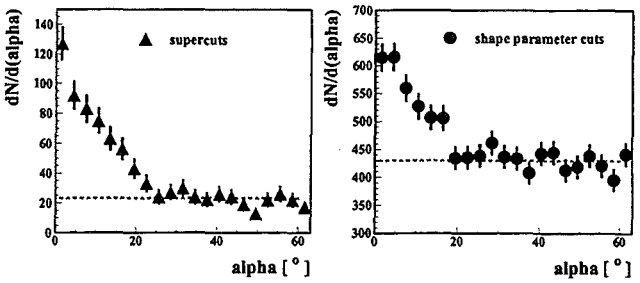

Fig. 4. Distribution of the α parameter for the Mrk421 data after cut on the shape parameters (width, length, D_2,D_6,B_2, and B_6) and after the Whipple standard cuts.

in 6.6σ, with 549 excess events. This can be compared with 5.1σ, with 763 excess events, obtained by cuts on the fractal parameters, only. These cuts on D_6, D_2, B_6, and B_2 have been optimized by comparing the simulated distributions for γ with the Crab off-source data. The fractal and the weakened Hillas cuts together (only shape parameters) result in a significance of 7.5σ, with 489 excess events, clearly improving the performance over both sets of cuts alone. The combined shape cuts were also applied to Mrk421 on-source data. Fig. 4 shows the α-distribution after this selection and after the supercuts. For the shape cuts the background remains larger but also the γ selection efficiency is increased.

7 Neural net investigations

The correlation between the parameters are not strictly linear and also have a varying dependence on the size. Therefore, linear cuts might not be the best way for the γ-selection. A multivariate non-parametric classifying method seems a better choice. To investigate this we use an artificial neural network tool (Lönnblad et al., 1994) with five input observables: width, length, D_2, B_2, and the size. We restrict the events to sizes > 500 to be far away from threshold problems (see also Fig. 2). The net is trained with the CORSIKA γ-sample for an output value of zero and the Crab off-source data (for 1 as output). After optimizing the net parameters the network-classification is applied to Crab and Mrk421 on-source data. Fig. 5 shows the distribution of the net output values after adjusting the network and the resulting α-distributions for events with a network output value of < 0.15. The significance of the γ selection for the Crab on/off data is 9.5σ. It should be noted that again only shape parameters are used and the significance reached after the neural network application is better than with linear cuts on the same parameters. The net is trained with Crab off-data. Though the result for the AGN data is very promising, we expect a bias for the application of the trained network to Mrk data. For a detailed investigation with the presented method off-data of the corresponding region of the sky should be used.

8 Implications for a telescope array

For forthcoming experiments which use telescope arrays, it is important how the image parameters work if several images of the same shower are available. The simplest ansatz is to average the parameters and take the mean value. This is done for the CORSIKA showers using telescope positions of VERITAS. On average 6 to 7 images with successful parameterisation are available for each γ event. Fig. 6 compares the mean values with the distributions of single telescope measurements for the width and one of the fractal parameters. The distributions get narrower for all parameters, especially for the new parameters which indicates a very welcome robustness of this analyses technique. Thus, with a given impact point an improved γ/hadron separation can be achieved, even in this simplest case of multi-telescope analysis. Certainly more sophisticated methods can be developed.

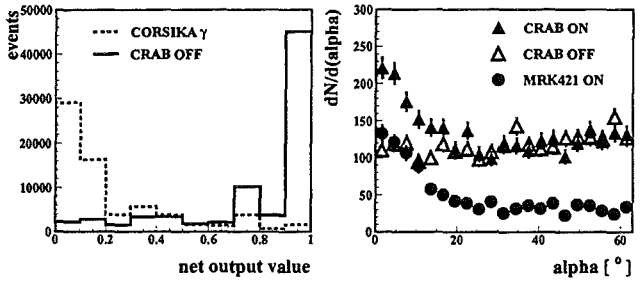

Fig. 5. Left: output of the neural network after training. Right: α distribution of Crab on/off and Mrk421 on-source data after a cut on the neural network output value < 0.15.

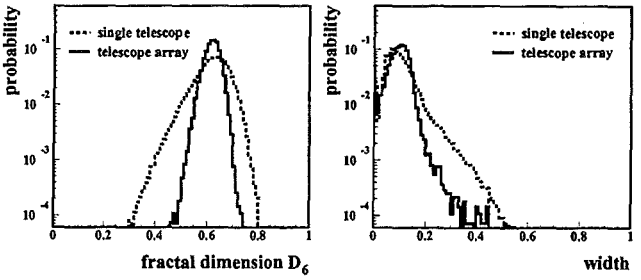

Fig. 6. Probability distribution of two image parameters for a single telescope and the mean value over an array of 7 telescopes.

9 Summary

Whipple images can be parameterised by fractal and wavelet methods. The parameters presented here contain complementary information to the well-known Hillas parameters. They are only shape dependent, i.e. can be used for the search of extended or diffuse sources. Non-parametric methods like artificial neural networks can improve the γ/hadron separation efficiency.

Acknowledgements. The authors thank Vladimir Vassiliev for providing the KASCADE simulations. A.H. greatly acknowledges the support of the Royal Society, UK. A.H. is also grateful to the Whipple Collaboration for the disposal of the data and analysis software, and to the Leeds group for the friendly working atmosphere.

References

Finley, J.P., et al., Proc. *Towards a Major Atmospheric Cherenkov Detector VI*, AIP Conf.Proc. 515, 301, 1999.
Haungs, A., et al., Astrop.Phys., 12, 145, 1999.
Heck, D., et al., FZKA 6019, Forschungszentrum Karlsruhe, 1998.
Hillas, A.M., Proc. 19th ICRC, La Jolla, Vol.3, 445, 1985.
Kalmykov, N., et al., Nucl. Phys. B (Proc. Suppl.), 52B, 17, 1997.
Kertzman, M.P. and Sembroski, G.H., NIM A, 343, 629, 1994.
Li, T.P. and Ma, Y.Q., Astrop.J., 272, 317, 1983.
Lönnblad, L., et al., CERN Preprint, CERN-TH. 7135/94, 1994.
Mohanty, G., et al., Astrop.Phys., 9, 15, 1998.
Vassiliev, V., private communication, 2001.

Proceedings of ICRC 2001: 944 © Copernicus Gesellschaft 2001

ICRC 2001

The charge ratio of atmospheric muons below 1.0 GeV/c: Status and Perspective

I. M. Brancus[1], J. Wentz[2], B. Vulpescu[1,3], H. Rebel[2], A. F. Badea[1], A. Bercuci[1,2], H. Bozdog[1], M. Duma[1], H. J. Mathes[2], M. Petcu[1], C. Aiftimiei[1], and B. Mitrica[4]

[1]IFIN-HH Bucharest, Romania
[2]Forschungszentrum Karlsruhe, Institut für Kernphysik, Germany
[3]Universität Heidelberg, Physikalisches Institut, Germany
[4]Faculty of Physics, Bucharest University, Romania

Abstract. The compact WILLI device, built in IFIN-HH Bucharest (44°26'N latitude, 26°04'E longitude and 85 m a.s.l.) at a vertical cut-off rigidity of 5.6 GV, has been used for measurements of the charge ratio in the vertical atmospheric flux at momenta below 1 GeV/c. In this low energy range the studies of muon charge ratio provide information useful for the discussion of the so-called atmospheric neutrino anomaly and for studies of atmospheric neutrino and antineutrino fluxes. The experimental method is based on the observation of the reduced effective lifetime of negative muons, stopped in matter, as compared to the lifetime of positive muons. Avoiding the difficulties and the systematic errors of magnetic spectrometers, results with high accuracy are obtained, indicating a decrease of the muon charge ratio from 1.30 (at 0.87 GeV/c) to 1.15 (at 0.24 GeV/c). The detector WILLI has been recently transformed in a rotatable device for measuring the muon charge ratio for different angles of incidence in azimuthal and zenithal range. With such perspective a systematic "muon charge ratio spectroscopy" may provide interesting geophysical observations.

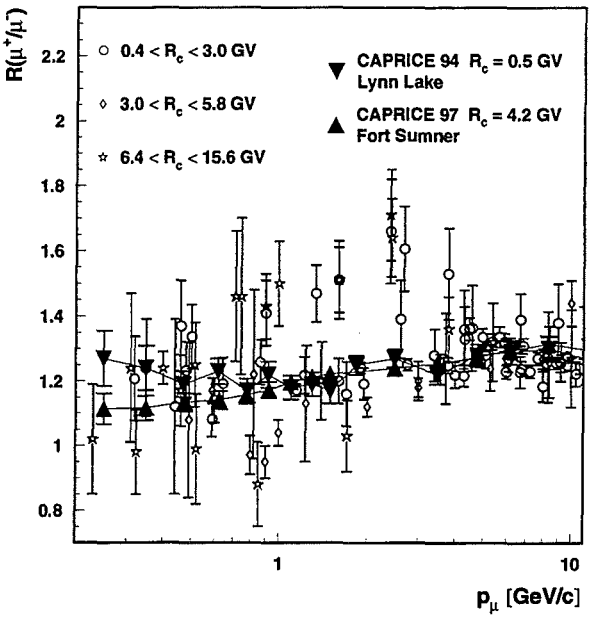

Fig. 1. Compilation of measurements on the charge ratio of vertical muons at low muon momenta. The different symbols stand for different intervals of the geomagnetic cut-off R_c at the location of the experiment (Vulpescu et al., 1998; Kremer et al., 1999).

1 Introduction

At low energies the actual interest in studies of the muon charge ratio arises from the aspects related to the so-called atmospheric neutrino anomaly and from examining the effects of the Earth's magnetic field on the propagation of secondary cosmic rays (Ryazhskaya, 1996). When the primary cosmic radiation interacts with the Earth's atmosphere, baryons and mesons are produced. Atmospheric muons originate mainly from the decay of charged pions and kaons in muons and the subsequent decay of the muons:

$$\begin{array}{llll} \pi^{\pm} & \rightarrow \mu^{\pm} + \nu_{\mu}(\overline{\nu_{\mu}}) & 99.99\,\% & \tau = 26\,ns \\ K^{\pm} & \rightarrow \mu^{\pm} + \nu_{\mu}(\overline{\nu_{\mu}}) & 63.51\,\% & \tau = 12\,ns \end{array}$$

Correspondence to: I. M. Brancus (iliana@ifin.nipne.ro)

Muons have a relative large lifetime $\tau_0 = 2.2\,\mu s$, thus only part of them decay:

$$\mu^+ \rightarrow e^+ + \nu_e + \overline{\nu_{\mu}}$$
$$\mu^- \rightarrow e^- + \overline{\nu_e} + \nu_{\mu}.$$

Considering the decay chains, it is obvious that the ratio of positive to negative atmospheric muons, called the muon charge ratio:

$$R_{\nu} = \frac{\mu^+}{\mu^-}$$

maps the neutrino production and carries information on the hadronic interactions, used in the calculations of atmospheric

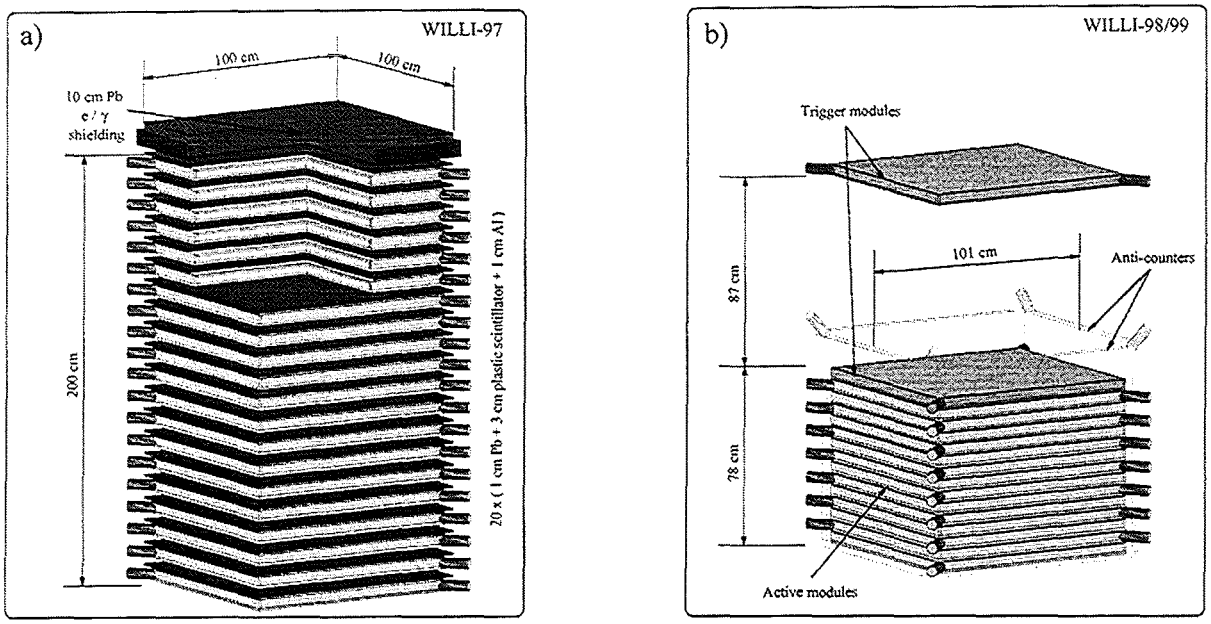

Fig. 2. a) The original sampling calorimeter configuration of the WILLI detector used in WILLI-97 runs. b) The second configuration, improved for the measurements on the muon charge ratio used in WILLI-98 and WILLI-99 runs.

neutrino fluxes. Super-Kamiokande (Fukuda et al., 1998) and other experiments find that the ratio of muonic to electronic neutrinos is much smaller than the theoretical predictions. In addition, the effect is depending on the angle of incidence of the neutrinos. A possibility to verify the invoked models, which are used for the neutrino flux calculations, is to compare the theoretical results for the muon flux, with the experimental data (Wentz et al., 2001).

The compilation of muon charge ratio values measured in the last decades shows that at higher energies all experiments are consistent with a value $\frac{\mu^+}{\mu^-} \approx 1.3$ (Fig. 1). At energies lower than 1.0 GeV, the experimental uncertainties appear to be larger and the data disagree with each other. This finding led us to perform measurements in this energy range.

2 The method and the apparatus

An experiment have been developed for studying the charge ratio of atmospheric muons with an electromagnetic calorimeter WILLI (Weakly Ionizing Lepton Lead Interactions) set-up in IFIN-HH Bucharest, related to studies of the KASCADE experiment. Differently from other experiments, using magnetic spectrographs, in which the charged particle trajectories are measured before and after traversing a magnetic field, our method (Vulpescu et al., 1998) to determine the muon charge ratio is based on the different behavior of positive and negative muons stopped in matter. While positive muons decay with their natural life time, the negative muons are captured in atomic orbits and form muonic atoms, leading to a shorter lifetime of negative muons in matter. The WILLI device measures the effective life-time of the stopped muons for both charge states by observing the appearance of decay electrons and positrons after the muon stopped.

The initial configuration, WILLI-97 (Fig. 2a), consisted of 20 modules, each made of a lead plate of 1 m^2 area, 1 cm thick and a plastic scintillator of 90 x 90 x 3 cm^3, contained in an aluminum box (1 cm thick lateral walls and bottom and 1 mm cover) (Vulpescu et al., 1998).

In a further step (Fig. 2b), the detector has been optimized for the measurement of the muon charge ratio by removing the lead plates and improving the geometry in order to have a background rejection using four scintillator modules in vertical position as anti-counters to cover the sides of the detector (Vulpescu, 1999). With this configuration two sets of measurements have been performed with the detector placed at the basement of the Nuclear Physics Department under 60 cm reinforced concrete (WILLI-98) and in another building with less shielding material above, where data have been taken for muons at lower energy, WILLI-99 (Vulpescu et al., 2001).

The detector is equipped with 40 photomultipliers providing energy deposit (amplitude, by 40 anodes and 40 dynodes) and time information (by 40 dynodes, from which 32 are analyzed, 28 signals of 14 layers and 4 signals of anti-counters). The trigger is made out of four separate signals corresponding to two of the detector layers which define the accepted solid angle of the device. The light of the scintillator is collected by two photomultipliers with wavelength shifters. The energy signals taken from the anode and the third dynode are conducted to an ADC. The timing signals, taken from the dynodes are analyzed by a Multiple Time Digital Converter. The signature of a stopped and decaying muon is a particle triggering the telescope, but not penetrating till the bottom of

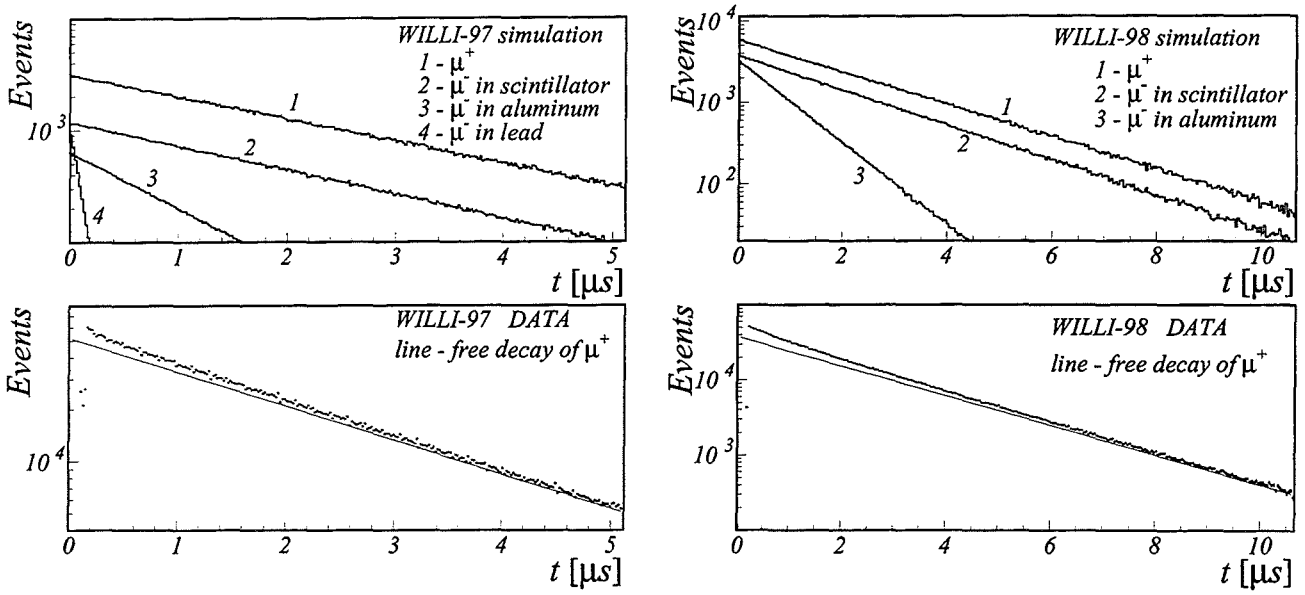

Fig. 3. Upper figures: Monte Carlo simulation results on the contribution of different absorber materials to the total decay curve, assuming $N(\mu^+)/N(\mu^-) = 1$. Lower figures: The experimental decay curves compared with the free decay of positive muons.

the scintillator stack, together with the appearance of a delayed particle in the surrounding of the stopping locus. From the time difference between the incoming muon and the decay electron, the spectrum of the decay times is registered.

3 Monte Carlo simulations and results

The total decay curve of all muons measured in the detector is a superposition of several decay laws :

$$\frac{dN}{dt} = \frac{N_0}{(R+1)}[Rc_0\frac{1}{\tau_0}exp(\frac{-t}{\tau_0}) + (\Sigma c_j \rho_j \frac{1}{\tau_j} exp(\frac{-t}{\tau_j}))]$$

where $R(\frac{\mu^+}{\mu^-}) = \frac{N^+}{N^-}$ represents the muon charge ratio, N^+, N^- being the number of positive and negative muons, respectively, $N_0 = N^+ + N^-$, ρ_j gives the decay probability, and τ_j indicating the mean lifetime of μ^- with index j for different absorber materials, index 0 standing for positive muons.

The expression contains four detector dependent constants c_j, for WILLI-97 and three constants for WILLI-98/99, accounting for the stopping power in the materials and the detection efficiencies, given by the detector geometry, laboratory walls, thresholds, and angular acceptance, which have been determined by extensive detector simulations using the code GEANT (CERN, 1993). The charge ratio of the muons is estimated by fitting the decay law above to the experimental data.

Fig. 3 shows the results of the simulations indicating the decay exponentials for different materials and the comparison of the experimental decay curve with the free decay of positive muons. One notices that aluminum provides the best discriminating effect, reducing significantly the effective mean life time of negative muons as compared to that of positive muons, and the decay probability for Al is 39.05 % while for Pb only 2.75 %. It is seen also the improvement by removing the lead absorbers in the new configuration, resulting in an increase of the number of the detected muons which are stopped in aluminum.

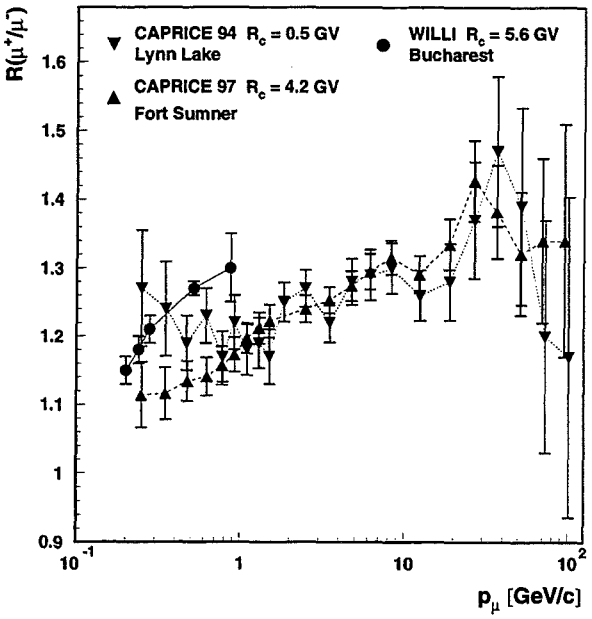

Fig. 4. The WILLI results for the muon charge ratio at sea-level together with recent results from CAPRICE experiment for two locations with different geomagnetic cut-off rigidities (Kremer et al., 1999).

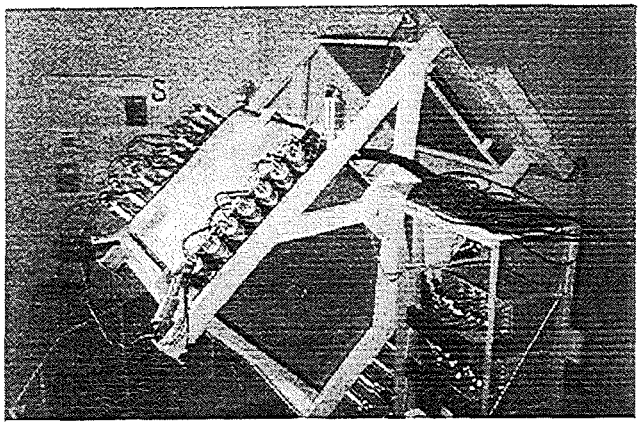

Fig. 5. A photograph of the modified WILLI detector for measuring muons with different angles-of-incidence.

The Tab. 1 presents the results of all three experiments with different detector configurations. In the WILLI-99 experiment the upper and the bottom sections of the detector have been analyzed separately.

$< p_\mu >$	$< \theta_\mu >$	$R(\frac{\mu^+}{\mu^-})$	ΔR	WILLI
0.87 GeV/c	26°	1.30	0.05	1997
0.52 GeV/c	19°	1.27	0.01	1998
0.28 GeV/c	16°	1.21	0.02	1999-lower half
0.24 GeV/c	17°	1.18	0.02	1999-full
0.20 GeV/c	19°	1.15	0.02	1999-upper part

Table 1. The results of the muon charge ratio measurements WILLI-97, WILLI-98 and WILLI-99 at sea level, p_μ and θ_μ stand for the momentum and zenith angle of the muons.

Fig. 4 shows the results of WILLI compared to other recent experiments (Kremer et al., 1999). The WILLI results indicate a smooth decrease of the charge ratio towards lower energy, which could be expected due to geomagnetic cut-off. The CAPRICE experiment reported a similar decrease, but with lower values, for New Mexico, at nearly the same geomagnetic cut-off as in Bucharest. The CAPRICE results for Lynn Lake (where actually no cut-off effect is expected) show higher values for lower energy, but with a strange modulation around $p_\mu = 0.8\,\mathrm{GeV/c}$.

4 Concluding remarks

The measurements of the muon charge ratio by means of magnetic spectrometers are affected by systematic effects at low muon energies due to problems in the particle and trajectory identification, leading to quite different results. Our method overcomes such difficulties by measuring the lifetime of muons stopped in matter. The measurements indicate a muon charge ratio value of 1.3 at a momentum of 0.8 GeV/c, decreasing to 1.15 at 0.2 GeV/c, what can be attributed to the geomagnetic cut-off. Our results are different from the CAPRICE results for Fort Summer in New Mexico where the geomagnetic cut-off is similar to that in Bucharest.

The WILLI detector is a suitable instrument for the further investigation of the modulation of the muon charge ratio and therefore of the neutrino fluxes by the geomagnetic cut-off. The details about the geomagnetic influence have not been systematically explored using the observation of muons with different arrival directions. The WILLI detector is now modified in a rotatable set-up (Fig. 5), which will allow precise measurements of the East-West effect, caused by the anisotropy of the primary proton flux and the local magnetic field, bending charged particles on their way through the atmosphere.

Acknowledgements. The authors affiliated to IFIN-HH Bucharest are grateful for the support received from the International Bureau Bonn, by WTZ-Project RUM-14-97 with the Romanian Ministry for Education and Research and from the Institut für Kernphysik, Forschungszentrum Karlsruhe. Parts of the work have been supported by the grant FZK I/72-709 of Volkswagen-Stiftung and by the grant WE 2426/1-1 by the Deutsche Forschungsgemeinschaft.

References

CERN Program Library Long Writeups W5013, 1993.
Y. Fukuda et al., Phys. Rev. Lett. 81, 1562–1567, 1998; Phys. Lett. B 433, 9–18, 1998; Phys. Lett. B 436, 33–41, 1998.
J. Kremer et al., Phys. Rev. Lett. 83, 4241–4244, 1999.
O.G. Ryazhskaya, Il Nuovo Cim. 19C, 655, 1996;
B. Vulpescu et al., Nucl. Instr. and Meth. A414, 205–217, 1998.
B.Vulpescu, Report FZKA 6368, Forschungszentrum Karlsruhe, 1999.
B. Vulpescu et al., J. Phys. G.: Nucl. Part. Phys. 27, 977–991, 2001.
J. Wentz et al., J. Phys. G. Nucl. Part. Phys, in press; these proceedings

Proceedings of ICRC 2001: 1167 © Copernicus Gesellschaft 2001

ICRC 2001

Simulation of atmospheric neutrino fluxes with CORSIKA

J. Wentz[1], A. Bercuci[1,2], D. Heck[1], H.J. Mathes[1], J. Oehlschläger[1], H. Rebel[1], and B. Vulpescu[2,3]

[1]Forschungszentrum Karlsruhe, Institut für Kernphysik, Karlsruhe, Germany
[2]"Horia Hulubei" National Institute of Physics and Nuclear Engineering, Bucharest, Romania
[3]Universität Heidelberg, Physikalisches Institut, Heidelberg, Germany

Abstract. The simulation program CORSIKA originally designed for the four-dimensional simulation of extensive air showers has been modified for the calculation of atmospheric neutrino fluxes. A detailed simulation of the geomagnetic cut-off with GEANT using the International Geomagnetic Reference Field, tables of the geomagnetic field, a description of the solar modulation, an elevation model for the whole Earth, and various atmospheric models for different climatic zones and seasons have been added to standard CORSIKA in order to allow the simulation of low energy primary particles. Different hadronic interaction models are compared on the basis of recent results for the flux and the charge ratio of atmospheric muons. The verified models are used to calculate separately the neutrino fluxes from the lower and upper hemisphere for Super-Kamiokande. The results of CORSIKA confirm the existence of the atmospheric neutrino anomaly.

1 Introduction

The new results of the Super-Kamiokande experiment provide high evidence for the atmospheric neutrino anomaly. Besides the deviation in the integral ratio $R = (\nu_\mu + \overline{\nu_\mu}) / (\nu_e + \overline{\nu_e})$ the dependence of R on the angle of incidence is a convincing proof of the anomaly (Fukuda et al., 1998). After establishing the effect the experiment turns now to a phase of precision measurements in order to identify the oscillation channel (Fukuda et al., 2000) and further effects, like the East-West asymmetry (Futagami et al., 1999). These investigations request the precise knowledge of the theoretical neutrino fluxes. Conventional simulations, done in one-dimensional approximations, neglecting all transversal momenta, the deflection of the charged particles in the atmosphere and most geographical influences, are hardly able to meet the required accuracy.

In this paper CORSIKA (Heck et al., 1998), being originally an air shower simulation code is extended to allow the simulation of low energy primary particles. The results are verified by simulating the fluxes and the charge ratio of atmospheric muons and comparing with experimental results. The results for the fluxes of atmospheric neutrinos at the Super-Kamioka site are compared with the experimental and theoretical results.

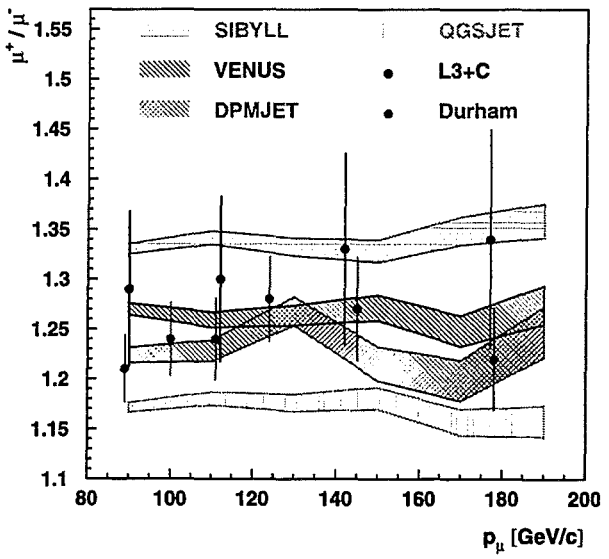

Fig. 1. Simulation of the muon charge ratio at higher energies in comparison with experimental data.

2 CORSIKA and the extensions for the simulation of low energy primary particles

CORSIKA enables fully four-dimensional simulations of extensive air showers. The particle transport includes the particle ranges defined by the life time of the particle and the cross-section with air. Ionization losses, multiple scattering, and the deflection in the local magnetic field are considered. The decay of particles is simulated in exact kinematics, and the muon polarization is taken into account. The

Correspondence to: J. Wentz (wentz@ik3.fzk.de)

difference of CORSIKA from other simulation tools is the optional availability of six different models for the high energy hadronic interaction and of three different models for the low energy hadronic interaction. The threshold between the high and low energy models is set to $E_{Lab} = 80\,\mathrm{GeV/n}$.

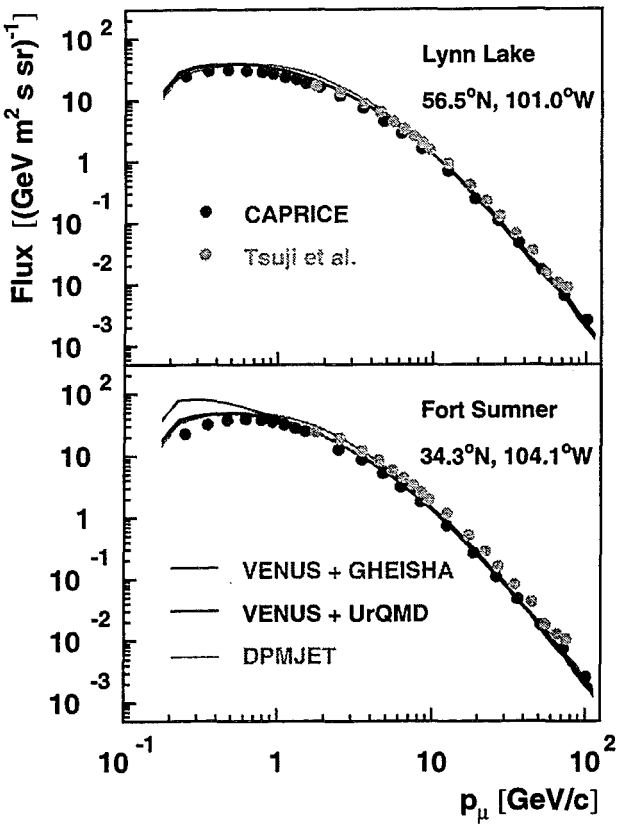

Fig. 2. The differential muon flux compared with experimental results. The results of Tsuji et al. are corrected for the altitude.

In order to simulate primary particles at very low energy, CORSIKA has been extended by a description of the geomagnetic cut-off and the solar modulation. For most places on Earth the geomagnetic cut-off is stronger than the visible influence of the solar modulation. Therefore the geomagnetic cut-off is simulated in a detailed microscopic calculation as described in Wentz et al. (2001) while the solar modulation is handled by the parameterization of Gleeson and Axford (1968).

In order to simulate all possible angles of incidence the "curved" version of CORSIKA is used, where the curvature of the Earth's atmosphere is approximated by sliding plane atmospheres. The flux, the composition, and the spectrum of the primary cosmic rays are compiled from the recent results of the prototype mission of the AMS experiment (Alcaraz et al., 2000).

The geographical influences for the different places on the Earth are taken into account by various parameter tables. In the computational procedure each primary particle is first randomly distributed over the whole Earth. After the check for the geomagnetic cut-off the correct atmospheric model for the geographical latitude and season, the values of the local magnetic field and the elevation over sea-level are set, before the interaction of the particle in the Earth's atmosphere is calculated. All neutrinos passing the area around Kamioka are selected and used in the further analysis. This complete way of the simulation avoids various error sources in the relative normalization between different simulations for different angles of incidence, different solid angles, etc.

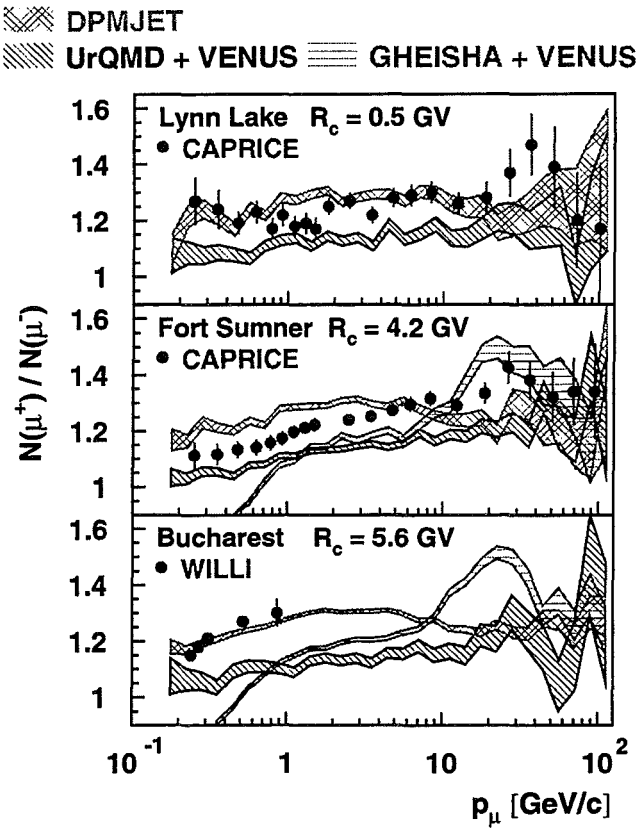

Fig. 3. The charge ratio of muons as simulated by CORSIKA compared with experimental results.

3 Simulation results for atmospheric muons

A verification of the calculation results for neutrino fluxes, and especially for the used interaction models can be done by studying atmospheric muon fluxes. In addition to the total muon flux which is biased by the error in the total primary flux the charge ratio of muons provides an independent test. Fig. 1 shows the results for a simulation of high energy muons with four different high energy interaction models in comparison with experimental data (Fletcher, 1994; Kalmykov et al., 1997; Baxendale et al., 1975; Hebbeker et al., 2000). VENUS (Werner, 1993) and DPMJET 2.5 (Ranft, 1999) agree best with the experimental results and are therefore used in all further simulations.

For the simulation of the low energy hadronic interaction there are three different, selectable models in CORSIKA. Beside GHEISHA (Fesefeldt, 1985) and UrQMD (Bleicher et

al., 1999), DPMJET can be used with some modifications, too.

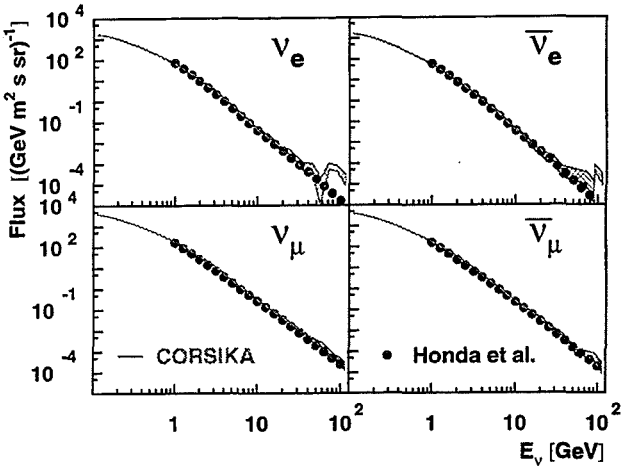

Fig. 4. Vertical neutrino fluxes in Kamioka.

Fig. 2 and Fig. 3 show the differential muon flux and the charge ratio for selected places on Earth where the results can be compared directly with experimental results (Kremer et al., 1999; Tsuji et al., 1998; Vulpescu et al., 2001). While the data for the differential muon flux exclude only GHEISHA as reliable interaction model, the muon charge ratio provides a more decisive test. GHEISHA is again far from reality but also UrQMD gives in all cases a low charge ratio, while the result of DPMJET show a good agreement with the experimental results. The deviation for Fort Sumner has to be questioned because the geomagnetic cut-off in Fort Sumner and Bucharest is nearly equal. Therefore the differences in the experimental values and the continuous increase of the charge ratio in the CAPRICE measurement for Fort Sumner far beyond the geomagnetic cut-off seem to indicate experimental problems in this particular measurement.

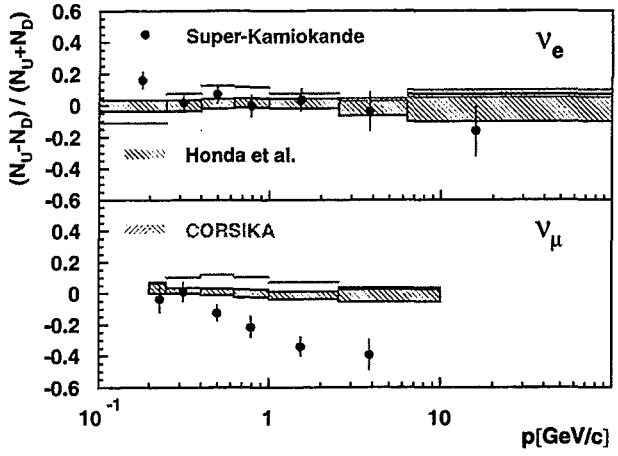

Fig. 5. The up-down asymmetry of the neutrino fluxes in Kamioka. The experimental angular resolution is taken into account.

The influence of the geomagnetic cut-off can be seen in the comparison of the CAPRICE results for Lynn Lake with the WILLI results for Bucharest. The charge ratio of muons is nearly constant unless the geomagnetic cut-off clips the high excess of low energy primary protons, as seen in the results for Bucharest. This effect is nicely reproduced by CORSIKA using DPMJET as interaction model, while using UrQMD the effect is covered by problems of the model.

4 Atmospheric neutrino fluxes for Kamioka

CORSIKA with DPMJET including the described extensions has been used to simulate the atmospheric neutrino fluxes for Kamioka. Fig. 4 shows the results for the vertical neutrino fluxes in comparison with the calculation results of Honda et al. (1995). The agreement in the spectral shape and the absolute normalization is impressingly good.

For the further comparisons of the simulations with the experimental results of Super-Kamiokande, the CORSIKA results have been processed further with a straight forward geometrical simulation of the detector. The scattering angle between the neutrino and the detected charged lepton and the corresponding energy difference are taken into account. The cylindrical shape of the detector and the ranges of muons are used to discriminate between the fully and partially contained events. The data are weighted for the linear increase of the neutrino cross-sections, but data are normalized in absolute scale to the Honda simulations, where necessary.

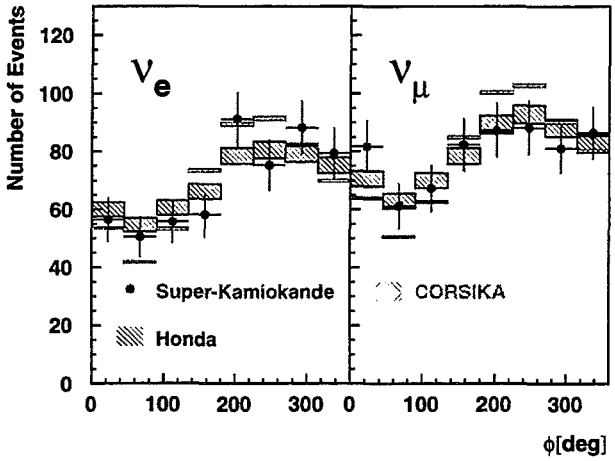

Fig. 6. Azimuthal dependence of the neutrino fluxes in Kamioka.

The CORSIKA result for the ratio between upward and downward neutrino fluxes reveals a substantial difference to previous calculations (Fig. 5). The flux of upward traveling neutrinos is about 15 % higher than the downward flux predicted by CORSIKA. This is a direct consequence of the difference in the geomagnetic cut-off between Kamioka and its antipode region in the South Atlantic. Kamioka is relatively near to the geomagnetic equator and has a high geomagnetic cut-off of 12.1 GV. The average cut-off for the areas where the upward traveling neutrinos result is less than half, giving rise to the primary cosmic ray flux between 6 and 12 GeV proton energy. In the experiment, this up-down asymmetry is obscured by the low angular resolution for neutrinos with

energies less than 1 GeV, but it should be observable for intermediate energies by the Super-Kamiokande detector.

The East-West effect is shown in Fig. 6 by the azimuthal distribution of the flux. The agreement of the CORSIKA simulation with experimental results is on the same level as the agreement with the simulation of Honda.

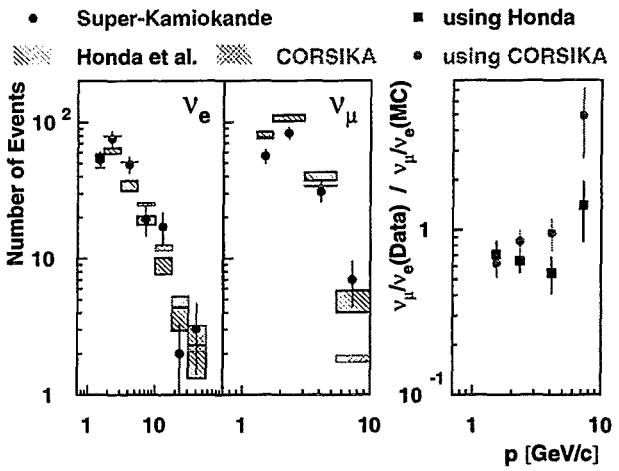

Fig. 7. Differential spectra of neutrino counts. The right figure presents the ratio of the experimental ratio $\nu_\mu/\nu_e(data)$ to the theoretical ratio $\nu_\mu/\nu_e(MC)$ of Honda (▪) and CORSIKA (•).

The preliminary results of CORSIKA for the differential spectra of neutrino counts and the ratio between the neutrino flavors are presented in Fig. 7. The observed difference is magnified for a direct comparison of the CORSIKA results with the results of Honda in Fig. 8. Especially the difference in the ratio $\nu_e/\overline{\nu_e}$ is remarkable. This ratio is directly coupled to the ratio μ^+/μ^-, the quantity where CORSIKA is explicitly verified and therefore the confidence for this result should be high.

5 Conclusion

CORSIKA, recently extended for the simulation of low energy primary particles including the precise description of all geographical influences, is now a program which allows the accurate simulation of neutrino fluxes in the energy range of the atmospheric neutrino anomaly. Various interaction models in CORSIKA can be checked by simulations of low energy muon fluxes. The muon charge ratio turns out to be the most critical test for the interaction models. The study proves that DPMJET has to be favored as the most reliable hadronic interaction model for the simulation of low energy neutrino fluxes.

The CORSIKA results for atmospheric neutrino fluxes are in a good overall agreement with the simulation of Honda, which are usually used for the interpretation of the atmospheric neutrino anomaly. Nevertheless the precise handling of all geographical factors reveals also deviations, mainly based on the difference in the geomagnetic cut-off between Kamioka and its antipode region which results in different

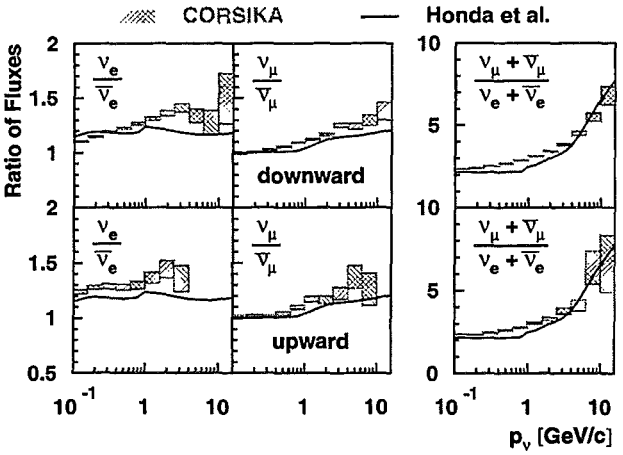

Fig. 8. Ratios between the vertical neutrino fluxes for downward (upper spectra) and upward (lower spectra) going neutrinos.

fluxes for up- and downward going neutrinos in the Super-Kamiokande detector. In conclusion, CORSIKA confirms the atmospheric neutrino anomaly but a more detailed analysis with an accurate detector simulation will presumably lead to modified oscillation parameters.

Acknowledgements. We are grateful to the Deutsche Forschungsgemeinschaft for the support of this work by the grant WE 2426/1-2 and to the International Bureau Bonn supporting enabling the personal exchange by the WTZ-Project RUM-14-97.

References

J. Alcaraz et al., Phys. Lett. B 472, 215–226, 2000.
J.M. Baxendale, C.J. Hume, M.G. Thompson, Jour. Phys. G 1, 781–788, 1975.
M. Bleicher et al., J. Phys. G: Nucl. Part. Phys. 25, 1859–1896, 1999.
H. Fesefeldt, Report PITHA-85/02, RWTH Aachen, 1985.
R.S. Fletcher et al., Phys. Rev. D 50, 5710–5731, 1994; J. Engel et al., Phys. Rev. D 46, 5013–5025, 1992.
Y. Fukuda et al., Phys. Rev. Lett. 81, 1562–1567, 1998; Phys. Lett. B 433, 9–18, 1998; Phys. Lett. B 436, 33–41, 1998.
S. Fukuda et al., Phys. Rev. Lett. 85, 3999–4003, 2000.
T. Futagami et. al. Phys. Rev. Lett. 82, 5194–5197, 1999.
L.J. Gleeson and W.I. Axford, Astrophys. Jour. 154, 1011–1026, 1968.
T. Hebbeker. et al., Proc. 30th Int. Conf. High Energy Phys., Osaka, July, 27th - Aug., 2nd, 2000.
D. Heck et al., Report FZKA 6019, Forschungszentrum Karlsruhe, 1998.
M. Honda et al., Phys. Rev D52, 4985–5005, 1995.
N.N. Kalmykov, S.S. Ostapchenko, and A.I. Pavlov, Nucl. Phys. B (Proc. Suppl.) 52B, 17–28, 1997.
J. Kremer et al., Phys. Rev. Lett. 83, 4241–4244, 1999.
J. Ranft, preprint hep-ph/9911213, 1999.
S. Tsuji et al., J. Phys. G: Nucl. Part. Phys. 24, 1805–1822, 1998.
B. Vulpescu et al., J. Phys. G.: Nucl. Part. Phys. 27, 977–991, 2001.
J. Wentz et al., these proceedings, 2001.
K. Werner, Phys. Rep. 232, 87–299, 1993.

Proceedings of ICRC 2001: 4213 © Copernicus Gesellschaft 2001

ICRC 2001

Simulation of the geomagnetic cut-off with GEANT using the International Geomagnetic Reference Field

J. Wentz[1], A. Bercuci[1,2], and B. Vulpescu[2,3]

[1]Forschungszentrum Karlsruhe, Institut für Kernphysik, Karlsruhe, Germany
[2]"Horia Hulubei" National Institute of Physics and Nuclear Engineering, Bucharest, Romania
[3]Universität Heidelberg, Physikalisches Institut, Heidelberg, Germany

Abstract. The International Geomagnetic Reference Field is used in a GEANT3 simulation to calculate the geomagnetic cut-off for cosmic rays entering in the Earth's magnetic field. The calculations are done in the back tracking method, where antiprotons start from the top of atmosphere and are tracked to outer space. The geomagnetic cut-off functions are estimated in momentum steps of 0.2 GeV for 131 directions in 1655 locations covering in a nearly equidistant grid the surface of the Earth. For special locations, where neutrino or low energy muon data have been measured, the cut-off functions are calculated in a fine grid of 21601 directions. The estimated geomagnetic cut-offs can be verified by the experimental results for primary protons and helium nuclei measured in different geomagnetic latitudes during the shuttle mission of the AMS prototype. These precise tables of the geomagnetic cut-off can be used in the frame of the CORSIKA code to calculate atmospheric muon and neutrino fluxes.

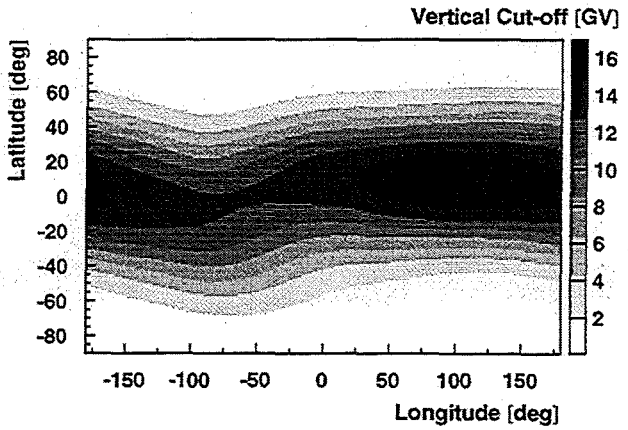

Fig. 1. World map of the vertical geomagnetic cut-off for an altitude of 112.3 km.

1 Introduction

A precise knowledge of the geomagnetic cut-off is a substantial ingredient to any calculation of low energy particle fluxes in the Earth's atmosphere. Especially the calculation of atmospheric neutrino fluxes for the investigation of the Atmospheric Neutrino Anomaly, requests precise, directional dependent tables of geomagnetic cut-off functions. In case of the Super-Kamiokande experiment in Kamioka, Japan, which delivers the most precise results on the Atmospheric Neutrino Anomaly (Fukuda et al., 1998), exist substantial differences between neutrinos produced above the detector and the neutrinos produced in the antipode region in the South Atlantic. This observation is commonly interpreted as clear evidence for neutrino oscillations.

Nevertheless there are also geographical differences between Japan and the South Atlantic which have to be taken in consideration. Due to the South Atlantic Magnetic Field Anomaly the geomagnetic cut-off in Japan is about 50 % higher than at the opposite point of the Earth. In addition, the experimental observation of a directional East-West dependency of the neutrino fluxes (Futagami et al., 1999) has to be accounted mainly to the asymmetry in the primary particle flux caused by the geomagnetic cut-off, while the deflection of charged secondary particles, like pions and muons in the atmosphere plays a minor, but not negligible role.

Correspondence to: J. Wentz (wentz@ik3.fzk.de)

2 The back tracking method for the calculation of the geomagnetic cut-off

The simulation of the geomagnetic cut-off is done in a complete microscopic calculation of possible proton trajectories in a realistic magnetic field for the Earth.

In principle there exist only four different types of particle trajectories:

- Start and end point of the trajectory are outside of the Earth's magnetosphere.

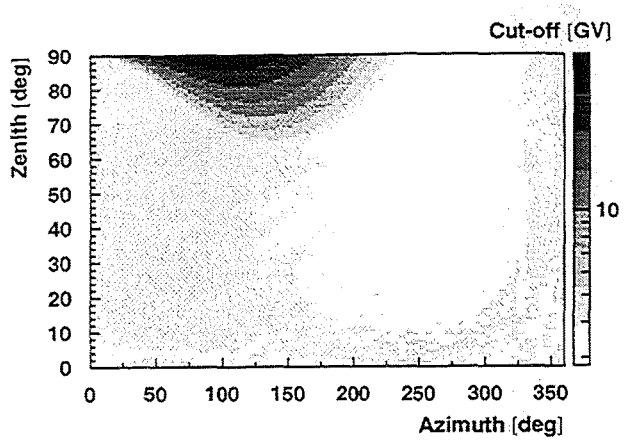

Fig. 2. The directional dependence of the geomagnetic cut-off for Fort Sumner, New Mexico (34.3° North, 104.1° West). The counting of the azimuth angle ϕ follows the convention used by the Super-Kamiokande detector, $\phi = 0°$ means looking to the South, $\phi = 90°$ to East, etc.

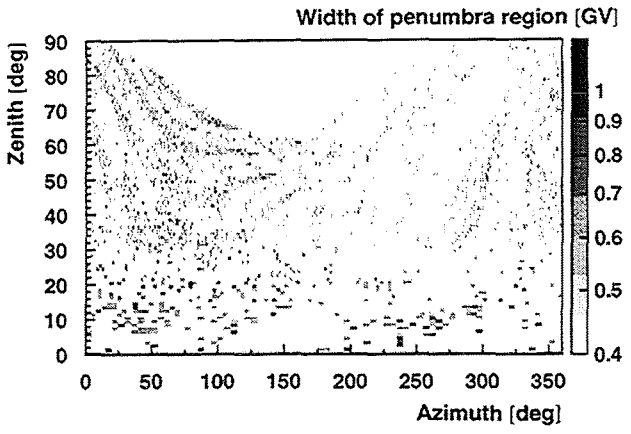

Fig. 3. The width of penumbra region, i.e. the difference between the open trajectory of lowest and the closed trajectory of highest momentum for Fort Sumner.

- The trajectory is enclosed in the magnetosphere, meaning that neither the Earth's surface nor the space outside the magnetosphere is reached ever.
- Start and end point of the trajectory are on the Earth's surface.
- The trajectory connects the outer space with the Earth's surface.

Only the trajectories of the last category represents particles above the geomagnetic cut-off. Thus the simulation of the geomagnetic cut-off can be reduced to the problem of calculating these trajectories. Due to the possibility of inverting the problem, the calculation of the geomagnetic cut-off can be done in the back tracking method, where antiprotons start from the Earth's surface and are tracked until they reach outer space, where the magnetic field vanishes, or they are bend back to the Earth.

Assuming an isotopic primary flux in outer space, which is only disturbed by the presence of the Earth and its magnetic field, the directional particle intensity can be calculated by taken out all forbidden trajectories, expressed in a table of the geomagnetic cut-off, depending on the geographical position, the local arrival direction and the momentum of the particle. This is a direct consequence of applying Liouville's theorem, as has been proved already by Lemaitre and Vallarta (1933) and Störmer (1930).

As starting altitude of the back tracking method, the top of atmosphere in an elevation of 112.3 km is selected. This particular choice of the starting altitude allows the direct use of the results within the CORSIKA simulation program (Heck et al., 1998). The magnetic field inside the Earth's atmosphere and the deflection of charged particle in it is handled in CORSIKA. CORSIKA is a code widely used for the simulation of extensive air showers. The extension by the tables of the geomagnetic cut-off allows now the simulation of low energy primary particles, too.

The antiprotons are tracked with the GEANT3 detector simulation tool (CERN, 1993). Due to the unusual dimensions for a GEANT simulation, the tracking precision has to be investigated. The tracking can be tested by reversing the trajectory, meaning that the momenta and charge of the antiproton are inverted, after the particle leaves the magnetosphere and the reversed particle is traced on its way back to the starting point. The error found by this method is some 10 m. Compared with an track length of typically 50000 km, this means a relative tracking error of $2 \cdot 10^{-7}$.

The Earth's magnetic field is described by the International Geomagnetic Reference Field (IAGA, 1992) for the year 2000. This allows a precise simulation of the penumbra region, too. While a pure dipole field leads always to a sharp cut-off, the precise irregular field with its inhomogeneities shows partly a diffuse region between the closed trajectory of highest and open trajectories of lowest momentum.

3 Calculations and results for the geomagnetic cut-off

For a world survey, geomagnetic cut-off functions have been simulated for 1655 locations, distributed nearly equidistant over the Earth's surface. The functions are simulated in 320 momentum steps for a momentum range between 0.4 and 64.4 GeV for 131 arrival directions. The momentum range covers all energies from the particle production threshold up to the maximum cut-off of a particle impinging horizontally at the geomagnetic equator from the East.

The simulation of the complete cut-off functions in fixed momentum steps allows to study the smoothness of the cut-off, the sometimes chaotic behavior of the cut-off in some regions and the existence of gaps for the primary protons well below the geomagnetic cut-off. The chosen resolution of 0.2 GeV/c is sufficient for the goal of the calculation of atmospheric particle fluxes. The obtained world map of the

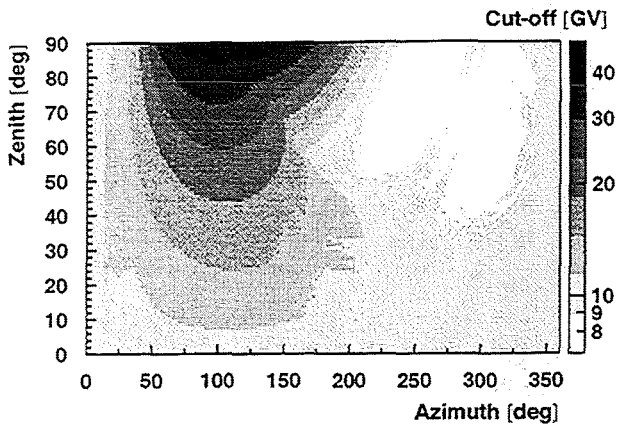

Fig. 4. The directional dependence of the geomagnetic cut-off for Kamioka (36.4° North, 137.3° East).

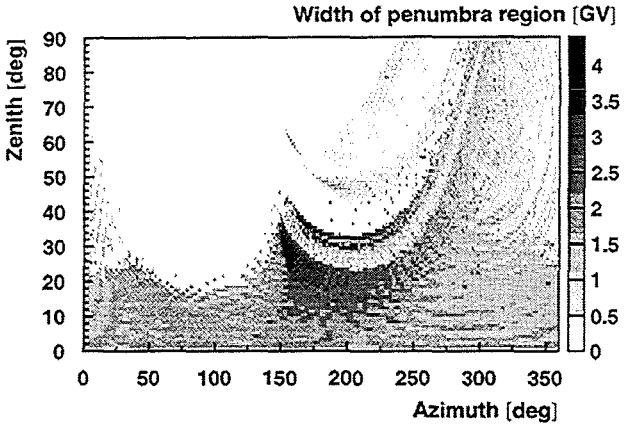

Fig. 5. The width of penumbra region for Kamioka site. Large values, i.e. bigger than 2 GeV indicate usually gaps in the cut-off.

vertical geomagnetic cut-off rigidity is shown in Fig. 1.

For some selected places, where experimental results exist for low energy muons or atmospheric neutrinos, precise tables of the geomagnetic cut-off with an angular resolution of 250 μsr have been calculated. As an example, the directional dependence of the geomagnetic cut-off for Fort Sumner in New Mexico is presented in Fig. 2. Fort Sumner has been used by many balloonborne detectors as launching place. Fig. 3 displays the sharpness of the cut-off, defined by the momentum difference between the first open and the last closed trajectory. In case of Fort Sumner the cut-off is relatively sharp, especially for directions with a higher cut-off the penumbra region is rather narrow or not found at all.

Fig. 4 shows the directional dependence of the geomagnetic cut-off for Kamioka. Remarkable is the strong deviation from a regular shape as observed in the calculation for Fort Sumner (Fig. 2) caused by some local irregularities of the magnetic field over Japan. This feature should be reflected in the azimuthal dependence of the particle intensity in Kamioka.

Interesting is the broad penumbra region in Kamioka. As can be seen in Fig. 5 the penumbra region has a width of more than 4 GV in some cases. This is about 4 times broader than in the calculation for Fort Sumner, while the maximum cut-off in both locations is practically comparable. Also the existence of cut-off gaps, meaning windows for primary protons some GV below the actual cut-off is observed.

Especially in the region around a zenith angle of 25° and an azimuth angle of 160° this effect is very pronounced and explains the chaotic behavior observed in the geomagnetic cut-off map. This feature is the result of higher order corrections of the magnetic field in this direction and can be accounted only in a detailed calculation, like the one presented here. Usual calculations with a pure dipole field used in many simulations of atmospheric particle fluxes fail completely in reproducing this effect. Due to the steep spectra of primary cosmic rays, the contribution of primary protons from such a gap may have a significant contribution to the neutrino flux from this direction.

4 The AMS results for the geomagnetic cut-off

Recently the geomagnetic cut-off was measured with high precision by the space shuttle mission of the AMS-prototype (Alpha Magnetic Spectrometer) (Alcaraz et al., 2000, 2001). Due to the inclination of 51.7° of the shuttle orbit, the shuttle passes geomagnetic latitudes from 0 to more than 1 rad. The experimental spectra of downward going protons and helium nuclei can be compared rather directly with the results of this simulation. Only a small correction in the order of 10 % for the difference in altitude between the top of atmosphere as assumed in CORSIKA and the shuttle orbit is applied.

In detail, the position of the shuttle and the detector acceptance are taken into account. Locations situated in the region of the South Atlantic Magnetic Field Anomaly are excluded, as they are in the published values of AMS. The primary isotropic spectra are simulated following the measured exponential energy spectra but being extrapolated downward to $E = 0$. The solar modulation is assumed to follow the parameterization of Gleeson and Axford (1968). Particles above the geomagnetic cut-off and being inside the detector acceptance are sorted out and compared with the measured spectra.

The spectra of primary protons for different regions of the geomagnetic latitude together with the simulation results are shown in Fig. 6, while Fig. 7 displays the corresponding results for primary helium nuclei. The lower flux of primary helium allows only the subdivision in 3 intervals of the geomagnetic latitude.

The excellent agreement of the actual cut-off calculation with the experimental results shows the high precision of the calculation, only the proton spectrum for geomagnetic latitudes $0.9 < \theta_{mag} < 1$ shows a slight difference, which has to be attributed to the smallness of the cut-off value which is more or less equal to the momentum steps of the cut-off functions. This disagreement has not any influence on the

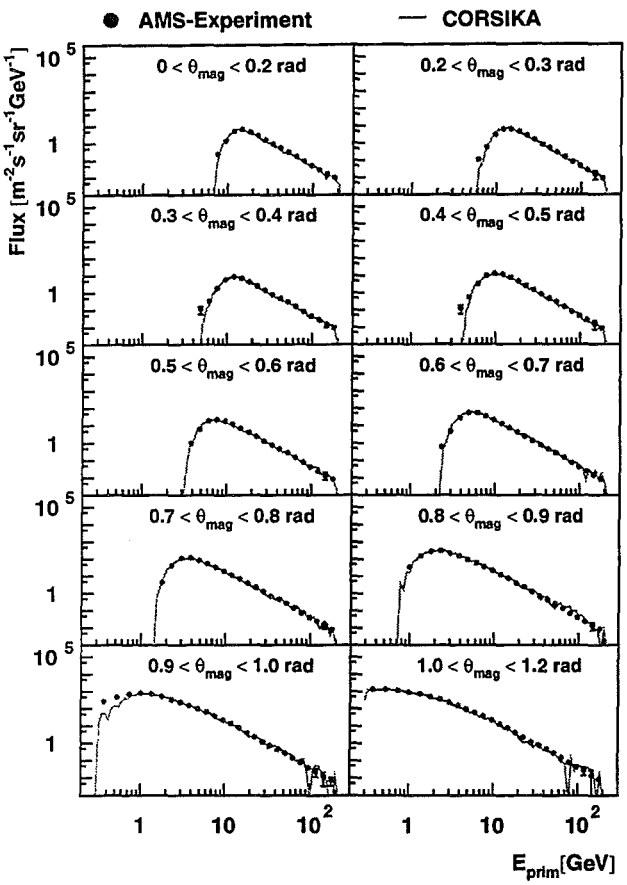

Fig. 6. Comparison of the AMS-results on primary protons for different intervals of the geomagnetic latitude with the results of the simulation of the geomagnetic cut-off.

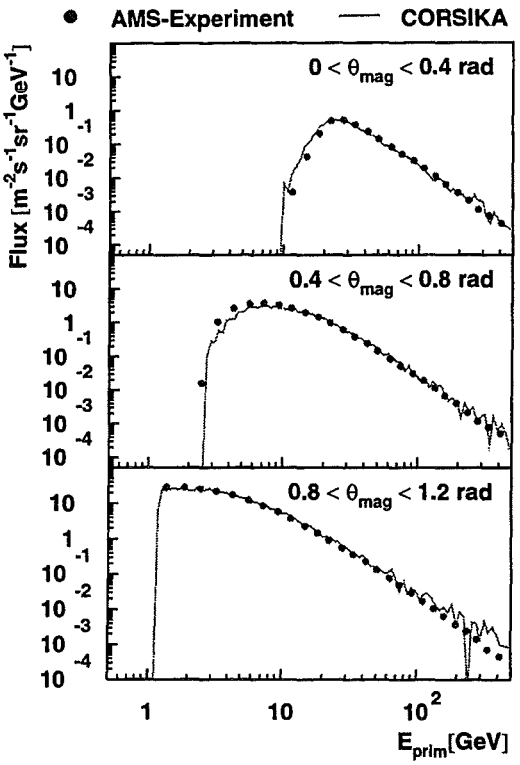

Fig. 7. Comparison of the AMS-results on primary helium nuclei with the results of the simulation of the geomagnetic cut-off.

simulation of atmospheric neutrino and muon fluxes, because the involved energies are already near the particle production threshold and the produced secondary particles hardly reach the Earth's surface with a valuable energy.

5 Conclusions

By using the International Geomagnetic Reference Field and the GEANT3 detector simulation tools, a program for simulating geomagnetic cut-off functions for primary cosmic ray particles at the top of the atmosphere was developed.

This program has been used to calculate a world wide table of geomagnetic cut-off functions for the epoch 2000 in momentum steps of 0.2 GeV/c, where the directional dependence is taken into account by simulating 131 different directions at any of the 1655 points on the Earth's surface.

The results of the calculation can be verified by the new results of the prototype of the AMS experiment. The measured spectra of primary protons and helium nuclei show a perfect agreement with the calculated values of the geomagnetic cut-off.

For selected locations on the Earth, where experimental results for low energy atmospheric neutrino or muon fluxes have been measured, detailed calculations in 21601 directions for the geomagnetic cut-off have been performed. The resulting cut-off tables have been used for the simulation of atmospheric muon fluxes and the simulation of the neutrino fluxes for Super-Kamiokande site with CORSIKA (Wentz et al., 2001).

Acknowledgements. We are grateful to the Deutsche Forschungsgemeinschaft for the support of this work by the grant WE 2426/1-2 and to the International Bureau Bonn supporting the scientific exchange by the WTZ-Project RUM-14-97.

References

J. Alcaraz et al., Phys. Lett. B 472, 215–226, 2000.
J. Alcaraz et al., to be published in Phys. Lett. B
CERN Program Library Long Writeups W5013, 1993.
Y. Fukuda et al., Phys. Rev. Lett 81, 1562–1567, 1998.
T. Futagami et al., Phys. Rev. Lett. 82, 5194–5197, 1999.
L.J. Gleeson and W.I. Axford, Astrophys. Jour. 154, 1011–1026, 1968.
D. Heck et al., Report FZKA 6019, Forschungszentrum Karlsruhe, 1998.
IAGA Division V, Working Group 8, AOS, Trans. AGU 73, 182, 1992.
G. Lemaitre and M.S. Vallarta, Phys. Rev. 42, 87–91, 1933.
S. Störmer, Zeitschr. f. Astrophys. 1, 237, 1930.
J. Wentz et al., this proceedings, 2001.